NORTHWESTERN UNIVERSITY

Embodiment in the Mammalian Whisker System:
How Anatomy and Biomechanics Facilitate Sensation and Movement

A DISSERTATION

SUBMITTED TO THE GRADUATE SCHOOL
IN PARTIAL FULFILLMENT OF THE REQUIREMENTS

for the degree

DOCTOR OF PHILOSOPHY

Field of Neuroscience

By

Chris S. Bresee

EVANSTON, ILLINOIS

September 2018

ABSTRACT

Embodiment in the Mammalian Whisker System:
How Anatomy and Biomechanics Facilitate Sensation and Movement

Chris S. Bresee

The rat whisker system has been a longstanding and fruitful model system for sensory neuroscience, because of its status as an "expert" active sensing system, and many open avenues of research still remain. One large-scale goal of the field is to "close the loop" from sensation to movement, modeling how sensory input is acquired, transformed and then used to select and refine specific motor programs, which in turn affect future sensation. This process must take into account the animal's embodiment – the morphology, physiology, biomechanics, and affordances of bodies – because the body is the intermediary between the brain and the world. The present work begins by describing the embodiment of the rat whisker system in detail, first at the level of individual whisker morphology and then at the level of the entire whisker array. However, as neuroscientists we are not only concerned with the morphology of organisms, but are also interested in behaviors and neural processing. Therefore, we also predict ways in which this embodiment can affect the rat's neural processing, first looking at whisker motor control, and then at sensory processing in second order sensory neurons. Finally, we begin to generalize this analysis to other species. We construct a similar morphological model of mice and contrast the findings with the model of the closely related rat, and the much more evolutionarily distant harbor seal. In all, this work documents intricate morphological relationships within the whisker system and predicts some mechanisms through which this morphology may facilitate active sensing, highlighting the importance of considering embodiment for sensory-motor neuroscience.

ACKNOWLEDGEMENTS

First, I would like to thank my thesis committee, Callum Ross, Jim Baker, and Dan Dombeck, and especially my adviser, Mitra Hartmann, for their unflagging mentorship and support of this work, through both challenges and smooth sailing. I would also like to thank some of the amazingly talented scientists I've had the privilege of getting to know and working with in the SeNSE Laboratory, many of whom have contributed invaluably to this work: Jasmine Ala'defa, Hayley Belli, Nick Bush, Hannah Emnett, Julia Freeman, Matt Graff, Jen Hobbs, Lucie Huet, Thomas Jansen, Pravin Kumarrappan, Yifu Luo, Brian Quist, Admir Resulaj, Anne Yang, Yan Yu, and Nadina Zweifel.

Also thanks those people who helped prepare me, personally, intellectually, and academically, for graduate school, including my former PI John Brigande, and my undergraduate advisers Steven St. John and Enriqueta Canseco Gonzales. Particular thanks go to Indira Raman and Callum Ross, for their roles in helping to show me there was still a place in academia for me during and after my transition.

Finally, thanks to my siblings Juan Espinet and Jennifer Bresee, for always being there to contribute emotional support and interesting philosophical conversation. Thanks to my partner, Liz Olney, for longstanding creative, economic, logistical, and emotional support, without which this work would not have been done. Thanks to my dear friend Keith Burman, for emotional support and important distraction. And thanks to my mom, Trudi Richards, for always supporting me in being who I am, no matter who that ends up being, for always being interested in my work, and for helping format this beast.

This work could not have been done without training and funding from the Moto-IGERT training program, and the NUIN-MRS T32 Training Program in the Neurobiology of Movement and Rehabilitation Sciences.

TABLE OF CONTENTS

LIST OF FIGURES

LIST OF TABLES

Chapter 1: Introduction

1.1 Motivation and Significance

1.1.1. Embodiment

The brain processes sensory stimuli, and gives motor commands, but the body is the intermediary between the brain and the world. Embodiment here refers to the many ways an animal's physical body affects how it interacts with the world, and includes the anatomy, physiology, mechanics, and affordances of musculoskeletal systems and sensory accessory structures. All animals have a particular embodiment, and information about this embodiment is frequently essential in interpreting information about neural responses.

1.1.2. Investigating the sense of touch

Sensory perception and movement are essential to an animal's survival, so a greater understanding of these faculties has the potential to inform our understanding of evolution and behavior. Because much of the brain is devoted to sensory and motor tasks, understanding the interplay between sensation and movement is also essential to understanding the function of the brain and how an animal interfaces with the world. There are myriad ways for animals to sense and move, but the sense of mechanical touch has a particularly close relationship with movement, arguably second only to proprioception. However, unlike proprioception, the sense of mechanical touch provides the animal with significant information about external stimuli. This ability of touch to inform about the external world, combined with the interrelationship between touch and movement, means that an understanding of the sense of touch is integral to an understanding of the interplay between an animal and its environment.

1.1.3. Whisker-based tactile sensing

An understanding of whisker-based tactile sensing in particular is important if we wish to understand the overall sense of mechanical touch. The importance of whiskers is underscored by two facts: first, that

many members of virtually all extant mammalian clades have whiskers (Pocock 1914, Ahl 1986, Muchlinski 2010), and second, there is evidence that the evolution of tactile hairs was involved in the cranial expansion of our ancestors as they diverged from more reptile-like cynodonts and stem mammaliaformes (Rowe, Macrini et al. 2011).

All hair shafts, whiskers included, have no sensors along their length (Chernova 2006, Sarko, Rice et al. 2011), yet the tip of the hair feels like part of one's body because the base is held inside a sensitive follicle, where the sensory receptor cells can be deformed in response to the deflection of the hair shaft (Ebara, Kumamoto et al. 2002). Interposing a sensory accessory structure like a whisker between the stimulus and mechanoreceptor introduces the possibility that various aspects of the energy affecting the sensor can be magnified or dampened. This potential role for filtering sensory stimuli highlights the need to consider embodiment when researching sensation, and the advantage of using the whisker system for such investigation.

Tactile hairs can be considered a submodality that is intermediate between proximal and distal, in that they allow the animal to tactually sense the nearby external environment that may not be immediately touching the rest of the animal. Inferences about distal stimuli based on proximal effects (deformations of mechanoreceptors within the follicle) highlight remarkable spatial processing abilities. The mechanisms of such spatial inferences are as yet poorly understood, but may be analogous to the human ability to sense stimuli at the tip of a pen one is using to write. Additionally, the hairs that actually interact with external objects are composed of non-living cells and tissue that grow, wear, and shed periodically and therefore may change shape or length as they interact with the environment. The ability of the nervous system to make consistent sensory inferences using these mutable structures is likewise remarkable, and may be analogous to the human ability to sense stimuli at the tip of any given, differently shaped pen. The mechanisms underlying such inferences are as yet poorly understood, though there is also not yet enough

of a basis of knowledge to tackle these questions directly. This dearth of knowledge is in part what provides motivation for basic science like the experiments described in this thesis.

Taken together, the ubiquity of whiskers in mammals, their potential for filtering, their remarkable spatial processing ability, and robustness of the system to morphological changes, mean that whiskers represent a sensory system for which it is particularly important to describe the mechanics, morphology, and physiology, and in which investigating effects of these variables may be particularly fruitful.

1.1.4: Spatial information in touch

In order to make inferences about stimuli interacting with touch receptors, the nervous system must incorporate spatial information. Sensory systems consist of organized arrays of sensors, and many modalities take advantage of such peripheral organization to encode some spatial information based on receptor location on the epithelium (Penfield 1937, Hemmen 2002). In the sense of touch, somatotopy can represent relative spatial relationships, especially at early levels (Erzurumlu, Murakami et al. 2010), similarly to vision encoding stimulus location retinotopically (Cang, Renteria et al. 2005). However, tactile sensors move in relation to each other, as the skin deforms or the animal actuates its vibrissae (whiskers) (Berg and Kleinfeld 2003, Huet and Hartmann 2014). Though there is a spatial correlation between any two touch receptors, given that animals' bodies deform within certain bounds, this correlation will necessarily not be as strong as the correlation between two photoreceptors fixed on a retina that does not change shape. This less-than-perfect spatial correlation means that inferring the spatial locations of an array of tactile sensors is not necessarily a straightforward task for the nervous system (Mehta S. B., Whitmer D. et al. 2007, Ahissar and Knutsen 2008, Kleinfeld and Deschenes 2011).

1.1.5: Embodiment and sensation

This flexible-yet-constrained spatial relationship between sensors especially holds true in the murine vibrissal system, which is a common model for somatosensory processing. In this system, the vibrissae sprout from a grid-like pattern of follicles in the cheek, with rows designated by letters, and columns designated by numbers (Brecht, Preilowski et al. 1997, Haidarliu, Simony et al. 2010, Mitchinson, Grant et al. 2011, Grant, Delaunay et al. 2017). However, since the vibrissae are under active control by the animal, the relative spatial arrangement of the tips changes drastically during movement. Therefore, the brain cannot rely solely on sensor position in the grid or in a follicle to encode stimulus location in the external world. Rather, the shape and movement of an animal's body fundamentally affect the spatial information available to the system. Considering motion and embodiment is therefore imperative to understanding mechanical touch, as these factors have the potential to influence the input, filtering, and interpretation of tactile information.

The overarching goal of this thesis is therefore to explore contributions of embodiment and active movement to spatial processing in the sense of touch.

1.2 Background:

1.2.1: Sensation and movement are interrelated

Senses relating to the position and movement of the body, such as balance and proprioception, are of course inextricably related to movement. However, senses mostly concerned with encoding the external environment are also highly affected by and dependent on movement. For example, human vision relies on natural nystagmus to ensure that photoreceptors are not saturated (Hartline 1937, Ahissar and Arieli 2001), and on saccades and fixations to actively explore a visual scene (Eckstein 2011). In most terrestrial vertebrates olfaction is intricately linked to respiration (Hillenius 1994, Rajan, Clement et al. 2006, Rowe, Macrini et al. 2011, Moore, Deschenes et al. 2013), and thus to the movement of the diaphragm and some

facial muscles (Haidarliu, Kleinfeld et al. 2013). Audition also has important active aspects, even in non-echolocating species. For example, movements of the pinnae and/or head are important in sound localization (Thurlow and Runge 1967, Populin and Yin 1998). Even the sense of taste frequently involves rhythmic licking (Weijnen 1998) or other active exploration of stimuli inside the mouth with the tongue. The sense of touch is no exception, with active movements of tactile sensors allowing the collection of particularly rich information about the external world (Hartmann 2009).

Perhaps the most striking example of the importance of self-generated movement for sensation is found in sensory substitution experiments done by Paul Bach-y-Rita. These experiments involve using assistive devices to transduce stimulus energy in a novel way, for example, using a video camera to capture light, and sending this information to an array of electrodes that tactually stimulate the tongue (Bach-y-Rita 2003). The brightness of a given coordinate in space is then represented to the user as the magnitude of stimulation at a given electrode, resulting in a two-dimensional pixelated grayscale scene "drawn" on the tongue. Crucially, Bach-y-Rita describes participants being able to form meaningful percepts from this novel sensory input only if the participant has control of the movements of the camera. Sensory substitution is a somewhat artificial case, but still is useful for demonstrating the importance of sensorimotor contingencies in forming coherent perceptions, in that it demonstrates that when no consistent sensorimotor contingencies can be established, no coherent perception can occur.

1.2.2: Rats as a model system

Rats can be considered "whisker specialists" (Grant, Haidarliu et al. 2013), and have been described as "experts" in tactile sensation (Diamond, von Heimendahl et al. 2008, Diamond and Arabzadeh 2013). They rely heavily on their whiskers during locomotion (The, Wallace et al. 2013, Arkley, Grant et al. 2014), sensing airflow (Yu, Graff et al. 2016), and even during social interactions (Wolfe, Mende et al. 2011). Krogh's principle states that "For many problems there is an animal on which it can be most conveniently

studied" (Lindstedt 2014), because effects within a particular system will be easier to find in organisms in which that particular faculty is emphasized.

The relatively simple peripheral organization of sensors is also a great advantage. The whiskers grow from follicles arranged in a grid-like array in a specialized area of the upper check, called the mystacial pad. This peripheral grid patterning is recapitulated in the somatotopy of many whisker-responsive areas of the brain, from the brainstem nuclei, through thalamus, and to cortex (Chapin and Lin 1984, Ma 1991, Petersen 2007, Erzurumlu, Murakami et al. 2010). The somatotopy underlines the spatial importance inherent in the system, and presents some technical advantages for targeting during neural recording, and for confirmation of receptive fields.

The comparatively simple motor plant of the whisker pad is also an advantage, especially as compared to limb or digit musculature. Rats and mice move their whiskers rhythmically in the rostrocaudal direction, sampling the shapes and textures of the external world at about 5 to 25 Hz (Carvell and Simons 1990, Knutsen, Pietr et al. 2006). These movements are executed by specialized facial musculature, both intrinsic and extrinsic to the mystacial pad (Haidarliu, Simony et al. 2010). Intrinsic muscles primarily actuate one follicle, and subserve protraction, while extrinsic muscles actuate multiple follicles, participate in retraction, and can change the relative spacing of the whiskers (Berg and Kleinfeld 2003, Hill, Bermejo et al. 2008). Together this vibrissal motor plant allows a diversity of whisker exploratory behavior, which in turn allows changes in the sensory volume and sensing resolution (Huet and Hartmann 2014), asymmetrical whisking (Towal and Hartmann 2008), and directed attention (Mitchinson and Prescott 2013).

This relatively simple motor plant is associated with comparatively reduced degrees of freedom of movement, especially when compared to limbs or hands. The comparatively simple movement results in relatively easily observed and documented whisker behavior (Grant, Mitchinson et al. 2009, Hobbs, Towal

et al. 2016), even in what approaches naturalistic settings (Arkley, Grant et al. 2014). Also, relatively computationally tractable models can be used to describe and predict certain behaviors (Huet and Hartmann 2014, Hobbs, Towal et al. 2015, Huet and Hartmann 2016).

The small number of sensors (individual whiskers), and their organization, is distinctly advantageous for study in that it results in the ability to continue to observe the sensors while the animal is actively using them or while the experimenter manipulates them (Harvey, Bermejo et al. 2009). A whisker's slender form factor means that the point of interaction with a stimulus, and how this interaction affects the whisker, is not occluded by the sensor itself, as is commonly the case with fingers.

There also exist distinct parallels between the whisker and hand tactile sensing systems that result in rats being advantageous for studying touch, something that could allow principles discovered using the rat to generalize to human sensing. In the mechanical touch system of the mammalian limb, mechanoreceptors in the skin synapse with or are the end organs of primary sensory neurons, which have cell bodies in the dorsal root ganglion. These cells send axons through the dorsal columns to secondary sensory neurons in medullar nuclei, which send axons to tertiary sensory neurons in the thalamus, which themselves send axons to cortical neurons (McGlone and Reilly 2010). Similarly, in the whisker system, mechanoreceptors in the follicle send information to primary sensory neurons in the trigeminal ganglion, which send axons to trigeminal brainstem nuclei, and then to thalamus and cortex.

Taken together, the sensory expertise of rats, simple whisker musculature, small number of whiskers, simple and stereotyped whisker organization, and parallels with touch systems in humans, all make the rat whisker system an excellent model system in which to study touch and active sensation.

1.2.3: Whisker system information flow: ascending sensory information

When a whisker collides with an object, mechanoreceptors in the follicle are deformed, and send signals to neurons in the trigeminal ganglion. Each follicle has multiple mechanoreceptors, and each neuron in the ganglion gets information from one follicle only (Kerr and Lysak 1964, Zucker and Welker 1969). Ganglion neurons therefore have receptive fields consisting of one whisker. Ganglion cells then project to the trigeminal nuclei in the brainstem (Hayashi 1980), forming the beginnings of multiple parallel pathways to the cortex. The local circuitry of individual nuclei is not well documented, though some cells' receptive fields and targets are known. Two well-documented nuclei are the beginning of the paralemniscal pathway, the rostral spinal trigeminal nucleus interpolaris (SpVir), and the beginning of the lemniscal pathway, the principal trigeminal nucleus (PrV) (Erzurumlu, Bates et al. 1980, Peschansk 1984, Williams, Zahrn et al. 1994, Veinante, Jacquin et al. 2000). Neurons in PrV have receptive fields that encompass one principle whisker, and a few neighboring surround whiskers (Erzurumlu and Killackey 1980, Williams, Zahrn et al. 1994, Veinante, Jacquin et al. 2000), while neurons in the rostral compartment of SpVi have large multi-whisker receptive fields spanning one or more whisker rows, and many columns (Nord 1968, Jacquin, Barcia et al. 1989, Furuta, Timofeeva et al. 2008).

Ascending signals then go to the thalamus. Cells from PrV synapse in barreloids of the ventral posterior medial nucleus (VPM) (Veinante and Deschenes 1999), while cells from SpVir send axons to the posteromedial nucleus (PoM) (Jacquin, Barcia et al. 1989, Veinante, Jacquin et al. 2000). From there both pathways project to barrel cortex, (Bureau, von Saint Paul et al. 2006, Meyer, Wimmer et al. 2010). The paralemniscal pathway also projects to secondary somatosensory cortex (S2) and primary motor cortex (M1) (Koralek, Jensen et al. 1988, Petreanu, Mao et al. 2009). These connections will be explored in more depth in subsequent sections.

1.2.4: Whisker system information flow: modulation of secondary sensory neurons

The trigeminal ganglion receives only input from peripheral mechanoreceptors, but the brainstem nuclei receive both this input, through the ganglion neurons, and modulatory input. Modulation related to general attention and arousal includes excitatory inputs from serotonergic projections from the raphae nuclei, noradrenergic projections from the locus coeruleus, and cholinergic projections from the pedunculopontine tegmental nucleus and the laterodorsal tegmental nucleus (Bosman, Houweling et al. 2011).

The spinal trigeminal nuclei receive some sparse inhibitory motor-related input from the pontomedullary reticular formation (RF), possibly from the vibrissal-related region of the intermediate band of the reticular formation (vIRT), the putative whisking central pattern generator (Moore, Deschenes et al. 2013, Deschenes, Takatoh et al. 2016). In contrast, PrV receives excitatory input from primary sensory neurons in the mesencephalic trigeminal nucleus that respond to whisker movement (MeV), and no input from the RF (Matesz 1981, Ndiaye, Pinganaud et al. 2000). Together, these movement-related modulatory inputs may reflect a greater participation of the paralemniscal pathway in whisking-related sensory modulation, while the lemniscal pathway may carry information relating to both internally and externally generated whisker movement.

Many intersubnuclear projections exist, and are mainly inhibitory (Jacquin, Golden et al. 1989, Furuta, Timofeeva et al. 2008, Martin, Negredo et al. 2014). The projection from SpVi to PrV is modulated by descending projections from primary somatosensory cortex (S1) that probably contain information related to whisking, contributed by M1 inputs to S1 (Woolston, La Londe et al. 1983, Furuta, Urbain et al. 2010). This connection theoretically allows for modulation of sensory sensitivity based on the intentional movement of whiskers.

Taken together, the modulation of the secondary sensory neurons in the trigeminal brainstem paints a picture of complex early sensory processing that is sensitive to the overall arousal state of the animal, as well as the rhythmic activity of whisker muscles, and to whisker movement.

1.2.5: Whisker system information flow: modulation at higher levels

From the trigeminal brainstem, ascending sensory information is mainly processed by thalamic nuclei, with the lemniscal pathway from PrV projecting to the ventral posterior medial nucleus (VPM), and the paralemniscal pathway projecting to the posteromedial nucleus (PoM). Other projections from brainstem to thalamus exist, besides the lemniscal and paralemniscal described above, but these additional parallel pathways are less well studied, and are outside the scope of this thesis.

Cells in the VPM thalamus respond with short latencies to whisker deflection, and form barreloids with single whisker receptive fields (Haidarliu and Ahissar 2001). These barreloids contain cells responsive to particular angular deflection directions, with multiple directions represented in each barreloid, and target layer 4 (L4) of S1 (Timofeeva, Merette et al. 2003).

Cells in the PoM thalamus respond with longer latencies, have multiwhisker receptive fields, and do not form barreloids (Ahissar, Sosnik et al. 2000). These cells target modulatory layers (L5, L3, and L1) of S1 and S2 cortex (Bureau, von Saint Paul et al. 2006, Petreanu, Mao et al. 2009, Meyer, Wimmer et al. 2010). The paralemniscal pathway also projects to the basal ganglia and cerebellum, and participates in reflex loops through the superior colliculus (Bosman, Houweling et al. 2011). One well documented modulatory input to the paralemniscal pathway is the zona incerta (Zi). This nucleus gates PoM with constitutively inhibitory input, but is itself inhibited SpVir, PrV, and M1. This inhibition of Zi disinhibits PoM (Urbain and Deschenes 2007), and could allow more information flow through the paralemniscal pathway during active whisking than during passive contact.

The reticular formation is also an important modulator of both the lemniscal and paralemniscal pathways, participating in negative feedback loops that allow adaptation to weak stimuli, so may contribute to bottom-up mechanisms of attention and salience (Bosman, Houweling et al. 2011).

While modulation at the level of the brainstem can be interpreted as mainly incorporating movement and arousal state information, modulation at the level of the thalamus can be interpreted as beginning the process of magnifying or diminishing the representation of different aspects of sensory stimuli that may be represented in conscious perception at the level of the cortex.

From the thalamus, the lemniscal pathway sends output to Layer 4 of the cortex, the input layer to the cortical column. The paralemniscal pathway projects to the output layer of the cortex, layer 5 (L5), and layer 1, which is up-regulatory to L5. This neuroanatomy positions the paralemniscal pathway as a modulator of the lemniscal information being processed by the cortical column. One general function of sensory cortex seems to be related to conscious sensory perception, but though the microcircuitry at this level is very well documented, the overall behavioral significance of particular aspects of the cortical circuit remain elusive.

1.2.6: Whisker system information flow: motor centers

The lower motor neurons that control the whiskers mainly reside in the lateral facial nucleus, though a small population exists in the hypoglossal nucleus (Mameli, Stanzani et al. 2008). Many higher motor areas participate in whisker control, with a brainstem central pattern generator (Deschenes, Takatoh et al. 2016), various reticular nuclei, pontine respiratory nuclei, the superior colliculus, the nucleus ambiguous, the red nucleus, the trigeminal nuclei, and M1 (though sparsely) all projecting to the facial nucleus directly (Bosman, Houweling et al. 2011). The cerebellum and basal ganglia participate as well, but mainly exert control of primary motor neurons via their effects on other intermediary structures.

The main driver of activation of primary motor neurons in the lateral facial nucleus remains unknown. Some prominent candidates include M1 (Grinevich, Brecht et al. 2005), which induces rhythmic whisker movements when stimulated (Sreenivasan, Karmakar et al. 2015), or the superior colliculus, which induces sustained protraction (Hemelt and Keller 2008). Other premotor regions include the trigeminal nuclei, vestibular nuclei, and various reticular nuclei, with the lateral paragigantocellular nucleus perhaps contributing significant excitatory drive (Takatoh, Nelson et al. 2013).

One other highly important region for inhibition of the primary motor neurons is the putative central pattern generator for rhythmic whisking, the vibrissal related region of the intermediate reticular formation (vIRT). This region sends inhibitory input to the lateral facial nucleus during retraction, inhibiting neurons that project to intrinsic whisker muscles and therefore halting protraction (Deschenes, Takatoh et al. 2016). The vIRT gets strong input from the pre-Bötzinger complex (preBötC), a structure involved in breathing, resulting in the entrainment of the whisking and breathing rhythms. While the vIRT only has ipsilateral connections to the facial nucleus, each preBötC has commissural connections to the contralateral preBötC, and so is able to synchronize drive to each vIRT and thus bilaterally affect whisking.

1.3 Overview:

1.3.1: Modeling the whisker system

As discussed above, the anatomy of sensory and motor structures is important to consider when investigating the effects of embodiment on sensation. One important tool in this investigation is making models of the system. Models can allow detailed quantitative descriptions of particular aspects of a system, and can also allow manipulation of the system in ways that may not be feasible, or even physically possible, in the real world. This ability to cleanly manipulate a simulation of a system also offers interesting possibilities for testing hypotheses when comparing the simulated and real-world systems.

Many of the studies presented in this thesis use this general approach: 1) make detailed anatomical observations, 2) describe these observations using statistical models, and 3) create three-dimensional digital models using these descriptions. Manipulations and simulations of the models are outside the scope of many of the studies reported here, but one study (Chapter 5) does incorporate simulations of the observed system, and others (Chapters 3, 4, and 7) make predictions for results of hypothetical manipulations. One study (Chapter 6) compares electrophysiological results of manipulating the system in the real world to modeled results of electrophysiological activity, to assess descriptive power of the model.

1.3.2: Brief outline

Chapter 2 begins this thesis with a study that underscores rats' status as whisker "experts," showing that rats can use their whiskers to sense airflow in addition to the more well-established faculty of mechanical touch discussed above. Chapters 3 – 7 then together serve to characterize the anatomy and sensory processing of the mammalian vibrissal system. The third chapter characterizes the geometry of individual rat whiskers. The fourth chapter characterizes the anatomy of the entire rat whisker array. The fifth chapter investigates motor effects, and shows that the geometry of the follicles and muscles in the rat whisker pad facilitates equivalent motor control across the array. The sixth chapter investigates sensory processing, and shows how the brain might make sense of inputs from these multiple diverse sensors. Finally, in the seventh chapter we come full circle and characterize the array of the mouse, beginning to generalize this approach of modeling and simulating anatomy to other species. Chapter 8 concludes the thesis with a summary of its contributions, main findings, and some suggestions for directions for future work.

Chapter 2: Whiskers aid anemotaxis in rats

This chapter was published in Science Advances as: Yu Y*, Graff MM *, Bresee CS, Man YB, Hartmann MJZ (2016) Whiskers aid anemotaxis in rats. Sci. Adv. 2016; 2: e1600716

*authors contributed equally

2.1. Abstract

Observation of terrestrial mammals suggests they can follow the wind (anemotaxis), but the sensory cues underlying this ability have not been studied. Here we identify a significant contribution to anemotaxis mediated by the whiskers (vibrissae), a modality previously only studied in the context of direct tactile contact. Five rats trained on a five-alternative forced-choice airflow localization task exhibited significant performance decrements after vibrissal removal. In contrast, vibrissal removal did not disrupt performance of control animals trained to localize a light source. Importantly, the performance decrement of individual rats was related to their airspeed threshold for successful localization: animals that found the task more challenging relied more on the vibrissae for localization cues. Following vibrissal removal rats deviated more from the straight-line path to the air source, choosing sources further from the correct location. Our results indicate that rats can perform anemotaxis and that whiskers greatly facilitate this ability. Because air currents carry information about both odor content and location, these findings are discussed in terms of the adaptive significance of the interaction between sniffing and whisking in rodents.

2.2. Introduction

The sensory cues that underlie anemotaxis in terrestrial mammals have not been studied. Studies in multiple other species, however, implicate hair and hair-like appendages in flow sensing behaviors. The antennae of arthropods, the sensory hairs of insects and bats, and the whiskers (vibrissae) of pinnipeds are all used as flow sensors, mediating flight maneuvers (Budick, Reiser et al. 2007, Sane, Dieudonne et al.

2007, Casas and Dangles 2010, Marshall, Chadha et al. 2015), escape responses (Casas and Dangles 2010), wake tracking (Dehnhardt, Mauck et al. 1998, Dehnhardt, Mauck et al. 2001), and contributing anemotaxic or rheotaxic information during olfactory search (Rust and Bell 1976, Baker and Kuenen 1982, Zimmerfaust, Finelli et al. 1995, Vickers 2000, Koehl 2006, van Breugel and Dickinson 2014). In analogy to these systems, the vibrissae of the terrestrial mammals would be a prime candidate to serve as flow-sensors.

Two additional lines of evidence suggest a role for vibrissae in flow sensing. First, the mechanical response of a rat vibrissa to airflow contains information about both flow direction and magnitude (Yu, Graff et al. 2016). A vibrissa bends in the direction of airflow, with an average bending amplitude that correlates with airspeed, and then vibrates around its new deflected position (Yu, Graff et al. 2016). Second, whisking and sniffing behaviors are synchronized by activity from the PreBötzinger nucleus (Moore, Deschenes et al. 2013), conferring a degree of temporal precision that could align anemotaxic information from the vibrissae with odorant information during olfactory search. Together, these findings suggest that anemotaxic information from the vibrissae may be of high behavioral salience even when multiple anemotaxic cues are available (e.g., from glabrous skin or pelage hairs). We therefore tested the hypothesis that the vibrissae contribute significantly to the ability of rats to localize airflow.

2.3. Results

Five rats (female, Long Evans, ~3 months) were trained to localize airflow emanating from one of five fans placed around the circumference of a circular arena, spaced ~30° apart as measured from the arena center (Figure 2.1A, and figs. A.1.S1 and A.1.S2). Each day of training included at least 45 trials; only one of the five fans was on during any given trial. On each day the sequence of fans was randomized while ensuring that each fan was on nine times (see Materials and Methods for details). At the start of each trial a door opened to allow the rat to leave a holding box, enter the arena, and localize the airflow source by running

towards a hole in front of the fan. Airspeed at the hole was 1.1±0.3 m/s and airspeed at the door was 0.5±0.2 m/s (Figure 2.1B).

In a preliminary study we found that rats could circumvent the task by circling around the arena, exploring several fans in turn, and making a decision only when extremely close to the correct fan. To prevent this behavior, a correct choice required rats first to cross a virtual checkpoint 21.6 cm (8.5 in) in front of the hole (Figure 2.1A). If the rat both crossed the checkpoint and approached the hole, an audible click signaled the delivery of a water reward from a fluid port beneath the table. To obtain the reward the rat had to go down a hole and follow a tunnel beneath the table to the water port. If the rat performed the trial correctly it received a second reward for running up a ramp from the water port back to the holding box. Another trial began after a ~10 second inter-trial interval.

Because a trial was counted as correct only if the boundary of the hole and the checkpoint were both crossed, all rats tended to follow a nearly straight-line path to the hole in front of the airflow source (Figure 2.1C). Movie S1 shows examples of both correct and incorrect trials.

Upon performing the task for ten consecutive days at a success rate above 55% (where chance = 20%), with no single day lower than 40%, a complete bilateral vibrissectomy was performed and the rats were then tested for an additional ten days. A control group of three rats was trained on the same task, except the fans were replaced with a white light source. The control group underwent the same bilateral vibrissectomy. Careful acclimatization procedures (see Materials and Methods for details) allowed us to cut off (trim) all vibrissae in both groups of animals without anesthesia, using only gentle manual restraint. All vibrissae were trimmed to a length less than 2 mm; this trimming included all macrovibrissae and the longer of the microvibrissae (see Materials and Methods for more detail). We observed no significant

group-wise change in locomotor speed or pausing of the rats after vibrissal trimming. Descriptive statistics for this analysis are shown in table A.1.S1.

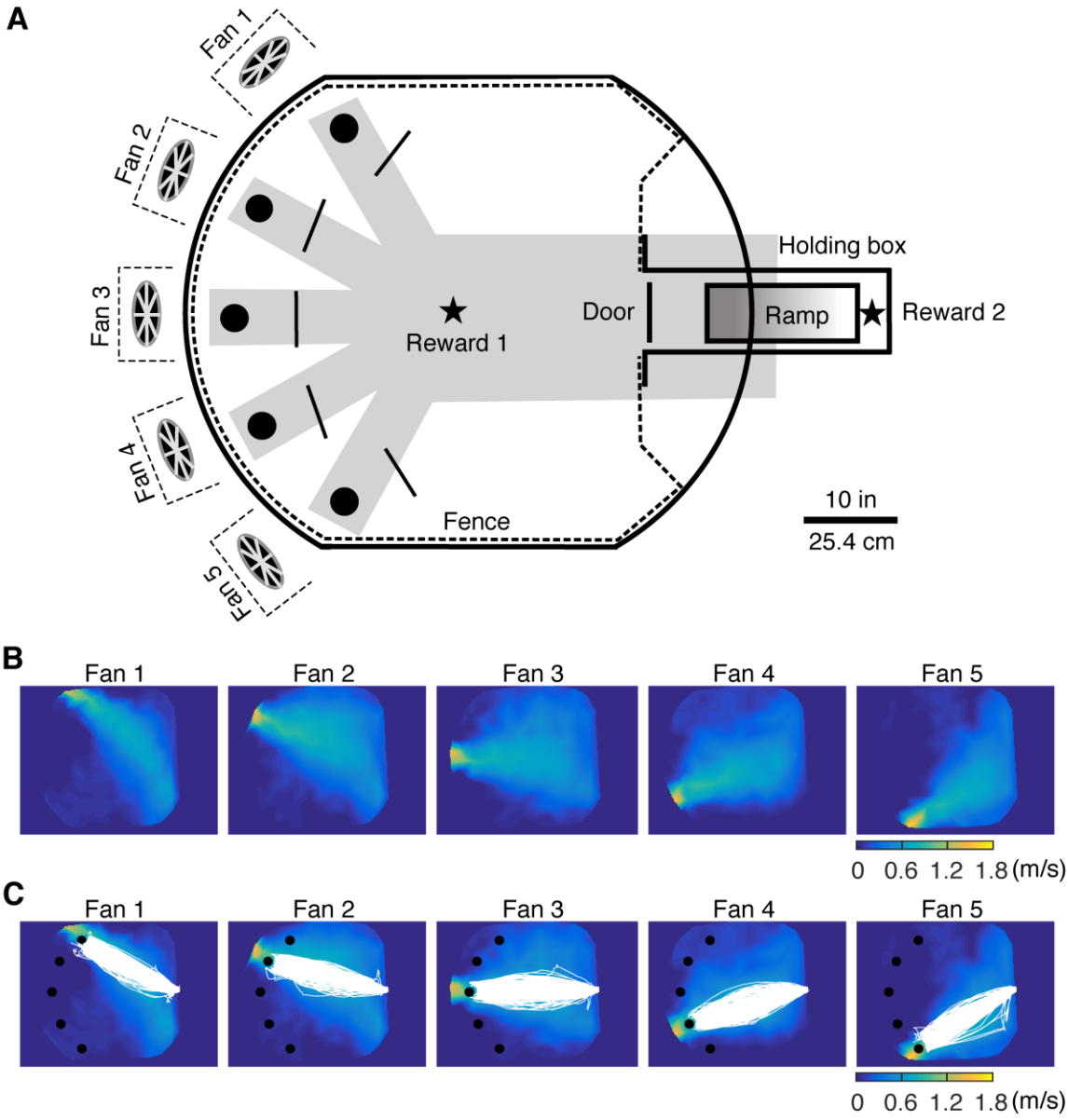

Figure 2.1. Rats were trained to localize airflow or light. (A) The arena's entrance door is opposite five fans, placed around the arena circumference. A fence confines the rat. Black solid lines indicate checkpoints. Five holes (black circles) allowed access to tunnels beneath the table (gray shadow) that led to a water reward port (Reward 1, black star), activated only for correct trials. A ramp led back to the holding box where a second reward (Reward 2, black star) was given for correct trials. (**B)** Airspeed colormap shows that the maximum speed lies approximately along the line connecting fans and the entry door. **(C)** Five rats' trajectories (all correct trials before vibrissal removal) superposed on airspeed colormap.

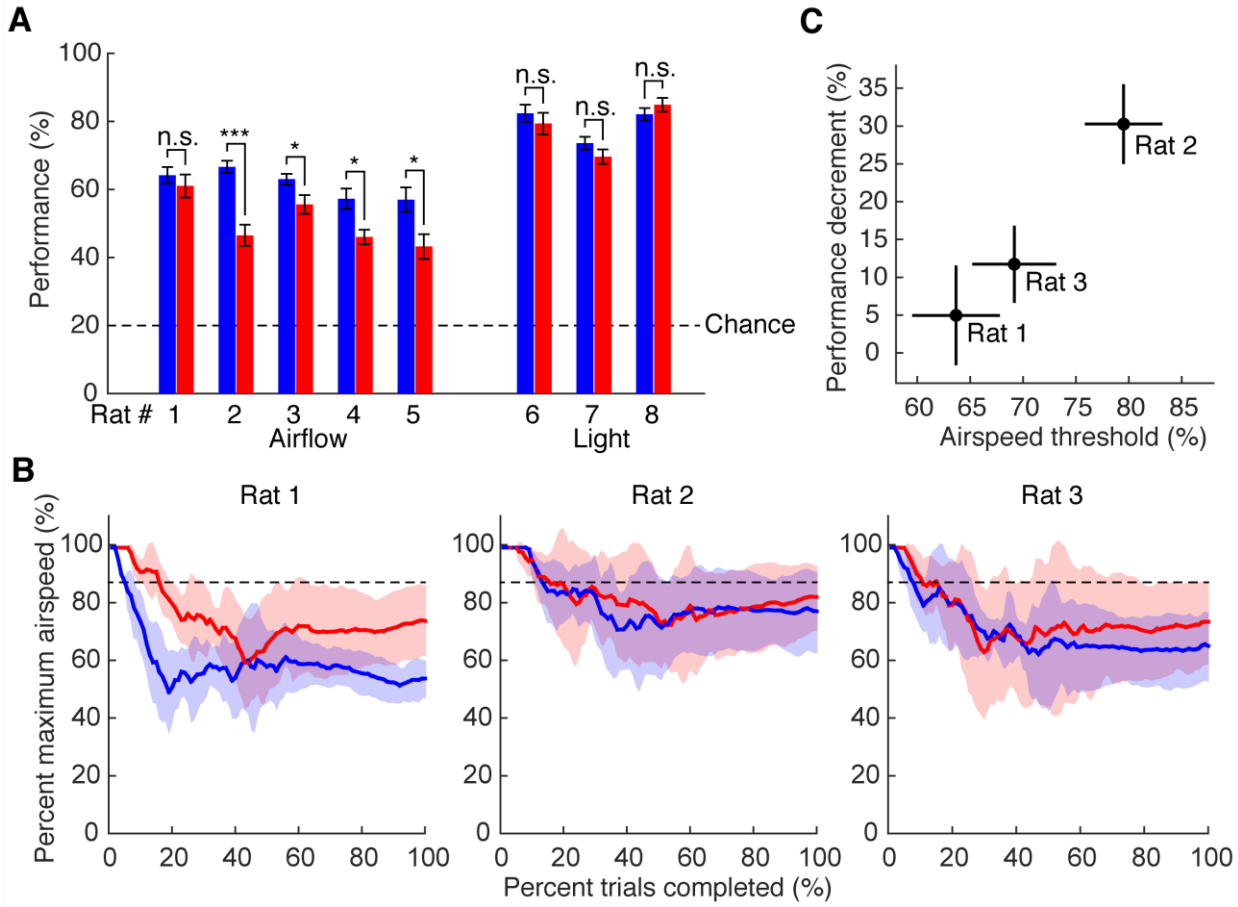

Figure 2.2. Vibrissal removal degrades performance in airflow but not light localization. (A) Average (10-day) performance before (blue) and after (red) vibrissal removal for rats trained to localize either airflow or light. Error bars show mean ± SEM. *** $p<0.001$, * $p<0.05$, n.s. $p\geq0.05$, Wilcoxon rank sum test, median values are reported in table A.1.S2. **(B)** Average (6-day) localization threshold before (blue) and after (red) vibrissal removal on the 2-up/2-down experiment. Data show mean ± SD percent maximum airspeed. Dashed lines indicate the fixed airflow speed used in Figure 2.2A (87% maximum). **(C)** Average performance decrement (10-day average) with fixed airspeed is related to localization threshold (12-day average). Data points show mean values; vertical lines indicate ±SEM performance decrement; horizontal lines indicate ±SEM threshold.

Following vibrissal removal, all rats exhibited a notable decrement (~20%) in their ability to localize the source of the airflow; this effect was statistically significant in four of the five rats (Figure 2.2A and table A.1.S2). In contrast, none of the rats trained to localize the light source showed a significant performance decrement. As expected, all rats could still perform the airflow localization task at levels well above

chance (20%) regardless of the presence of vibrissae, confirming that these sensors are not the exclusive modality used for flow sensing.

To investigate the basis for inter-rat performance variability after vibrissal removal we replicated the original experiment while manipulating airspeed. This new experiment determined the localization thresholds of individual rats using a 2-up/2-down staircase paradigm. The vibrissae of three rats were allowed to regrow for one month and rats were then retrained for two weeks on the original experimental task (air speed = 1.1±0.3 m/s at the hole). After two weeks, the threshold experiment started. Each day of training began with the fans running at full speed (1.4±0.3 m/s at the hole); note that full speed is higher than the original experiment. Fan speed was decreased by 10% if the rat completed two trials correctly and increased by 10% following two incorrect trials. After the fan speed was reversed six times the resolution of the speed change was decreased to 2%. On each day, data collection stopped either after a total of 12 reversals (six reversals at 10% and six at 2%) or after ~1.5 hours of testing, when the rat had lost interest in the task (Figure A.1.S3).

Comparing the results of the localization threshold experiment across rats (Figure 2.2B) offers a compelling explanation for the variability in performance decrement. The localization threshold for Rat 1 was lower than the airspeed used during the original experiment, both before and after vibrissal removal. This rat was sufficiently sensitive to airflow that, although vibrissal removal caused a performance decrement, it was not large enough to reach statistical significance. In contrast, the localization thresholds for Rats 2 and 3 more closely bracketed the 1.1±0.3 m/s airspeed used in the original experiment (87% of max); these rats exhibited significant performance reductions with vibrissal removal. Figure 2.2C illustrates the relationship between performance decrement and localization threshold for these three rats.

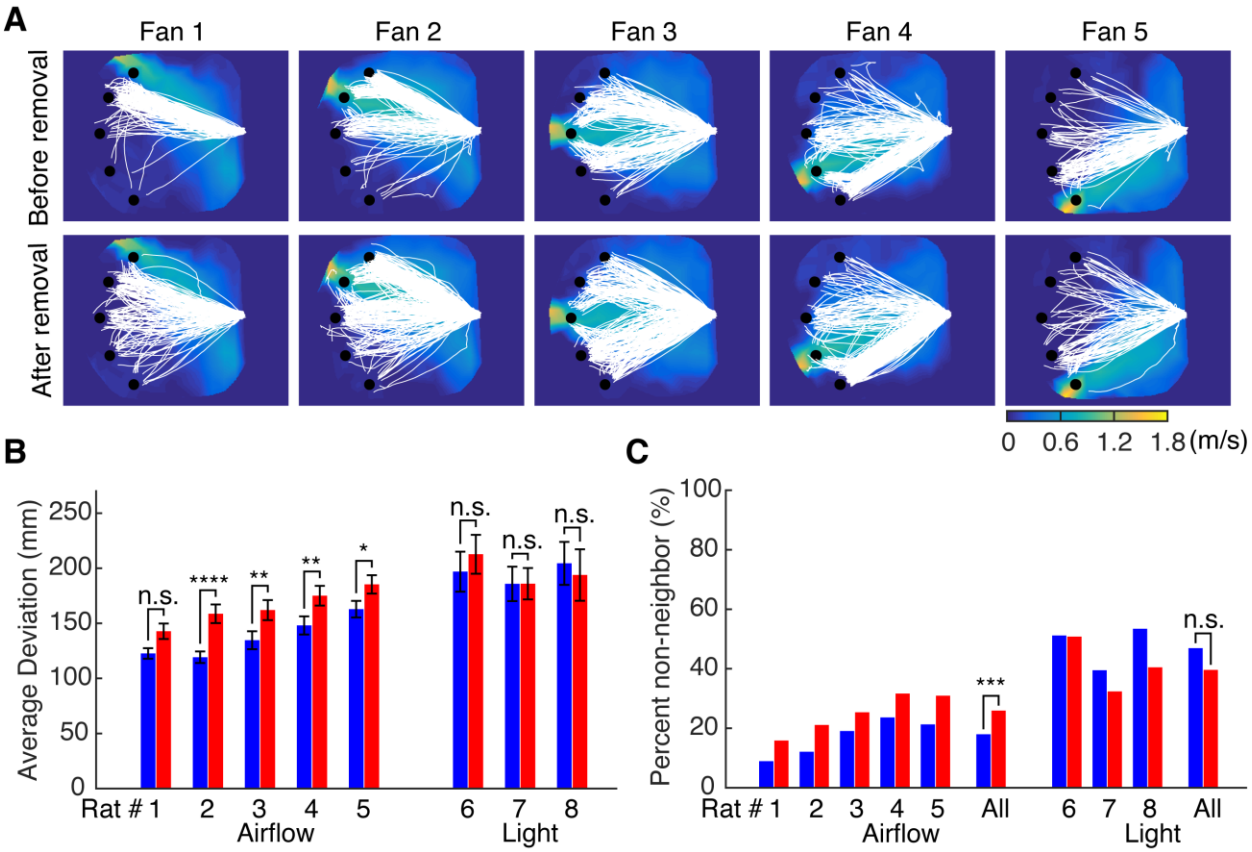

Figure 2.3. For incorrect trials, vibrissal removal causes rats localizing airflow to deviate more from the straight-line path to an airflow source but not a light source. (A) Trajectories of all incorrect trials of five rats trained to localize airflow ten days before vibrissal removal (top row) diverge less than after removal (bottom row). (**B)** For incorrect trials, deviation of each rat before vibrissal removal (blue) is smaller than after removal (red). Error bars show mean ± SEM. **** $p<0.0001$, ** $p<0.01$, * $p<0.05$, n.s. $p\geq0.05$, Wilcoxon rank sum test, median values are reported in table A.1.S2. (**C)** The percent of incorrect trials for which a non-neighboring fan was chosen before (blue) and after (red) vibrissal removal. *** $p<0.001$, n.s. $p\geq0.05$, Yates's corrected chi-square test.

Complementing the performance decrement, the magnitude of the localization error was also found to increase after vibrissal removal. Although rats' trajectories during correct trials were generally straight-line paths (Figure 2.1C), their trajectories on incorrect trials deviated from these paths, and this deviation increased after vibrissal removal (Figure 2.3A). Deviation was quantified as the shortest (i.e., orthogonal) distance from the rat's position to the straight-line trajectory. Average deviation was calculated in a two-step process: we first computed the area enclosed by three curves: the straight-line trajectory to the correct fan, the boundary of the arena, and the rat's actual trajectory (Figure A.1.S4), and then divided the area by

the length of the straight-line trajectory. Average deviation thus captures the extent to which the rat's trajectory diverges from the straight-line path to the correct fan; see Materials and Methods for more detail on this metric. Figure 2.3B shows that on average, deviation from the straight-line path increased 20.4% for all rats trained to localize the airflow source; this effect was significant for all but Rat 1. In contrast, no significant changes in path length deviation were observed for any rats in the control group trained to localize the light source (Figure 2.3B, Figure A.1.S5, and table A.1.S2).

The changes in path length deviation shown in Figure 2.3 (A and B) suggest that rats were choosing fans further away from the correct source of airflow. We confirmed this possibility by computing the percent of incorrect trials in which rats chose either a neighboring (incorrect) source, or a non-neighboring (incorrect) source. This analysis effectively measures the degree of spatial error in the rat's localization choice (Figure 2.3C). All rats trained to localize the airflow showed an increased tendency to choose non-neighboring fans after vibrissal removal. When pooled, the increase reached significance. In contrast, rats trained to localize the light source showed no consistent change.

2.4. Discussion

Our results demonstrate that the rodent vibrissal-trigeminal system, which has a well-established role in tactile detection and texture discrimination (Kleinfeld, Ahissar et al. 2006, Jadhav and Feldman 2010), also contributes significantly to the detection and localization of airflow. Importantly, results show not only that rats can exploit information from the macrovibrissae for anemotaxis, but that they do exploit it, even when multiple cues are available. The task used here did not require rats to use their macrovibrissae; the animals were free to choose whichever cues were most helpful. Performance after macrovibrissal removal decreased for all rats, but remained above chance, indicating that rats do not rely on the macrovibrissae alone for anemotaxis. Alternative cues could include thermal information from the snout, pinnae, and corneas, and mechanical cues from other sensory hairs: the pelage (fur), tylotrichs, the microvibrissae, and

the residual lengths (< 2 mm) of the macrovibrissae. Further studies are required to assess the relative contributions from each of these other submodalities.

Although the present work does not directly demonstrate that anemotaxic information obtained by the vibrissae is used for olfactory localization, we suggest that during an animal's natural exploration, the most behaviorally relevant information to be obtained from air currents is the location of distant odor sources. While local odor concentrations within an odor plume generally provide limited information about a source location (Murlis, Elkinton et al. 1992, Koehl 2006), the vibrissal system offers a parallel stream of trigeminal-based tactile signals that contain spatial cues. Receiving parallel olfactory and vibrissal cues could greatly simplify olfactory search within the "patchy" odor plumes that typically characterize natural environments (Murlis, Elkinton et al. 1992, Koehl 2006). Determining the odor concentration gradient using olfaction alone is time intensive, requiring the animal to take time-averaged concentration measurements of an odor plume at multiple locations (Murlis, Elkinton et al. 1992, Vickers 2000). In contrast, airflow signals are inherently vector quantities that can be combined with olfactory cues at a single spatial location to provide the animal with a rapid estimate of odor location. The direction of the airflow vector indicates the azimuthal angle to the odor source (Vickers 2000); the magnitude of the airflow vector (speed) and the scalar odorant concentration could jointly indicate the distance to the odor source. The position vector to the odor source could thus be efficiently computed. Similar chemo-anemotaxic strategies are observed in other species (Rust and Bell 1976, Baker and Kuenen 1982, Zimmerfaust, Finelli et al. 1995, Vickers 2000, Koehl 2006, van Breugel and Dickinson 2014).

Airflow sensing by the vibrissae offers a mechanical explanation for the anemotaxic contribution to olfactory search observed in behavioral experiments (Bhattacharyya and Singh Bhalla 2015). The cross-modal nature of this proposed vibrissotactile-olfactory information stream underscores the need for rodents to continuously adjust the relationship between whisking and sniffing, as reflected in the dynamic

relationship between the coupled neural oscillators known to drive these rhythmic behaviors (Moore, Deschenes et al. 2013, Ranade, Hangya et al. 2013, Kleinfeld, Deschenes et al. 2014). Passive displacements due to airflow will be easiest to sense if the vibrissae are held relatively immobile to avoid contamination with a peripheral reafferent signal (Fee, Mitra et al. 1997, Leiser and Moxon 2007, Khatri, Bermejo et al. 2009, Wallach A., Bagdasarian et al. 2016). Thus at times when anemotaxis is paramount the rat may minimize whisking, while at other times the animal may exploit bilateral nostril comparisons (Rajan, Clement et al. 2006, Khan, Sarangi et al. 2012, Catania 2013) and is likely to generate synchronized ~8 Hz sniffing and whisking (Smear, Shusterman et al. 2011, Moore, Deschenes et al. 2013, Ranade, Hangya et al. 2013, Kleinfeld, Deschenes et al. 2014, Bhattacharyya and Singh Bhalla 2015). Future studies that directly assess involvement of the macrovibrissae in olfactory search would help to elucidate characteristics of the mechano-tactile information that vibrissal-responsive regions of the nervous system evolved to process.

2.5. Materials and Methods

All procedures were approved in advance by Northwestern's Animal Care and Use Committee.

2.5.1 Experimental Setup

Five computer fans (Cooler Master, Blade Master 80) were placed radially around the edge of a 1.83 m (6 ft) diameter circular table. Each fan was inserted into a 12.70x7.62x7.62 cm (5x3x3 in) enclosure that helped direct the airflow forward. Each fan and enclosure was supported by a free-standing base that was weighted to the floor with heavy iron plates. No part of the fan or the enclosure touched the table. Fan vibrations were barely detectable when the fan enclosure was directly touched with a finger. Although we were not able to directly quantify the magnitude of these tiny vibrations, it is unlikely they influenced the behavior of the rat, as they would have had to have traveled from the fan, through the heavy iron base, through the cement laboratory floor, and back up through the table. The distance between each fan and the

entrance door into the arena ranged from 1.41 to 1.56 m (55.5 to 61.25 in), ensuring that airflow speeds at the entrance differed by no more than 0.2 m/s. All airflow speeds were measured using a hot wire anemometer (Omega, model HHF42, resolution = 0.1m/s). The left and right edges of the table, outside of the fence, were removed to ensure that the entire area of the table was visible in the overhead camera frame.

Control stimuli consisted of white light emitting diodes (LEDs) mounted to the top of each of the fan enclosures and directed towards the door. The light intensity of the bulbs was less than 0.1 lux in the center of the table as measured by a light meter (Digi-Sense, Model 20250-00). To ensure against bias towards any particular location each of the five fans or lights was activated the same number of times per training session, and the order of fans was randomized using the C++ "random_shuffle" algorithm (libstdc++, v6.0.19). The randomization was reseeded for each new training session.

We controlled for extraneous cues from audition and vision for all rats. Ambient noise in the room due to building mechanicals was measured to be 50.5 dB (Casella Cel-63X sound meter). The manufacturer's specifications indicated that the sound emitted from each fan was between 13 and 28 dB; the sound meter did not register a change when a fan was turned on. A masking stimulus was played continuously during training. It consisted of audio recordings from all of the fans with additional bandpass-limited white noise superimposed. The masking stimulus was played back through two speakers beneath the arena (Juster AC-691N), located between fans 1 and 2, and between fans 4 and 5. Amplitude of the masking stimulus was measured to be 67.8 dB. An ultrasound detector (Pettersson D-230) confirmed that the fans did not emit ultrasonic cues.

The experiments were run in a dark room in which a computer monitor behind a curtain was the only ambient visible spectrum light source. Matte black cloth was mounted behind each fan to reduce the contrast between the fan's blades and the background.

2.5.2. Behavioral Shaping

Rats were trained five days a week, for three to five months, starting at three months of age. All rats completed 45 to 50 trials per day (usually ~30 min/rat) and the order in which the rats were trained changed each day. The rats were deprived of water for 23 hours prior to training, but received ad libitum water two days per week.

Each day of training began with a 5 minute gentling session in which the rat was conditioned to tolerate being held firmly while its vibrissae were brushed with a set of blunt-tipped scissors. This conditioning allowed us to cut off the vibrissae without anesthesia during the original experiment (stage 5b in Figure A.1.S1) and during the localization threshold experiment.

Rats were trained to localize airflow emanating from one of five fans. Training consisted of several stages of increasing difficulty, as schematized in Figure A.1.S1. During training, a correction procedure was used such that when a trial was completed incorrectly the trial was repeated with the identical stimulus until the rat gave a correct response. In the final stage, the correction procedure was stopped. After rats achieved a success rate above 40% for 10 consecutive days with an average above 55%, all vibrissae (both macrovibrissae and microvibrissae) were trimmed to < 2 mm in length. Macrovibrissae included mystacial, supraorbital, genal, and the mental (whisker trident). Microvibrissae under 2 mm were not trimmed. Vibrissae were re-trimmed every other day to ensure that they never exceeded 2 mm in length.

Nineteen rats were initially trained. Of those, ten were excluded from the experiment during the first stage of training (stage 1a in Figure A.1.S1). These ten rats refused ever to traverse the open-field arena, choosing instead to sit within the tunnel system and groom. One rat was excluded in the last stage of training (stage 4a in Figure A.1.S1). This rat gradually became lethargic over a period of ~3 weeks, choosing to sit and groom in the tunnel underneath the table. Although her overall performance on the task (both percent correct and locomotor speed during the trial) resembled that of the other rats, training sessions gradually extended to one or two hours due to these extended periods of grooming, and she was therefore excluded from the study. Of the remaining eight rats, five composed the experimental group (localized airflow) and three composed the control group (localized light). A total of 7,217 trials were recorded. 6.7% of the trials were removed from the dataset because the rats were grooming, climbing, following the arena's edge or retreating back into the holding box before completing the trial. A total of 0.6% of all trials were removed due to computer malfunction.

On the third day after trimming the vibrissae of Rat 2 a fire alarm went off after it had performed 26 trials. Only 26 trials were used on that day.

2.5.3. Reward Criteria

Reward criteria for training are shown in Figure A.1.S2. In order to receive rewards, the rat was required to run towards the operating fan and cross two trigger regions along the way. All triggers were implemented digitally through images taken by an overhead camera and were not physically observable. The first (checkpoint) set of triggers consisted of five linear regions of interest, 15.24 cm (6 in) wide, located 21.59 cm (8.5in) in front of their corresponding holes. Each trigger line was oriented to be orthogonal to the straight-line path connecting the center of its hole to the entrance of the arena. The second (hole) set of triggers consisted of 11.43 cm (4.5 in) circles surrounding each hole. During training stages 1a, 2a and 3a the checkpoint triggers were turned off to promote a smoother transition between increasingly difficult

training stages. The distances between the door and the holes ranged between 93.98 cm (37 in) and 106.68 cm (42 in).

Upon reaching the hole trigger the rat was required to go down one of the 7.62 cm (3 in) diameter holes located in front of the fans leading to a tunnel system beneath the table. The tunnels led to the first reward and provided a path back to the holding box to receive a second reward. To prevent the rat from looping in the opposite direction, one-way doors were installed in each of the five branches of the tunnel system as well as a one-way hatch at the top of the ramp. In the event that a rat did not return to the holding box within a ~1 minute time span, rats were gently guided up the ramp by the trainer.

The first reward was a 0.09±0.02 ml drop of fresh water and was dispensed by a solenoid valve in the center of the chamber beneath the table. The second reward was a 0.1±0.07 ml drop of sucrose solution (85.575 g/L) and was dispensed manually with a pipette at the rear of the holding box (Figure 2.1A). The purpose of the second reward was to motivate the rat to return to the holding box. Both rewards were contingent on the rat getting the trial correct. A new trial was started once the rat returned to the holding box. The start of each trial was controlled manually by the trainer.

2.5.4. Video recording and rat tracking

An infrared light source (15 W) illuminated the arena from above. Video was recorded at 20 fps at a resolution of 480x640 pixels by a surveillance camera (model: Swann PRO-760) and a video capture card (Pinnacle, AV to USB2 Rev. 1.2A). Custom circuitry and software were developed to monitor the checkpoints as well as to control the actions of the camera, vertical lift door to enter the arena, fans, LEDs, and the reward solenoid. The triggers were implemented by monitoring their respective regions of interest for changes in pixel intensity from the white background. If the intensity within the trigger's region of interest fell below a threshold value, the trigger was activated. Upon reaching a hole trigger the arena door

was automatically closed and the fan was turned off. For correct trials the solenoid was automatically activated, producing a clicking sound and alerting the rat of the presence of a reward. The trial number, correct fan number, checkpoint trigger number, hole trigger number and full video for each trial were automatically recorded.

Rat positions were automatically tracked in post-processing using MATLAB®. The tracking algorithm exploited the contrast between the rat (brown) and arena (white) to measure the position of the rat. An image of the empty arena was used to find and mask out persistently dark regions. Any remaining dark regions greater than a size threshold represented the rat. The position of the rat was defined as the centroid of the dark region.

2.5.5. Average Deviation

The straight-line trajectory is defined as the line that connects the door with the correct hole. The rat's deviation at each point in time is defined as the orthogonal distance between the rat's position and the straight-line trajectory. Intuitively, the average deviation can be thought of by imagining that the rat has taken a trajectory in which its deviation is constant throughout its entire path. The rectangular area enclosed by this hypothetical trajectory is defined by the straight-line trajectory and the average deviation value. It follows that the average deviation is equal to the enclosed area divided by the length of the straight-line path. The average deviation values plotted in Figure 2.3B were therefore calculated by measuring the enclosed area shown in Figure A.1.S4 and dividing by the length of the straight-line path.

2.5.6. Airflow maps

To monitor for changes in airspeed between training days, airspeed measurements were taken at 11 points throughout the arena for each fan for a total of 55 measurements each day. For each fan, the first measurement point was taken at the door, the next five points were taken half way between the door and

each hole, and the final five points were taken in front of each hole. Typical fan speeds along the lines connecting the fans to the door were 1.1±0.3 m/s, 0.8±0.2 m/s, and 0.5±0.2 m/s (mean ± maximum difference) as measured from the door to the hole. We also recorded three days of higher spatial resolution measurements taken at 162 points for each fan, spaced evenly throughout the arena. To produce the color map images for Figs. 1.1 (B and C), 1.3A, Figure A.1.S4, and Movie S1, small markers were placed at the 162 measurement locations and the overhead camera was used to take a picture of the arena. The positions of the markers were then manually extracted from the image and used to linearly interpolate the airspeed for every pixel location within the arena.

2.5.7. Localization threshold experiment

For three of the five rats trained to localize airflow (Rats 1, 2, and 3) a follow-up experiment was performed to investigate the threshold at which the rats were able to localize airflow. In this experiment we used a 2-up/2-down paradigm to alter the magnitude of the airspeed based on the rat's performance. After the rat performed two correct trials the airspeed was lowered, increasing difficulty. Conversely, after performing two incorrect trials the airspeed was raised, decreasing difficulty. For the first six reversals the airspeed was changed in 10% increments. For the next six reversals the airspeed was changed in 2% increments (Figure 2.2B and fig. A.1.S3). Each day, this process was continued until the airspeed was reversed 12 times (12 "reversals") or after ~1.5 hours of testing. The speed of each fan was adjusted via a pulse-width modulation signal (PWM). On average, a 1% change in the duty cycle of the PWM signal resulted in a 0.015 m/s change in airflow speed at the hole. The duty cycle could be adjusted within the range of 1-99%.

Rats 1 and 3 performed the staircase procedure for six days with vibrissae and six days without vibrissae. For several days Rat 2 did not achieve an adequate number of reversals. Therefore it was tested for 10 days before trimming and 10 days after trimming. The subset of six days with the highest number of reversals

before and after trimming was used in the threshold analysis. Table S3 shows the number of reversals achieved for each rat on each day. To normalize for the variable number of trials that each rat took to achieve convergence, we analyzed percent complete as opposed to trial number. The percentage of maximum fan speed was then resampled using linear interpolation at integer values of percent complete. Means and standard deviations were computed at these integer values.

Chapter 3: Variations in vibrissal geometry across the rat mystacial pad: base diameter, medulla, and taper

This chapter has been published in the Journal of Neurophysiology as: Belli HM, Yang AE, Bresee CS, Hartman MJ (2017) "Variations in vibrissal geometry across the rat mystacial pad: base diameter, medulla, and taper." Journal of Neurophysiology. Vol. 117, Issue 4, Pages 1807-1820

3.1. Abstract

Many rodents tactually sense the world through active motions of their vibrissae (whiskers), which are regularly arranged in rows and columns (arcs) on the face. The present study quantifies several geometric parameters of rat whiskers that determine the tactile information acquired. Findings include the following. 1) A meta-analysis of seven studies shows that whisker base diameter varies with arc length with a surprisingly strong dependence on the whisker's row position within the array. 2) The length of the whisker medulla varies linearly with whisker length, and the medulla's base diameter varies linearly with whisker base diameter. 3) Two parameters are required to characterize whisker "taper": radius ratio (base radius divided by tip radius) and radius slope (the difference between base and tip radius, divided by arc length). A meta-analysis of five studies shows that radius ratio exhibits large variability due to variations in tip radius, while radius slope varies systematically across the array. 4) Within the resolution of the present study, radius slope does not differ between the proximal and distal segments of the whisker, where "proximal" is defined by the presence of the medulla. 5) Radius slope of the medulla is offset by a constant value from radius slope of the proximal portion of the whisker. We conclude with equations for all geometric parameters as functions of row and column position.

3.2. Introduction

Rats use rhythmic motions of their whiskers to tactually explore the world around them (Richardson, Peterson et al. 1909, Vincent 1912, Welker 1964). There are no sensors along the whisker length; instead,

all tactile signals are transmitted to mechanoreceptors embedded in a richly innervated follicle at the whisker base (Ebara, Kumamoto et al. 2002). Mechanoreceptors in the follicle transduce these tactile signals into electrical activity that is subsequently transmitted to the trigeminal ganglion (Zucker and Welker 1969, Gibson and Welker 1983, Lichtenstein, Carvell et al. 1990, Jones, Depireux et al. 2004, Szwed, Bagdasarian et al. 2006, Leiser and Moxon 2007, Lottem and Azouz 2011) and from there to the trigeminal nuclei, sensory thalamus, and ultimately somatosensory cortex (Bosman, Houweling et al. 2011).

The geometry of the vibrissa plays an important role in the mechanical signals generated at the whisker base (Boubenec, Shulz et al. 2012) (Carl, Hild et al. 2012) (Hartmann, Johnson et al. 2003) (Hires, Pammer et al. 2013) (Huet and Hartmann 2016) (Huet, Schroeder et al. 2015) (Kan, Rajan et al. 2013) (Neimark, Andermann et al. 2003) (Quist and Hartmann 2012) (Yang and Hartmann 2016) and hence the neural responses generated by trigeminal ganglion neurons ((Bush, Schroeder et al. 2016) (Campagner, Evans et al. 2016). As yet, however, several of the geometric properties of the whiskers are poorly quantified, including their base diameter and "taper," which has been defined in several different ways in previous studies. In addition, previous studies (Birdwell, Solomon et al. 2007) (Boubenec, Shulz et al. 2012) (Hartmann, Johnson et al. 2003) (Hires, Pammer et al. 2013) (Hires, Schuyler et al. 2016) (Kan, Rajan et al. 2013) (Neimark, Andermann et al. 2003) (Quist, Seghete et al. 2014) have modeled the whisker as a solid, conical, cantilever beam, but it is well known that the proximal portion of the whisker contains a low density region called the medulla that can be approximated as hollow (Adineh, Liu et al. 2015) (Carl, Hild et al. 2012) (Chernova 2003) (Chernova and Kulikov 2011) (Hausman 1930) (Latzke and Hesse 1988) (Latzke and Hesse 1988) (Voges, Carl et al. 2012).

In the present study we aimed to quantify variations in whisker arc length, base diameter, taper, and medulla geometry across the array, and to develop equations that describe relationships between these

parameters. In a companion paper (Yang and Hartmann 2016) we use these equations to investigate some consequences of vibrissa geometry for whisking dynamics.

3.3. Methods

All procedures involving animals were approved in advance by the Animal Care and Use Committee of Northwestern University.

3.3.1. Data collection

Two datasets were collected for the present work. In both datasets the row and column position of each whisker was identified and recorded according to the convention depicted in Figure 3.1A.

All whiskers were extracted within hours after euthanasia in unrelated experiments. Whiskers were not plucked from their follicles. Instead, each whisker was grasped near its base with fine surgical forceps and then cut at its base with surgical scissors. This procedure ensured that we did not mass the portion of the whisker internal to the follicle. Extreme care was taken to ensure consistency in the location at the base at which the whisker was cut.

3.3.1.1. Dataset 1: Geometric parameters (excludes mass and medulla measurements): 348 vibrissae were acquired from the left and right arrays of six female Long Evans rats (Charles River LE #006). Each rat was between 3 months and 1.5 years old and weighed between 226 and 300 grams.

To obtain measurements of arc length, whiskers were scanned at a resolution of 2,400 dpi (10.6μm/pixel) on a flatbed scanner (Epson Perfection 4180 Photo). These images were then either imported into the commercial software Reconstruct™ or into MATLAB™ to measure arc length. Measurement error was

approximately two pixels on each end of the whisker, or ~10.6μm/pixel x 2 pixels/endpoint x 2 endpoints = ~42.4μm.

The diameter at the whisker base was measured using one of two upright transmitted light microscopes to capture digital images. The first microscope was a Phenix XSP-10 Series microscope with a 40x objective and a high-resolution (3,088 x 2,056 pixels) digital camera (Canon Digital EOS Rebel) mounted on a 10x eyepiece. These images were imported either into the software Reconstruct™ or into MATLAB™ where the whisker base diameter was measured. The second microscope was a Leica DM750 microscope with a 10x objective and an Excelis HDS Accuscope HD Camera (1920 x 1080 pixel-resolution) through a trinocular head. Rather than importing images into Reconstruct™ or into MATLAB™, the base diameters were measured under the microscope using software associated with the camera (CaptaVision Imaging Software).

In order to determine measurement error, both the resolution and resolving power of visible light through the particular camera, microscope, and objective were calculated. The resolution of each imaging apparatus was calibrated by capturing an image of a laser etched 100μm grid with the appropriate objective and measuring this known length with the associated software. Resolving power was calculated based on the wavelength range of visible light and the numerical aperture of the objective. The resolving power of visible light through all scopes and objectives was found to be larger than the resolution of the camera, so measurement error was calculated based only on resolving power. In each case measurement error was found to be approximately one pixel on each side of the base of the whisker, which corresponds to approximately 1μm for the first microscope and 2μm for the second microscope.

3.3.1.2. Dataset 2: Mass and medulla measurements in addition to geometric parameters: A total of 70 vibrissae were collected from the left and right arrays of three Sprague-Dawley rats (Charles River SD

#400). Of these 70 whiskers, 37 were obtained from a female rat: 14 from the left array and 23 from the right array; 19 whiskers were obtained from the left array of a male rat; and 14 whiskers were obtained from the right array of a second male rat. The female rat was approximately 13 months old and weighed ~350 grams, and both male rats were ~3 months old and weighed ~300 grams.

Whole whiskers were massed using a Mettler-Toledo UMX2 microbalance (resolution 0.1μg). The mass measurements were performed within two to three hours after cutting to prevent dehydration.

After massing, whole whiskers were scanned at 1,200 dpi (~21.2μm / pixel) on the flatbed scanner (Epson Perfection 4180 Photo). These images were then imported into the commercial software Reconstruct™ to measure the total arc length of the vibrissa. Measurement error was approximately two pixels on each end of the whisker, or ~21.2μm/pixel x 2 pixels/endpoint x 2 endpoints = ~85μm.

Again, one of two upright transmitted light microscopes was used to capture digital images. The first was the same Phenix XSP-10 Series microscope described previously, with a 4x or 10x objective and a high-resolution (3,088 x 2,056 pixels) digital camera (Canon Digital EOS Rebel) mounted on a 10x eyepiece. This microscope was primarily used to identify the location of medulla termination in order to bisect the whisker shaft at this point (Figure 3.1B). For cases in which the medulla termination was ambiguous (e.g., discontinuous, as shown in Figure 3.1C), a judgment call had to be made about the position of medulla termination. The point of medulla termination was selected by cutting at the location where the length of the discontinuous segments began to consistently decrease in relationship to the length of the spacing between these segments. For most whiskers, the difference between possible medulla termination sites was less than 1mm. Both proximal and distal segments were then re-massed within 24-48 hours of their initial cutting from the rat and re-scanned on the same scanner to estimate the arc length of each segment.

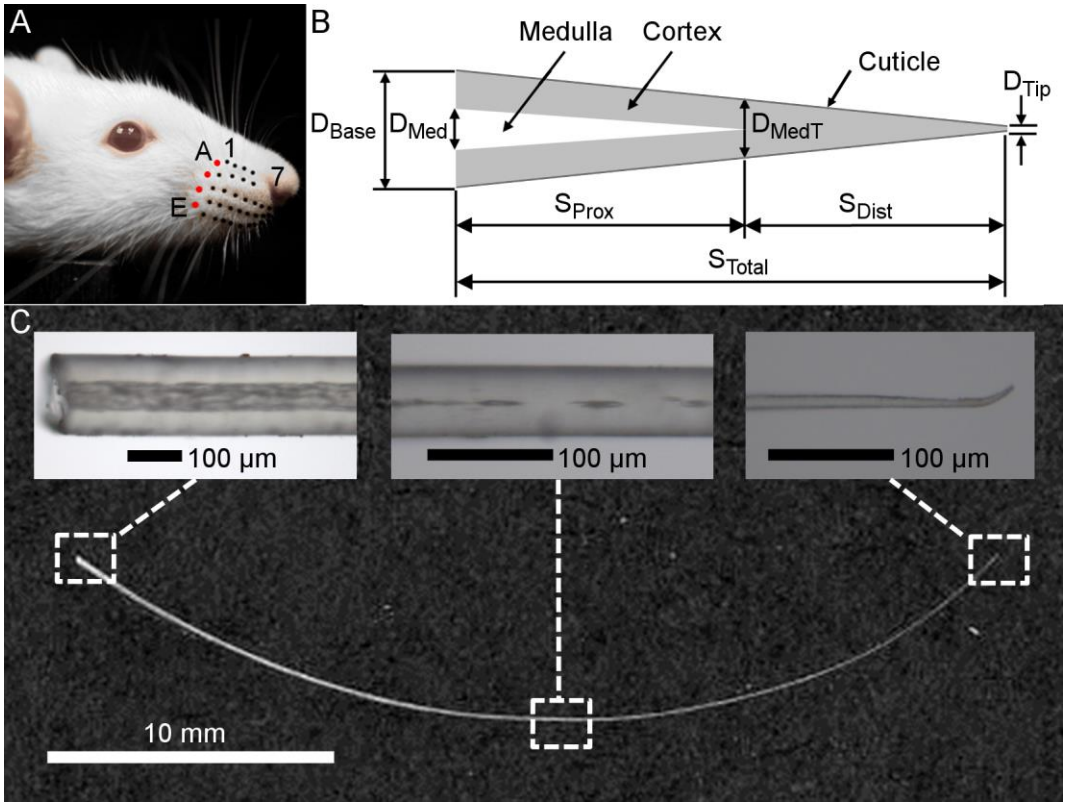

Figure 3.1: Geometric parameters of the whisker. (A) Each whisker is identified by its row and column position. In this photo, black and red dots have been drawn on the basepoint locations of the whiskers for visual clarity. From dorsal to ventral the five rows are identified by the letters A – E, while the arcs (columns) are given the numbers 1 – 7 from caudal to rostral. The four whiskers of the caudal-most arc (colored red) are called the "Greek arc" or "Greek column" and are denoted from dorsal to ventral by the letters α, β, γ, and δ. **(B)** A schematic (not to scale) of the structural elements of the whisker. The whisker is modeled as a straight, tapered, conical frustum with base diameter (D_{Base}), and tip diameter (D_{Tip}). The medulla is represented as a hollow cone that occupies the proximal region of the whisker. The diameter of the medulla at its base is denoted by D_{Med}, and the diameter of the whisker at the point of medulla termination is labeled as D_{MedT}. The total whisker arc length (S_{Total}) is divided into a proximal portion occupied by the medulla (S_{Prox}) and a distal portion that does not include the medulla (S_{Dist}). The geometry of the cuticle was not quantified separately from the cortex in the present work. **(C)** A scanned image of the E2 whisker is shown along with three representative images to illustrate typical whisker geometry near the base, middle and tip. The three images were not obtained from the E2 whisker; they were chosen to best illustrate the features described. The image near the base is from a C1 whisker (10x magnification). The image at the location of medulla termination is from an E5 whisker (20x magnification). The image near the tip is from an E3 whisker (20x magnification).

The second microscope was an Olympus BX60 with 10x, 20x, and 40x objectives, and a MBF Bioscience Stereo Investigator DV-47 color camera. Images were imported into the software Reconstruct™, where four measurements were obtained: the diameter of the whisker at its base (10x), the diameter of the

whisker at the location of medulla termination (20x), the diameter of the whisker at its tip (40x), and the diameter of the medulla at the whisker base (10x).

Again, to determine measurement error, both the resolution and resolving power of visible light through the particular camera, microscope, and objective were calculated. The resolution and resolving power were calculated as described above. At all magnification levels, resolving power was found to be greater than the resolution of the microscope, so measurement error was calculated based only on resolving power. Estimated measurement error was therefore ~1μm/pixel x 1 pixel/endpoint x 2 endpoints = ~2μm at 10x magnification, ~0.7μm/pixel x 1 pixel/endpoint x 2 endpoints = ~1.4μm at 20x magnification, and ~0.5μm/pixel x 1 pixel/endpoint x 2 endpoints = ~ 1μm at 40x magnification. Using the methods described above, we measured and computed the parameters shown in Figure 3.1B and Table 3.1.

Table 3.1: *Measured and calculated whisker variables.*

Measured variables	
Variable name	**Description**
D_{Base}	Diameter of the whisker at its base
D_{Tip}	Diameter of the whisker at its tip
D_{MedT}	Diameter of the whisker at the location where the medulla terminates
D_{Med}	Diameter of the medulla at its base
$D_{Med\ TIP} \equiv 0$	Diameter of the medulla at its tip is defined to be zero
S_{Total}	Total arc length of the whisker
S_{Prox}	Arc length of the whisker proximal to medulla termination
S_{Dist}	Arc length of the whisker distal to medulla termination
M_{Total}	Total mass of the whisker
M_{Prox}	Mass of the whisker proximal to medulla termination
M_{Dist}	Mass of the whisker distal to medulla termination
Calculated variables	
Variable name	**Description**
$R_{Base} \equiv D_{Base}/2$	Radius of the whisker at its base
$R_{Tip} \equiv D_{Tip}/2$	Radius of the whisker at its tip
$R_{MedT} \equiv D_{MedT}/2$	Radius of the whisker at the location where the medulla terminates
$R_{Med} \equiv D_{Med}/2$	Radius of the medulla at its base

3.3.2. Data reduction

Dataset 2 included a total of 70 whiskers (used in Figures 3.2, 3.3, and 3.4); however, no tip diameter measurements were collected for the 14 whiskers of the left array of the female Sprague-Dawley rat. In addition, four distal segments were lost during diameter measurements. Because distal whisker segments were often less than 10 micrograms in mass and less than 10 millimeters in length, it was easy to lose segments due to static electricity or air currents when transporting between experimental setups. Figure 3.6 therefore uses a reduced dataset of 52 whiskers (70 – 18 = 52).

3.3.3. Datasets used in meta-analysis

Several previous studies have measured geometric parameters across the whisker array for both male and female rats of various strains (Sprague-Dawley, Wistar Hannover, and Long Evans). We combined data from the present study with that from six earlier studies to perform a meta-analysis of whisker diameter and arc length. Four of the previous studies measured diameters at the base and tip, as well as total whisker arc length (Hartmann et al. 2003; Ibrahim and Wright 1975; Neimark et al. 2003; Voges et al. 2012). Two of the previous studies only measured base diameter and arc length (Birdwell et al. 2007; Kan et al. 2013). All six studies identified the row and column position of the whiskers within the array. Birdwell et al. 2007 used 7 whiskers from female Sprague-Dawley rats (age not specified), and Kan et al. 2013 used 24 whiskers from one 3-month old female Sprague-Dawley rat. The number of whiskers from all other datasets are indicated in column 1 of Table 3.5 of Results.

3.3.4. Statistical analysis and error propagation

All statistical analyses were performed in MATLAB™. As described above, we carefully accounted for measurement error of whisker parameters by comparing the resolution and resolving power of visible light through the particular camera, microscope, and objective when acquiring these geometric parameters. Rather than plot the individual measurement error in Figures 3.2 and 3.4, 95% confidence bounds were

plotted about each fit to account for both measurement error and the natural deviation in biological data. These confidence limits were generated using the MATLAB™ prediction interval function ("predint") with simultaneous observation bounds. Because radius ratio and radius slope were calculated, not measured, variables, error propagation (NIST/SEMATECH E-Handbook of Statistical Methods 2012) was used to compute the error bars for each whisker in Figure 3.5.

3.4. Results

All data used in the present study are provided in a Microsoft Excel® file as supplementary material. This same file is also publicly available on GitHub® (https://github.com/SeNSE-lab/RatWhiskerGeometry.git) with the goal of allowing other researchers to add additional datasets.

3.4.1. A meta-analysis of arc length and base diameter as a function of arc length

We surveyed the literature for data that described the diameter and arc length of rat vibrissae. We excluded studies that used mice (Hires, Pammer et al. 2013, Pammer, O'Connor et al. 2013, Hires 2016). Our survey yielded six studies, in addition to the present work, that provided measurements of both base diameter and arc length (Ibrahim and Wright 1975, Hartmann, Johnson et al. 2003, Neimark, Andermann et al. 2003, Birdwell, Solomon et al. 2007, Voges, Carl et al. 2012, Kan, Rajan et al. 2013). As described in Methods, the present study contained two datasets (Datasets 1 and 2), and the remaining six studies constituted Datasets 3 – 8.

We began with the goal of finding an expression for whisker arc length (S_{Total}) as a function of the whisker's row and column position within the array. Using the MATLAB™ prediction interval function ("predint") with simultaneous observation bounds, prediction bounds were determined on linear fits for S_{Total} as a function of both row and column identity for each of the eight datasets. Considerable overlap

was observed across all eight sets of bounds (see Discussion for more details), indicating that across datasets there were no substantial differences in S_{Total} as a function of row and column identity. Note that this analysis implicitly contains comparisons across rat sex and strain as well as across different laboratories; see column 1 of Table 3.5 for a list of the sex and strain used in each study.

Given the consistency of results across datasets, all data were grouped and the best linear fit relationship between S_{Total} and row and column position across all 519 whiskers was found to be:

$$S_{Total} = 43.1 + 1.8\,Row - 7.6\,Col, \quad Adj.R^2 = 0.850 \qquad \text{(eq. 3.1)}$$

where S_{Total} has units ofmm, *Row* varies between 1 and 5 (representing the A through E rows), and *Col* varies between 0 and 8. The adjusted R^2 is 0.850.

We next aimed to find the functional relationship between base diameter and total arc length. Two previous studies on whisker resonance approximated the relationship between base diameter and arc length as a power law (Hartmann, Johnson et al. 2003, Neimark, Andermann et al. 2003). Although this relationship served as a useful empirical approximation in the context of these resonance experiments, it is statistically inappropriate to assert a power-law relationship unless the data vary over several orders of magnitude (Clauset, Shalizi et al. 2009).

When the relationship between D_{Base} and S_{Total} for each of the eight datasets was plotted individually, the highest order fit for each of the eight individual data sets that avoided overfitting was found to be linear. For Dataset 1 (348 whiskers) the best fit was D_{Base} = 0.002 S_{Total} + 0.054, while for Dataset 2 (70 whiskers) the best fit was D_{Base} = 0.002 S_{Total} + 0.071. In these equations, D_{Base} and S_{Total} both have units of millimeters. The equation for Dataset 2 is identical to that used in Yang and Hartmann (2016), except for rounding differences. S_{Total}

Again using the MATLAB™ prediction interval function with simultaneous observation bounds, prediction bounds were determined on the linear fits between D_{Base} and S_{Total} for each of the eight datasets. Considerable overlap was observed across all eight sets of bounds, so all data were grouped. When the eight datasets were combined, the quadratic model yielded a slightly better fit than the linear model on the basis of the Akaike Information Criterion (AIC). However, the linear regression models fit by individual dataset suggested that a quadratic model was overfitting the data. Thus for the combined data, a linear model was selected as the best fit (Root MSE: 0.023, R^2: 0.691). Results are shown in Figure 3.2 for all 519 whiskers. The line of best fit shown in the figure is: D_{Base} = 0.002 S_{Total} + 0.056, again with D_{Base} and S_{Total} both expressed in units of mm.

The linear model shown in Figure 3.2 is dissatisfying for two closely related reasons. First, there is large variance about the fit for all seven studies. Second, visual inspection suggests that the trend consists of several diagonally-slanted "bands" of data points, rather than a single trend. We tested the possibility that these diagonal bands were related to the row and column positions of the whiskers within the array.

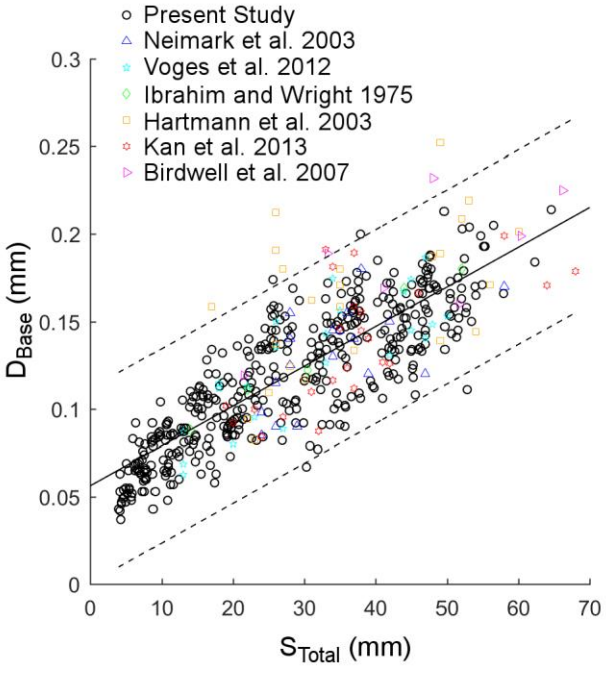

Figure 3.2: Diameter of the whisker base as a function of arc length for seven studies (519 whiskers total). The relationship between base diameter (D_{Base}) and arc length (S_{Total}) obtained in the present study (418 whiskers) is not significantly different from the relationship for 101 whiskers obtained from six previous studies. Notice the large scatter about the trend line and the presence of 4 – 5 distinct diagonal "bands" within the data, sloping upwards from left to right.

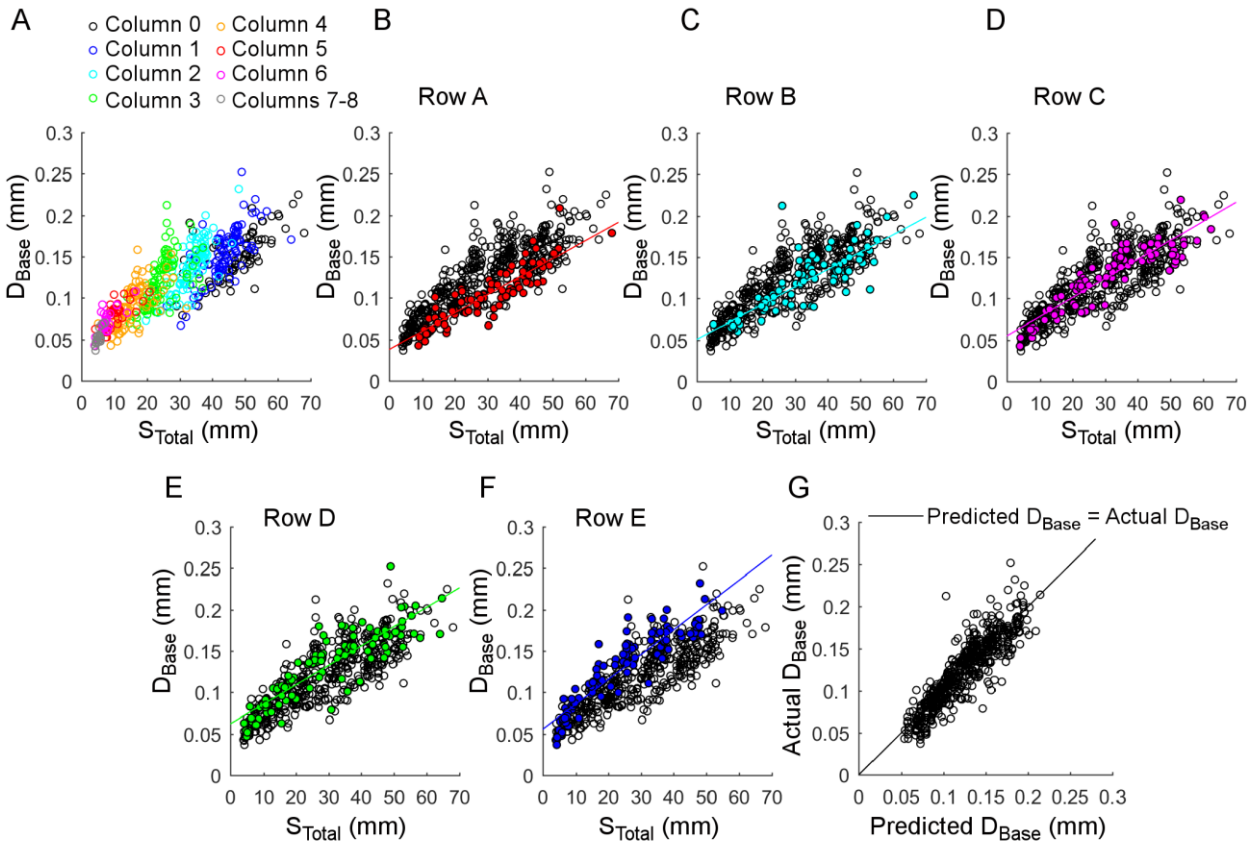

Figure 3.3: Relationship between base diameter and whisker arc length as a function of column and row position. (A) When color coded by column position within the array, clear diagonal bands characterize the relationship between base diameter and arc length. Best linear fits for each of the columns are indicated in Table 3.2. Column 0 indicates the Greek arc. **(B-F)** Clear groupings also emerge when the relationship between D_{Base} and S_{Total} is color coded by row position within the array. Although the slope is similar for all rows, the intercept varies considerably, as can be seen in the upwards vertical translation of the line of best fit from Row A to Row E (see Table 3.2). **(G)** Equation 3.2 predicts D_{Base} with a high degree of accuracy as a function of S_{Total} and row and column position.

3.4.2. The relationship between whisker base diameter and arc length varies with row and column position in the array

Continuing to use all 519 whiskers from all seven studies, we investigated the possibility that the large variance and diagonal bands observed in Figure 3.2 were associated with the whiskers' positions within the array. Figure 3.3 shows these relationships and the corresponding equations are provided in Table 3.2.

Because a whisker's column position within the array is strongly correlated with its arc length (Brecht, Preilowski et al. 1997, Towal, Quist et al. 2011), color coding the data by column position as in Figure 3.3A clearly reveals clusters within the relationship between D_{Base} and S_{Total}. There are remarkably distinct gaps between some of the column clusters, particularly notable between columns 1 and 2 and between columns 2 and 3. More surprising, however, is that the relationship between base diameter and arc length also varies strongly with row (Figures 3.3B – 3.3F). For a given arc length, whiskers in more dorsal rows have smaller diameters than whiskers in more ventral rows. The equations of Table 3.2 show that the relationship between base diameter and arc length is best expressed on a per-row, rather than a per-column basis.

Because both row and column position influence the relationship between D_{Base} and S_{Total}, the best single predictor function varies as a function of both row and column. To determine the single predictor model for base diameter as a function of arc length, we expanded the single linear regression to include predictors for column and row. Interaction terms between S_{Total} and row and between S_{Total} and column were not significant. With D_{Base} and S_{Total} expressed in millimeters, the best single predictor model with significant coefficient estimates was found to be:

$$D_{Base} = 0.041 + 0.002\, S_{Total} + 0.011\, Row - 0.004\, Col, \quad Adj.R^2 = 0.800 \qquad \text{(eq. 3.2)}$$

where *Row* ranges between 1 and 5 and *Row* varies between 0 (for the Greek arc) to 8. Figure 3.3G shows the actual base diameter vs. predicted base diameter as calculated from Equation 3.2. The prediction of Equation 3.2 is strong, having a Root MSE of 0.018 and an adjusted $R^2$of 0.800.

3.4.3. Medulla length varies linearly with whisker arc length; medulla diameter varies linearly with whisker base diameter

Although several studies have quantified whisker base diameter and arc length, few have quantified the hollow region known as the medulla. This structure will have important consequences for whisker dynamics because it will change the mass distribution of the whisker (Hartmann, Johnson et al. 2003, Neimark, Andermann et al. 2003, Boubenec, Shulz et al. 2012, Kan, Rajan et al. 2013, Quist, Seghete et al. 2014).

Table 3.2: *Equations for diameter at the whisker base (D_{Base}) as a function of whisker arc length (S_{Total}) when examined by row and column position. Abbreviations: Root MSE: Root Mean Squared Error; R^2: R-Square.*

Equations for D_{Base} as a function of S_{Total} when examined by column				
Model	**Number of whiskers**	**Equation**	**Root MSE**	**R^2**
Column 0 (Greek)	**77 whiskers**	$D_{Base} = 0.002\, S_{Total} + 0.032$	0.023	0.463
Column 1	**97 whiskers**	$D_{Base} = 0.003\, S_{Total} + 0.008$	0.022	0.493
Column 2	**90 whiskers**	$D_{Base} = 0.005\, S_{Total} - 0.026$	0.018	0.634
Column 3	**97 whiskers**	$D_{Base} = 0.004\, S_{Total} + 0.028$	0.024	0.372
Column 4	**80 whiskers**	$D_{Base} = 0.003\, S_{Total} + 0.041$	0.020	0.387
Column 5	**36 whiskers**	$D_{Base} = 0.003\, S_{Total} + 0.048$	0.011	0.487
Column 6	**24 whiskers**	$D_{Base} = 0.004\, S_{Total} + 0.043$	0.010	0.523
Columns 7 & 8	**18 whiskers**	$D_{Base} = 0.009\, S_{Total} + 0.007$	0.006	0.588
Equations for D_{Base} as a function of S_{Total} when examined by row				
Model	**Number of whiskers**	**Equation**	**Root MSE**	**R^2**
Row A	**89 whiskers**	$D_{Base} = 0.002\, S_{Total} + 0.038$	0.015	0.779
Row B	**95 whiskers**	$D_{Base} = 0.002\, S_{Total} + 0.051$	0.020	0.671
Row C	**108 whiskers**	$D_{Base} = 0.002\, S_{Total} + 0.055$	0.016	0.833
Row D	**117 whiskers**	$D_{Base} = 0.002\, S_{Total} + 0.062$	0.019	0.793
Row E	**110 whiskers**	$D_{Base} = 0.003\, S_{Total} + 0.056$	0.018	0.852

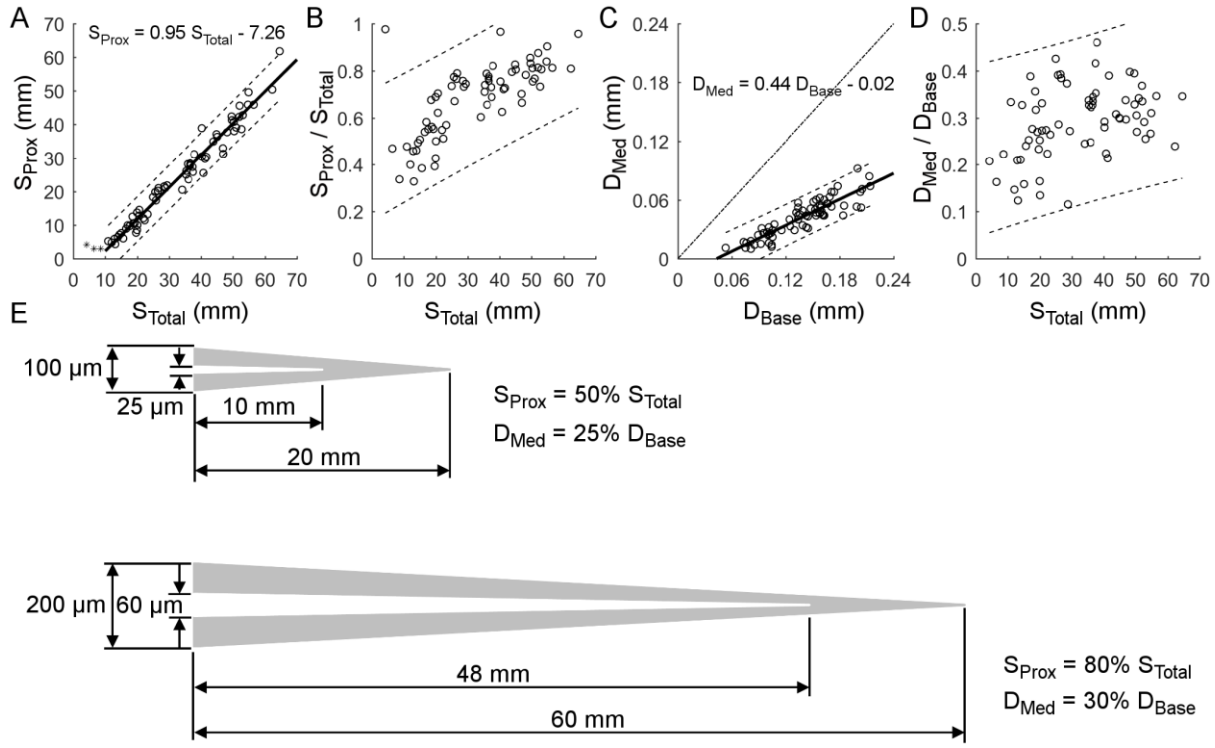

Figure 3.4: Length of the medulla as a function of whisker arc length. Subplots A - D show data from the 70 whiskers of Dataset 2 **(A)** The length of the medulla (S_{Prox}) is linearly related to the total arc length of the whisker (S_{Total}). The linear fit excludes 3 whiskers with length less than 10mm. **(B)** The fraction of the total arc length occupied by the medulla increases for longer whiskers. **(C)** The diameter of the medulla at the whisker base (D_{Med}) is linearly related to the base diameter (D_{Base}). Dashed line is where the medulla diameter at the base equals the base diameter. **(D)** The diameter of the medulla at the whisker base occupies 11% - 46% of the diameter of the whisker base. **(E)** Schematics provide visual intuition for the size and shape of the medulla compared to the shape of the whole whisker. Relative to shorter whiskers, longer vibrissae have a larger fraction of their length occupied by the medulla, but the ratio of medulla base diameter to whisker base diameter increases only slightly for larger whiskers.

Previous studies have found that the medulla occupies between 50% to 75% of the overall length of the whisker (Voges, Carl et al. 2012). The resolution of this result was limited, however, because it was based on dividing the whisker length into quartiles and determining within each quarter where the medulla terminated. Examining the location of medulla termination as a continuous variable (Figure 3.4A) shows that medulla length is tightly linearly correlated with whisker arc length for vibrissae longer than ~10mm (R^2 = 0.966). This relationship is provided in equation 3.3, and predicts negative (non-physical) values of S_{Prox} when S_{Total} is less than 7.26mm / 0.95 = 7.64mm.

$$S_{Prox} = 0.95\, S_{Total} - 7.26 \qquad \text{(eq. 3.3)}$$

If the intercept in Figure 3.4A were zero, the medulla would occupy a constant fraction of the total whisker length. However, the intercept is not zero, so the fraction occupied by the medulla varies widely: it occupies anywhere between 32.9% and 97.6% of the total arc length (Figure 3.4B). On average, longer whiskers have a larger fraction of their length occupied by the medulla than shorter whiskers.

A similar analysis is shown for the base diameter of the medulla in Figure 3.4C-D. The base diameter of the medulla scales linearly with the base diameter of the whisker (Figure 3.4C). This relationship is provided in Equation 3.4 (R^2 = 0.804). The ratio of medulla base diameter to whisker base diameter, however, is quite variable: D_{Med} varies between 11% and 46% of D_{Base} (Figure 3.4D).

$$D_{Med} = 0.44\, D_{Base} - 0.02 \qquad \text{(eq. 3.4)}$$

Summarizing the results of Figures 3.4A-D, features of the medulla geometry (both length and diameter at the base) scale linearly with whisker geometry, but non-zero intercepts mean that variable fractions of the whisker are occupied by the medulla. An intuition for these relationships is provided in the schematic of Figure 3.4E. The percent of the total whisker length occupied by the medulla is much larger for longer whiskers than for shorter whiskers, whereas the percent of the total base diameter occupied by the medulla diameter is only slightly greater for larger whiskers than for shorter whiskers.

3.4.4. Defining the "taper" of a whisker: a meta-analysis of radius slope and radius ratio

A variety of studies of mammalian vibrissae and hairs have used the word "taper" and similar phrases differently. Williams and Kramer (2010) define whisker taper as the ratio of base radius to tip radius. Quist et al. (2011) and Quist and Hartmann (2012) use the phrase "taper ratio" to mean the exact same quantity.

The difference between the base and tip radii divided by the length of the whisker is defined as the “slope of radius” by Neimark et al. (2003). This same quantity is implicitly defined as taper by Hires et al. (2016) and is explicitly defined as taper by Sterbing-D'Angelo et al. (2016).

As can be seen in the schematics in Figure 3.5A, two parameters are required to describe the taper of a whisker. The ratio of base radius to tip radius can vary dramatically while the slope of the whisker remains constant. Conversely, the ratio of base radius to tip radius can remain constant while the slope varies. To avoid this semantic confusion, we avoid use of the word taper entirely, and instead propose:

$$Diameter\ Ratio \equiv Ratio_D \equiv \frac{D_{Base}}{D_{Tip}} \quad \text{(eq. 3.5a)}$$

$$Radius\ Ratio \equiv Ratio_R \equiv \frac{R_{Base}}{R_{Tip}} \quad \text{(eq. 3.5b)}$$

$$Diameter\ Slope \equiv Slope_D \equiv \frac{D_{Base}-D_{Tip}}{S_{Total}} \quad \text{(eq. 3.6a)}$$

$$Radius\ Slope \equiv Slope_R \equiv \frac{R_{Base}-R_{Tip}}{S_{Total}} \quad \text{(eq. 3.6b)}$$

Note that diameter ratio and radius ratio will always be exactly equal, but diameter slope will always be larger than radius slope by a factor of two.

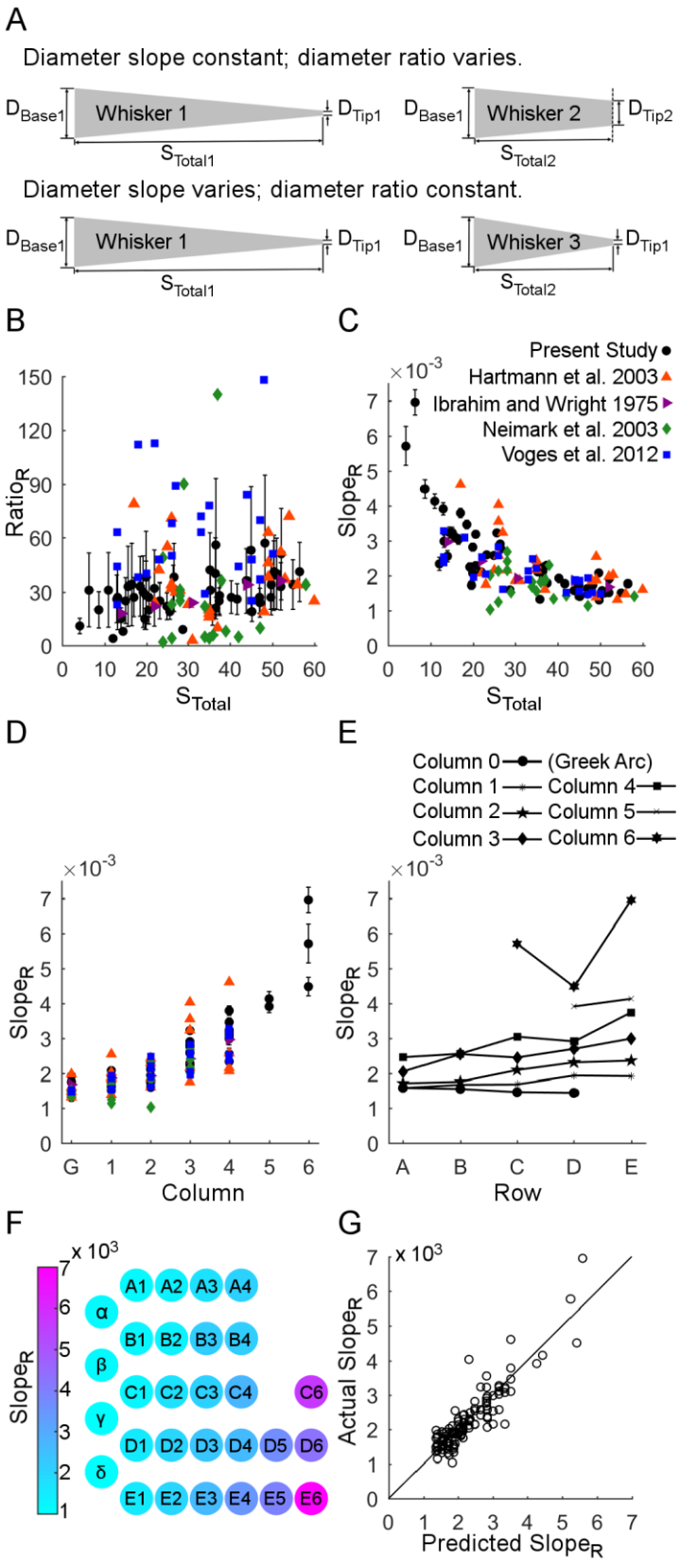

Figure 3.5: Quantification of radius ratio and radius slope as functions of whisker arc length. Subplots B – G use data from all 122 whiskers across the five studies of the meta-analysis, with error bars computed via propagation of error. **(A)** Two parameters are required to define the geometry of a whisker. The top schematic illustrates that two whiskers with the same radius slope can have very different radius ratios. The bottom schematic illustrates that two whiskers with different radius slopes can have the same radius ratio. **(B)** The radius ratio (R_{Base}/R_{Tip}) is extremely variable and does not exhibit a strong relationship with arc length (S_{Total}). $Ratio_R$ is extremely sensitive to changes in the radius of the whisker tip, which can vary considerably due to wear, damage, and barbering. Error bounds vary greatly. **(C)** Radius slope ($\frac{R_{Base}-R_{Tip}}{S_{Total}}$) is larger for shorter whiskers than for longer whiskers. Error bounds are much smaller than those calculated for $Ratio_R$. **(D)** $Slope_R$ increases with column position from caudal to rostral. **(E)** Within each column, $Slope_R$ tends to increase slightly from dorsal (row A) to ventral (row E). **(F)** A schematic of radius slope as a function of both row and column position across the array shows a strong trend by column and weak trend by row. **(G)** The best prediction for $Slope_R$ (equation 7) is linear with row and quadratic with column. The diagonal line represents the relationship where actual $Slope_R$ = predicted $Slope_R$.

In performing a meta-analysis of radius ratio and radius slope, we were able to use only those studies that included measurements of the whisker tip, as well as

measurements of whisker base diameter and arc length. Of the six previous studies used in the meta-analysis of Figures 3.2 and 3.3, four included values for tip diameter (Ibrahim and Wright 1975, Hartmann, Johnson et al. 2003, Neimark, Andermann et al. 2003, Voges, Carl et al. 2012). One of these four studies (Neimark, Andermann et al. 2003) explicitly tabulates data for 18 whiskers, including arc length, base and tip diameters, and radius slope. The data from Neimark et al. (2003) are not repeated in the present work as they can be found in Table 2 of that study.

Data for the other three studies (Ibrahim and Wright 1975, Hartmann, Johnson et al. 2003, Voges, Carl et al. 2012) are provided in Table 3.3 in the present work. To obtain the data in Table 3.3, we scanned in the figures from Ibrahim and Wright (1975) and extracted these points in MATLAB™, yielding a total of 5 whiskers. We also obtained the original measures of base and tip diameter and arc length for the 24 whiskers used in Hartmann et al. (2003) and the 23 whiskers from Voges et al. (2012). Results from the 52 whiskers of the present study (reduced dataset 2; see Methods, section 3.2), are tabulated in Table 3.4.

Tables 3.3 and 3.4 together with data from Neimark et al. (2003) thus provide measurements of arc length, base diameter, and tip diameter from a total of 122 (24 + 5 + 18 + 23 + 52) whiskers across five studies, corresponding to Hartmann et al., (2003), Ibrahim and Wright (1975), Neimark et al, (2003), Voges et al. (2012), and the present work. These studies were used to perform a meta-analysis of radius ratio and radius slope. Results are plotted in Figure 3.5 and summarized in Table 3.5. To best understand the data it is useful to iterate between the figure and the table.

Table 3.3: *Quantification of radius ratio and radius slope obtained from previous studies. The tip radius in Ibrahim and Wright (1975) was not visible at the resolution of the figure, so the mean tip radius from the present study was used as an approximation for R_{Tip} for all five whiskers.*

3.3A: Data from Ibrahim and Wright, 1975

Origin of data	Whisker	R_{Base} (µm)	R_{Tip} (µm)	S_{Total} (mm)	$\frac{R_{Base}}{R_{Tip}}$	$\frac{R_{Base}-R_{Tip}}{S_{Total}}$
We scanned Figure 2.6 from Ibrahim and Wright, 1975	β	90	2.5	52	36	1.68×10^{-3}
	A1	84.5	2.5	44	34	1.86×10^{-3}
	A2	61	2.5	30.5	24	1.92×10^{-3}
	A3	55.5	2.5	22	22	2.41×10^{-3}
	A4	44	2.5	14	18	2.96×10^{-3}

3.3B: Data from Hartmann et al., 2003

Origin of data	Whisker	R_{Base} (µm)	R_{Tip} (µm)	S_{Total} (mm)	$\frac{R_{Base}}{R_{Tip}}$	$\frac{R_{Base}-R_{Tip}}{S_{Total}}$
R_{Base} and arc length are shown in Figure 2.6c of Hartmann et al., 2003. R_{Tip} was obtained by re-examining the data used in Hartmann et al., 2003.	α	104.4	2	52	52	1.97×10^{-3}
	β	72.14	0.98	54	74	1.32×10^{-3}
	γ	100.8	4	60	25	1.61×10^{-3}
	δ	85.5	2.38	56	36	1.48×10^{-3}
	A1	69.6	1.5	49	46	1.39×10^{-3}
	B1	94.5	2.63	49	36	1.88×10^{-3}
	C1	109.8	2.75	53	40	2.02×10^{-3}
	D1	126	1.75	49	72	2.54×10^{-3}
	E1	93.6	4.75	48	20	1.85×10^{-3}
	A2	66.7	7.13	37	9	1.61×10^{-3}
	B2	81	23.25	31	3	1.86×10^{-3}
	C2	58.36	2.63	30	22	1.86×10^{-3}
	D2	90	5	35	18	2.43×10^{-3}
	E2	85.5	5.5	35	16	2.29×10^{-3}
	A3	41.33	1.13	23	37	1.75×10^{-3}
	B3	106.2	1.38	26	77	4.03×10^{-3}
	C3	79.2	4	35	20	2.15×10^{-3}
	D3	90	2.75	27	33	3.23×10^{-3}
	E3	95.4	3	26	32	3.55×10^{-3}
	A4	47.13	1.75	22	27	2.06×10^{-3}
	B4	54.74	1	25	55	2.15×10^{-3}
	C4	68.51	1.75	26	39	2.57×10^{-3}
	D4	62.1	2	28	31	2.15×10^{-3}
	E4	79.2	0.75	17	106	4.61×10^{-3}

3.3C: Data from Voges et al., 2012

Origin of data	Whisker	R_{Base} (µm)	R_{Tip} (µm)	S_{Total} (mm)	$\frac{R_{Base}}{R_{Tip}}$	$\frac{R_{Base}-R_{Tip}}{S_{Total}}$
Original data was obtained from the authors of Voges et al., 2012.	α	70.17	1.17	47	60	1.47×10^{-3}
	A1	65.34	1.34	42	49	1.52×10^{-3}
	A2	44.34	0.67	27	67	1.62×10^{-3}
	A3	40.00	1.00	20	40	1.95×10^{-3}
	A4	31.34	0.50	13	63	2.37×10^{-3}
	β	76.50	1.50	50	51	1.50×10^{-3}
	B1	72.50	1.67	45	44	1.57×10^{-3}

	B2	63.17	0.84	33	76	1.89×10^{-3}
	B3	47.67	0.84	23	57	2.04×10^{-3}
	B4	34.34	1.50	13	23	2.53×10^{-3}
	C1	83.50	1.00	44	84	1.88×10^{-3}
	C2	71.50	1.17	33	61	2.13×10^{-3}
	C3	56.50	0.67	22	85	2.54×10^{-3}
	C4	43.50	1.00	13	44	3.27×10^{-3}
	δ	74.17	0.50	48	148	1.53×10^{-3}
	D1	87.00	3.50	45	25	1.86×10^{-3}
	D2	78.17	1.00	35	78	2.20×10^{-3}
	D3	67.67	0.84	26	81	2.57×10^{-3}
	D4	55.84	0.50	18	112	3.07×10^{-3}
	E1	93.34	2.67	47	35	1.93×10^{-3}
	E2	87.34	3.17	34	28	2.48×10^{-3}
	E3	75.00	1.67	26	45	2.82×10^{-3}
	E4	57.34	1.50	18	38	3.10×10^{-3}

Table 3.4: *Whisker parameters from the present study used in the calculation of whisker slope and radius ratio (Reduced Dataset 2: 52 whiskers).*

Rat, Sex, Side	**Whisker**	R_{Base} **(µm)**	R_{Med} **(µm)**	R_{MedT} **(µm)**	R_{Tip} **(µm)**	S_{Total} **(mm)**	S_{Prox} **(mm)**	S_{Dist} **(mm)**	$\frac{R_{Base}}{R_{Tip}}$	$\frac{R_{Base}-R_{Tip}}{S_{Total}}$
1, F, R	A1	69.5	24.5	22.5	2.5	37.5	25.8	11.7	28	1.79×10^{-3}
1, F, R	A2	52	6	22.5	6	28.7	21.0	7.7	9	1.60×10^{-3}
1, F, R	A3	42.5	7	25.5	1.5	19.9	8.5	11.4	28	2.06×10^{-3}
1, F, R	B1	80	27	21.5	3	46.9	32.9	14.0	27	1.64×10^{-3}
1, F, R	B2	36.5	8.5	24	2.5	19.6	7.7	11.9	15	1.73×10^{-3}
1, F, R	C1	81.5	22	19.5	2	50.4	38.0	12.4	41	1.58×10^{-3}
1, F, R	C2	83	28	21.5	2	35.2	25.0	10.2	42	2.30×10^{-3}
1, F, R	C3	62.5	16.5	25	2.5	23.2	13.2	10.0	25	2.59×10^{-3}
1, F, R	C4	50	12	32	1.5	15.6	6.0	9.6	33	3.11×10^{-3}
1, F, R	C6	26.5	5.5	24.5	2.5	4.2	4.1	0.1	11	5.71×10^{-3}
1, F, R	D1	102.5	35.5	19	2.5	56.5	45.9	10.6	41	1.77×10^{-3}
1, F, R	D2	89	37	22.5	3.5	37.4	27.3	10.1	25	2.29×10^{-3}
1, F, R	D4	53.5	17.5	29	7	14.4	7.1	7.3	8	3.23×10^{-3}
1, F, R	E1	106.5	42	19	4	49.6	42.4	7.2	27	2.07×10^{-3}
1, F, R	E3	87	34	18.5	4.5	25.6	19.8	5.8	19	3.22×10^{-3}
1, F, R	E4	67	26	26	2.5	17.0	9.9	7.1	27	3.79×10^{-3}
1, F, R	α	72.5	21.5	21.5	3	47.0	31.2	15.8	24	1.48×10^{-3}
1, F, R	β	80.5	22.5	21.5	3	40.3	38.9	1.4	27	1.92×10^{-3}
1, F, R	γ	79	27	21.5	2	51.0	39.1	11.9	40	1.51×10^{-3}
2, M, R	A1	71.5	22	14.5	2	43.9	34.9	9.0	36	1.58×10^{-3}
2, M, R	A3	47.5	13	22	1.5	21.9	12.0	9.9	32	2.10×10^{-3}
2, M, R	A4	37.5	5.5	27.5	9.5	12.0	4.8	7.2	4	2.33×10^{-3}
2, M, R	B1	81.5	30	20	2.5	52.0	42.3	9.7	33	1.52×10^{-3}

2, M, R	B2	74	25.5	18.5	3.5	36.6	28.4	8.2	21	1.93×10^{-3}
2, M, R	B3	44.5	12	23.5	1.5	19.2	10.6	8.6	30	2.24×10^{-3}
2, M, R	B4	40.5	5	31	1.5	13.1	4.3	8.8	27	2.98×10^{-3}
2, M, R	C2	79.5	26	20	2	36.5	28.0	8.5	40	2.12×10^{-3}
2, M, R	C3	57.5	14.5	19	1.5	19.9	13.7	6.2	38	2.81×10^{-3}
2, M, R	C4	50.5	8	26.5	2	15.0	7.6	7.4	25	3.23×10^{-3}
2, M, R	D1	101.5	34	17	2	52.1	45.6	6.5	51	1.91×10^{-3}
2, M, R	D5	52.5	11	30	2	12.9	5.9	7.0	26	3.91×10^{-3}
2, M, R	E3	75.5	29	19.5	2	26.6	21.0	5.6	38	2.76×10^{-3}
2, M, R	E4	66	23.5	22.5	2	18.5	12.5	6.0	33	3.46×10^{-3}
2, M, R	E5	46.5	15.5	27.5	1.5	10.9	5.2	5.7	31	4.13×10^{-3}
2, M, R	α	77	23.5	19.5	2	50.3	40.8	9.5	39	1.49×10^{-3}
2, M, R	β	67	20	19	3.5	45.1	36.3	8.8	19	1.41×10^{-3}
2, M, R	γ	67	22	20.5	2	49.7	41.3	8.4	34	1.31×10^{-3}
2, M, R	δ	50.5	12.5	20.5	3	35.8	28.2	7.6	17	1.33×10^{-3}
3, M, L	A1	77	30	19.5	3	41.7	30.3	11.4	26	1.77×10^{-3}
3, M, L	A4	38	8	24	2.5	13.9	6.4	7.5	15	2.55×10^{-3}
3, M, L	B1	85.5	34	20	1.5	48.2	37.7	10.5	57	1.74×10^{-3}
3, M, L	B2	76.5	25	19	2.5	35.3	26.1	9.2	31	2.10×10^{-3}
3, M, L	B3	49.5	13.5	20.5	2.5	20.6	12.8	7.8	20	2.28×10^{-3}
3, M, L	C2	83.5	28	20	1.5	36.6	27.7	8.9	56	2.24×10^{-3}
3, M, L	C4	51.5	13	25.5	1.5	16.5	8.9	7.6	34	3.03×10^{-3}
3, M, L	D3	67	28.5	20.5	3	24.9	18.3	6.6	22	2.57×10^{-3}
3, M, L	D4	68	22.5	23	2.5	20.6	14.5	6.1	27	3.18×10^{-3}
3, M, L	D6	40.5	9	32.5	2	8.6	2.9	5.7	20	4.48×10^{-3}
3, M, L	E3	79	31	22	2.5	26.4	20.2	6.2	32	2.90×10^{-3}
3, M, L	E6	46	7.5	29.5	1.5	6.4	3.0	3.4	31	6.95×10^{-3}
3, M, L	α	80	24	24	1.5	44.9	37.1	7.8	53	1.75×10^{-3}
3, M, L	β	85.5	26.5	19	2.5	54.9	49.6	5.3	34	1.51×10^{-3}

Table 3.5. *Meta-analysis of radius ratio and radius slope across five studies. Columns 1 and 2 provide the study information and origin of data respectively. Column 3 shows the mean, standard deviation, and median for the five studies for radius ratio. Column 3 of Ibrahim and Wright, 1975 also shows extremum for radius ratio due to data from only five whiskers. Column 4 displays the mean, standard deviation, and median across each of the five studies for radius slope.*

Study **Age, Sex, Strain, Whiskers (#)**	**Origin of data**	**Radius Ratio**	**Radius Slope**
Ibrahim and Wright, 1975 3 –6 months Male	***page 52:*** "In rats α, β, γ and δ vibrissae are 3-5 μm at their tips and 160-180 μm at the widest part excluding the club." ***Figure 8A*** provides data about the arc length of	Smallest possible ratio: 80/2.5 = **32** Largest possible ratio: 90/1.5 = **60**	Arc length data (in mm) taken from Fig. 8A, ~140 days: α = 44; β = 51, γ = 52, δ = 59 Min possible radius slope = (80 – 2.5)/59,000 = $\mathbf{1.31\times10^{-3}}$

Wistar rat 5 whiskers	whiskers α, β, γ and δ		Max possible radius slope = (90 – 1.5)/44,000 = **2.01×10^{-3}**
	Figure 6 plots diameter as a function of arc length for the β, A1, A2, A3, and A4 rat vibrissae. The resolution of Figure 6 is severely limited at the tip. The data were extracted from the figure and are provided as Table 3A in the present manuscript.	Based on data from Table 3A in prese Work (from Fig. 6 of Ibrahim and Wright, 1975) Mean ± STD: **27 ± 8** Median: **24**	Based on data from Table 3A in present work (from Fig. 6 of Ibrahim and Wright, 1975) Mean ± STD: **$2.17\times10^{-3} \pm 0.52\times10^{-3}$** Median: **$1.92\times10^{-3}$**
Neimark et al., 2003 Unknown age, sex strain 18 whiskers	***Table 2*** provides arc length, base diameter, and tip diameter for 18 whiskers. The whiskers include the Greek column and columns 1, 2, and 3 of rows A through E.	Based on Table 2 in Neimark et al, 2003: Mean ± STD: **29 ± 35** Median: **22.5**	Based on data from Table 2 in Neimark et al, 2003: Mean ± STD: **$1.76\times10^{-3} \pm 0.46\times10^{-3}$** Median: **$1.75\times10^{-3}$**
Hartmann et al., 2003 Adult Female Sprague Dawley, 24 whiskers	***Figure 6c*** shows a log-log plot of radius vs. arc length for 24 rat whiskers. These original data are provided as Table 3B in the present manuscript, along with tip diameters.	Based on Table 4B in present work (from Fi 6c in Hartmann et a 2003) Mean ± STD: **39 ± 24** Median = **34.5**	Based on Table 4B in present work (from Fig. 6c in Hartman et al., 2003) Mean ± STD: **$2.27\times10^{-3} \pm 0.83\times10^{-3}$** Median = **$2.04\times10^{-3}$**
Voges et al., 2012 14 months, Female, Wistar Hannover, 23 whiskers	***Figures 3 and 4*** show data for arc length, base diameter, and tip diameter. The origina data was obtained from the authors and provided as Tabl 3C in the present manuscript	Based on data fro Table 4 C in present work (fro Figs. 3 & 4 of Voges al., 2012) Mean ± STD: **61 ± 29** Median = **57**	Based on data from Table 4C in present work (from Figs. 3 & 4 of Voges et al., 2012) Mean ± STD: **$2.17\times10^{-3} \pm 0.55\text{x}10^{-3}$** Median = **$2.04\times10^{-3}$**
Belli et al., 2016 (present study) 3-13 months, Male & Female, Sprague-Dawley, 52 whiskers	Data collected in present study and tabulated in Table 4.	Mean ± STD: **29 ± 11** Median = **28**	Mean ± STD: **$2.48\times10^{-3} \pm 1.10\times10^{-3}$** Median = **$2.18\times10^{-3}$**

Figure 3.5B plots the radius ratio for the raw data presented in Tables 3.3 and 3.4, as well as for Neimark et al. (2003). The radius ratio is extremely variable, ranging between 2 and 148. This variability is expected, because the tip of the whisker is highly susceptible to damage due to wear and barbering. There is a small but significant trend for the radius ratio to increase with arc length. Radius ratio for each of the five studies is summarized in the third column of Table 3.5. The average radius ratio across all five studies (122 whiskers), is 37 ± 25 (mean ± std) with a median of 32. The mean and median values are more than twice the previous estimate of 15 obtained by Williams and Kramer (2010); this discrepancy is addressed further in Discussion.

Columns are as follows: study information; age, sex, strain, and number of whiskers; origin of data; means, SD, and median for the five studies for radius ratio; and the means, SD, and median across each of the five studies for radius slope. The Radius Ratio and Radius Slope columns for Ibrahim and Wright (1975) show only extrema for radius ratio because of the large measurement uncertainties in the tip and base diameters. Another version of this table is available as a Supplemental Table at https://github.com/SeNSE-lab/RatWhiskerGeometry.git, formatted for readability and scientific clarity.

Radius slope is much more consistent across all five studies, as shown in Figure 3.5C and summarized in the fourth column of Table 3.5. Figure 3.5C plots $Slope_R$ as a function of total whisker arc length for the raw data presented in Tables 3 and 4 and from Neimark et al. (2003). A strong relationship between $Slope_R$ and arc length is observed: shorter whiskers get thinner along their length faster than do longer whiskers. Values of $Slope_R$ range between 0.00104 and 0.00695 (mean ± std = 0.00226 ± 0.00089; median = 0.00205).

The functional relationship shown in Figure 3.5C is obviously dominated by the factor of inverse arc length ($1/S_{Total}$) included in the definition of $Slope_R$. To differentiate between the effects of whisker arc

length and whisker position within the array, we constructed plots of radius slope as a function of row and column position, as shown in Figures 3.5D-F. Radius slope clearly increases with column position, from caudal to rostral (Figure 3.5D). In addition, when plotted as a function of row position, Figure 3.5E further shows that radius slope increases very slightly from dorsal to ventral: The E-row whiskers get thinner along their length just slightly faster than the A-row whiskers. Figure 3.5F shows the effects of row and column position on radius slope presented in Figures 3.5D-E on a color-coded schematic of the rat vibrissal array. We fit univariate models for $Slope_R$ as a function of row and column respectively in order to determine the highest order model. Criteria for selecting the highest order model while avoiding overfitting was on the basis of AIC and predicted vs. actual value plots. We then combined these univariate relationships into a multivariate model and found $Slope_R$ to be a function of both row and column with a clear dependence on column squared:

$$Slope_R = 0.00119 + 0.00017\,Row\, - 0.00007\,Col + 0.00011\,Col^2 \qquad \text{(eq. 3.7)}$$

In Equation 3.7, as in all previous equations, *Row* varies between 1 and 5. However, because the dataset has been reduced (from 519 to 122 whiskers), *Col* varies between 0 and 6. The quality of the fit of Equation 3.7 to the experimental data is shown in Figure 3.5G, and the adjusted R^2 is 0.806.

It is important to note that because R_{Tip} is so much smaller than R_{Base}, it will typically contribute very little to the calculation of slope in Equations 3.6a and 3.6b. Across the five datasets that included tip diameter measurements (122 whiskers), we found that excluding R_{Tip} (i.e. setting R_{Tip} equal to zero in Equation 3.6b) increased slope by a median value of only 3.23% and by less than 15% for all but nine whiskers. This result means that to first order, the ratio of D_{Base} to S_{Total} is generally an excellent approximation for $Slope_D$, and the ratio of RBase to S_{Total} is an excellent approximation for $Slope_R$.

In principle, then (after dividing by a factor of 2 and S_{Total}), Equation 3.2 could be used to approximate the radius slope of the whisker instead of Equation 3.7. We compared the quality of fit for radius slope computed using equation 3.2 after dividing by $2S_{Total}$ with that computed using Equation 3.7. We calculated the difference between the actual value for $Slope_R$ and each value for $Slope_R$ predicted by Equations 3.2 and 3.7. We then found the mean of these differences. We found that on average Equation 3.2 was approximately 13% in error of the actual data, with a tendency to overpredict $Slope_R$. On average Equation 3.7 was approximately 12% in error of the actual data, with a tendency to underpredict $Slope_R$.

3.4.5. Variations in radius slope between proximal and distal regions of the whisker

Given that the proximal region of the whisker contains the medulla, a natural thought was to look for differences in radius slope between the proximal and distal regions of the whiskers. In analogy to the definition for radius slope of Equation 3.6b, we computed the proximal and distal radius slope as:

$$Proximal\ Radius\ Slope \equiv Slope_{R,Prox} \equiv \frac{R_{Base} - R_{MedT}}{S_{Prox}} \qquad \text{(eq. 3.8a)}$$

$$Distal\ Radius\ Slope \equiv Slope_{R,Dist} \equiv \frac{R_{MedT} - R_{Tip}}{S_{Dist}} \qquad \text{(eq. 3.8b)}$$

Using the data from Table 3.4 that included measurements of the medulla (reduced Dataset 2, 52 whiskers), we compared these estimates of proximal and distal radius slope from Equations 3.8a and 3.8b with the radius slope calculated from Equation 3.6b. As shown in Figure 3.6A, and confirmed by a Bonferroni corrected Wilcoxon Signed-Rank Test between each paired set, no significant differences were observed between these three estimates.

However, when the ratio of proximal slope to distal slope was analyzed as a function of column, the majority of whiskers in columns 1 and 2 had proximal slopes greater than distal slopes (12 out of 18). In contrast, the majority of whiskers in columns 3 – 6 had proximal slopes smaller than distal slopes (19 out of 25). Surprisingly, the majority (8/9) whiskers in the Greek column also had proximal slopes smaller than distal slopes. Across all whiskers, the ratio of proximal to distal slopes ranged between 0.002 and 1.5. Finding systematic differences between proximal and distal radius slope is likely to require a higher resolution analysis in which radius is measured at many points along the whisker arc length (Ibrahim and Wright 1975, Williams and Kramer 2010, Hires 2016).

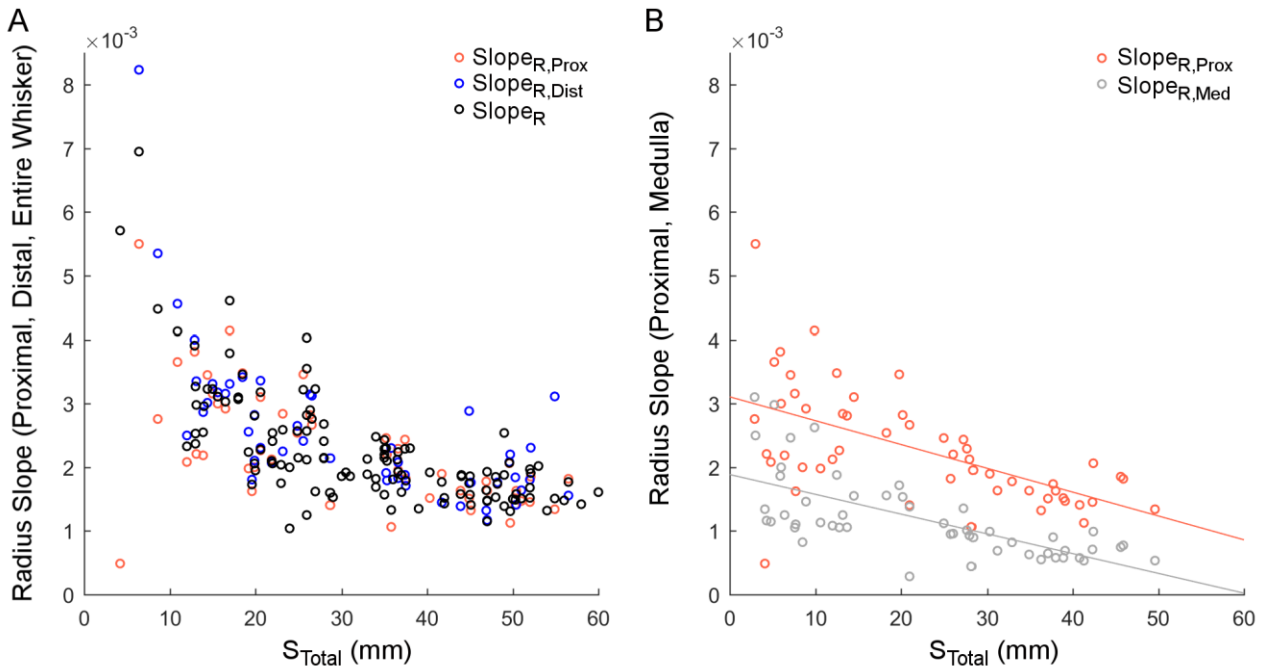

Figure 3.6: Both subplots use reduced Dataset 2 which consisted of 52 whiskers. (A) Within the resolution of the present study, radius slope is not significantly different between proximal and distal whisker segments. Out of 52 whiskers, 36.5% had a proximal slope greater than that in the distal region; the remaining 63.5% had a distal slope greater than the proximal slope. **(B)** The radius slope of the medulla is smaller by a constant offset than the radius slope of the proximal region of the whisker. The offset is 0.00122.

Finally, we compared the radius slope measured in the proximal portion of the whisker (eq. 3.8a) with the radius slope of the medulla, defined as:

$$Medulla\ Radius\ Slope \equiv\ Slope_{R,Med}\ \equiv \frac{R_{Med}}{S_{Prox}} \qquad \text{(eq. 3.9)}$$

Figure 3.6B reveals a significant difference between the radius slope of the whisker and the radius slope of the medulla (two-sided Wilcoxon signed rank text, $p < 0.0001$). On average, the radius slope of the medulla is significantly less than that of the radius slope of the proximal portion of the whisker. The best fit equations for the radius slope of the proximal portion of the whisker and the radius slope of the medulla were respectively, $Slope_{R,Prox} = 0.00311 - 0.00004\, S_{Prox}$ and $Slope_{R,Med} = 0.00189 - 0.00003\, S_{Prox}$. We tested the hypothesis that the difference between these two slopes was equal to zero using a Z-score method (Paternoster, Brame et al. 1998). We found no significant difference between these two slopes ($Z = 0.7301$, $p < 0.4653$). This suggests that medulla slope is approximately a constant offset from proximal slope by the difference in intercepts of our two equations, i.e., $0.00311 - 0.00189 = 0.00122$.

3.4.6. Summary: equations for whisker geometry across the vibrissal array

The present work has developed equations that describe how the geometry of individual whiskers varies across the array. All equations assume that the variable *Row* varies between 1 and 5. Equations 3.1 and 3.2 assume that *Row* varies between 0 and 8, while Equation 3.7 assumes *Col* varies between 0 and 6, with 0 representing the Greek arc.

We assume that the three quantities easiest for experimentalists to measure are row, column, and arc length. In the case that only row and column position are known, S_{Total} can be estimated (in units ofmm) based on Equation 3.1:

$$S_{Total} = 43.1 + 1.8\,Row - 7.6\,Col, \quad Adj.R^2 = 0.850 \qquad \text{(eq. 3.1)}$$

Equations 3.2, 3.3, 3.4, and 3.7 developed in the present work can then be used in conjunction with S_{Total} (either as measured experimentally or from Equation 3.1) to calculate the whisker's base diameter, medulla length, medulla, diameter, and radius slope.

To describe base diameter (D_{Base}) as function of arc length (S_{Total}), we recommend referencing the equations in Table 3.2 by individual row and column position. If a single equation is necessary, Figure 3.3G shows that base diameter is well described as a function of total arc length while adjusting for differences across row and column:

$$D_{Base} = 0.041 + 0.002\,S_{Total} + 0.011\,Row - 0.004\,Col, \quad Adj.R^2 = 0.800 \qquad \text{(eq. 3.2)}$$

Figure 3.4A shows that medulla arc length is a function of total arc length for whiskers longer than 10mm:

$$S_{Prox} = 0.95\,S_{Total} - 7.26, \quad R^2 = 0.966 \qquad \text{(eq. 3.3)}$$

Figure 3.4C shows that the base diameter of the medulla is a function of the base diameter of the whisker:

$$D_{Med} = 0.44\,D_{Base} - 0.02, \quad R^2 = 0.804 \qquad \text{(eq. 3.4)}$$

Figure 3.5F shows that radius slope varies according to both row and column position:

$$Slope_R = 0.00119 - 0.00007\,Col + 0.00017\,Row + 0.00011\,Col^2, \quad Adj.R^2 = 0.806 \qquad \text{(eq. 3.7)}$$

Together, Equations 3.2, 3.3, 3.4, and 3.7 can then be used to estimate whisker geometry for use in simulations.

3.5. Discussion

The present work has identified systematic trends in whisker geometry across the array, including trends in the geometry of the whisker medulla. A shorter whisker is not simply a scaled version of a larger whisker. These results mean that whiskers in different row and column positions will bend differently when they touch an object. In addition, whiskers in different row and column positions will have different density distributions along their lengths, which will alter their dynamics (Yang, Belli et al. 2016).

3.5.1. Variations in whisker arc length across the array

As indicated in Results, considerable overlap was observed in the prediction bounds for all eight datasets when S_{Total} was plotted as a function of row and column identity. Therefore, all data were grouped to obtain the best linear fit between S_{Total} and row and column position (Equation 3.1). However, the bounds for the Kan et al., 2013 and Birdwell et al., 2007 datasets were wider than both the upper and lower limits of those from the present study. For completeness, we therefore also found the best linear equation for S_{Total} as a function of row and column position after excluding these two datasets. The equation after excluding the two datasets was found to be $S_{Total} = 42.2 + 2.0\,Row - 7.6\,Col$ $(Adj.R^2 = 0.873)$. Whisker lengths computed using this equation differ from those computed using Equation 3.1 by less than 0.8mm, indicating that the datasets from Kan et al., 2013 and Birdwell et al., 2007 had little effect on the final relationship.

It is also informative to compare Equation 3.1 with the equation for whisker arc length obtained by Towal et al, 2011. The equation for arc length as a function of row and column position given by Towal et al., 2011 is:

$$S_{Total} = 52.1 + 2.2\,Row - 7.9\,Col \quad \text{(eq. 3.10)}$$

In Equation 3.10, *Row* varies between 1 and 5 as in the present work, but all column variables are coded as [1,2,3,…] rather than the convention used here, in which *Col* varies between 0 and 7. The values for S_{Total} obtained from Equations 3.1 and 3.10 differ by less than 3mm for the largest whiskers, and by less than 1.5mm for the smaller, more rostral whiskers.

3.5.2. The relationship between the diameter of the whisker base and whisker arc length

When evaluated over whiskers of all lengths, the relationship between the diameter at the whisker base (D_{Base}) and the total whisker arc length (S_{Total}) may at first appear linear (Figure 3.2). However, closer examination reveals that the relationship depends on both column and row position (Figure 3.3). The dependence on column position is somewhat expected, because the arc length of the whisker is itself correlated with column (Ibrahim and Wright 1975, Brecht, Preilowski et al. 1997, Towal, Quist et al. 2011). The equations in the top half of Table 3.2 indicate that when separated by column, D_{Base} and S_{Total} are linearly related with an average correlation coefficient of approximately 0.5.

Surprisingly, however, the relationship between D_{Base} and S_{Total} depends even more strongly on row position than it does on column position. Table 3.2 indicates that when separated by row, D_{Base} and S_{Total} are strongly linearly related with an average correlation coefficient close to 0.8. Thus the relationship between D_{Base} and S_{Total} is much more linear within a row than within a column. For a given length, whiskers in more ventral rows have larger base diameters than whiskers in more dorsal rows. We suggest that whiskers in the ventral rows are thicker because they tend to be in more continuous contact with the ground (The, Wallace et al. 2013, Arkley, Grant et al. 2014, Hobbs, Towal et al. 2016, Hobbs, Towal et al. 2016).

3.5.3. Parameters that define the "taper" of a whisker

The word "taper" has been defined differently across studies. Some have used the radius ratio (or diameter ratio) to define taper (Williams and Kramer 2010, Quist, Seghete et al. 2014, Huet, Schroeder et al. 2015, Huet and Hartmann 2016). Other studies have used the radius slope (or diameter slope) to define taper (Neimark, Andermann et al. 2003, Hires, Pammer et al. 2013, Hires 2016).

The schematic of Figure 3.5A illustrates why neither of these definitions alone is sufficient to characterize the geometry of the whisker – both are needed. The aspect ratio of the whisker is defined by three parameters (RBase, RTip, S_{Total}). If any one of those three parameters is fixed, two equations are then required to define the whisker's geometry. These are Equations 3.5 and 3.6 in the present work, defining the radius ratio and radius slope.

The radius ratio is extremely sensitive to tiny variations in tip radius: even a 2-3μm change in tip radius can change the radius ratio by a factor of two. Accordingly, a comparative analysis across five studies from separate laboratories (Figure 3.5B, Table 3.5), shows that the radius ratio varies greatly even for whiskers in the same row and column position. Across all five studies, the median radius ratio was 37.00, but the range was extremely large. For example, the data of Neimark et al. (2003) include radius ratios that range from 2.43 to 140, with an average of 29. If two outliers are removed, however, the average decreases to ~15, consistent with the analysis of Williams and Kramer (2010). The whisker tip is often damaged due to wear, breakage, and barbering, and its exact size is unlikely to be of behavioral importance to the rat.

In contrast, the radius slope exhibits clear and systematic variations across the array. The slope of a whisker will have a strong influence on its quasistatic bending as well as on its dynamic behavior (Hartmann, Johnson et al. 2003, Neimark, Andermann et al. 2003, Ritt, Andermann et al. 2008, Solomon and Hartmann 2008, Wolfe, Hill et al. 2008, Solomon and Hartmann 2010, Solomon and Hartmann 2011,

Hires, Pammer et al. 2013, Hartmann 2015, Yu Y. 2016). Radius slope is not constant across the array – it is larger for shorter, more rostral whiskers than for longer, more caudal whiskers (Figure 3.5D). There is also a slight increase in radius slope from dorsal to ventral, except for the Greek column of whiskers (Figure 3.5E). Shorter whiskers exhibit a steeper variation in cross-sectional diameter per unit length than longer whiskers. Thus, when the same point load is applied to a rostral and caudal whisker at the same radial distance of contact, the rostral whisker will exhibit larger variations in local curvature change along its length than will the caudal whisker (Solomon and Hartmann 2011, Yang and Hartmann 2016).

3.5.4. Medulla geometry varies between rostral and caudal whiskers

To date, all studies of whisker dynamics have assumed that the whisker is a solid conical frustum (Hartmann, Johnson et al. 2003, Neimark, Andermann et al. 2003, Boubenec, Shulz et al. 2012, Yan, Kan et al. 2013, Quist, Seghete et al. 2014, Lucianna, Albarracin et al. 2016). The presence of the medulla, however, will change the mass distribution along the whisker length, which will have a significant effect on whisker dynamics.

The present work reveals close linear relationships between medulla geometry and whisker geometry. As shown in Figure 3.4A, there is an exceptionally close linear relationship between medulla arc length (S_{Prox}) and total whisker length (S_{Total}), $R^2 = 0.966$. A somewhat weaker linear relationship is found between medulla base diameter (D_{Med}) and whisker base diameter (D_{Base}), $R^2 = 0.804$ (Figure 3.4C). Because both of these equations have non-zero intercepts, the fraction of the whisker occupied by the medulla increases for longer whiskers (Figure 3.4B, D, E). Some implications of these results for whisker dynamics are considered in the companion paper (Yang, Belli et al. 2016).

3.5.5. Conclusions and future directions

To develop models of whisker mechanics during natural exploratory behavior requires accurate quantification of geometry both at the level of the entire whisker array (Knutsen, Biess et al. 2008, Towal, Quist et al. 2011) as well as at the level of individual vibrissae. The geometry of the individual whisker will have a large influence on the mechanical signals generated at the whisker base during both non-contact and contact whisking. The equations developed in the present work can be incorporated into mechanical models to quantify the signals at the base of each whisker during exploratory whisking behavior.

Chapter 4: Quantifying the three-dimensional facial morphology of the laboratory rat with a focus on the vibrissae

This chapter was published in PLOS One as: Belli HM*, Bresee CS*, Graff MM, Hartmann MJZ (2017) Quantifying the three-dimensional facial morphology of the laboratory rat with a focus on the vibrissae. PLOS One 13(4): e0194981

*authors contributed equally

4.1. Abstract

The morphology of an animal's face will have large effects on the sensory information it can acquire. Here we quantify the arrangement of cranial sensory structures of the rat, with special emphasis on the mystacial vibrissae (whiskers). Nearly all mammals have vibrissae, which are generally arranged in rows and columns across the face. The vibrissae serve a wide variety of important behavioral functions, including navigation, climbing, wake following, anemotaxis, and social interactions. To date, however, there are few studies that compare the morphology of vibrissal arrays across species, or that describe the arrangement of the vibrissae relative to other facial sensory structures. The few studies that do exist have exploited the whiskers' grid-like arrangement to quantify array morphology in terms of row and column identity. However, relying on whisker identity poses a challenge for comparative research because different species have different numbers and arrangements of whiskers. The present work introduces an approach to quantify vibrissal array morphology regardless of the number of rows and columns, and to quantify the array's location relative to other sensory structures. We use the three-dimensional locations of the whisker basepoints as fundamental parameters to generate equations describing the length, curvature, and orientation of each whisker. Results show that in the rat, whisker length varies exponentially across the array, and that a hard limit on intrinsic curvature constrains the whisker height-to-length ratio. Whiskers are oriented to "fan out" approximately equally in dorsal-ventral and rostral-caudal directions. Quantifying

positions of the other sensory structures relative to the whisker basepoints shows remarkable alignment to the somatosensory cortical homunculus, an alignment that would not occur for other choices of coordinate systems (e.g., centered on the midpoint of the eyes). We anticipate that the quantification of facial sensory structures, including the vibrissae, will ultimately enable cross-species comparisons of multi-modal sensing volumes.

4.2. Introduction

Facial anatomy, and particularly the anatomy of sensory accessory structures, has a long history of study. Many cranial sensory structures have been investigated in the context of psychophysics, biomechanics, and neuroanatomy, from the pinnae (Koka, Jones et al. 2011), to the eye (Green, Powers et al. 1980, Kiltie 2000, Burton 2006), the nostrils (Rajan, Clement et al. 2006), and the teeth (Byers and Dong 1989, Koenigswald, Anders et al. 2010). In addition, animal skulls and muscles have been the subject of extensive morphometric analyses (Gunduz, Jaarola et al. 2007, Khammes-El Homsi and Aulagnier 2010, O'Higgins, Cobb et al. 2011, Schlanbusch, Jensen et al. 2011, O'Higgins, Fitton et al. 2012, Baverstock, Jeffery et al. 2013, Pfaff, Martin et al. 2015) with the semicircular canals receiving considerable attention (Hullar 2006, Cox and Jeffery 2008).

Although these earlier studies provide a rich description of facial and sensory anatomy, few studies have examined the spatial relationships amongst the sensory structures. For example, the positions of a rat's eyes relative to its mouth have not been compared with the corresponding relative positions in the cat. This knowledge gap limits our ability to determine how various animals differ in their acquisition of multi-modal sensory information as they navigate their environment.

The goal of the present work is to develop an approach towards quantifying the morphology of facial sensory structures in a manner that facilitates cross-species comparisons. This goal leads to an interesting

problem: although all mammals have two eyes, two ears, two nostrils, and a single mouth, they can have very different numbers and arrangements of facial vibrissae (whiskers). Only mammals have true vibrissae, but vibrissal-like structures have evolved at least twice in vertebrates: in the mammalian lineage, as hair (Paul 1972), and also in the avian lineage, as feathers, with birds showing a similar diversity of facial tactile feather arrangement (Seneviratne and Jones 2008, Cunningham, Alley et al. 2011). This convergent evolution underscores the importance of this tactile sensory modality, and also highlights the need to characterize the morphology of these diverse sensory accessory structures.

The mammalian vibrissae are exquisitely sensitive tactile sensors, generally arranged in an array of rows and columns across the face (Muchlinski, Durham et al. 2013). The whiskers serve a multitude of behavioral functions across species, including navigation and climbing (The, Wallace et al. 2013, Arkley, Grant et al. 2014), wake following (Dehnhardt, Mauck et al. 2001, Gaspard, Bauer et al. 2017), anemotaxis (Yu, Graff et al. 2016), foraging (Van Horn 1970, Muchlinski 2010), predation (Anjum, Turni et al. 2006, McGovern, Marshall et al. 2015), and social interactions (Wolfe, Mende et al. 2011). However, all previous studies that have examined the arrangement of whiskers on the face have quantified array morphology in terms of the discretized row and column positions of the whiskers (Brecht, Preilowski et al. 1997, Knutsen, Biess et al. 2008, Towal, Quist et al. 2011). A quantification approach based on discretized rows and columns is clearly incompatible with the need for cross-species comparisons.

In the present work, we first consider several possible choices for coordinate systems in which to quantify facial morphology and then deliberately choose “whisker-centric” axes based on the three-dimensional (3D) positions of the whisker basepoints. This choice allows us to quantify the morphology of the vibrissal array as well as the arrangement of other facial features and skull landmarks in terms of the whisker basepoint coordinates.

We anticipate that cross-species comparisons of the morphology of cranial sensory structures may lead to insights into the evolution and physiology of animal senses, thereby illuminating selection pressures within particular environmental niches that resulted in a variety of animal adaptations (Simpson and Graf 1981, Ruf, Frahnert et al. 2009, Anthwal, Joshi et al. 2013). The present work begins what we anticipate will be a series of studies that quantify the 3D spatial relationships between whiskers, rhinarium, incisors, pinnae, mouth, and eyes across multiple species.

4.3. Methods

All procedures were approved in advance by the Animal Care and Use Committee of Northwestern University.

4.3.1. Data collection

Two Datasets containing a total of 518 macrovibrissae whiskers from nine rats were used. All animals were female Long Evans rats between the ages of 5 and 36 months.

4.3.1.1. Dataset 1: We reanalyzed data from 167 whiskers from three of the six rats used in the study of Towal et al., 2011. These three rats were first scanned in a three dimensional (3D) volumetric scanner. Then each whisker was plucked from the animal and scanned in 2D on a flatbed scanner. Of the 167 whiskers, 158 2D scans were analyzed to obtain measurements of arc length, and 130 were analyzed to obtain measurements of intrinsic curvature. The whiskers from the other three rats from Towal et al., 2011 were scanned only in 2D and were not reanalyzed in the present study.

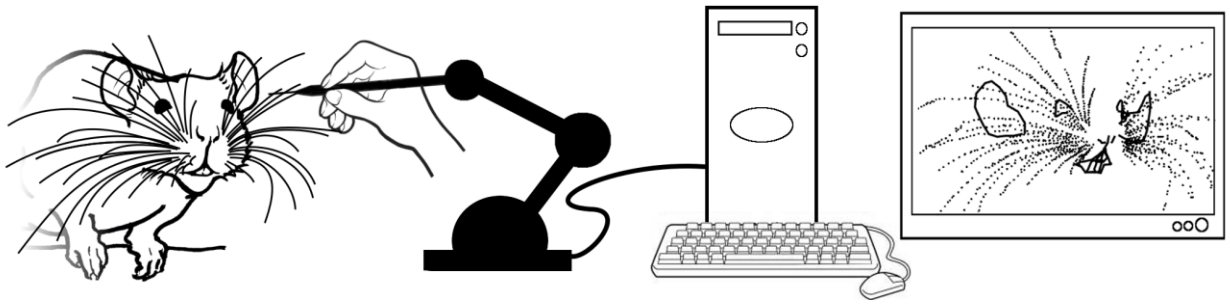

Figure 4.1: Schematic depicting the data collection process for Dataset 2. The shapes of the whiskers and facial features of anesthetized rats were manually traced using a Microscribe™ 3D Digitizer. These 3D traces were imported into Matlab™ and placed in standard orientation and position.

Details of the methods for whisker acquisition are provided in Towal et al., 2011, but to summarize, euthanized rats were placed in a 3D laser scanner (Surveyor DS-3040) yielding a finely digitized 3D point cloud. The point cloud was imported into the software package RAPIDFORM XOR, where data points corresponding to each macrovibrissa were manually extracted from the point cloud. Manual rotation of the 3D scanned image was used to visually determine the set of points that clearly belonged to each whisker through all angles of rotation. Whisker basepoints were identified as the centroid of a small number of points (typically 8-20) on the mystacial pad that rotated the least relative to that identified macrovibrissa. A moving average (21-sample window) was used to smooth the shape of each macrovibrissa, finally yielding a set of 3D (x, y, z) points along each whisker length for each of the three rats. These same whiskers, from both right and left sides of the animal, were plucked from the rat and scanned in 2D on a flatbed scanner (Epson Perfection 4180 Photo) at a resolution of 2,400 dpi (10.6μm per pixel) to quantify whisker arc length and curvature. No skull or facial features were acquired from the rats in Dataset 1.

4.3.1.2. Dataset 2: A schematic of the data collection process for Dataset 2 is shown in Figure 4.1. A total of 351 whiskers were acquired from the left and right arrays of six rats using the following methods.

4.3.1.3. Anesthesia and surgery

Animals were anesthetized with an intraperitoneal injection of a ketamine/xylazine mixture (58.3 mg/kg ketamine hydrochloride, 2.92 mg/kg xylazine hydrochloride, and 0.58 mg/kg acepromazine maleate in a saline vehicle). A deep plane of anesthesia was maintained throughout the procedure by monitoring for the toe pinch withdrawal reflex every fifteen minutes and administering booster doses of anesthetic as needed. The animal was placed on a heating pad and secured in a stereotaxic apparatus including a bite block and ear bars. The stereotaxic unit ensured that the animal's head, neck, and forepaws were suspended in air and no vibrissae touched the heating pad. An incision was made along the scalp midline, and three skull screws were secured to form a triangle, with one screw in the frontal bone and one in each temporal bone. A bridge of methyl methacrylate (dental acrylic) was then constructed between the arm of the stereotaxic and the skull screws, taking care to leave the skull landmarks lambda and bregma exposed when possible (Paxinos, Watson et al. 1985). Once the acrylic had cured and the animal's head was stable, the bite block and ear bars were removed, ensuring that no object touched any part of the animal's face or vibrissae.

4.3.1.4. Data acquisition with the Microscribe™

Whiskers were traced using a G2X Microscribe™ 3D Digitizer (Revware). This device consists of a passively movable five degree-of-freedom mechanical arm with a probe of known length on the tip. A user manipulates the arm to place the tip of the probe at a location in space. The device reports (x, y, z) coordinates of this spatial location relative to a previously defined home location [0,0,0]. Manufacturer listed mean precision is 0.13mm and mean accuracy is 0.23mm, using a conical steel tip measuring 24.5mm in length x 5.0mm in diameter, with a slope of 0.5 (the default tip). This tip was too thick to maneuver easily between whiskers, so instead we used a 0.5mm x 4.4 cm steel wire held in a pin vice (Starrett; 75.0mm in length x 5.0mm in diameter), custom machined to thread into the probe-holder of the Microscribe™ tip. The portion of the steel wire clamped in the vice was 2.4 cm long, and 2 cm of the steel

wire was exposed. Manufacturer's instructions for calibrating to the custom tip were followed prior to collecting data from each animal.

As schematized in Figure 4.1, the probe at the end of the Microscribe™ was held in the experimenter's dominant hand, and the tip was sequentially placed at a series of points on each of the anatomical structures of interest. At each point, a button was pressed to record the 3D coordinates (x, y, z) representing the position of the Microscribe™ tip. For all six rats in Dataset 2, we digitized the basepoint of each whisker and multiple points along each whisker's length. For four rats in Dataset 2, we digitized the skull features lambda and bregma. For five of the six rats in Dataset 2, we digitized points corresponding to the corners and contours of prominent facial features including the eyes, nostrils, rostrum, mouth, pinnae, and incisors.

4.3.1.5. Error assessment

At the start of each experiment we established an origin for the Microscribe™ by making a small divot in a piece of laboratory labeling tape on the operating table near the animal. We sampled this origin from ~20 different orientations to calibrate the device. Over all scans and experiments, we recorded a mean resolution of 0.5mm. This resolution includes error due to any hand tremor of the user, any slight eccentricities of the tip, and the intrinsic precision limitations of the device. Note that, because each point along the whisker is an independent observation for that whisker, the 0.5mm error does not compound along the length of the whisker.

To obtain an accurate estimate of measurement error for Dataset 2, we performed simulations in which we randomly varied all the points along the whisker length (including the basepoint) by +/- 0.5mm in all three spatial dimensions, and observed the effect on the 3D position and orientation of the whiskers. We performed these simulations for two whiskers from each row (1 caudal, 1 rostral). The whisker basepoint

locations were found to have a maximum error of 0.01mm in r_{bp}, 0.24° in θ_{bp}, and 0.19° in φ_{bp}, and the whisker emergence angles were found to have a maximum error of 4.8° in θ_w, 3.0° in φ_w, and 2.7° in ζ_w. Each of these variables is defined in the sections below.

4.3.1.6. 2D whisker scanning

After data collection with the Microscribe™ was complete, animals were euthanized with an overdose of the ketamine-xylazine-acepromazine combination, followed by decapitation. Whiskers from four of the six rats were trimmed at the base using forceps and micro scissors, and stored in folded rectangles of aluminum foil for one to two days. The whiskers were then scanned, along with a calibration ruler (1mm resolution), using a flatbed scanner (Epson Perfection 4180 Photo) at a resolution of 2,400 dpi (10.6μm per pixel). A total of 244 whiskers were scanned in 2D for Dataset 2. Of those 244 whiskers, 226 were of high enough quality to obtain measurements of arc length, and 222 were of high enough quality to obtain measurements of intrinsic curvature.

4.3.2. Definition and quantification of whisker morphological parameters

A total of eight parameters were used to quantify whisker array morphology. Two parameters described 2D whisker geometry: the arc length (S) and the intrinsic curvature coefficient (A). Three parameters described the 3D coordinates of the whisker basepoints (r_{bp}, θ_{bp}, φ_{bp}), and three parameters described the Euler angles at which the whiskers emerged from the mystacial pad (θ_w, φ_w, ζ_w).

4.3.2.1. Quantifying whisker arc length

Values for arc length for 158 of the 167 whiskers of Dataset 1 (Towal, Quist et al. 2011) were obtained from the original study. No new measurements for arc length were made for these rats.

Values for arc length for 226 of the 244 whiskers of Dataset 2 scanned in 2D were obtained by importing the scanned images into Matlab™. The whisker shape was extracted by manually clicking on 8-15 points along the whisker in the images. Those traces were upsampled to 100 points using cubic spline interpolation. The arc length was calculated by summing the lengths of the discretized segments that composed the trace. Measurement error was approximately two pixels on each end of the whisker, or ~42.4μm (~10.6μm per pixel x 2 pixels per endpoint x 2 endpoints).

It is important to note that the whiskers were plucked from the rats in Dataset 1 (Towal, Quist et al. 2011), while the whiskers were trimmed from the rats in Dataset 2. The average arc length values for Dataset 1 were therefore slightly larger than those for Dataset 2. To correct for this discrepancy, we performed a separate analysis of follicle morphology. We serially sectioned four mystacial pads from three animals (female, Long Evans rats, between three and eight months in age) and formed z-stacks of the sections to quantify the length of each follicle. For each whisker identity (e.g., the C3 whisker), we found the median length of the follicle across all four mystacial pads. We then subtracted this median length from the arc length reported for each whisker of Dataset 1.

To validate this approach, we grouped whiskers by their (row, column) identity and then plotted whisker arc length from Dataset 1 against whisker arc length from Dataset 2, before and after application of the follicle-length correction factor. The arc lengths of Dataset 1 were a better match to those in Dataset 2 after subtracting the median follicle length for each whisker (Wilcoxon signed rank test: $p < 0.0084$ before correction; $p < 0.44$ after correction).

4.3.2.2. Quantifying the intrinsic curvature coefficient

Previous studies have shown that the proximal ~60%-70% of the whisker lies in a plane, with a 2D shape that can be approximated by the parabola $y = Ax^2$ (Knutsen, Biess et al. 2008, Towal, Quist et al. 2011).

However, the value for the intrinsic curvature coefficient (A) depends strongly on exactly how the base of the whisker is aligned with the x-axis.

In the present work, we aimed to reduce variability in the alignment of the proximal portion of the whisker. The whisker basepoint was first placed at the origin (0,0) and the whisker was oriented concave up along the x-axis such that the majority of the whisker lay in the first quadrant. The whisker was then truncated to 65% of its total arc length. To determine what fraction of the truncated whisker to align with the x-axis, we performed an optimization routine that iteratively rotated the whisker such that between 1 and 30% of the proximal portion of the truncated arc length was aligned with the x-axis. The curve $y = Ax^2$ was then fit to the truncated whisker at each of these rotations. The mean squared error (MSE) was calculated between the actual smoothed whisker trace and the curve $y = Ax^2$ at each of the alignments. When averaged across all truncated whiskers, error was minimized by aligning at a point 8% out along the truncated whisker length from the base. All whiskers were therefore aligned with the x-axis at a point 8% out along their truncated length from the base.

4.3.2.3. Choice of axis conventions in which to analyze the morphology of the array

Before we could define the 3D coordinates of the whisker basepoints (r_{bp}, θ_{bp}, φ_{bp}) and the Euler angles (θ_w, φ_w, ζ_w) at which the whiskers emerged from the mystacial pad, we first needed to choose an origin and horizontal plane in which to orient the rat's head.

In the present work, we chose the origin (0,0,0) to be the mean position of all whisker basepoint locations on both left and right sides of the array. This placed the origin inside the animal's head, near the center of the muzzle (Figure 4.2A). Note that this procedure required "matched" basepoints between right and left sides; in the case that a basepoint for a particular whisker identity was missing on one side, its non-missing complement was omitted from the calculation of the origin.

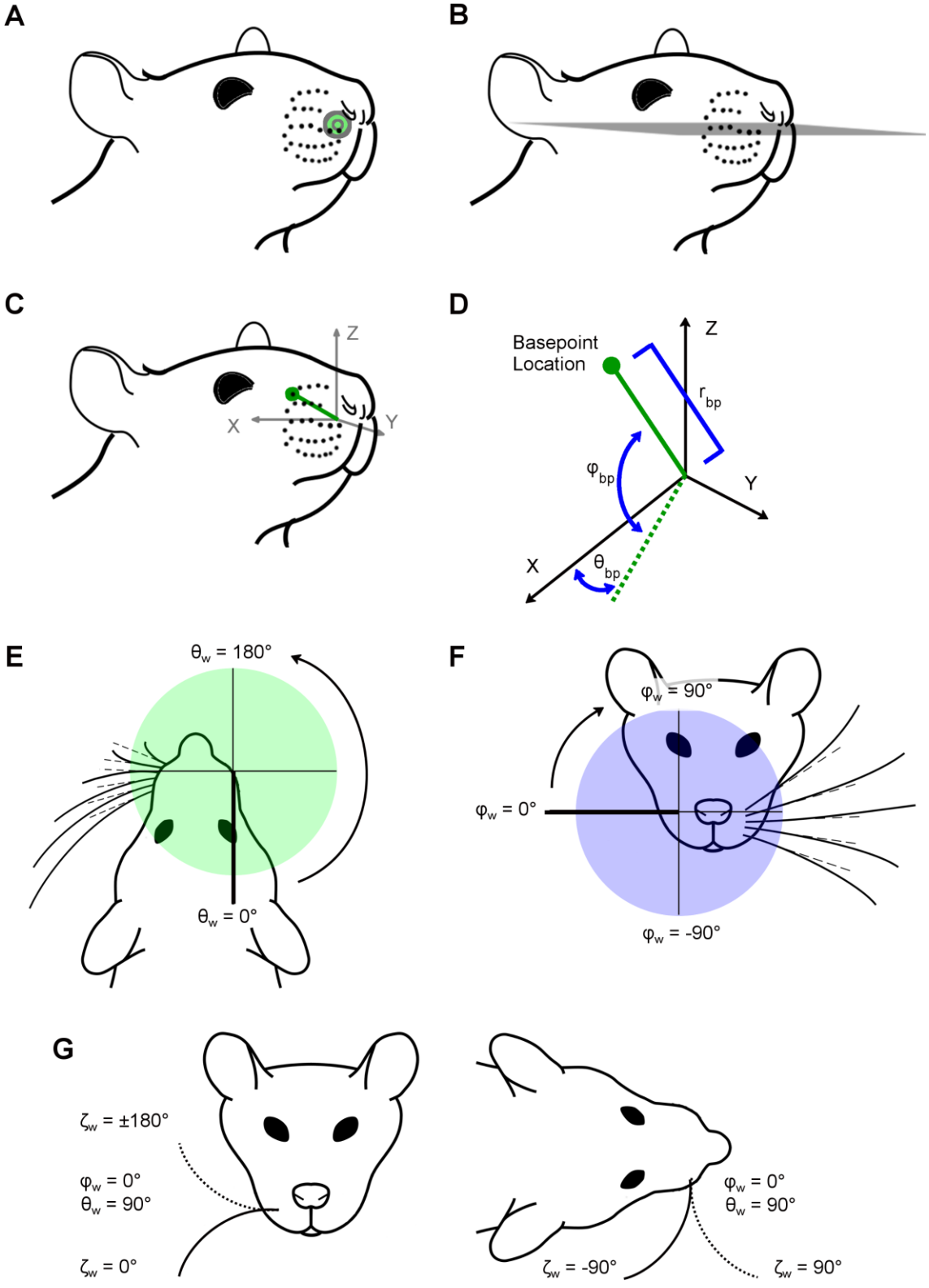
A
B
C
Z
X
Y
D
Basepoint
Location
Z
r_{bp}
φ_{bp}
Y
X
θ_{bp}
E
θ_w = 180°
θ_w = 0°
F
φ_w = 90°
φ_w = 0°
φ_w = -90°
G
ζ_w = ±180°
φ_w = 0°
θ_w = 90°
ζ_w = 0°
φ_w = 0°
θ_w = 90°
ζ_w = -90°
ζ_w = 90°

Figure 4.2: Definitions of whisker basepoint coordinates and angles of emergence. Subplots A-D describe whisker basepoint coordinates, while subplots E-G describe whisker emergence position and orientation. (**A)** The origin (green dot) is defined as the average of all left and right whisker basepoint locations. The origin is not on the surface of the snout, but is the bilateral center of the array. **(B)** The horizontal plane is defined by the average whisker row plane, i.e., the mean of the five planes fit individually to each of the five whisker rows. **(C)** Axis conventions in the context of the head, illustrating that the origin is at the mean location of all whisker basepoints and the centroid of the right array basepoints lies along the positive x-axis. **(D)** A schematic of the axis conventions used to describe basepoint coordinates shows how the radius (r_{bp}), azimuth angle (θ_{bp}), and elevation angle (φ_{bp}) are measured. The angle θ_{bp} is defined in the x-y plane from -90° (caudal) to +90° (rostral), where θ_{bp} = 0° lies along the x-z plane. The angle φ_{bp} is defined as the signed angle between the basepoint's position vector (connecting the origin to the basepoint location) and the x-y plane, from -90° (ventral) to +90° (dorsal), where φ_{bp} = 0° lies along the x-y plane. **(E)** Top-down (horizontal) view of the rat face, illustrating the axis conventions in which θ_w is defined. Dashed lines represent the vector aligned with the proximal, approximately linear portion of the whisker. The angle θ_w describes the rostral/caudal angle at which the whisker emerges from the mystacial pad. Values range from 0° to 360°, where θ_w= 0° lies along the negative y-axis. The value of $\theta_w$is independent of the intrinsic curvature of the whisker. **(F)** Front-on (coronal) view of the rat face, illustrating the axis conventions in which φ_w is defined. The angle φ_w describes the dorsal/ventral angle at which the proximal portion of the whisker emerges from the mystacial pad. Values range from -90° to 90°, and φ_w= 0° lies along the positive x-axis. **(G)** Schematics showing front-on and top-down views of the rat face, illustrating the axis conventions in which ζ_w is defined. The angle ζ_w describes the orientation of the whisker about its own axis. Solid and dashed lines represent extreme positions of the whisker in each view. ζ_w is the rotation of the whisker around its own axis. This subplot illustrates ζ_w for the case that θ_w= 90° and φ_w= 0° in order to show the whisker in a more naturalistic position. ζ_w= 0° points concave down, ζ_w= 90° concave forward, ζ_w= -90° concave back, and ζ_w= 180° concave up.

Following the approach used in Towal et al., 2011, we used the "average whisker row plane" as the horizontal (x-y) plane. Planes were fit to the basepoints of the combined left and right whisker rows using least squares, producing one plane for each of the five whisker rows A – E. The mean of these five planes defined the average whisker row plane (Figure 4.2B).

From the average whisker row plane, axis conventions were established (Figure 4.2C). The x-axis was defined by connecting the centroid of the whisker basepoints on the right side of the face with the centroid of the whisker basepoints on the left side of the face. The center of the left array lay along the negative x-axis and the center of the right array along the positive x-axis. The rat head was then pitched about the x-axis such that the average whisker row plane defined the x-y plane. The y-axis pointed rostrally, and the negative y-axis pointed caudally. Finally, the z-axis was defined to be perpendicular to the x-y plane.

4.3.2.4. Quantifying 3D basepoint coordinates of the whiskers

Having chosen an origin and horizontal plane, the 3D coordinates of all recorded points on the animal's head, including the whisker basepoints, could be determined.

Previous studies have used a standard spherical coordinate system to define the positions of the whisker basepoints (Towal, Quist et al. 2011). The advantage of this system is that it is mathematically consistent in a way that makes it easy to run simulations (Hobbs, Towal et al. 2015, Hobbs, Towal et al. 2016, Hobbs, Towal et al. 2016, Yang and Hartmann 2016, Zhuang, Kubilius et al. 2017). However, a major disadvantage of this choice is that the left and right arrays are described in the context of the whole head, not in terms of an individual array, i.e., corresponding whiskers on left and right sides have completely different coordinates. A conventional head-centered spherical coordinate system essentially ignores the bilateral symmetry of the head, treating left and right sides as qualitatively distinct. This description is counterintuitive if one wishes to describe a canonical array, whether on the left or right of an animal.

We therefore chose axis conventions that mirror the left array across the midline of the head (y-z plane), in effect describing it as a right array. Mirroring the full left array (basepoints and whiskers) was completed with the head placed in standard position and orientation, prior to any calculations being performed. This technique constructs an "array-centered" axis convention that describes right arrays. Therefore, all calculations, figures, and equations are presented in terms of right-sided whisker arrays. To generate a left array, for the purposes of a simulation, for example, the final step of generating an array shape would be to mirror the Cartesian coordinates back across the midline of the head.

As shown in Figure 4.2D, the coordinate θ_{bp} describes the rostro-caudal location of the basepoint with respect to the positive x-axis. A positive value of θ_{bp} indicates that the whisker is rostral to the x-z coronal plane (at the location y = 0), while a negative angle indicates that the whisker is caudal to this coronal

plane. The coordinate φ_{bp} describes the dorsoventral location of the basepoints with respect to the x-y horizontal plane. A positive value of φ_{bp} indicates that the basepoint location is dorsal to this horizontal plane, while a negative coordinate indicates a basepoint location is ventral to this horizontal plane. The third basepoint coordinate is the radius (r_{bp}). The variable r_{bp} is defined as the straight-line distance between the origin (the intersection of the above-described horizontal and coronal planes with the mid-sagittal plane) and the basepoint. The basepoint radii define the size of the rat's mystacial pads.

4.3.2.5. Quantifying 3D whisker angles of emergence

The angles that describe the orientation of the whiskers as they emerge from the mystacial pad at their basepoint locations are called the angles of emergence. In previous studies, the angles of emergence were defined in terms of projection angles, and the corresponding Euler angles were provided in Supplementary Information (Towal, Quist et al. 2011). In the present work, we chose to describe the whiskers using Euler angles applicable to the right array.

The angle θ_w describes the rostrocaudal orientation of the proximal, approximately linear portion of the whisker. An angle of θ_w= 180° points in the rostral direction, parallel to the positive y-axis, while an angle of θ_w= 0° points caudally, parallel to the negative y-axis (Figure 4.2E). The angle φ_w describes the elevation of the proximal, approximately linear portion of the whisker. A φ_w angle of 90° points dorsally, parallel to the positive z-axis, while an angle of -90° points ventrally, parallel to the negative z-axis (Figure 4.2F). Because whiskers have intrinsic curvature, they require a third angle, ζ_w, to describe the roll about their own axis. An angle of ζ_w= 180° orients the whisker concave upward, ζ_w= 90° is concave forward, 0° downward, and -90° backward (Figure 4.2G). Note that the orientation of the whisker's curvature in the laboratory frame depends on all three orientation angles, not just ζ_w.

We performed an optimization using the built-in Matlab™ function "fmincon" to determine the angles of emergence. The variables θ_w, φ_w, ζ_w, along with S and A, were chosen as the optimization parameters. Constraints for the optimization were: θ_w= [0°, 360°], φ_w= [-90°, 90°], ζ_w= [-180°, 180°], S = [straight distance from base to tip, lower bound + 50mm], and A = [0 to 1]. Starting with the whisker point cloud in standard position and orientation (Figure 4.2A, Figure 4.2B, Figure 4.2C), the individual points within the cloud were sorted by distance from the basepoint, and their x, y, z coordinates were smoothed with a moving average filter (window size of five samples). The whisker was then resampled into 500μm segments and translated to the origin. Next, the routine varied five parameters, θ_w, φ_w¬, ζ_w, S, and A to fit an idealized whisker model to the whisker point cloud. The idealized model began with the base at the origin, and the proximal portion of the whisker aligned along the negative y-axis. The model's initial orientation was concave down. To match the idealized model with the whisker point cloud, we performed a rotation sequence. The order of the Euler rotations was y-axis (roll, ζ_w), x-axis (pitch, φ_w), z-axis (yaw, θ_w). All rotations were extrinsic about the global y-x-z axes. Additionally, the arc-length and curvature were varied to best match the idealized model to the point cloud. The arc-length and curvature parameters described in the 3D optimization were used only as a means to improve the whisker fitting and were not used for analytical purposes. All S and A results were derived from the 2D whisker traces. The optimization's cost function minimized the mean sum squared distance between the whisker point cloud and the points in the idealized whisker model.

4.3.3. Statistical analysis: Developing equations for morphological parameters

4.3.3.1. Arc length and intrinsic curvature as functions of θ_{bp} and φ_{bp}

A total of 158 measurements of arc length were obtained from the 2D traces in Dataset 1 and 226 measurements from the 2D traces in Dataset 2, for a total of 384 unique observations of arc length. To identify outliers, the whiskers were grouped by row and column identity, and the mean and standard deviation for each group were calculated. If an individual whisker was greater than two standard deviations

above or below the mean, that whisker was eliminated from analysis. Out of 384 whiskers, 27 outliers (5.72%) for arc length were removed, yielding a total of 357 whiskers available for further analysis.

A total of 130 measurements of intrinsic curvature were obtained from Dataset 1 and 222 measurements from Dataset 2, for a total of 352 unique observations of intrinsic curvature. After grouping by whisker row and column identity, 16 outliers (4.55%) for the intrinsic curvature coefficient (A) were eliminated leaving a total of 336 whiskers for further analysis.

We next aimed to construct models for S and A as functions of θ_{bp} and φ_{bp} without overfitting the data. To avoid overfitting, we did not fit a model directly to the entire dataset for each parameter. Instead, we first found the best fit model for each of the seven rats individually. The methods for selecting the best fit model were as follows:

First, we divided each dataset for S and A with outliers removed into seven subgroups by rat identity. For each of the seven rats, histograms of S and A were found to not be quite normally distributed. We analyzed the data both with and without applying log-transformations to the S and A coefficients to improve normality. Linear regression models were then constructed for each rat using both the original non-transformed and the log-transformed data.

Second, for both the original and log-transformed data, we tested whether S and A were univariately associated with θ_{bp} and/or φ_{bp}. We tested the null hypothesis that the regression coefficients for θ_{bp} and/or φ_{bp} were equal to zero. If the p-value for the independent variable coefficients was less than or equal to 0.05, we rejected the null hypothesis and a second order model (square of θ_{bp} and/or square of φ_{bp}) was fit and again the hypothesis that the regression coefficients for these higher order terms were equal to zero was tested. For each quadratic order coefficient in the model, if the p-value was greater than 0.05, the

model remained first order. If the p-value was less than 0.05, a third order model (cube of θ_{bp} and/or cube of φ_{bp}) was fit and tested for significance. If the p-value for each cubic coefficient was greater than 0.05, the model reverted to second order, but if the p-value was less than 0.05, the model remained third order. We did not find any models for whiskers from an individual rat to have independent variable predictors greater than second-order.

Third, if both basepoint parameters (θ_{bp} and φ_{bp}) were univariately associated to either first or second order with either the original data or log-transformed *A* or *S*, both parameters were then included in a multivariable linear regression model for each individual rat. The method of "forward selection" was used to introduce the terms as first linear predictors. Again, the hypothesis that the regression coefficients for θ_{bp} or φ_{bp} were equal to zero was tested. If the p-value for the independent variable coefficients was less than or equal to 0.05, a second order model (square of θ_{bp} and/or square of φ_{bp}) was fit and again the hypothesis that the regression coefficients for these higher order terms were equal to zero was tested. We used Akaike Information Criterion (AIC) as an additional metric to avoid overfitting. If both the independent variable coefficients were significant and the AIC for the higher order model was more than two points lower than the lower order model, the higher order model was selected.

The best fit univariate or multivariable linear regression model was compared across all seven rats for the original data and log-transformed *A* or *S*. An overall model, based on data from all rats together, was fit only after taking into account the results of the models fit to each individual rat. This model was fit similarly to the individual models, except that a parameter was included in the final combined model only if it had first appeared as a significant predictor in at least six of the seven individual rat models. If a parameter met this criterion it was initially included in the model and retained or discarded using the same forward selection procedure described for the individual models. The order of the combined model was not allowed to exceed the highest order of the six out of seven individual rat models to avoid overfitting.

4.3.3.2. Euler angles of emergence (θ_w, φ_w, and ζ_w) and r_{bp} as functions of θ_{bp} and φ_{bp}

Together, Datasets 1 and 2 contained a total of 518 whiskers, but 3D data was not obtained for two whiskers in Dataset 2. Thus, a total of 516 3D basepoint coordinates (r_{bp} θ_{bp} φ_{bp}) and 3D angles of emergence (θ_w, φ_w, ζ_w), were obtained from the nine rats of Datasets 1 and 2.

To identify outliers for each parameter, the whiskers were grouped by row and column identity, and the mean and standard deviation for each group were calculated. As before, if a parameter from an individual whisker was greater than two standard deviations above or below the mean, the value of that parameter for that whisker was eliminated from analysis.

Out of 516 whiskers, 41 outliers (7.95%) were removed for r_{bp}, 24 outliers (4.65%) were removed for θ_{bp}, 24 outliers (4.65%) were removed for φ_{bp}, 23 outliers (4.46%) were removed for θ_w, 23 outliers (4.46%) were removed for φ_w, and 29 outliers (6.01%) were removed for ζ_w. Thus, after outlier removal, 475 values remained for r_{bp}, 492 values remained for θ_{bp} and φ_{bp}, 493 values remained for θ_w and φ_w, and 487 values remained for ζ_w. Note that each parameter was considered independently for outlier removal.

We next aimed to construct models for r_{bp} θ_w, φ_w, and ζ_w as functions of θ_{bp} and φ_{bp} without overfitting the data. To avoid overfitting, we did not fit a model directly to the entire dataset for each parameter. Instead, we first found the best fit model for the parameters r_{bp}, θ_w, φ_w, and ζ_w for each of the nine rats individually. The method for selecting the best fit model was identical to the procedure for selecting the best fit model for S and A, as follows:

We first divided each dataset for r_{bp}, θ_w, φ_w, and ζ_w with outliers removed into nine subgroups by rat identity. For all of the nine rats, histograms of r_{bp}, θ_w, φ_w, and ζ_w were found to be normally distributed, and thus a log-transformation to achieve normality was not necessary. Linear regression models were then constructed for each rat.

Second, we tested whether r_{bp}, θ_w, φ_w, and ζ_w were univariately associated with θ_{bp} and/or φ_{bp} using the forward selection procedure described previously. We did not find any models for whiskers from an individual rat to have statistically significant independent variable predictors greater than second-order.

Third, if both basepoint parameters (θ_{bp} and φ_{bp}) were univariately associated to either first or second order with r_{bp}, θ_w, φ_w, and ζ_w, then both parameters were included in a multivariable linear regression model for each individual rat. The method of "forward selection" was used to introduce the terms as first linear predictors. Again, the hypothesis that the regression coefficients for θ_{bp} and/or φ_{bp} were equal to zero was tested. If the p-value for the independent variable coefficients was less than or equal to 0.05, a second order model (square of θ_{bp} and/or square of φ_{bp}) was fit and again the hypothesis that the regression coefficients for these higher order terms is equal to zero was tested. We also used Akaike Information Criterion (AIC) as a metric to avoid overfitting. If both the independent variable coefficients were significant and the AIC for the higher order model was more than two points lower than the lower order model, the higher order model was selected.

The best fit univariate or multivariable linear regression model was compared across all nine rats for r_{bp}, θ_w, φ_w, and ζ_w as a function of θ_{bp} and/or φ_{bp}. An overall model, based on data from all rats together, was fit only after taking into account the results of the models fit to each individual rat. This model was fit similarly to the individual models, except that a parameter was included in the final combined model only if it had first appeared as a significant predictor in at least seven of the nine individual rat models. If a parameter met this criterion, it was initially included in the model and retained or discarded using the same forward selection procedure described for the individual models. The order of the combined model was not to exceed the highest order of the seven out of nine individual rat models to avoid overfitting.

4.3.4. Quantifying facial and skull features on the rat

4.3.4.1. Positioning facial and skull features in standard orientation

The (x, y, z) coordinates of the facial and skull features collected using the Microscribe™ were imported into Matlab™. These coordinates were translated and rotated to match the axis conventions shown in Figure 4.2C.

4.3.4.2. Defining the lambda bregma plane

Lambda is defined by the intersection of the sagittal and lambdoid skull sutures, while bregma is located at the intersection of the sagittal and coronal sutures. In the rat, the lambdoid suture exhibits a characteristic rostral deviation from the coronal plane as it intersects the sagittal suture, thus forming a rostral-pointing triangle with an open caudal side. We recorded the three points of this triangle for lambda, and the single intersection point for bregma. The centroid value for lambda was calculated, as was the distance between the 3D point for bregma and the centroid value of lambda. The angular offset between the lambda-bregma line and the average row plane was found by taking the difference in z-coordinates between lambda and bregma and then dividing this difference by the 3D distance between bregma and lambda. The inverse sine of this ratio yields the angular offset between the lambda-bregma line and the average row plane.

4.3.4.3. Digitization of lateral semicircular canal orientation

The data used for the lateral canal coordinates came from serial CT scans of Rattus norvegicus skull, specimen M-2272, available through the digital morphology database DigiMorph.org [43]. The specimen was originally scanned along the coronal axis, for a total of 1571 slices. Each 1024 x 1024 pixel slice is 0.02961mm thick, with an interslice spacing 0.02961mm and a field of reconstruction of 28mm, resulting in a resolution of 0.02734mm in x and y (within each coronal plane slice) and interslice resolution of 0.02961mm in z.

We recorded 3D coordinates of the bony labyrinth and other skull features in serial coronal CT images using Reconstruct™. Structures traced included the entire right and left bony labyrinths, the left and right external auditory meatuses, the coronal, sagittal, and lambdoid sutures, and the lateral corners of the right and left upper incisors. These data were imported into Matlab™. The (x, y, z) coordinates of the following key features of skull anatomy were then manually obtained: (1) lambda and bregma; (2) the locations at which each of the two lateral canals terminated in a crista; (3) the lateral-most point of each of the two lateral canals; (4) five distinct points around the circumference of each meatus; (5) the lateral corners of the incisors.

We brought the points from the CT scan data into the same reference frame as the Microscribe™ data by aligning a subset of corresponding points between the two datasets. These points included lambda, bregma, and the corners of the incisors. We found the rotations and translations that brought these points into register, and then applied these same rotations and translations to the points for the other features, thus bringing the points describing the bony labyrinth and external auditory meatus into the shared reference frame as well.

A plane was fit to the lateral semicircular canals bilaterally, using the Matlab™ function “affine_fit” (Sun 2016). This function finds the plane of best fit to a set of points based on the least squares of the normal distance of the set of points to the plane. The angle between the horizontal canal plane and the average row plane was found as the arccosine of the dot product of the normal vectors of the two planes.

4.4. Results

As described in the introduction, a primary goal of the present work was to develop a model of the rat facial features, with special emphasis on the vibrissal array, that permitted quantitative comparisons with the arrays of other animal species. However, species differ in numbers of rows and columns of whiskers,

and the whiskers span different regions of the face. It is also unclear which whiskers best correspond between species. Therefore, instead of identifying whiskers by row and column position, we aimed to identify whiskers by their three-dimensional (3D) geometric location on the animal's face, within a chosen coordinate system. To achieve this goal required three steps, described in the first three sections of Results.

First, we had to "renumber" the columns of rat whiskers to ensure consistency with the numbering schemes used for other species. Second, we chose an origin and a horizontal plane, thereby establishing axis conventions by which to localize the whiskers on the animal's face. Third, we could then assign a 3D coordinate (r, θ, φ) to all measured points on the rat's face, including all whisker basepoints (r_{bp}, θ_{bp}, φ_{bp}), where the subscript $_{bp}$ stands for basepoint.

These three steps establish r_{bp}, θ_{bp}, and φ_{bp} as fundamental parameters that can then be used to quantify the remaining five parameters that describe whisker geometry. Accordingly, the fourth section of results quantifies whisker arc length (S) and whisker intrinsic curvature (A) as functions of the whisker basepoints, and the fifth section of results quantifies the three angles at which each whisker emerges from the mystacial pad. These three "angles of emergence" are denoted as θ_w, φ_w, ζ_w, where the subscript "w" stands for whisker.

Finally, the sixth and last section of Results characterizes the location of a variety of skull and facial features (e.g., lambda, bregma, eyes, nostrils, mouth, incisors, pinnae) relative to the position and orientation of the whisker array.

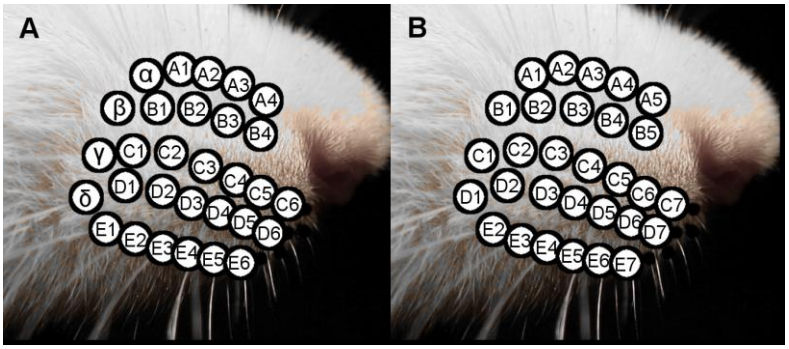

Figure 4.3: Standardized whisker nomenclature to enable cross-species comparisons. (A) Close-up of the whisker basepoints on the mystacial pad, showing the traditional nomenclature. Greek letters are assigned to the whiskers of the caudal-most arc and more rostral arcs are assigned the numbers 1 – 6. **(B)** Close-up of the whiskers of the mystacial pad, showing a nomenclature more suited for cross-species comparisons, with columns assigned values from 1 – 7.

4.4.1. Numbering the whisker columns of the rat

The rat vibrissal array is illustrated in Figure 4.3A, showing the standard nomenclature. This nomenclature labels the caudal most arc of whiskers the "Greek" or "straddler" arc, and subsequent arcs are numbered from 1 – 6 (Zucker and Welker 1969, van der Loos and Woolsey 1973, Simons 1978).

However, not all species have vibrissal arrays that contain an easily identifiable Greek arc (Muchlinski 2010). For example, the whisker array of the harbor seal has a diamond-like shape, and the caudal-most column is numbered beginning with 1 (Dehnhardt and Kaminski 1995). We therefore re-assigned the caudal most Greek arc of the rat a column identity of 1, with increasingly rostral columns numbered from 2 – 7 (Figure 4.3B).

4.4.2. Defining 3D axis conventions: Choosing the origin and the horizontal plane

In principle, our methodology allows the origin to be placed at any location. The origin determines the location relative to which every structure is referenced, so its location should be meaningful. Two earlier studies chose the origin near the center of the nose (Knutsen, Biess et al. 2008, Towal, Quist et al. 2011). However, because the current work focuses particularly on the whiskers, we chose the origin as the average of all right and left whisker basepoints. This choice specifically emphasizes distances from the center of the whisker array.

igure 4.4: Schematics illustrating four possible choices of horizontal plane and the consequences of varying head pitch on the mathematical description of basepoint coordinates and whisker orientation. (A) The average whisker row plane is found by averaging the planes of best fit for each individual whisker row across left and right sides of the face. This plane is defined as "horizontal" in the present work. **(B)** Connecting the eye corners and nose yields an ~+12° offset from the average whisker row plane, tilting the rat head slightly upward. **(C)** The bregma-lambda plane is offset from the average whisker row plane by ~-8°, pitching the rat head slightly downward. **(D)** The semi-circular canal plane is offset by ~-38.5°, tilting the rat head substantially downward. **(E)** The left panel shows the angular basepoint coordinates (θ_{bp}, φ_{bp}) of two example whiskers (B2, D6) when the average row plane is defined as the horizontal x-y plane. The coordinate for B2 is (-21.5°, 22.3°) and the coordinate for D6 is (27.6°, -15.9°). The pale purple horizontal line at φbp = 0° represents the average row plane. The x-axis is also colored purple to highlight that it is parallel with the average row plane. The right panel shows the angular coordinates (θ_{bp}, φ_{bp}) of the same two whiskers (B2, D6) when the semi-circular canal plane is defined as horizontal. The coordinate for the B2 whisker is now (-2.2°, 30.2°) and the D6 whisker coordinate is now (13.1°, -29.5°). The pale green horizontal line indicates the semi-circular canal plane. The x-axis is also shown in green to highlight that it is now parallel to the semi-circular canal plane. Values in image have been truncated for visual clarity. **(F)** The left panel shows the angles of emergence for the C3 whisker, projected into the x-y plane (blue) and the x-z plane (red). These projection angles are denoted as θ_{proj} and φ_{proj}. In this panel, the average whisker row plane is defined as the horizontal plane, and the blue and red vectors represent projections of the proximal (approximately linear) portion of the whisker. The right panel illustrates the same angles of emergence when the semi-circular canal plane is defined as the horizontal plane. The redefined x-y plane is shown in green and the x-z plane in orange. New projection angles for the proximal, approximately linear portion of the whisker, are illustrated by the green and orange vectors. Again, although the relative orientation of the whisker with respect to all other facial features remains constant, the projection angles describing the orientation of that whisker are affected by choice of head pitch.

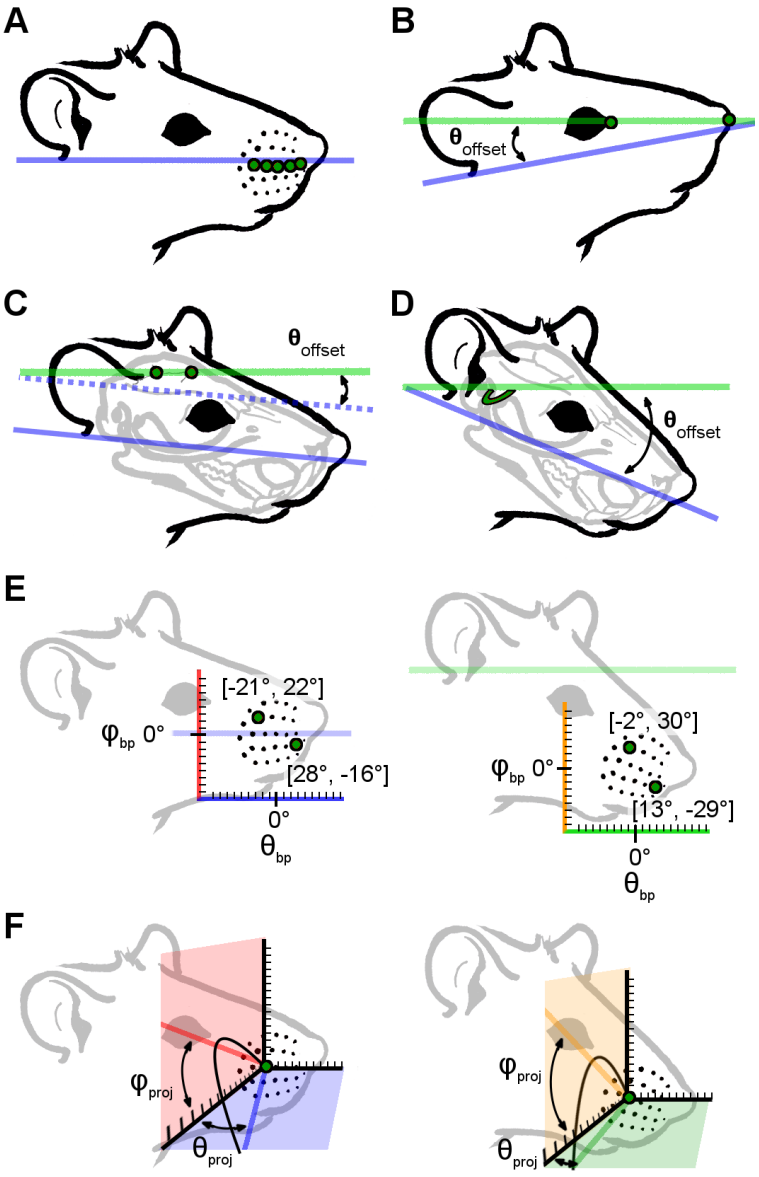

The choice of horizontal plane (i.e., the plane of zero head pitch) is a similarly important yet flexible parameter. We considered four possible choices for the horizontal plane: 1) the average row plane (the plane of actuation of the whiskers); 2) the plane defined by the corners of the eyes and nose (a plane easily observable in behavioral studies); 3) the plane defined by the skull landmarks lambda and bregma (a plane relevant to electrophysiological studies); 4) the plane defined by the lateral semicircular canals (a plane relevant to cross-modal sensory processing). Each of these choices for the horizontal plane will have its own costs and benefits, and each will result in different equations relating whisker basepoints to the angles at which the whiskers emerge from the face. Ultimately, we chose the horizontal plane to be the average whisker row plane (Figure 4.4A) because of its clear biomechanical relevance during whisker actuation.

In considering the remaining three planes, we define a negative head pitch (snout pointing down relative to the average row plane) as a negative angle, and a positive head pitch (snout pointing up relative to the average row plane) as a positive angle.

4.4.2.1. Connection of eye corners and nose: An earlier study (Knutsen, Biess et al. 2008) defined the horizontal plane by connecting the anterior-most corners of the eyes with the top-most, anterior-most point located on the hemispheric midline of the nose (Figure 4.4B). For the five rats for which 3D coordinates of the eyes and nostrils were acquired, the angular offsets relative to the average whisker row plane were found to be +9.35°, +11.4°, +15.0°, +11.9°, +13.9°, yielding an average of +12.3°, a median of +11.9°, and a standard deviation of 2.20°. Selecting this orientation would on average tilt the snout up by ~12° relative to the average whisker row plane head orientation. This orientation is most similar to that used in an analysis of binocular vision of the rat (Meister 2013, Wallace, Greenberg et al. 2013).

4.4.2.2. The bregma-lambda line: Lambda and bregma are skull coordinates defined by the coronal, sagittal, and lambdoid skull sutures, and in the rat, they lie relatively flat on top of the skull. As illustrated

in Figure 4.4C, defining the lambda-bregma line as horizontal would tip the rat's head down relative to the average row plane. For the four rats for which 3D coordinates for bregma and lambda were acquired, the angular offsets were -8.51°, -9.92°, -8.61°, and -5.14°, yielding a mean of -8.04°, a median of -8.56°, and a standard deviation of 2.04°. This orientation would, on average, pitch the head down by ~8°. Although the value for the last rat appears to be relatively low, all four values are within the error range for single point measurements.

4.4.2.3. Semi-circular canals*:* As described in Methods, we measured the points at which the horizontal semicircular canals terminate in ampulae, yielding four points in total, two on either side of the head. The angular offset of the plane fit to these points (the semi-circular canal plane) to the average whisker row plane is approximately -38.5° (Figure 4.4D). Selecting this orientation would on average tilt the head down by about 38.5° relative to the average whisker row plane.

Each of these choices for the horizontal plane will have its own costs and benefits, and each will result in different equations relating whisker basepoints to the angles of emergence. A close examination of these different equations is outside the scope of the present study, but a few examples of differences in whisker basepoint coordinates and emergence angles are illustrated in Figures 4.4E and 4.4F. The left panel of Figure 4.4E shows basepoint coordinates of two example whiskers in standard head pitch, while the right panel shows coordinates of those same whisker basepoints after the head pitch has been changed to align the lateral semicircular canal plane with the horizontal plane. Although the relative position of all basepoints of course remains constant, the coordinates describing those points change due to the change in reference frame. The left panel of Figure 4.4F shows the projection of the proximal, linear portion of the whisker into the x-y plane (defining the azimuthal angle θ_{proj}) and into the x-z plane (defining the elevation angle φ_{proj}). As shown in the right panel, the values of these angles change with head pitch, although of course the geometry of the whiskers themselves do not change.

4.4.3. Three-dimensional coordinates of the whisker basepoints as functions of row and column identity

With axis conventions established, every point on the rat's face and whiskers can be assigned a 3D coordinate. Specifically, each basepoint is assigned a coordinate (r_{bp}, θ_{bp}, φ_{bp}). Average experimental values for these coordinates by whisker identity are provided in A.2.S2 Table. Given that the vast majority of work in this model species has been done using row and column identity (Brecht, Preilowski et al. 1997, Knutsen, Biess et al. 2008, Towal, Quist et al. 2011)[31-33], we began by quantifying the relationships between θ_{bp} and φ_{bp} and whisker row and column identity.

The azimuthal coordinate, θ_{bp}, was found to be linearly related to column identity (Equation 4.1) and the elevation coordinate, φ_{bp}, was quadratically related with row identity (Equation 4.2):

$$\theta_{bp} = 13.4Col - 48.6, Adj.R^2 = 0.87 \quad \text{(eq. 4.1)}$$

$$\varphi_{bp} = 1.49\,Row^2 - 26.3\,Row + 68.0, Adj\,R^2 = 0.95 \quad \text{(eq. 4.2)}$$

In Equation 4.1 and Equation 4.2, *Col* varies from 1 to 7, *Row* varies from 1 to 5, and θ_{bp} and φ_{bp} are in degrees. It is important to note that the form of these equations depends critically on the choice of origin and horizontal plane, an idea elaborated further in the Discussion.

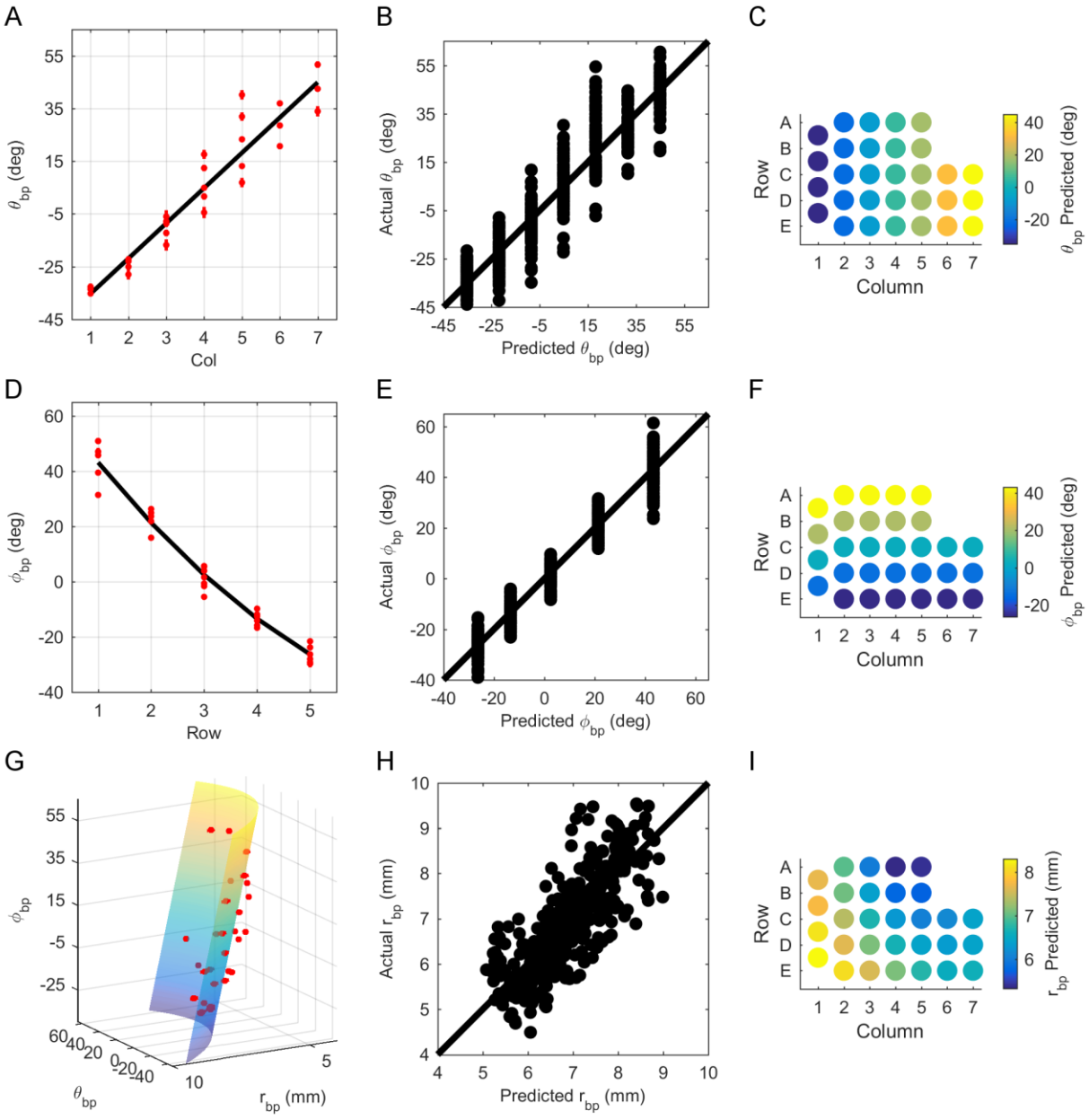

Figure 4.5: Relationship between basepoint parameters and row and column position on the array. **(A)** θ_{bp} increases linearly with column identity (Col). The black line represents Equation 4.1. Red dots show average θ_{bp} when grouped by whisker identity, with the red bars representing standard error (SE). **(B)** Relatively uniform dispersion of actual vs. predicted values for θ_{bp} about the identity line indicates correct model choice for Equation 4.1. **(C)** Predicted variation of θ_{bp} by column (Equation 4.1) when grouped by whisker identity. **(D)** φ_{bp} decreases as *Row* increases. Equation 4.2 is shown as a black line. Red dots represent average φ_{bp} when grouped by whisker identity, where the red bars show SE. **(E)** Relatively uniform dispersion of actual vs. predicted values for φ_{bp} about the identity line indicates correct model choice for Equation 4.2. **(F)** Predicted variation of φ_{bp} with *Row* (Equation 4.2) when grouped by whisker identity. **(G)** r_{bp} decreases with both θ_{bp} and φ_{bp}. Equation 4.3 is shown as a 3D surface. Plotting r_{bp} on the y-axis and φ_{bp} on the z-axis demonstrates the approximate shape of the rat's cheek. Red dots represent

mean r_{bp} when grouped by whisker, and red bars show SE. **(H)** Relatively uniform dispersion of actual vs. predicted values for r_{bp} about the identity line indicates correct model choice for Equation 4.3. **(I)** Predicted variation of r_{bp} with row and column (Equation 4.3) when grouped by whisker identity.

The positive coefficient for column identity (Col) in Equation 4.1 indicates that θ_{bp} increases from caudal to rostral. This relationship is highlighted when θ_{bp} is plotted as a function of column (Figure 4.5A). Relatively uniform dispersion of actual vs. predicted values about the identity line (Figure 4.5B) indicates that the correct model was chosen (Figure 4.5B). Figure 4.5C shows the strong dependence on column for θ_{bp}, predicted by Equation 4.1, by whisker identity across the array.

Equation 4.2 indicates that φ_{bp} decreases from dorsal to ventral, a relationship easily observed in Figure 4.5D, which plots φ_{bp} as a function of row. For all nine rats, a quadratic relationship between φ_{bp} and row was found to be statistically better than linear on the basis of AIC; however, it is critical to note that this relationship will change depending on the definition of the horizontal plane. Figure 4.5E shows relatively uniform dispersion of actual vs. predicted values about the identity line, reflecting correct model choice. Finally, the quadratic variation of Equation 4.2 for φ_{bp} across the whisker array is shown in Figure 4.5F as a colormap.

We next examined the relationship between r_{bp} and the basepoint parameters θ_{bp} and φ_{bp}. Figure 4.5G shows r_{bp} to be quadratically related to θ_{bp} and linearly related to φ_{bp}:

$$r_{bp} = 0.000511{\theta_{bp}}^2 - 0.0295\theta_{bp} - 0.0162\varphi_{bp} + 6.50, Adj.R^2 = 0.65 \qquad \text{(eq. 4.3)}$$

where θ_{bp} and φ_{bp} are in degrees and r_{bp} is in millimeters. Although rat whisker pads curve in both the rostral-caudal and dorsal-ventral directions, qualitative observation suggests that the curvature in the

rostrocaudal direction is much steeper than the curvature in the dorsoventral direction. Consistent with this appearance, we found that the equation for r_{bp} is statistically significant only to first-order in φ_{bp}.

Figure 4.5H shows relatively uniform dispersion of actual vs. predicted values about the identity line. Dispersion was smaller than for all other fits tested, reflecting correct model choice. However, there is also high variability, as indicated by the lower adjusted R^2value (0.65). This variability may partly arise from size differences between rats. Figure 4.5I shows the predicted variation in r_{bp} when grouped by whisker identity. Note that the caudal-most and ventral-most basepoints are furthest from the origin. This occurs because the rostral region contains a denser grouping of whiskers. Each whisker basepoint is weighted identically when defining the origin as the mean position of all basepoints. The origin is therefore "pulled" slightly closer to the rostral region.

4.4.4. Two-dimensional whisker shape: Arc length and intrinsic curvature coefficient

We next quantified the parameters that describe 2D whisker geometry, arc length and curvature, as functions of basepoint coordinates θ_{bp} and φ_{bp}. The parameter r_{bp} was omitted because it depends more on head size than relative position of the whisker in the array. Arc length was found to be best described as an exponential function of θ_{bp}:

$$S = e^{-0.0246\theta_{bp} + 3.12}, Adj.R^2 = 0.85 \qquad \text{(eq. 4.4a)}$$

Or alternatively

$$S = \frac{22.6}{e^{0.0246\theta_{bp}}},\ Adj.R^2 = 0.85 \qquad \text{(eq. 4.4b)}$$

where θ_{bp} is in degrees and S is in mm.

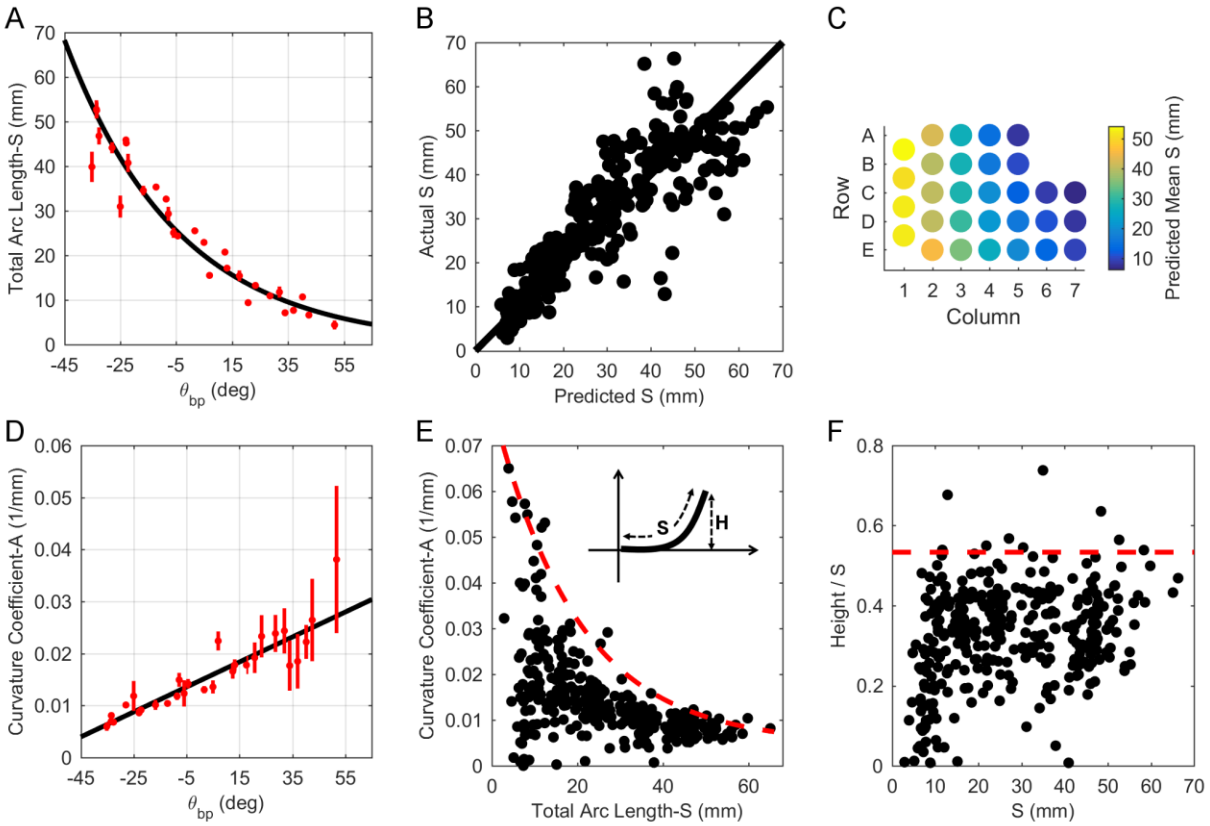

Figure 4.6. Relationship between 2D whisker geometry and basepoint parameters. (A) Whisker arc length (*S*) can be described as a decaying exponential function of θ_{bp}, decreasing from caudal to rostral. The black line represents Equation 4.4a. Mean ± standard error (SE) by whisker identity is shown in red. **(B)** Relatively uniform dispersion of actual vs. predicted values for *S* about the identity line indicates correct model choice for Equation 4.4a. **(C)** When grouped by whisker identity, Equation 4.4a predicts that arc length decreases with column position. **(D)** Intrinsic curvature coefficient (A) can be described as a linearly increasing function of θ_{bp} from caudal to rostral. The black line represents Equation 4.5. Mean ± SE by whisker identity is shown in red. **(E)** Plotting A vs. *S* highlights that shorter whiskers have higher variability in curvature. This relationship is bound by the curve given by Equation 4.6. Inset: The upper bound on *A* constrains the "height" (H) of a whisker. **(F)** The height (H) of the whisker tip does not typically exceed more than 53.3% of the whisker's arc length (*S*).

The negative coefficient for θ_{bp} in Equation 4.4a indicates that *S* exponentially decays from caudal to rostral. This relationship is shown in Figure 4.6A. Consistent with the intuition provided by the form of Equation 4.4b, the figure shows that *S* is ~23mm for central whiskers, where θ_{bp} = 0, with experimental values of *S* varying between 2.9 and 66.3mm over the entire pad. Relatively uniform dispersion of actual vs. predicted values for *S* about the identity line indicates correct model choice for Equation 4.4a (Figure

4.6B). Finally, Figure 4.6C provides an intuition for variations in *S* across the array as predicted by Equation 4.4a and when grouped by whisker identity. To compare with earlier studies, an expression for *S* as a function of column can be found in Appendix A.1.

Intrinsic whisker curvature (A) was quantified using the parameterization $y = Ax^2$ (see Methods). No strong relationship between *A* and the basepoint coordinates was found. The best relationship described *A* as a linear function of θ_{bp}:

$$A = 0.000240\,\theta_{bp} + 0.0148, Adj.R^2 = 0.34 \qquad \text{(eq. 4.5)}$$

where θ_{bp} is in degrees and *A* is in units of 1/mm. The low adjusted R^2indicates that the fit is poor, confirmed in Figure 4.6D. The figure shows that the fit is particularly poor for rostral whiskers, which exhibit much higher variability in curvature than caudal whiskers. Overall Equation 4.5 yields a reasonable approximation to whisker shape (Fig. A.2.S1), but the relationship is not strong.

To explore the origin of the poor fit, we investigated the relationship between curvature and arc length, as shown in Figure 4.6E. The relationship for *A* as a function of *S* was worse than that found for Equation 4.5. Instead, Figure 4.6E suggests that a whisker's intrinsic curvature is not fixed by an average value, but rather forced to lie below an upper bound (c.f., (Quist and Hartmann 2012)).

To compute this upper bound, we performed a sliding window analysis. We found the maximum value of *A* for arc lengths between 0 – 4mm, then for arc lengths between 1 – 5mm, and so on, up to the window *S* = 62 – 66mm. This analysis yielded a curve based on the maximum value of *A* in each window. The best equation was fit to those maximal points and found to be:

$$A = 0.0746\, e^{-0.0506\, S} + 0.00479, Adj.R^2 = 0.95 \qquad \text{(eq. 4.6)}$$

In general, whisker curvature will not be greater than values that lie along this curve.

The upper bound on the value of *A* tightly constrains the height (H) of a whisker relative to its arc length (*S*) (Figure 4.6E, inset). This effect is quantified in Figure 4.6F, which shows the ratio of height to arc length, plotted as a function of arc length. In this figure, black dots represent data from all whiskers for which 2D geometry was measured, and the red dashed line indicates the upper bound on the data at a constant value of 0.533. This line was found using the same moving average window used to calculate the bound in Figure 4.6E, and indicates that the vertical distance of the whisker tip does not extend a height greater than 53.3% of the whisker's arc length.

4.4.5. Angles of emergence of the whiskers as a function of basepoint coordinates

The 3D angles of emergence (θ_w, φ_w, ζ_w) were quantified as functions of the basepoint coordinates θ_{bp} and φ_{bp}.

The azimuthal angle of emergence, θ_w, was best described as a linear function of both θ_{bp} and φ_{bp}:

$$\theta_w = 0.598\, \theta_{bp} - 0.314\, \varphi_{bp} + 67.4, Adj.R^2 = 0.64 \qquad \text{(eq. 4.7)}$$

where θ_w, θ_{bp}, and φ_{bp} all have units of degrees.

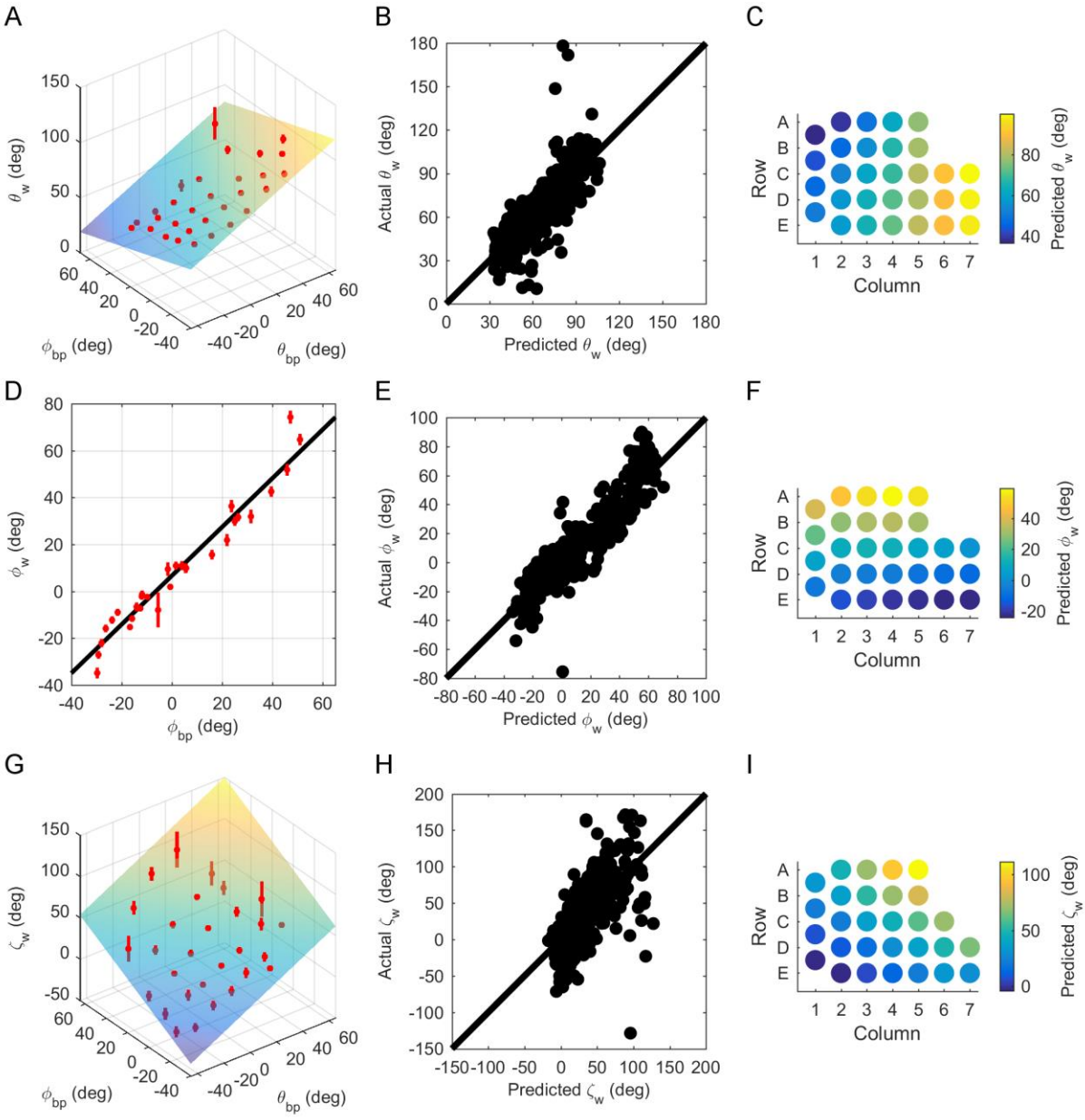

Figure 4.7: Relationship between whisker angles of emergence and basepoint parameters. (A) $\theta_w$is a linear function of θ_{bp} and φ_{bp}. Mean ± standard error (SE) by whisker identity is shown in red. **(B)** Relatively uniform dispersion of actual vs. predicted values for θ_w about the identity line indicates selection of the correct model choice for Equation 4.7. **(C)** Equation 4.7 is plotted as a colormap to show the variation of θ_w across the array. **(D)** φ_w can be described as a linear function of φ_{bp}. Mean ± SE by whisker identity is shown in red. **(E)** Relatively uniform dispersion of actual vs. predicted values for φ_w about the identity line indicates selection of the correct model for Equation 4.8. **(F)** Equation 4.8 is plotted as a colormap to show the variation of φ_w across the array. **(G)** ζ_w can be described as a polynomial function linear in φ_{bp} and linear in θ_{bp}. Mean ± SE by whisker identity is shown in red. **(H)** Relatively uniform dispersion of actual vs. predicted values for ζ_w about the identity line indicates selection of the correct model for Equation 4.9. **(I)** A colormap shows how Equation 4.9 varies across the array.

The positive coefficient for θ_{bp} indicates that θ_w increases from caudal to rostral, and the negative coefficient for φ_{bp} indicates that θ_w decreases from ventral to dorsal. These effects are shown in Figure 4.7A, and the relatively uniform dispersion of actual vs. predicted values for θ_w about the identity line indicates correct model choice for Equation 4.7 (Figure 4.7B). Variations in θ_w across the array are shown in Figure 4.7C. This figure confirms the intuition that whiskers in columns 1-3 are oriented more caudally than whiskers in columns 4-7, but also reveals a small but consistent effect: the whiskers are oriented slightly more caudally for the A and B rows than for the D and E rows. This effect is small but was found for all nine rats. A 5° increase in θ_{bp} (approximately the angular offset between adjacent whisker basepoints) will increase θ_w by ~3°, while a 5° increase in φ_{bp} will decrease θ_w by ~1.6°.

The elevation angle, φ_w, was not dependent on θ_{bp}, varying linearly only with φ_{bp}:

$$\varphi_w = 1.04\,\varphi_{bp} + 6.68, Adj.R^2 = 0.85 \qquad \text{(eq. 4.8)}$$

where φ_w and φ_{bp} are in degrees.

The positive coefficient in front of φ_{bp} in Equation 4.8 indicates an increase in φ_w from ventral to dorsal, a relationship shown in Figure 4.7D. Relatively uniform dispersion of actual vs. predicted values for φ_w about the identity line indicates correct model choice for Equation 4.8 (Figure 4.7E), and Figure 4.7F shows the prediction of Equation 4.8 for φ_w when grouped by whisker identity. Interestingly, the range of φ_w is about the same as the range of θ_{bp}. Whiskers emerge at θ_{bp} from -43.9° to 60.5° (a range of ~104°), and at φ_w between -39.0° and 61.4° (a range of ~100°). This result indicates that the array fans out equally in both dorsal-ventral and rostral-caudal directions.

Finally, the angle ζ_w was best described as a linear function of both θ_{bp} and φ_{bp}:

$$\zeta_w = 0.876\,\theta_{bp} + 0.845\,\varphi_{bp} + 37.9, Adj.R^2 = 0.42 \qquad \text{(eq. 4.9)}$$

where ζ_w, θ_{bp}, and φ_{bp} are in degrees. This relationship holds only for whiskers with arc length (S) greater than or equal to 8mm. Whiskers shorter than 8mm had too few data points acquired along their length to generate an accurate curve fit, and were not included in this analysis.

Equation 4.9 predicts ζ_w fairly well for whiskers more centrally located within the array. This is reflected first in Figure 4.7G, and also in Figure 4.7H, by the somewhat even dispersion of points about the identity line for predicted vs. actual ζ_w values. However, Equation 4.9 is a poor fit for whiskers further from the center of the array, and the data has high variability, as indicated by the low adjusted R^2(0.42). Nonetheless, Equation 4.9 serves as an acceptable first order prediction of the mean value of ζ_w. The positive coefficients for θ_{bp} and φ_{bp} suggest that ζ_w increases from caudal to rostral and from ventral to dorsal. Figure 4.7I also shows this relationship; when the predicted values for ζ_w from Equation 4.9 are grouped by whisker identity, ζ_w is highest in rows A-C and columns 6 and 7.

The large variability in ζ_w is likely a result of measurement error. In contrast to θ_w and φ_w, which represent rotations within a plane, ζ_w represents the twist of the whisker about its own axis. This angle is inherently more sensitive to small deviations in the raw data points collected using the Microscribe™. Although a detailed analysis lies outside the scope of the present work, we predict that the fit for ζ_w could improve given another choice of head pitch. This idea is elaborated further in the discussion.

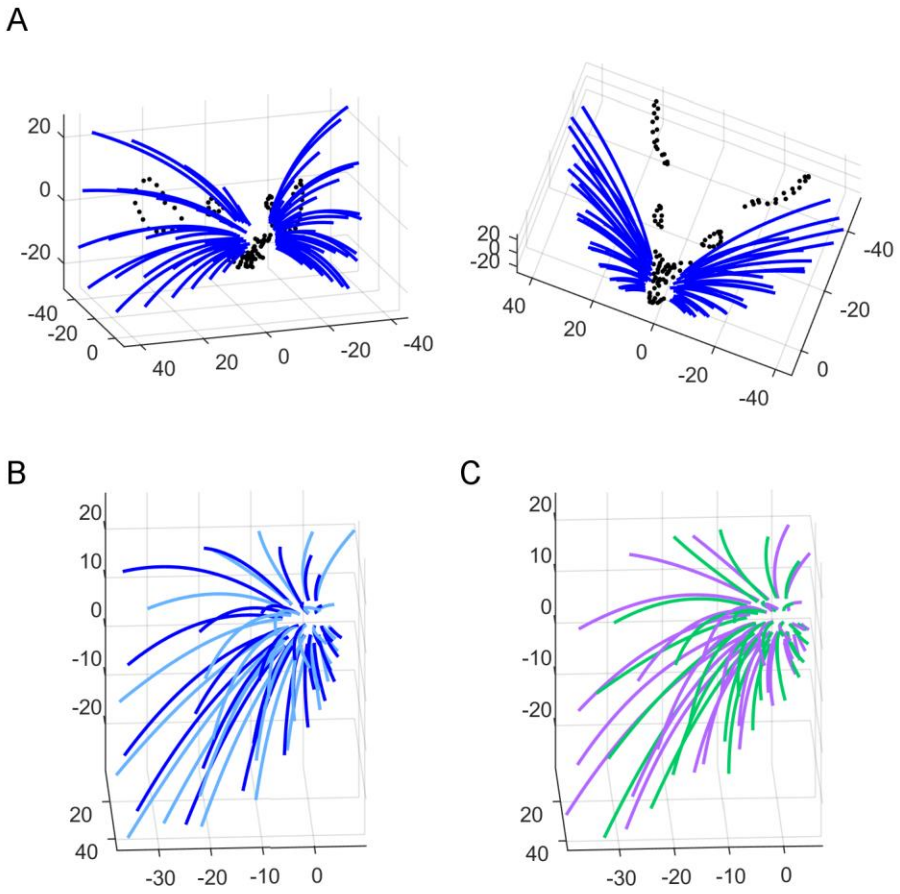

Figure 4.8: Comparison between the equation-based model and both the average and individual rats. **(A)** Front-on and top down views of the full whisker array model are shown in blue. A detailed trace of facial features collected from one rat (black dots) has been superimposed. **(B)** Equation-based model (blue) vs. smoothed traces from the averaged rat (cyan), allowing visual assessment of the model quality. **(C)** Smoothed traces from two individual rats superimposed, allowing visual assessment of the variability between individual animals.

4.4.6. The final vibrissal array model in the context of other facial features

Using the experimental basepoint parameters from Table A.2.S2 and Equations 4.3-5, 4.7-9 from Results, we constructed a full 3D model of the rat whisker array and superimposed the facial features obtained from one rat for visual context (Figure 4.8A). To provide an intuition for error in the model, Figure 4.8B compares the model with the "average array" found by taking the mean of individual fits to each whisker across all nine rats. This error can be visually compared with the difference between individual fit whiskers for two of the nine rats, shown in Figure 4.8C.

We quantified the error in Figures 4.8B and 4.8C by finding the Euclidian distances between the tips of each corresponding whisker. This error metric pools all sources of variance that affect tip position, including emergence angles, length, curvature, and basepoint location. The average rat and our model differ on average by 5.47 ± 3.28mm (mean ± standard deviation) between corresponding whisker tips, while the two individuals differ by 4.55 ± 2.79mm. The large standard deviation indicates that our model is as close to the average rat as two individuals are to each other.

One concern with this error metric might be that basepoint location is identical between the model and average array, but varies slightly between the two individual rats. Although this discrepancy means that the two error estimates are not strictly perfectly comparable, it is likely that the difference in basepoint location serves to increase some tip distances but decrease others, so over the total 30 whiskers the effect is small.

Both the average rat whisker array and our statistical model can be considered equally valid, though qualitatively different, ways of approximating the central tendency of the population distribution of rat whisker positions and orientations. Although the mean array might be more similar to any given individual rat from our sample, the equation-based model allows quantitative comparisons across species.

4.4.7. Relationship of facial markers to basepoint parameters (θ_{bp} and φ_{bp})

Our measurement procedures for Dataset 2 included quantifying the location of facial and skull features on the array relative to the whisker basepoints. These data provide important context in which to place the whisker array and allow for cross-modal comparisons in future work.

Figure 4.9A provides the reader with an intuitive presentation of the anatomical layout of the rat's face from the "point of view" of the whiskers. This figure shows the 2D angular locations of facial and skull features relative to the origin, i.e., the center of all whisker basepoints. To interpret this figure, you should

imagine yourself as the rat, with your nose placed near the nostrils, looking into the page. Notice that the mouth spans nearly the entire horizontal axis (from θ_{bp} = -60° on the left to θ_{bp} = -60° on the right), and that the nose is central and almost completely surrounded by whiskers, while the eyes and ears are proportionately much smaller and at extreme horizontal angles. Note that the relative emphasis of these different facial features is a direct result of having chosen the origin as the center of the whisker basepoints.

Complimenting these angular distances, Figure 4.9B shows the 3D Euclidean distance between facial features, including two whiskers, C3 and C4 (C2 and C3 in standard nomenclature). The C4 whisker was chosen because it is closest to the origin, and the C3 whisker was chosen because it has been used in many physiological studies (Lefort, Tomm et al. 2009, Meyer, Wimmer et al. 2010, Meyer, Schwarz et al. 2011, Hobbs, Towal et al. 2015, Varga, Jia et al. 2011). These distances were calculated first on each individual rat for which facial and skull feature measurements were extracted, and then each computed distance was averaged across all rats. Notice again that features of the mouth, nose, and whisker pad tend to cluster, as indicated by the block of green in the upper left, while the eyes and ears are farther away from the origin, indicated by the blue regions in the upper right and lower left. Also, the eyes and ears tend to cluster together, as indicated by the second green block at the lower right.

Some interesting comparisons can be made using Figure 4.9B. For example, if one compares distances between complementary left and right sensory structures, the distance can be seen to increase from nostrils (2.2mm between right and left) to mouth (11mm), followed by eyes (14mm), and corners of the pinnae (19mm). These distances are likely to reflect the importance of bilaterality for distal as opposed to proximal senses.

A

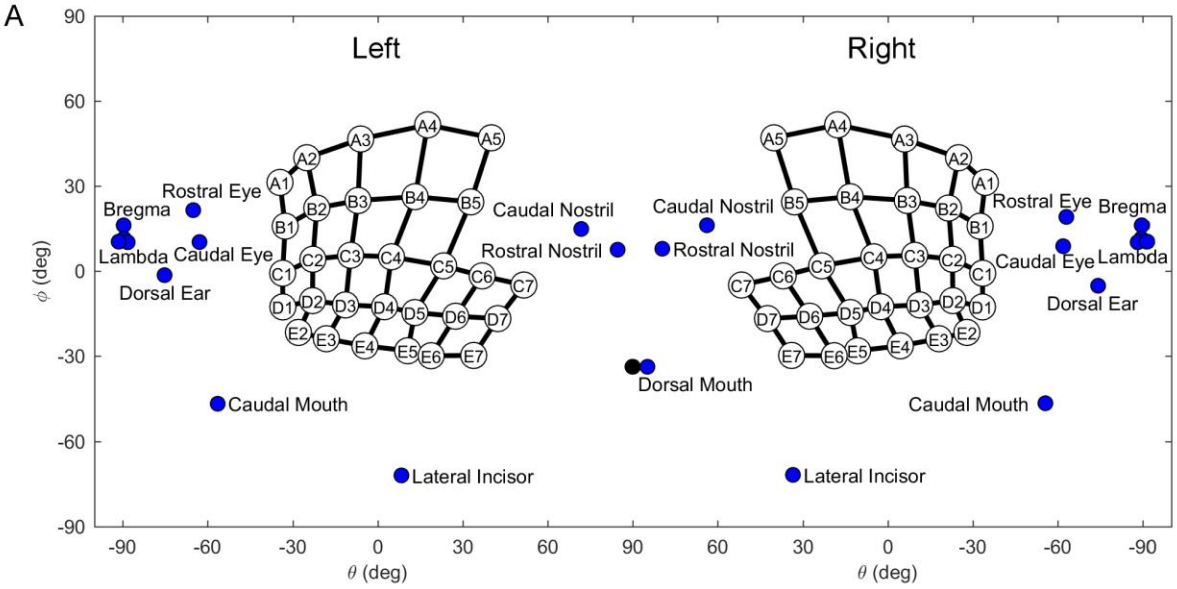

B

	Origin	Mouth Do.	Rt. C4 B.P.	Lt. C4 B.P	Lt. Nostril Cd.	Rt. Nostril Cd.	Rt. C3 B.P.	Lt. C3 B.P.	Lt. Incisor La.	Rt. Incisor La.	Lt. Nostril Rs.	Rt. Nostril Rs.	Rt. Mouth Cd.	Lt. Mouth Cd.	Lt. Eye Rs.	Rt. Eye Rs.	Lt. Eye Cd.	Rt. Eye Cd.	Bregma	Lambda	Lt. Ear Do.	Rt. Ear Do.
Origin	0	5.2	5.7	5.7	6.3	6.3	6.6	6.6	6.7	6.8	7.5	7.7	14	14	16	17	22	22	27	35	36	36
Mouth Do.	5.2	0	7.5	7.9	5.2	5.3	8.9	9.3	5.4	5.2	5	5.3	15	15	21	22	26	27	32	40	40	40
Rt. C4 B.P.	5.7	7.5	0	11	9.5	6.1	1.7	12	10	8.5	9.5	8.4	13	18	19	16	25	21	28	36	38	36
Lt. C4 B.P	5.7	7.9	11	0	6.7	9.8	12	1.6	8.5	10	8.6	10	17	14	15	20	20	26	28	36	38	37
Lt. Nostril Cd.	6.3	5.2	9.5	6.7	0	4.6	11	8.2	9.5	10	2.3	3.8	19	19	20	23	26	28	33	41	42	41
Rt. Nostril Cd.	6.3	5.3	6.1	9.8	4.6	0	7.7	11	10	9.6	4	2.6	18	20	21	21	28	26	33	40	40	42
Rt. C3 B.P.	6.6	8.9	1.7	12	11	7.7	0	13	11	9.2	11	10	12	18	19	24	25	19	27	34	35	38
Lt. C3 B.P.	6.6	9.3	12	1.6	8.2	11	13	0	9.2	11	10	12	17	13	14	20	19	25	27	34	37	34
Lt. Incisor La.	6.7	5.4	10	8.5	9.5	10	11	9.2	0	2.4	9.9	10	11	11	20	21	24	25	31	37	37	37
Rt. Incisor La.	6.8	5.2	8.5	10	10	9.6	9.2	11	2.4	0	10	10	10	12	21	21	25	25	31	37	37	38
Lt. Nostril Rs.	7.5	5	9.5	8.6	2.3	4	11	10	9.9	10	0	2.2	19	20	22	24	28	29	35	42	43	43
Rt. Nostril Rs.	7.7	5.3	8.4	10	3.8	2.6	10	12	10	10	2.2	0	19	20	23	23	29	29	35	42	43	29
Rt. Mouth Cd.	14	15	13	17	19	18	12	17	11	10	19	19	0	11	20	17	23	18	26	32	28	0
Lt. Mouth Cd.	14	15	18	14	19	20	18	13	11	12	20	20	11	0	17	21	19	24	26	32	31	29
Lt. Eye Rs.	16	21	19	15	20	21	19	14	20	21	22	23	20	17	0	14	6.8	18	14	22	28	24
Rt. Eye Rs.	17	22	16	20	23	21	24	20	21	21	24	23	17	21	14	0	18	6.3	15	22	23	28
Lt. Eye Cd.	22	26	25	20	26	28	25	19	24	25	28	29	23	19	6.8	18	0	20	13	18	26	18
Rt. Eye Cd.	22	27	21	26	28	26	19	25	25	25	29	29	18	24	18	6.3	20	0	13	19	18	26
Bregma	27	32	28	28	33	33	27	27	31	31	35	35	26	26	14	15	13	13	0	8.1	19	18
Lambda	35	40	36	36	41	40	34	34	37	37	42	42	32	32	22	22	18	19	8.1	0	18	16
Lt. Ear Do.	36	40	38	38	42	40	34	37	37	37	43	43	29	31	28	23	26	18	19	18	0	19
Rt. Ear Do.	36	40	36	36	41	42	38	34	37	38	43	44	32	29	24	28	18	26	18	16	19	0

mm between structures: 0 5 10 15 20 25 30 35 40 45

Figure 4.9: Quantification of coordinates of whisker basepoints, skull and facial features, and distances between these structures. (A) Position of the eyes, pinnae, nostrils, mouth, incisors, and bregma and lambda on the rat using coordinates θ and φ. The whisker array has been aligned into standard position and orientation using the average row plane. θ and φ are measured from the origin representing the average of all matched left and right whisker basepoints. The black dot indicates the theoretical dorsal mouth location. Notice that in this figure, the right and left facial features were not averaged. The left [right] facial features represent the average of the left [right] sides of five rats. **(B)** Average straight-line

distances (mm) between facial features. Green indicates smaller distances, while blue indicates larger magnitudes. Entries in the array are sorted by proximity to the origin. Abbreviations: Lt. = left, Rt. = right, B.P. = basepoint, Cd. = caudal, Rs. = rostral, Do. = dorsal, La. = lateral

4.5. Discussion

4.5.1. Establishing conventions to enable cross-species comparisons of facial morphology

The specific goal of the present work was to quantify the morphology of the rat's facial features and vibrissal array in a manner that permits cross-species comparisons. Ideally, as in the present work, comparisons of vibrissal morphology will involve quantification based on the basepoint coordinates of the whiskers; however, this level of precision may not always be possible. Some studies may require comparisons using only relative position within the array, i.e., row and column identity. Therefore, it is essential that the row and column designations given to whiskers are comparable across species.

This requirement is problematic given the nomenclature traditionally used to identify rodent vibrissae: whiskers in the caudal most arc are termed the "Greek" vibrissae (denoted α through δ), with the other vibrissae given alphanumeric labels indicating row and column identity (van der Loos and Woolsey 1973). Although this nomenclature makes good sense from a biomechanical point of view (the Greek vibrissae have intrinsic muscles that interdigitate with fibers of extrinsic muscles (Haidarliu, Simony et al. 2010)), it is not consistent with the numbering system used for other species (e.g., the harbor seal). We therefore renumbered the whiskers within the array (Figure 4.3) and defined a coordinate system robust to variations in whisker geometry (Figure 4.2). Our decision to rename the Greek arc with the number 1 comes at the cost of acknowledging the special muscular anatomy of these whiskers, but is required for a comparative approach.

For similar reasons, the present work also establishes new axis conventions that provide an intuitive sense for the location of the mystacial pad relative to other facial features. The coordinate system shown in

Figure 4.2 is not appropriate for mechanical simulations, but emphasizes the bilateral symmetry of the head, and ensures that corresponding right and left vibrissae have the same angular coordinates. Because different species have different numbers of rows and columns of whiskers, and some species (e.g., perissodactyls), lack a grid like arrangement entirely (Pocock 1914, Muchlinski, Durham et al. 2013) the basepoint coordinates θ_{bp} and φ_{bp} are used as fundamental parameters for quantification, replacing row and column identity. For the majority of animals, which have grid-like arrays, choosing the average row plane as horizontal (Figure 4.4) will ensure that θ_{bp} is strongly related to column and φ_{bp} to row (Equation 4.1 and Equation 4.2).

4.5.2. Whisker length and shape: Intrinsic curvature constrains the whisker's "height"

Even a cursory glance at a rat's face reveals that caudal whiskers are longer than rostral whiskers (Brecht, Preilowski et al. 1997, Haidarliu and Ahissar 2001, Towal, Quist et al. 2011, Belli, Yang et al. 2017). There is some controversy, however, as to whether the length of the whiskers more accurately follows a linear or an exponential fit as a function of basepoint coordinates or whisker identity (Brecht, Preilowski et al. 1997, Haidarliu and Ahissar 2001, Hartmann, Johnson et al. 2003, Towal, Quist et al. 2011, Belli, Yang et al. 2017). The present work finds that the arc length varies as an exponential function of θ_{bp} (Equation 4.4), as well as column (Appendix A.1). We suggest that the origin of the controversy is that the variance in the data is just large enough to yield a high R^2value for either an exponential or linear fit. To determine the appropriate fit requires comparing the raw data to predicted values from both linear and exponential models to ensure selection of the correct fit based on uniform dispersion about the identity line.

The present work also provides new insights into the possible functional significance of the intrinsic curvature of the whisker. When plucked from the animal, the first 60 -70% of a whisker lies in a plane and, when appropriately aligned in a standard Cartesian coordinate system, is well fit by the equation $y = Ax^2$, where A is termed the intrinsic curvature coefficient. The value of A is highly variable for the shorter

whiskers (Knutsen, Biess et al. 2008, Towal, Quist et al. 2011, Quist and Hartmann 2012). Although fits between *A* and the whisker's arc length, row, column, or basepoint coordinates are poor, there is a strict upper bound on the value of *A* for a whisker of a given arc length (Quist and Hartmann 2012).

We conjectured that the upper bound on arc length (Figure 4.6E) might serve to constrain the "height" of the whisker, i.e., the vertical distance of the tip when the whisker is aligned with the x-axis (inset to Figure 4.6E). This conjecture was confirmed in Figure 4.6F: the ratio of height to arc length as a function of arc length is constrained to lie below 53.3%. Only 2.7% (9/332) of whiskers in the present study had a height to arc length ratio greater than this value. To summarize: the curvature coefficient for a given whisker identity can vary considerably, but must be small enough to ensure that the height of the whisker is less than ~53% of its arc length. Although the fit between A and *S* is poor (Equation 4.5), it yet yields whisker shapes that are within experimental variability for that whisker identity (Fig. A.2.S1).

These findings lead to two predictions. First, we predict that rats exhibiting a mutation such as "rex," which leads to particularly curly whiskers (Robinson 1981) might be more clumsy than wild type rats. This prediction is confirmed anecdotally by breeders of "fancy rats," which exhibit this mutation. Second, we predict that species with an ethology different from rats might have a different bound on the curvature. Accordingly, chinchillas and viscachas, both medium-sized herbivorous alpine rodents, appear to have much straighter whiskers than rats.

4.5.3. Arrangement of facial features relative to the vibrissal array

The present work improves on previous models of the rat head and vibrissal array, and its deviation from the average rat is comparable to the variability observed between individual rats (Figure 4.8). The present results also extend previous studies to quantify the locations of different facial features relative to the vibrissal array (Figure 4.9). It is important to note that Figure 4.9 illustrates a view of the rat's face that is a

particularly “whisker-centered” in two respects. First, the angular coordinates of all facial features are plotted with respect to a whisker-centered origin, namely, the average of the whisker basepoints. Second, the average row plane was defined as horizontal (thereby defining relative values for θ_{bp} and φ_{bp}) specifically because it is the primary plane of actuation for the whiskers.

With this “whisker-centeredness” in mind, it is informative to compare the distances between structures with the “ratunculus” (Welker 1971) that characterizes primary somatosensory cortex (Figure 4.10). When the whisker basepoints are aligned and scaled to match the rat barrel cortical representation, other facial features occupy proportionately about the same area in cortical real-estate as they do in angular coordinates in our model, without scaling. This result hints at the idea that the rat’s sensorium may be “whisker-centered.” If we had chosen the origin to be the midpoint of the eyes, for example, the angular area spanned by the mouth would not match the corresponding area in the cortical map.

4.5.4. The effects of head pitch and origin

Our axis conventions place the origin at the center of the array and align the horizontal plane with the axis of actuation of most whiskers (the average row plane). With these conventions, the azimuthal angle of emergence, θ_w, varies with both θ_{bp} and φ_{bp} (Equation 4.7), while the elevation angle of emergence, φ_w, varies only with φ_{bp} (Equation 4.8). Both relationships are quite strong, with adjusted $R^2$of 0.643 and 0.847, respectively. This geometry means that whiskers within a single row will have different values of θ_w, but they will have approximately the same values of φ_w. Whiskers within a single column (arc) will contain five unique values of φ_w, and every column will have roughly those same five φ_w values.

Assuming that the rat holds its head stationary, whisking will cause successive columns of whiskers to pass through roughly the same column of space. This allows the rat to sample the space with a series of whiskers that have approximately the same distribution of φ_w values, potentially facilitating the comparison

of information gathered from different columns of whiskers. Thus, this arrangement of φ_w may set up each column as an easily comparable fan of sensors.

In contrast to the strong relationships found between θ_w, φ_w, and the whisker basepoint locations, ζ_w is not well predicted by either θ_{bp} or φ_{bp} (Equation 4.9, Adj. R^2= 0.42). One possible reason for this low correlation is that ζ_w is more sensitive to measurement error. However, we also strongly suggest that a better fit for ζ_w might be found for a different choice of horizontal plane. This suggestion may seem unintuitive, because the inherent geometry of an animal's face does not change with head pitch. The key insight here, however, is that the sensing space for an animal requires not only a description of its sensory organs relative to each other, but also relative to gravity. In other words, the orientation of an animal's sensors in world coordinates affects the sensory data that the animal acquires; thus the choice of "horizontal" is critical to morphological quantification.

In this context, it should be noted that the horizontal plane in the current work was specifically chosen so as to highlight variation with regard to the plane of vibrissal actuation in the rat. However, this plane may not be optimal for describing every aspect of the vibrissal system, different sensory modalities, or different species, especially those that do not whisk. This issue should be explored in future work.

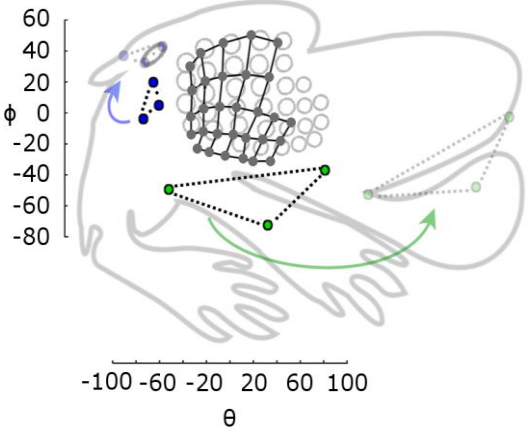

Figure 4.10: Proportion of angular area of facial features corresponds with proportion of cortical area. The ratunculus (grey outline, adapted from Welker 1971) is rotated and scaled to approximately align the barrel representations (grey circles) with the angular locations of the basepoints from the present study (black circles connected by black grid lines). Blue points represent angular locations of the rostral and caudal points of the eye, and the dorsal corner of the pinna. When these are translated and rotated (but not scaled) they align with the features on the ratunculus (light blue circles). Similarly, the green points, representing the rostral and caudal corners of the mouth and the incisors, align with those features after repositioning (but not scaling). The nose shows a similar pattern but is not shown for visual clarity.

In all, the current work describes the rat vibrissal array in detail in a way that is easily compared to other species, and establishes a foundation for future work to compare morphologies across different modalities. For example, a recent study found that the tips of the whiskers form a portion of a sphere whose center lies at the midpoint of the rat's eyes (Huet, Schroeder et al. 2015). One might ask whether a similar geometry holds for carnivores and lagomorphs, which presumably use their whiskers differently than rodents. Insights obtained through this type of comparative work could potentially contribute to bioinspired engineering solutions to problems of sensation, and will deepen our understanding of the rich diversity of animal life that surrounds us.

Chapter 5: The neuromechanics of the rat whisker pad facilitates whisker motor control

A version of this chapter is in preparation for submission to Current Biology as: Bresee CS, Alade'Fa JL, Hartmann MJZ (2018) "The neuromechanics of the rat whisker pad facilitates whisker motor control"

5.1. Summary

Differential control of whiskers across the array allows the rat to tailor its whisker movements to particular sensory tasks. For example, rats change sensory resolution (Huet and Hartmann 2014), explore different areas of space in preparation for head movement (Towal and Hartmann 2008), and pay attention to particular features (Mitchinson and Prescott 2013) (Grant, Mitchinson et al. 2009), as the task demands.

An open question is how the rat accomplishes this differential control given substantial variations in whisker morphology across the array (Belli, Yang et al. 2017), (Towal, Quist et al. 2011) (Belli, Bresee et al. 2018). It is possible that the internal structures of the pad, such as follicles and sling muscles also vary correspondingly with position. Given that whiskers are effectively the long arm of a lever, with the follicle being the short (actuated) arm, the dimensions and relative positions of the follicles and muscles also must play a part in determining whisker movements.

Here we investigated the contribution of follicle geometry and the intrinsic muscles to motor variability. We reconstruct the three-dimensional anatomy of four whisker pads and use these to simulate the kinematics of whisker protraction generated by intrinsic muscle contraction. This effectively asks the question: through what angle will each of the whiskers move for a given muscle contraction?

Results indicate that if any intrinsic muscle across the pad is shortened by a given percent, the associated whisker will rotate the same number of degrees, no matter where the whisker is in the array. Effectively, the anatomy of the system allows the lower motor neurons to use the same rate code across the entire array.

5.2. Methods

All procedures were approved in advance by the Animal Care and Use Committee of Northwestern University.

Our approach was carefully designed to address four separate problems often associated with histological analyses of gross anatomy. First, mechanical distortion of the soft tissue surrounding the follicles was minimized by sectioning entire pads without flattening, and without dissecting individual rows or follicles. Second, we minimized uneven muscle contraction during fixation by using a non-formaldehyde-based fixative. Third, we minimized tissue shrinkage and distortion during specimen preparation by using frozen sections that required less aggressive dehydration than paraffin or plastic sections, and by very quickly freezing the tissue on a liquid-nitrogen cooled aluminum block. Fourth, we developed semi-automatic reconstruction software to enable rapid extraction of follicle shape from tissue cross-sections. Each of these procedures is described in more detail in the sections that follow.

5.2.1. Specimen preparation

The present study was based on three female Long Evans rats, between three and eight months old. After use in an unrelated electrophysiology experiment, rats were perfused with 1x phosphate buffered saline solution (PBS) with 10 units/ml heparin and then with Histochoice™. HistoChoice was used in place of formaldehyde because the sling muscles, being type II fibers (Jin, Witzemann et al. 2004), are susceptible to formaldehyde-induced contraction (Berchtold, Brinkmeier et al. 200).

To dissect the mystacial pad, scissors were used to free the soft tissue of the snout from the underlying bone in two large flaps, each containing all of the soft tissue directly associated with one whisker pad.

The dissection procedure was as follows: the first incision cut approximately around the nose and then along the philtrum to the incisors. A second incision was made connecting the corner of the mouth to the dorsal aspect of the snout. These two incisions were then connected dorsally along the snout and ventrally along the midline of the hard palate from the level of the first molar to the incisors, and continuing around the incisors. This procedure resulted in a flap of tissue with at least a few millimeters on all sides bordering the macrovibrissae.

The tissue flap was then detached from the underlying bone by gently peeling up the skin and underlying tissue and using microscissors to cut any anchoring connective tissue at the bone. After dissection, the tissue was placed in 100% HistoChoice overnight.

After 24 hours, tissue was sequentially cryoprotected in 10%, 20%, and 30% sucrose in PBS, each until osmotic pressure was equalized, as indicated by the tissue resting on the bottom of the vial. Tissue was then flash-frozen in Optimal Cutting Temperature compound (Tissue-Tek OCT, Sakura Finetek) on a level aluminum block partially submerged in liquid nitrogen. The block had previously been temperature equilibrated as indicated by the liquid touching the block no longer boiling. This procedure ensured that one face of the tissue was in contact with a surface very near -195° C, minimizing the Leidenfronst effect, and allowing a fast-moving unidirectional front of ice crystal formation to pass through the tissue. This quick unidirectional freezing is believed to generate very small crystals and minimize compression or stretching that would warp the tissue. Tissue was then sectioned at 20μm on an upright freezing microtome, and mounted on gelatin coated slides. We chose 20μm sections because they provide greater spatial resolution than thick (40 – 60μm) sections. Although thick sections would have been easier to interpret visually, we were interested in determining the exact contact points of the sling muscle on the follicle; hence the higher resolution was necessary.

Tissue sections were fixed to gelatin coated slides using a 4% paraformaldehyde solution for 15 min, permeabilized with acetone for 5 min, washed, bleached, stained in Mallory's Phosphotungstic Acid Hematoxilin (PTAH), washed and dehydrated, stained in 0.1% Fast Green (FG) in ethanol, washed, cleared, and coverslipped. FG stains collagen blue-green, and PTAH stains muscle striations purple-blue and many tissues (including collagen) various shades of red-pink. When we double-stained for collagen and muscle, the pink PTAH pigments were washed out with ethanol and the collagen was re-stained with FG to achieve darker and more distinct color.

5.2.2. Quantifying the geometry of the intrinsic ("sling") muscles

Sequential slides were visually examined at 10x to 40x through an Olympus BX60 microscope to obtain the coordinates of the most medial and lateral part of the intrinsic muscle loop. Figure 5.1 shows the procedure, using follicle E6 as an example. The top section, taken 1,400μm below the skin surface, shows a cross-section of the follicles immediately superficial to the intrinsic muscle loop. Notice that there are no muscle fibers crossing the midline of the row of follicles. The next section, at 1,440μm, shows the most lateral section in which the muscle fibers first cross the midline of the row, here indicated by a gray dashed line. The muscle fiber (here just a single fiber) is indicated with an arrow. The next image, taken at 1,920μm below the skin surface, shows a section in which much of the muscle sling is visible. The second-to-last image, taken at 2,180μm below the skin, shows the most medial section in which the muscle fibers, again indicated with an arrow, cross the midline of the row. The last image, 2,220μm below the skin surface, shows a more medial section in which muscle fibers no longer cross the midline of the row.

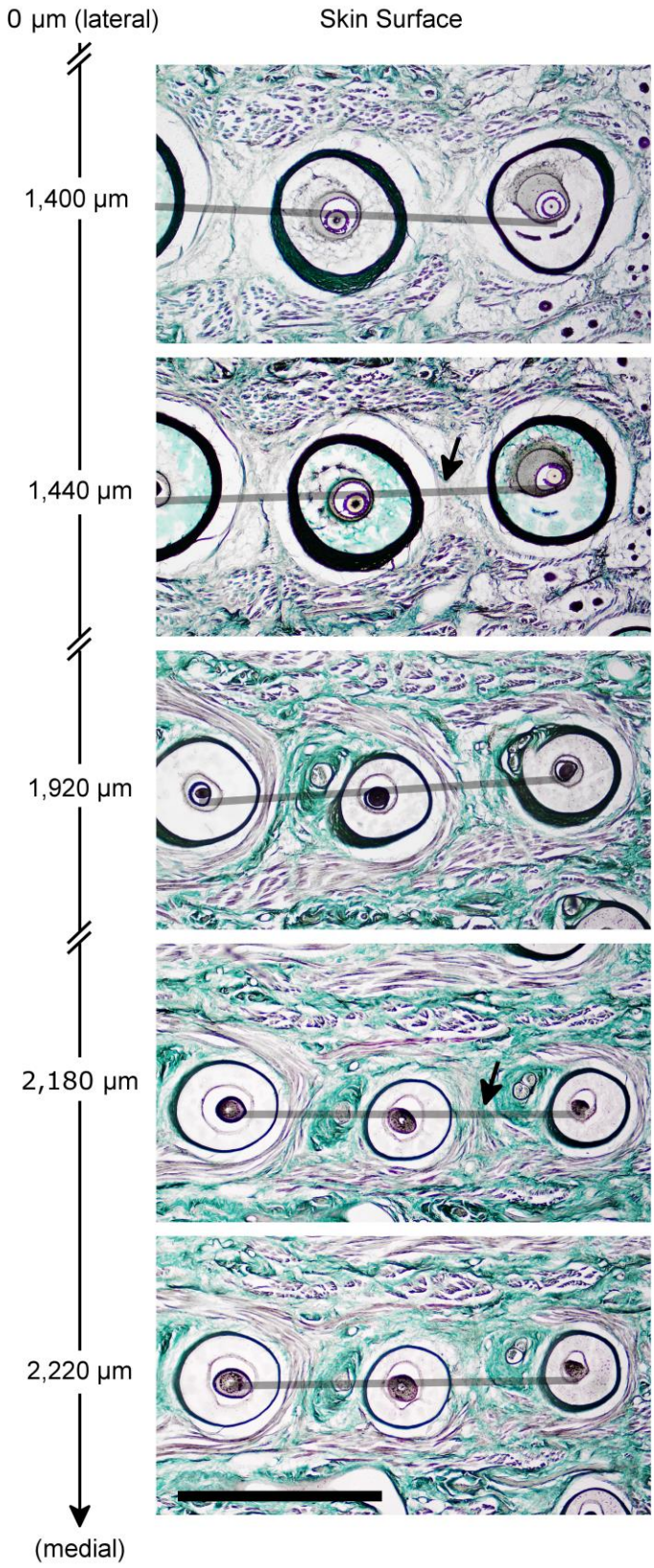

Figure 5.1: The lateral and medial extent of the sling muscle was determined by identifying the sections in which muscle fibers crossed the follicle row midline. All images show PTAH and FG stained sections of the whisker pad, cut tangential to the skin surface. From left to right the three follicles are E5, E6, and E7. In all images the midline of the row (grey line) was determined by fitting a straight line to the centers of all three follicles. The first section, approximately 1,400 µm medial to the skin surface, contains no muscle fibers that cross the midline of the row. It is thus determined to be lateral to the muscle loop. The follicle capsule wall is very thick, which is typical of apical follicle sections. The section at 1,440 µm, is the first in which a muscle fiber (purple line highlighted with arrow) is observed to cross the midline of the row. The section at 1,920 µm shows many fibers crossing the midline of the row. The section at 2,180 µm is the last in which muscle fibers (arrow) are observed to cross the midline. The final section, approximately 2,220 µm medial to the skin surface, shows no fibers crossing the midline of the row. Scale bar is 1mm. Brightness and contrast have been globally enhanced to aid visualization.

As will be shown in Results, simulating a protraction required us to quantify the circumference of the muscle loop around the follicle capsule. We took this circumference to be the perimeter of the ellipse fit to the outer edge of the follicle at the most medial location at which the muscle looped around the follicle. The circumference was calculated in a plane normal to the long-axis of the follicle. For example, in Figure 5.1, the circumference of

the E6 whisker would be determined by the perimeter of the ellipse found at section 2,180μm, after compensating for the skew of the follicle with respect to the plane of section. For one follicle of one pad, the ellipse at this section was poorly fit, so the circumference of the adjacent section (20μm more lateral) was used.

5.2.3. Photographs, image registration, follicle length, and orientation angles

Each slide-mounted section of a whole pad was placed under a Zeiss Opmi 6-CFC dissecting microscope. Photomicrographs were taken at 8x magnification with a Canon Digital Rebel camera. The software Reconstruct™ (ref) was used to manually identify the center of each follicle in each section. The center was identified as either the center of the whisker shaft (when present) or the visually estimated center of the elliptical follicle cross-section. With the centers identified, the serial slice photomicrographs could then be aligned (rotated and translated) by their centers, shown as a z-stack in Figure 5.3A with one follicle center indicated as an asterisk across sections.

After sections had been aligned, lines were fit to each follicle's (manually defined) centers along the z-dimension. These centerlines were smoothed using a ten-slice moving average filter. Note that smoothing was not part of the alignment; it was performed on each follicle individually. The points of the apex and base for each follicle were then found using the smoothed follicle centerlines. Connecting the apex and the base defines the follicle length, and connecting adjacent follicle apices defines the inter-follicle gap (Figure 5.2D).

These reconstructions also allowed us to quantify the orientation of each follicle, and hence the whisker that emerges, with respect to the skin surface. The whisker's orientation is defined by two angles: θ, a rotation generally in the plane of protraction (horizontal), and φ, essentially dorsoventral. Both θ and φ were measured with respect to the skin surface, and their values were determined in a four-step process.

First, we defined a shared spatial reference frame for all whisker pads. To do this we aligned the apices of each pad, which were initially each in different arbitrary reference frames, with the basepoints of the whiskers from a previously published morphological model of the rat whisker array (ref). This model consists of a set of three-dimensional curves describing the whisker shapes and lengths of an average rat whisker array, based on the digitized whisker arrays of 6 rats. Alignment was calculated by minimizing the Cartesian distance between the basepoints of the morphological model and the follicle apices. This alignment – based only on follicle apices -- yielded a translation and rotation that was then applied to all points on all reconstructed follicles. This procedure placed all pads in the same coordinate system.

Second, the skin surface was found by fitting a surface to all of the apices of all of the follicles in all four pads, as illustrated in Figure 5.3A. This defined an equation for the 3D skin surface averaged over all four pads. For each pad, the centerline of each follicle was then projected through the surface to determine that whisker's angle of emergence.

Third, given that our goal was to find the angle of emergence of each whisker relative to the skin surface, we then define a reference frame at each follicle apex with respect to the skin surface. We defined a unique local coordinate frame for each apex, as shown in Figure 5.3C through E. At each follicle apex, the plane tangent to the skin surface was found by taking the gradient of the surface in the rostrocaudal and dorsoventral directions. The origin of each coordinate frame was set to the apex location. The normal vector to the skin-surface tangent plane at the follicle apex defined the x axis. The y-axis was defined as the axis that is orthogonal to both the x-axis and the normal vector to the horizontal plane (the average row plane as defined in Towal et al., 2011). The y-axis points roughly rostro-caudally, while following the rostro-caudal curve of the skin. The z-axis is defined as orthogonal to the x and y axes. The z-axis points roughly dorsoventrally while following the dorsoventral curve of the skin. θ was defined as the whisker angle projected into the x-y plane, and φ was defined as the angle projected into the x-z plane. Therefore, a

θ of 0 describes to a whisker that is flush with the skin surface in a protracted position, while 90 describes to a whisker that is protracted or retracted equally, so is orthogonal to the skin in the horizontal plane, and 180 describes to a whisker that is retracted so as to be flush with the skin surface. Similarly, a φ of 0 describes to a whisker that is elevated so as to be flush with the skin, pointing roughly dorsally, a φ of 90 describes a whisker orthogonal to the curvature of the skin in the coronal plane, and a φ of 180 describes a whisker that is flush with the skin while pointing roughly ventrally.

5.2.4. Three-dimensional coordinates of the whiskers

Data were taken from Dataset 2 described in (Belli, Bresee et al. 2018). In brief, we used a 3D digitizer to collect [x y z] coordinates representing the entire whisker arrays of 4 rats. Unprocessed data were used in the present study.

5.2.5. Reconstruction of three-dimensional follicle shape and identifying collisions during a simulated protraction

The three-dimensional (3D) shape of each follicle was then reconstructed from the aligned two-dimensional (2D) follicle cross-sections. A custom-written Matlab program was used to semi-automatically fit ellipses to follicle cross-sections in each slice (Figure 5.2B). A region of interest around each follicle was defined, images were converted to black and white, and edges were detected using the built in Matlab function “edge.” An ellipse was fit using the Matlab function fit_ellipse (Copyright 2003, Ohad Gal). The user manually corrected the fit if necessary, and the x-y coordinates of 100 nodes along the ellipse in each section were recorded.

The position of the first ellipse was then used to predict the position of the follicle cross section in the next section and automatically fit an ellipse, which was also manually corrected by the user if necessary. This procedure was continued until ellipses were fit to all of the follicle capsule cross-sections in the entire pad.

In principle, these 2D extracted ellipses could be stacked along the z-axis to obtain an estimate of the 3D follicle shape, as shown in Figure 5.2C. Then, the 3D follicle shape could be combined with the muscle attachment points identified for each follicle to obtain the geometry of the intrinsic muscles associated with each follicle. However, each follicle lay slightly skewed in a different direction relative to the plane of section. A skewed follicle would give incorrect values for many muscle parameters, as shown in Figure 5.2D, left. To solve this problem, we "digitally re-sliced" each follicle individually so that its sections were perpendicular to the long-axis of that follicle (Figure 5.2D, right).

The following filtering and re-sampling steps were done in order to create smooth follicle structures that allowed us to determine follicle volume and diameters as a function of follicle length. First, we filtered the x and y positions of the center points of each fit ellipse. This filtering was done to eliminate histological and tracking error noise, while preserving follicle contours. The filters were implemented over the depth of the stack (z-direction) at a wavelength of 800 μm. Note that the center points used in this analysis, computed automatically as the centroid of the ellipse, are distinct from the manually defined follicle centers obtained from the software Reconstruct. In practice, the values were found to differ by an extremely small amount. Next, we re-stacked the fit ellipses using the unfiltered ellipse radii and orientations but filtered center positions. This hybrid raw-filtered ellipse stack was then resampled at 20 μm slices perpendicular to the orientation of the individual follicle's long axis. Finally, the lengths of the major and minor radii, and the orientation of the radii of the new ellipses in this re-sliced stack were filtered similarly to the centers.

The z-coordinates of each of the intrinsic muscle loop contact points at the rostral edge of each follicle were acquired manually, as described above (Figure 5.1). The full three-dimensional coordinates for these medial and lateral contact points were re-identified on the orthogonally re-sliced ellipse fits by finding 1)

the rostral arc of the medial most extent of the muscle loop, and 2) the line from the follicle center to the center of its immediate caudal neighbor. The intersection of these two lines is the contact point.

To estimate the muscle arm length (see Figure 5.2D) the medial point at which the intrinsic muscle contacted the follicle was projected onto the line describing the follicle center linear fit. Because it was difficult to determine when the rigid follicle became the soft bulb, we truncated the follicle the point closest to the medial intrinsic muscle contact point and re-fit a line to the remaining center points. If no follicle cross-section could be fit within 100μm of the section containing the contact point, then that follicle was eliminated from the data set. These follicle shapes and muscle contact points then allow us to find the point on the center line of the follicle that corresponds to the most medial point at which the muscle will directly exert force on the follicle. This muscle contact center point, together with the apex of the same follicle, determine the length of the follicle that serves as a lever with which to move the whisker, here referred to as the "lever length." The muscle contact center point, together with the apex of the next caudal follicle, also allow us to define the length of the muscle that stretches between follicles, here called "muscle arm length." Using this method, the digitally re-sliced follicle shapes correctly quantify the geometry of the intrinsic muscle, as shown in the right panel of Figure 5.2D. The muscle also wraps around the rostral follicle base, creating what is here referred to as the "rostral muscle arc," defined by half the circumference of the follicle at the level of muscle contact point. Therefore, the full length of the muscle at rest, here called "muscle total length," is double the muscle arm length plus the rostral loop. This total length is the length of the muscle that shortens during a contraction. However, as illustrated in Figure 5.3A, though the entire muscle contracts, only the distance between the follicles can shorten (the length of the muscle arm), because the muscle still must traverse the relatively incompressible follicle capsule (the length of the rostral arc).

The digitally re-sliced follicle yields the correct circumference and area for each slice, allowing us to compute the volume of the area of each slice ($\pi \cdot r1 \cdot r2$), multiplying that by the 20μm thickness, and summing across slices.

As will be shown in Results, the anatomy obtained from the pad reconstructions was used to derive equations to simulate a whisker protraction. One possible result of a muscle contraction is that a follicle could collide with its caudal neighbor. The 3D shape shown in Figure 5.4B allowed us to incorporate follicle diameters into the simulation in order to check for collisions. To do this each rostro-caudal pair of follicles was represented as a pair of two-dimensional polygons moving in a shared plane. During each time step of the simulated protraction the shapes were rotated about their respective apices as if their respective intrinsic muscles had each contracted by a given percent. At each time point, we checked whether the two polygons were touching or intersecting by computing the minimum distance between all vertices and edges, using the function from the Matlab file exchange min_dist_between_two_polygons (ref). If a collision occurred, the simulation was stopped.

5.2.6. Statistical analysis

We ran multiple linear regressions to characterize the relationships between previously published mean whisker measurements and newly measured mean follicle geometric parameters, and between follicle geometric parameters and array position. We also conducted repeated measures linear models to analyze the results of the simulation. In most cases the linearity, homogeneity of variance, and normality assumptions were not violated. In the few cases in which the assumption of normality was violated we used a log transformation to normalize the data.

We did not proceed with the analysis for the single case in which the assumption of linearity was violated (follicle circumference by row-wise position with column-wise position as a covariate). In all analyses, we started with one linear location parameter (row- or column-wise position) and used forward selection to

introduce the second location parameter and higher order terms. We judged the fit of the model based on the significance of the p-value for each added term, and a threshold of a 2-point lower Akaike Information Criterion (AIC) value. All statistics were performed in Matlab.

5.3. Results

5.3.1. Three-dimensional follicle geometry

We used histological and digital reconstruction techniques to determine three-dimensional (3D) follicle geometry. Four mystacial pads from three rats were sectioned, stained with Fast Green and PTAH, and aligned in a z-stack (Figure 5.2A). This allowed manual identification of the slice at which the most medial part of the intrinsic muscle sling wrapped around the rostral edge of the follicle. Within each section, the dark outline of each follicle capsule was semiautomatically traced in Matlab (Figure 5.2B) and ellipses were stacked, yielding fully reconstructed 3D follicle arrays (Figure 5.2C). These reconstructions allowed identification of follicle apices, bases, and muscle attachment points. Accounting for the angle at which each pad was sectioned (Figure 5.2D and E) allowed identification of accurate follicle circumferences. These reconstructions allowed the measurement of the length of the sling muscle span between a caudal follicle apex and a rostral follicle base (the muscle arm length, m), the distance between the apices of adjacent row-wise follicles (the gap, G), the distance between the follicle apex and the medial muscle contact point (the lever length, L), and the circumference at the medial muscle contact point (circumference, C).

We investigated variation G, L, and C, by row and column position across the array using simple and multivariable linear regressions. We used the method of “forward selection”. If the individual P-value for the predictor variable was significant at the ≤ 0.05 level, then a higher order term was added to the model (square of row and/or square of column). To judge the best fit model, while avoiding overfitting, we considered both the significance of the individual coefficients, an Akaike Information Criterion of at least

two points lower than the competing candidate model, and a similar pattern of effects in at least three of the four pads for individual fits. All variables were best predicted by a first order fit, but the predictive efficacy of row and column was more complicated.

G, L, and C were found to vary significantly as linear functions of column for each pad individually, as well as for pooled data (Figure 5.2, E). Two of four pads varied significantly with row for each variable (not the same two pads), but row was significant for each variable with pooled data. This may reflect a significant, though small, effect of row that may be obscured by the small sample size. Therefore, we tested whether row and column were good predictors together. First, we found G predicted well by column, $F(1,98) = 223$, $p = 5.59 \times 10\text{-}27$, $R^2 = 0.69$, and slightly better by row and column, $F(2,97) = 128$, $p = 5.69 \times 10\text{-}28$, $R^2 = 0.73$ (Figure 5.2F, left). L is predicted moderately by column, $F(1,113) = 51.9$, $p = 6.88 \times 10\text{-}11$, $R^2 = 0.31$, but better by row and column, $F(2,112) = 105$, $p = 2.12 \times 10\text{-}26$, $R^2 = 0.65$ (Figure 5.2F, center). Finally, C is predicted moderately by column $F(1,113) = 49.2$, $p = 1.82 \times 10\text{-}10$, $R^2 = 0.30$, and no better by adding row $F(2, 112) = 24.4$, $p = 1.63 \times 10\text{-}09$, $R^2 = 0.29$ (Figure 5.2F, right).

Figure 5.2: Follicle lever length, inter-follicle gap, and follicle circumference across the pad. (A) Illustration showing rat mystacial pad sectioned, stained for collagen (green) and striated muscle (purple), then imaged and aligned. Follicle centers were manually traced (red asterisks). **(B)** Green channel was thresholded (inset) and the outer border of follicle capsule cross sections were semiautomatically traced **(C)** Ellipse stacks were smoothed, yielding fully reconstructed follicle arrays **(D)** Left: before correction for plane of section only gap is accurately measured. Right: after correction, by digitally "re-slicing" the follicle orthogonally to its long axis, muscle arm, lever length, and follicle diameter/circumference can be accurately measured. **(E)** Plots show means ±standard deviations, with data from pads 1 through 4 identified in red, purple, blue and green, respectively. Left: Follicle gap varies weakly with row (not shown) and strongly with column. Middle: follicle lever length varies weakly with row (not shown) and moderately by column. Right: follicle circumference varies weakly with row (not shown) and moderately with column. **(F)** Observed versus predicted plots for linear regressions using both row and column as predictors. Left: Follicle gap is well-predicted by an equation linear in both row and column, but not appreciably better than by column alone. Middle: follicle lever length is well-predicted by an equation linear in both row and column. Right: Follicle circumference is not better predicted by row and column combined.

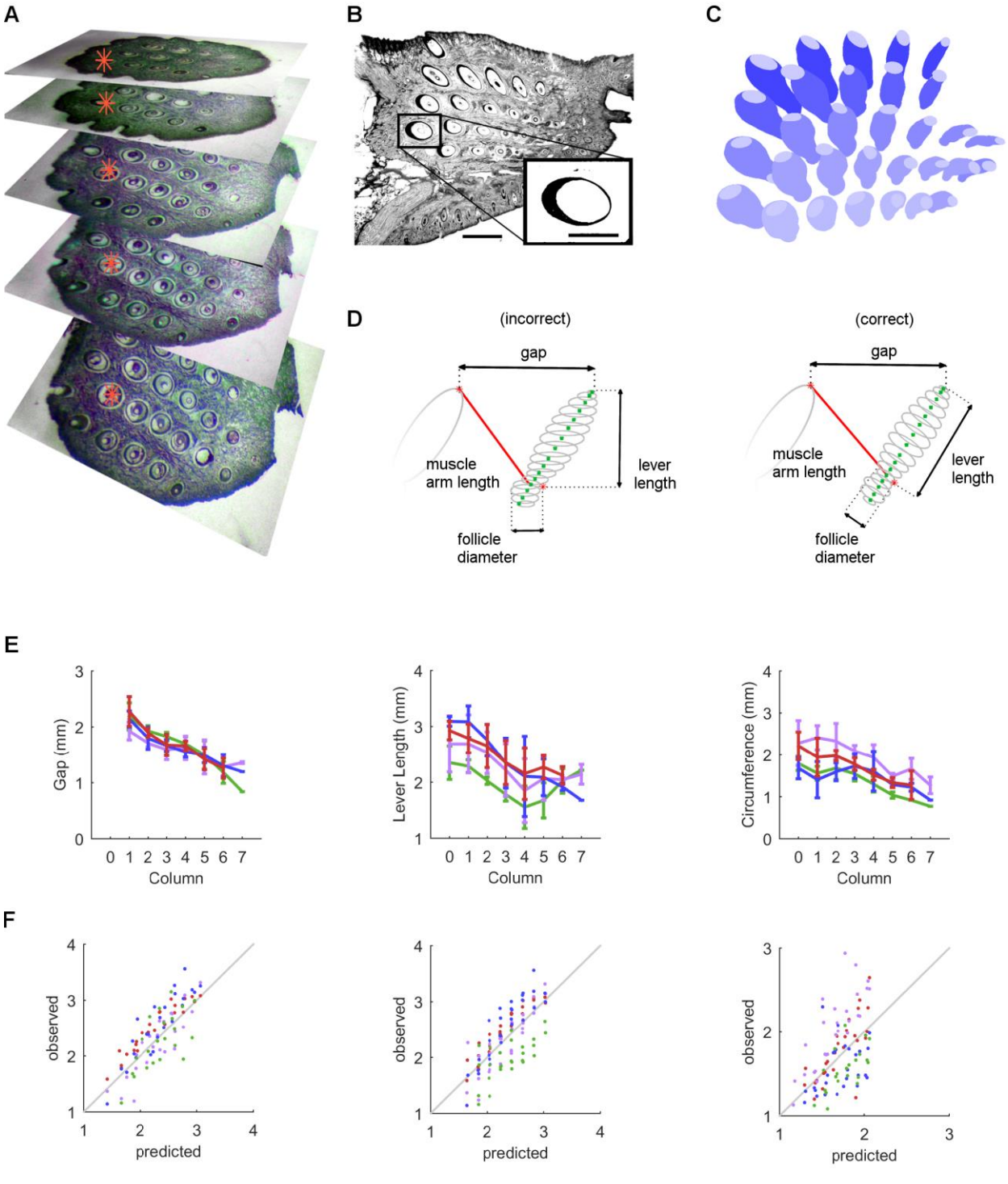
A
B
C
D
(incorrect)
gap
muscle
arm length
lever
length
follicle
diameter
(correct)
gap
muscle
arm length
lever
length
follicle
diameter
E
Gap (mm)
Column
Lever Length (mm)
Column
Circumference (mm)
Column
F
observed
predicted
observed
predicted
observed
predicted

5.3.2. Vibrissal angles of emergence relative to the skin

In order to simulate a whisk from resting we needed to determine the resting angle of the whiskers. Therefore, we measured the angle of the whisker that would project from each reconstructed follicle, with respect to the skin, in the row-wise axis (θ) and column-wise axis (φ) (Figure 5.3). We fit a surface to the apices of all follicles, then found the angle relative to the skin surface tangent plane at the apex of the follicle, in the direction of the apex of the next caudal or dorsal follicle, depending on the angle measured (Figure 5.3A-C). We also used comparable measurements taken from anesthetized rats, collected using a MicroScribe (see Methods). In brief, we collected 3D coordinates of whisker bases, and a few points along the basal, linear, portion of each whisker, from four anesthetized, head fixed rats. These data are not susceptible to error due to fixation or freezing artefact, so not only provide a naturalistic starting point, but also allow assessment of artefact in our histological data (Figure 5.3D, E).

Statistical analyses, using the same techniques described above, show θ from histological follicle arrays varies very weakly with row, $F(1,109) = 21.4$, $p = 1.04 \times 10\text{-}05$, $R^2 = 0.16$, and not with column (Figure 5.2D). Conversely, θ as measured from anesthetized whisker arrays varies moderately with column, $F(1,125) = 105$, $p = 3.03 \times 10\text{-}18$, $R^2 = 0.45$, but not with row (Figure 5.2D). Both datasets show significant quadratic relationships between φ and row, $F(1,109) = 40.9$, $p = 6.12 \times 10\text{-}14$, $R^2 = 0.42$, for follicles, and $F(2,124) = 105$, $p = 3.91 \times 10\text{-}31$, $R^2 = 0.67$, for whiskers, but φ does not vary by column (Figure 5.2E).

While the φ angle of the histological data largely agrees with the anesthetized data, the θ angles differ. This difference likely reflects contraction of striated muscles in the pad. This is unsurprising, because, though a non-cross-linking fixative was used in tissue preparation, striated muscle contraction can be stimulated even by simple saline perfusion. Note that only the rostro-caudal axis is affected, indicating that probably only intrinsic muscles were contracted. We therefore consider θ from the anesthetized data as reflecting a naturalistic resting angle.

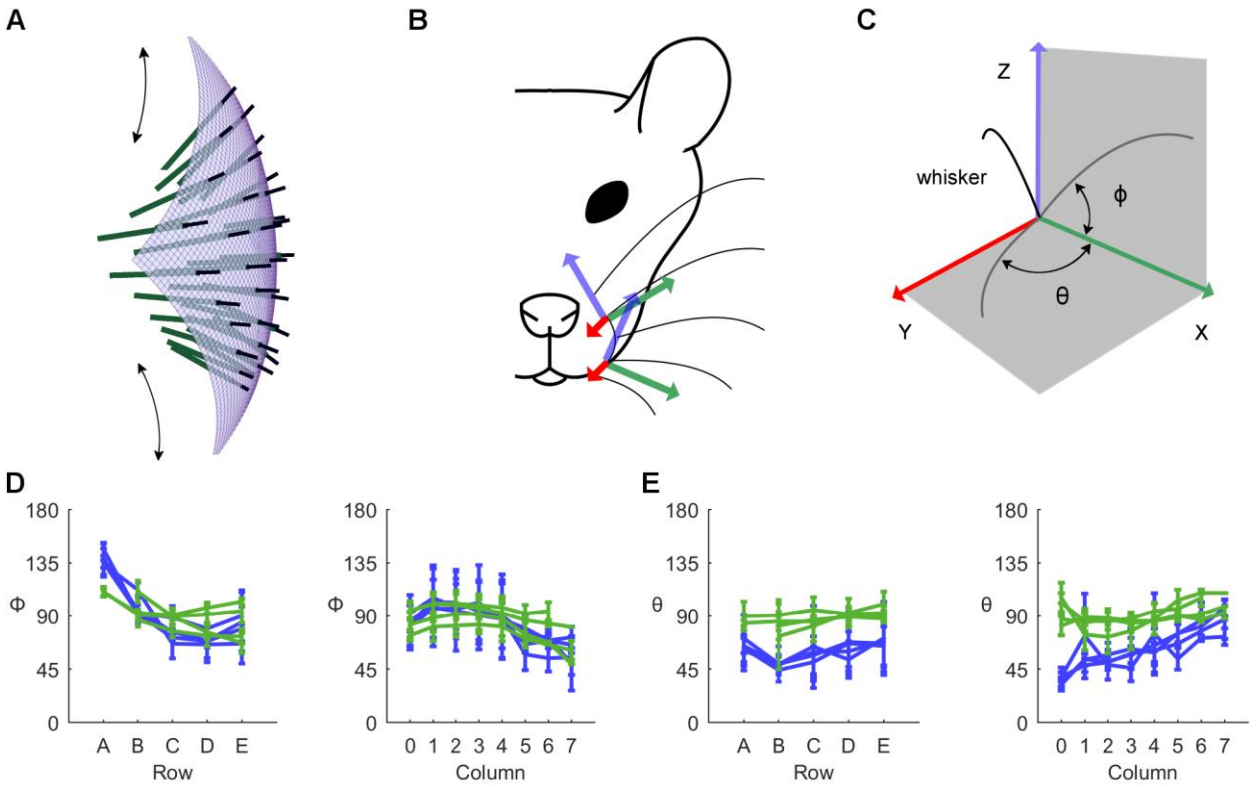

Figure 5.3: Elevation angles vary between rows, while protraction angles vary between columns. (A) To reconstruct the skin, a surface was fit to the apices of the follicles, or the bases of the whiskers, for the histological and MicroScribe datasets respectively (see Methods) **(B)** A whisker base-centered reference frame was established for each follicle/whisker. The y-z plane consists of the skin surface tangent at the whisker base. The x-y plane is orthogonal to that, in the direction of the next caudal follicle. The x-z plane is orthogonal to the skin tangent and the x-y plane **(C)** θ (angle in the plane of actuation) is measured as the angle of the projection of the whisker into the x-y plane relative to the x-axis, and φ (angle of elevation) is measured as the projection into the x-z plane. **(D, E)** Plots show means ± standard deviations for follicle arrays (green) and whisker arrays (blue). An angle of 90° indicates whisker emergence perpendicular to the skin surface; angles of 0° or 180° indicate emergence parallel to the skin. (D) φ is plotted as a function of row, left, and column, right. Both follicle and whisker arrays vary quadratically by column. Despite the consistent trend visible in the means, the raw data for φ does not significantly vary with column, in agreement with the wide standard deviations. (E) θ is plotted as a function of row, left, and column, right. Three of four follicle arrays show significant variation by row, while no whisker arrays do. Note that, though two of the green traces have very shallow slopes, they also show tight error bars, in accordance with the significant, though small, effect for these. Three of four whisker arrays show significant variation by column, while no follicle arrays do.

5.3.3. The geometry of whisker protraction due to intrinsic muscles

With the parameters quantified above it is now possible to simulate a hypothetical whisk that would occur if all intrinsic muscles contracted equally across the array. The fact that intrinsic muscles have no fiber type or pennation differences (Dorfl 1982, Jin, Witzemann et al. 2004, Haidarliu, Simony et al. 2010) allows a simulation of all intrinsic muscles as responding similarly to a given rate of motor neuron activation. Here each row-wise pair of follicles is represented as a pair of two-dimensional polygons moving in a shared plane (Figure 5.3A). Differences between pads were nonsignificant (based on comparisons of estimated marginal means with Fisher's LSD correction) so we perform the simulations using an average pad.

First the law of cosines is used to find the muscle arm length (m).

$$m = \sqrt{L^2 + G^2 - 2LGcos(\pi - \theta)} \qquad \text{(eq. 5.1)}$$

where θ is the angle of the whisker relative to the skin.

Equation 1 can be rearranged in terms of the angle θ:

$$\theta = \pi - acos\left(\frac{L^2 + G^2 - m^2}{2LG}\right) \qquad \text{(eq. 5.2)}$$

The total muscle length (M) is computed based on the muscle arm length (m) and the circumference (C):

$$M = \left(2m + \frac{C}{2}\right) \qquad \text{(eq. 5.3a)}$$

And for the specific case that the follicles are at rest Equation 5.3a becomes:

$$M_{rest} = \left(2m_{rest} + \frac{C}{2}\right) \quad \text{(eq. 5.3b)}$$

The shape and position of each polygon was based on measurements of the 3D follicle reconstructions and anesthetized whisker positions. During each time step of the simulated protraction, each shape was rotated about its apex as if its intrinsic muscle had contracted by a given percent (illustrated in Figure 5.3A, Time 1, Time 2, and Time 3), and the ending whisker angle was calculated using the following equations:

At each time step k the total muscle length is shortened relative to its resting length:

$$M_k = (n_k)\, M_{rest} \quad \text{(eq. 5.4)}$$

where n_k is a fraction between 1 and 0 that decreases linearly with the timestep k.

Importantly, the length that the muscle must traverse as it wraps around the follicle (C/2) cannot change. Thus, at each timestep of the simulation, the muscle arm length must be recomputed as:

$$m_k = \frac{1}{2}\left(M_k - \frac{C}{2}\right) \quad \text{(eq. 5.5)}$$

The protraction angle θ_k at each timestep can then be obtained by inserting m_k from Equation 5.5 as the variable m in Equation 5.2.

The results of the simulated whisker movement are shown in Figure 5.4, either in terms of angle relative to the skin (Figure 5.4 B), or degree translation from rest (Figure 5.4 B inset, and C). The resulting movements for whiskers in each column are plotted against the range of muscle contractions used in the simulation, from 0 to 50% (mean +- 95% CI) (Figure 5.2B, C). Results are very similar when whiskers are grouped by row (data not shown). Note that confidence intervals overlap at each contraction tested, indicating that all whiskers within a row or column respond with a similar degree rotation when their respective intrinsic muscles shorten by a given percent. Confidence intervals were calculated using a repeated measures model as described in Methods. These results indicate both that whiskers span a large range of angles with respect to the skin, and that all whiskers rotate a similar number of degrees from starting position, for a given percent contraction of their associated sling muscles. Essentially, this simulation shows that if the facial motor nucleus sent an identical motor command to a rostral and caudal whisker in the same row, the whiskers would move through approximately the same angles.

These results reflect a remarkable degree of neuromechanical precision. To get a sense for how important the observed values of G, L, and C, are for the consistency above, we replicated the simulation, with either G, L, or C set to the mean values of that parameter all across the pad. When G is held constant there is much more deviation by both row (not shown) and column (Figure 5.3C, Top). Similarly, when L is held constant, the confidence intervals are larger than for the simulation using observed values, though the confidence intervals are much more overlapping than for G (Figure 5.3C, Middle). Finally, holding C constant does not have much of an effect (Figure 5.3C, Bottom). It is interesting to compare these results with the plots of G, L, and C in Figure 5.1 E-G. Note that the observed values for G are the least variable compared to L and C, and that of the three parameters, changes in G have the greatest effect on whisker movement. This suggests that G in particular is under selection pressure to fairly precisely maintain the observed values, possibly because those values contribute to consistency in movement.

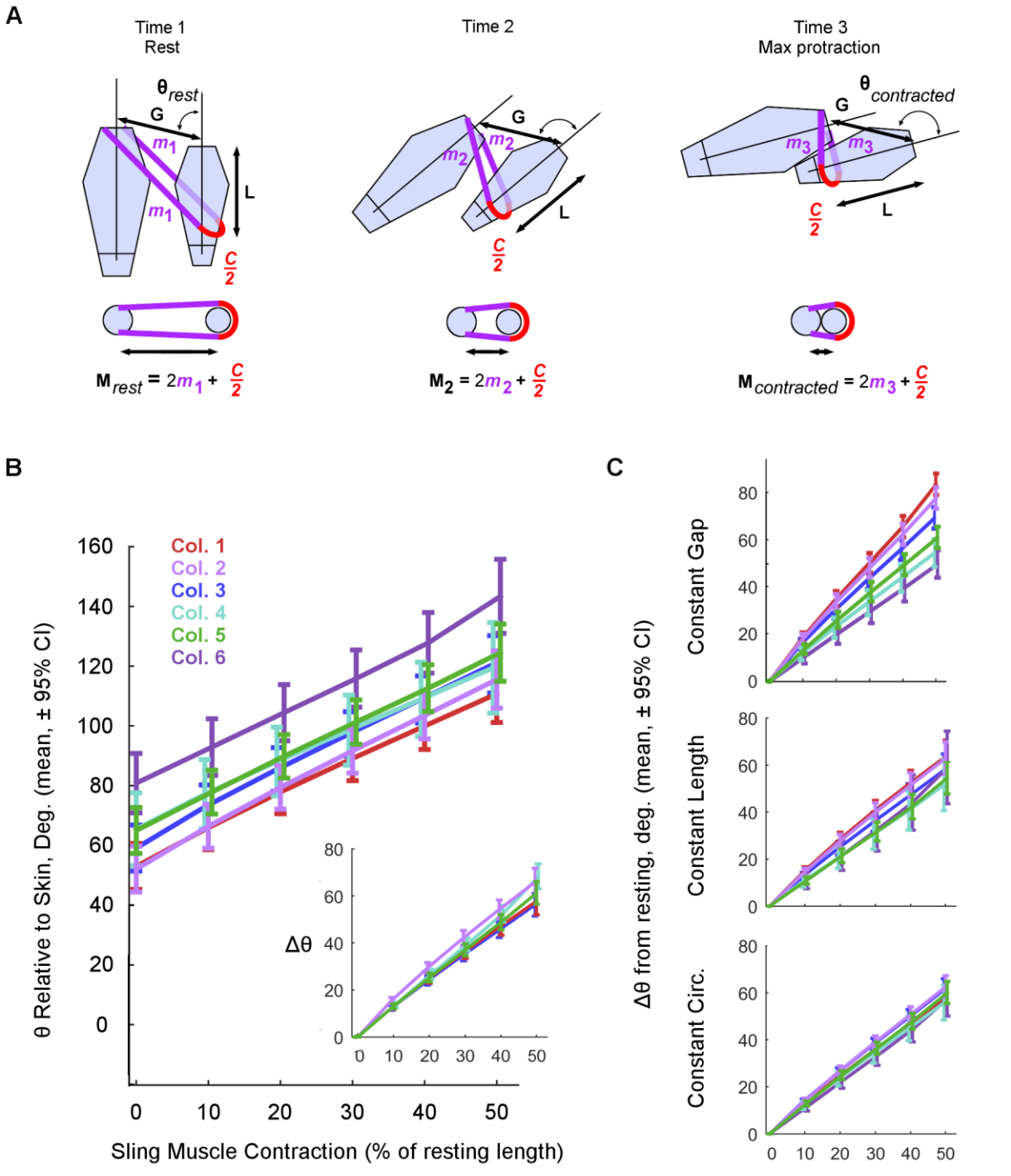

Figure 5.4: Simulated whisking shows a given percent contraction will cause all whiskers to move through similar angles. (A) Schematic illustrating simulation. The muscle lengths at rest (M_{rest}) and after a contraction (Mcontracted) are constrained by the lever length of the rostral follicle (L), the gap between the follicle apices (G), the angle of the whisker with respect to the skin (θ_{rest}), and the circumference of the rostral follicle at the point of muscle contraction (C). Time 1: When at rest the law of cosines can be used to find the intrinsic muscle arm length, m1, from anatomical observations of L, G, C, and θ_{rest}. The entire

muscle length, M1 is determined by m1 and C/2, half the follicle circumference, shown in red. Time 2-3: After muscle contraction, the law of cosines can be used to find $\theta_{contracted}$ from L, G, and $M_{contracted}$. **(B)** Mean degree rotation of whiskers within each column with respect to the skin surface after simulated uniform contraction of intrinsic muscles. X-axis shows the simulated contraction of all sling muscles across the entire array, represented as percent contraction from resting length. Y-axis shows the resulting protraction of the whisker, represented as angle relative to the skin tangent at the end of protraction. Error bars represent 95% confidence intervals offset slightly for visual clarity. Inset shows movement relative to the starting position of the whisker, with X-axis identical to larger plot and Y-axis showing change in angle, calculated by subtracting the starting angle of the whisker relative to the skin tangent from the ending angle of that whisker. **(C)** Results of simulations involving changing values of G, L, or C from observed values to mean values for all whiskers. Plot axes are the same as in B. Top: Results of a simulation in which values for the inter-follicle gap are changed from the values observed to at the mean observed value for all whiskers across the pad. Middle: identical to Top, but instead holding follicle length constant at the mean value. Bottom: identical to Top, but instead holding follicle circumference constant at the mean value.

5.4. Discussion

Excluding extrinsic muscles and simulating the effects of a uniform motor command to intrinsic muscles allows us to control for behavioral variability, unmasking any variability due to biomechanical constraints, and showing that the geometry of the rat mystacial pad ensures that all whiskers will protract through the same angle if the intrinsic muscles contract the same percent. This similarity in actuation of whiskers across the pad could allow the rat to use the same rate code (Groh 2001) from lower motor neurons in the facial nucleus (Grinevich, Brecht et al. 2005) to control any whisker in the pad. Because the same type of control could be used for every whisker, the rat needs only to vary the timing or intensity of activation of intrinsic muscles between different whiskers to vary its sensing resolution.

Chapter 6: Representation of Stimulus Speed and Direction in Vibrissal-Sensitive Regions of the Trigeminal Nuclei: A Comparison of Single Unit and Population Responses

This chapter was published in PLOS One as: Kaloti AS*, Johnson EC*, Bresee CS, Naufel SN, Perich MG, Jones DL, Hartmann MJZ (2016) "Representation of Stimulus Speed and Direction in Vibrissal-Sensitive Regions of the Trigeminal Nuclei: A Comparison of Single Unit and Population Responses" 11(7): e0158399.

*authors contributed equally

6.1. Abstract

The rat vibrissal (whisker) system is one of the oldest and most important models for the study of active tactile sensing and sensorimotor integration. It is well established that primary sensory neurons in the trigeminal ganglion respond to deflections of one and only one whisker, and that these neurons are strongly tuned for both the speed and direction of individual whisker deflections. During active whisking behavior, however, multiple whiskers will be deflected simultaneously. Very little is known about how neurons at central levels of the trigeminal pathway integrate direction and speed information across multiple whiskers. In the present work, we investigated speed and direction coding in the trigeminal brainstem nuclei, the first stage of neural processing that exhibits multi-whisker receptive fields. Specifically, we recorded both single-unit spikes and local field potentials from fifteen sites in spinal trigeminal nucleus interpolaris and oralis while systematically varying the speed and direction of coherent whisker deflections delivered across the whisker array. For 12/15 neurons, spike rate was higher when the whisker array was stimulated from caudal to rostral rather than rostral to caudal. In addition, 10/15 neurons exhibited higher firing rates for slower stimulus speeds. Interestingly, using a simple decoding strategy for the local field potentials and spike trains, classification of speed and direction was higher for field potentials than for single unit spike trains, suggesting that the field potential is a robust reflection of population activity. Taken together, these

results point to the idea that population responses in these brainstem regions in the awake animal will be strongest during behaviors that stimulate a population of whiskers with a directionally coherent motion.

6.2. Introduction

The rat vibrissal system is one of the most prominent models in neuroscience for the study of active touch and sensorimotor integration. Mechanical signals from the vibrissae are represented in the responses of primary sensory neurons in the trigeminal ganglion, each of which responds to one and only one whisker (Zucker and Welker 1969, Shoykhet, Doherty et al. 2000, Jones, Lee et al. 2004, Leiser and Moxon 2006, Szwed, Bagdasarian et al. 2006, Leiser and Moxon 2007, Kwegyir-Afful, Marella et al. 2008). Signals are then sent to the trigeminal brainstem nuclei, which are the first site of neural response integration (Jacquin, Woerner et al. 1986, Jacquin, Barcia et al. 1989, jacquin, Renehan et al. 1993, Jacquin, Zahm et al. 1993, Shortland P. J., Demaro J. A. et al. 1996, Timofeeva, Lavellee et al. 2004, Furuta, Timofeeva et al. 2008, Furuta, Urbain et al. 2010, Mosconi, Woolsey et al. 2010, Jacquin, Arends et al. 2014, Xiang, Arends et al. 2014, Matthews, Deschenes et al. 2015). A fundamental distinction between the responses of neurons in the trigeminal ganglion and those in the trigeminal nuclei is the emergence of multi-whisker receptive fields in the latter (Ma 1991, Jacquin, Rhoades et al. 1995, Nicolelis 1996, Pierret, Lavellee et al. 2000, Veinante, Jacquin et al. 2000, Timofeeva, Lavellee et al. 2004, Furuta, Timofeeva et al. 2008, Furuta, Urbain et al. 2010). It is well established that neurons of the trigeminal ganglion exhibit strong angular tuning (Zucker and Welker 1969, Lichtenstein, Carvell et al. 1990, Shoykhet, Shetty et al. 2003), meaning that the neural response is stronger depending on the direction in which a single whisker is pushed. During active whisking behavior, however, multiple whiskers will tend to be deflected in a coherent manner across the array. Although each individual whisker might bend to a slightly different angle, each whisking motion will generate an overall direction of deflection across regions of the array. A critical open question, then, is how neurons at central levels in the trigeminal pathway represent and integrate information about stimulus speed and direction present across multiple whiskers.

The spinal trigeminal nuclei (the first structures containing neurons exhibiting multi-whisker receptive fields (Jacquin, Golden et al. 1989)) have also been shown to contain neurons that exhibit angular tuning (Sosnik, Haidarliu et al. 2001, Furuta, Nakamura et al. 2006). It is still not known, however, how trigeminal nuclei neurons with multi-whisker receptive fields represent movement through the whisker array. The present study was undertaken to begin to understand the integrative properties of neurons in the trigeminal nuclei and the extent to which stimulus speed and direction are reflected in the responses of individual neurons compared to responses of the population. Specifically, the study examines the extent to which multi-whisker receptive field neurons code for stimulus directionality across a larger group of neighboring whiskers, and whether there exist differences in neural responses at different speeds of stimulus contact. To further test the encoding of speed and direction, we also consider the problem of classifying, or decoding, the experimental condition from the local
field potentials and spike trains recorded experimentally.

6.3. Materials and Methods

We investigated the integrative properties of neurons in the trigeminal nuclei by stimulating the entire rat whisker array with a vertical brass post mounted on a precise servo motor. The post was swept through the vibrissal array at three different speeds (90°/*s*, 180°/*s*, and 360°/*s*) and in both rostral-caudal and caudal-rostral directions. We recorded both single unit and population activity of multi-whisker receptive field neurons in spinal trigeminal nucleus interpolaris (SpVi) and oralis (SpVo) to quantify responses under these different conditions.

6.3.1. Surgical procedures

All procedures were approved in advance by Northwestern University's Animal Care and Use Committee. Six female Sprague-Dawley rats (Charles River Laboratories) weighing 240–330 g were used for these experiments. Anesthesia was initially induced with isoflurane (1–2 ml) to minimize handling of the animal.

To ensure access to the whiskers a deep surgical plane of anesthesia was maintained using an intraperitoneal injection of ketamine hydrochloride (75.8 mg/kg), Xylazine HCl (3.78 mg/kg) and Acepromazine Maleate (0.76 mg/kg). Supplementary doses were administered to maintain adequate anesthesia (suppressed toe pinch response). Heart rate was monitored throughout the experiment to ensure the health of the animal. Body temperature was maintained at 37.5°C using a servo-controlled heating pad. A craniotomy was performed to expose the cerebellar surface overlying the spinal trigeminal nuclear complex (≈11–14mm caudal to bregma and 2–3mm lateral to the midline of the skull). The cerebellar surface was kept moist with mineral oil throughout the experiment.

6.3.2. Single unit and field potential recordings

Extracellular recordings were performed with tungsten microelectrodes (2–4MΩ FHC, Inc., Bowdoin, ME, USA). Electrodes were advanced through the cerebellum using a manually controlled micromanipulator (MM33, Sutter Instruments, Novato, CA, USA). While the electrode was advanced into the trigeminal nuclear complex area, whiskers on the ipsilateral side of the face were stimulated manually to detect whisker sensitive units.

Only multi-whisker-sensitive units were recorded in this study. Once a well-isolated whisker sensitive unit was encountered, the receptive field was determined using manual stimulation with a thin (1mm) wooden probe. Manual stimulation allowed us to locate the principal whisker that elicited the maximum response, as observed on the oscilloscope screen and confirmed by listening to the amplified audio recordings of unit activity. We then stimulated the whiskers surrounding the principal whisker to systematically determine all whiskers belonging to the unit's receptive field, i.e., all the whiskers that elicited a measurable single unit response to whisker deflection. We did not attempt to classify the strength of response of the adjacent whiskers, as our goal was to examine the integrative properties of multi-whisker receptive field neurons.

The smallest receptive field was two whiskers (E1 and E2) and the largest receptive field was ten whiskers (C1, C2, C3, C4; D2, D3, D4; B1, B2, B3).

Electrical signals were amplified and filtered (1–10,000 Hz; AM systems, Carlsborg, WA, USA) and digitized at 40 kHz (National Instruments, Austin, TX, USA). To ensure unit isolation throughout the experiment, we noted the response to manual stimulation of the principal whisker between trials and the consistency of spike shape from trial to trial. During recording, care was taken to ensure good spike isolation, so that at least one clearly distinguishable spike waveform with a good signal-to-noise ratio greater than or equal to three was seen on the oscilloscope.

After recordings were complete the rat was deeply anesthetized and then euthanized via perfusion with saline and paraformaldehyde, followed by decapitation. The brainstem was removed and sectioned, slide-mounted and stained with cytochrome oxidase using standard histological protocols. Typical coronal sections are shown in Figure 6.1A.

6.3.3. Whisker stimulation

All whiskers on both sides of the face were left intact. The left whisker array was stimulated in these experiments using the setup schematized in Figure 6.1B. A brass metal post (2mm diameter, 5 cm tall) was vertically mounted on a hard fiber rod (27 cm long, 1/4 inch diameter) attached to the shaft of a servo motor (Animatics, Inc., SM3420, Milpitas, CA, USA) via a custom-made aluminum fitting. The post was swept through the whisker array at three different speeds (90°/*s*, 180°/*s* and 360°/*s*) in Rostral-Caudal (RC, clockwise directed curved arrow) and Caudal-Rostral (CR, counter-clockwise directed curved arrow) directions at an orientation perpendicular to the rows of the whisker array (Figure 6.1B). This stimulation resulted in linear velocities of 42 cm/s, 85 cm/s, and 170 cm/s, respectively for the corresponding angular speeds.

6.3.4. Analysis of electrophysiological data

Recordings of electrophysiological data were taken from fifteen brainstem locations, and the digitized waveforms loaded into the MATLAB programming environment (The MathWorks, Natick, MA, USA). Because the time of contact varied slightly from trial-to-trial due to variations in the speed of the servo motor, trials were aligned based on the start of the physiological response. For each recording location and condition, the threshold for activity was taken to be 60% of the mean peak value of the local field potential waveform. The start of the physiological response was taken to be the time in each trial where the local field potential exceeded this threshold. For each trial, a 750 ms length of data was extracted, centered at the threshold crossing point. These data were then used to extract spike times for the units.

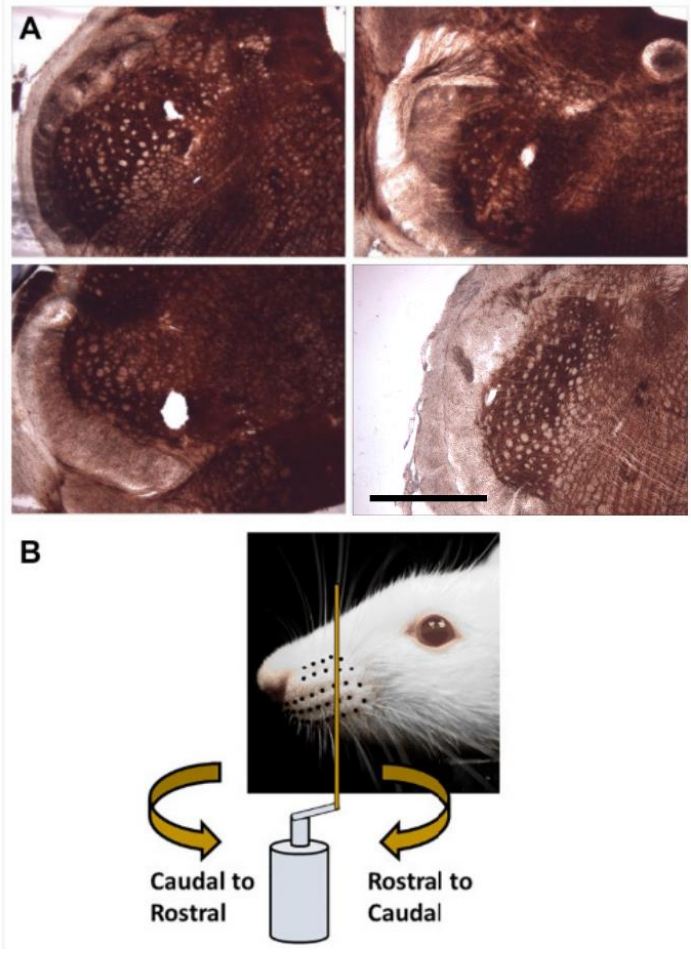

Figure 6.1: Recording location and whisker stimulation. (A) Histological analysis showed lesions either in spinal trigeminal nucleus interpolaris or spinal trigeminal nucleus oralis. The scale bar represents 1mm. **(B)** During stimulation a vertical metal post is mounted on a servo motor and swept through the whisker array in either Rostral- Caudal (RC; clockwise directed curved arrow) or Caudal-Rostral (CR; counter-clockwise directed curved arrow) directions and oriented perpendicular to the whisker array.

A MATLAB based, semi-supervised spike-sorting algorithm was used to identify the best isolated single unit from each recording site. The sampled data were first digitally band-pass filtered between 300 and 3,000 Hz. Putative spike events were detected using a thresholding operation, and a window of data extracted around each event. Spike events were then clustered using peak height, peak width, trough depth, trough width, and the projection onto the first three principal components using a standard mixture-of-Gaussians model (Dayan and Abbott 2001). The clustering results were then visually inspected to select for the best isolated spike cluster, which was chosen as the target neuron for that recording. This cluster was used to generate a spike template for the best isolated spike.

All spike events were compared to this template and the least-squares error computed using a small window around the spike event. A threshold on the least-squares error determined which events were labeled as a spike from this unit. This threshold was manually determined for each unit and condition in order to balance detected spikes against noise events. Using this approach, 15 well-isolated units were found from 15 recording sites across six animals. Spike times and local field potential waveforms (the raw waveforms) were saved for further analysis.

6.3.5. Analysis of spike times and local field potentials

Because the experiment could not provide absolute times of stimulus onset, it was necessary to estimate the contact duration from the spiking responses of each unit. For each unit, a peristimulus time histogram (PSTH) was formed using a bin width of 15 ms. The start of contact was taken to be the point at which the PSTH exceeded three times the mean firing rate. The end point of contact was defined as the point at which the PSTH returned below twice the mean firing rate. Spikes within this window were taken to be spikes in response to the stimulus, and spikes outside this window taken to be background spikes. Spike rates and response durations were calculated using this window. All statistical tests (two-sided t-tests, ANOVA) reported below were computed using the MATLAB statistics toolbox.

To classify the experimental condition from the recorded local field potential response, a maximum likelihood approach was tested. For each condition at each recording site, the broad-band LFP was pointwise-averaged to create a mean template waveform. Using a leave-one-out cross-validation approach, one trial was reserved for testing while the other 28 trials were averaged to create the template waveforms. The test trial was classified using a maximum likelihood approach with a multivariate Gaussian assumption (Smola and Vishwanathan 2008). Under these assumptions, the likelihood of the local field potential as an N-dimensional vector of voltages v in condition j was given by

$$p(\mathrm{v}|j) = \frac{1}{(2\pi)^{N/2}|\Delta_j|^{1/2}} \exp\left(-\frac{1}{2}\left(V - \mu_j\right)' \Delta_j^{-1}\left(v - \mu_j\right)\right) \qquad \text{(eq. 6.1)}$$

where μ_j was the mean field-potential voltage, estimated over 28 training trials for condition *j*, which was an *N*-dimensional vector. The covariance matrix Δ_j was assumed to be diagonal with all entries given by σ^2_j. The quantity σ_j was estimated by taking the mean over time of the standard deviation of the voltage calculated at each time *t* using the data from the 28 trials. This form of the covariance assumed independence between each time sample and constant variance over time. Given a voltage trace recorded experimentally, classification was done by selecting the condition with the largest posterior likelihood, which was proportional to the likelihood times the prior for each condition *j*. Assuming equiprobable conditions, the decision rule was

$$j^* = \mathrm{argmax}_j p(\mathrm{v}|j) \qquad \text{(eq. 6.2)}$$

This was implemented using the log of the likelihood function, by finding the maximum over *j* of the expression $-0.5\left(\mathrm{v} - \mu_j\right)'\left(\mathrm{v} - \mu_j\right)\sigma_j^2 - 0.5\sum_{i=1}^{N} \ln\left(\sigma_j^2\right)$

One additional complication, however, was that it was unreasonable to assume an absolute start time to the template in each trial. There was trial-to-trial variability in the start time, and, as can be seen in Figure 6.2, the responses for different conditions began at different absolute times. To compensate for the unknown start time, the template was compared to the test voltage trace at different shifts from 100 ms before to 100 ms after the stimulus, with a resolution of 2.5 ms. Classification was then done with the following rule

$$j^* = \text{argmax}_j \text{argmax}_\tau p(\text{v}_{t-\tau}|j) \qquad \text{(eq. 6.3)}$$

This created a template matching scheme which was invariant to shifts in the target template. This shift allowed for asynchronous classification of the waveform.

In order to classify the experimental condition based on the measured spike trains, a probabilistic model of the experimental spiking was used to compute the likelihood of each condition. Using the leave-one-out cross validation approach on each trial, the PSTH was formed for each condition of each single unit response using 3 ms bins. The single unit PSTHs were normalized to a maximum value of 1, if at least one spike occurred in that bin in every trial, and to a minimum probability set by the average spontaneous spike rate. Each bin was modeled as an independent binary random variable with a probability of spiking given by the normalized PSTH. This resulted in a joint distribution for each condition. This approach assumed independent spike times, which were used to compute the posterior distribution of a stimulus (Dayan and Abbott 2001). Using this model, the test spike train was classified using a maximum likelihood approach. This provided an approximation of the encoding of stimulus conditions by individual spike trains.

The joint probability distribution of a set of spike times $t_1, t_2, \ldots, t_n$ over the interval T divided into N bins was then given by

$$p(t_1, t_2, \ldots, t_n|j) = \prod_{\{i|\phi(i)=1\}} p_i \prod_{\{i|1-\phi(i)=1\}} 1 - p_i \qquad \text{(eq. 6.4)}$$

where $\phi(i)$ is a function which has value 1 if for any spike j, $(i-1)T/N \leq t_j < iT/N$ (otherwise zero), and p_i is the probability of spiking in the ith bin (derived from the normalized PSTH). To classify the experimental condition, the condition with the maximum likelihood was selected

$$j^* = \text{argmax}_j p\,(t_1, t2, \ldots, t_n|j) \qquad \text{(eq. 6.5)}$$

As with the local field potentials, it was not reasonable to assume that an absolute start time was known. It was therefore necessary to test over a range of time shifts in the experimental spike train. This gave a classification approach that does not rely on knowledge of an absolute start time. For time shifts τ ranging from 100 ms before to 100 ms after the start of stimulation (with a resolution of 2.5 ms), the probability of each condition given the shifted spike train was calculated. The maximum probability was taken as the probability for that class.

$$j^* = \text{argmax}_j \text{argmax}_\tau p\,(t_1 - \tau, t_2 - \tau, \ldots t_n - \tau\,|j) \qquad \text{(eq. 6.6)}$$

The classification schemes for the spike trains and local field potentials were used to decode the experimental condition from the recorded activity, yielding a measure of the potential to discriminate between experimental responses in different conditions. Higher classification rates indicated a larger difference in the experimental response. These methods estimate the lower bound on the optimal decoding performance, which may require more advanced statistical modeling and processing.

6.4. Results

The present study was limited to recordings from multi-whisker-projection neurons from spinal trigeminal nuclei interpolaris and oralis. We begin by demonstrating that these neurons exhibit a central tendency to code for either stimulus direction, stimulus speed, or both, and then develop a lower bound on the performance of an optimal estimator for speed and direction based on the field potentials and spike trains of individual neurons. The relevant data for the figures presented in this section can be found in the supporting information online.

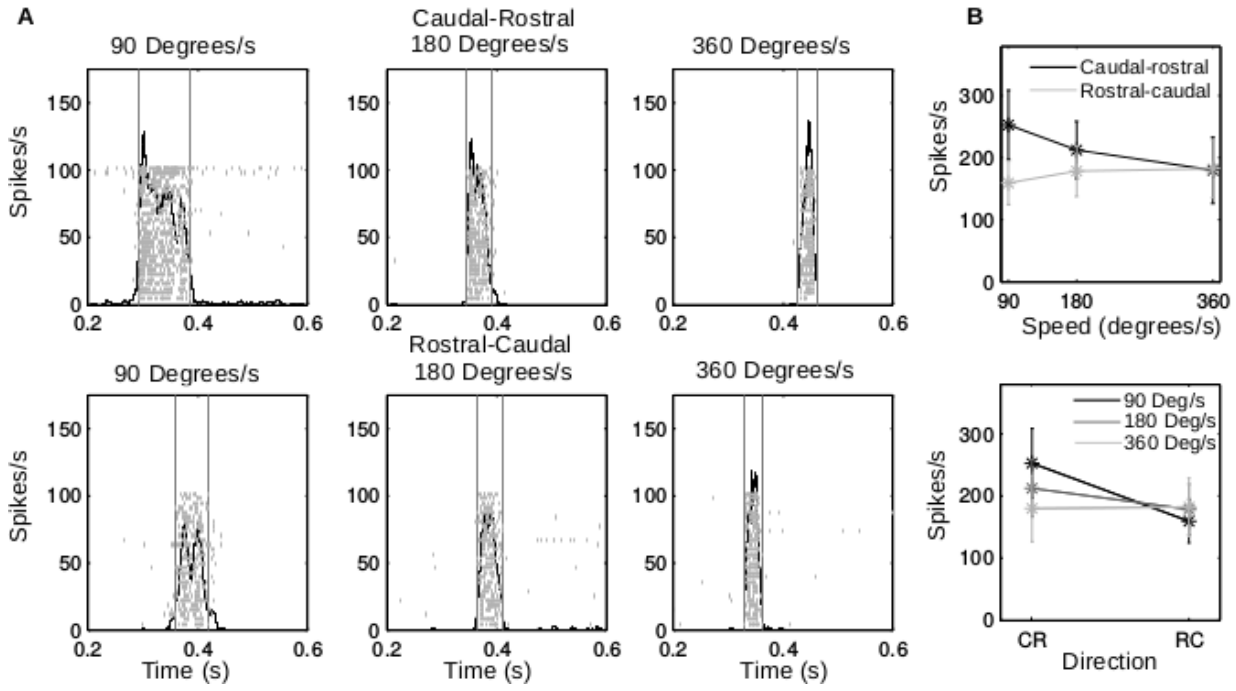

Figure 6.2: Response of one example neuron to stimulation at different speeds and directions. (A) Raster plots and PSTHs. The vertical lines indicate the contact window determined by thresholding the PSTH. The shifts in the response along the time axis between the different conditions are due to the differences in stimulus alignment between conditions. All PSTHs indicate a strong response to the stimulus and a relatively low baseline firing-rate. **(B)** Mean spike rate for each condition, with error bars indicating the standard deviation across all trials.

6.4.1. Examples of responses to varying stimulation speed and direction

The neural responses of the 15 units were analyzed to study the response of trigeminal brainstem neurons to variation in the speed and direction of stimulation. Figure 6.2 shows the response of a typical recorded neuron. As expected, the peri-stimulus time histograms (PSTHs) show a clear increase in the spike rate over the baseline activity for all conditions. At higher speeds the response becomes narrower in duration, consistent with the decrease in contact time (shown by the light grey vertical lines).

Different conditions also appear to show different patterns in the spiking activity. At slower speeds, there is an initial burst of spikes followed by a drop in spike rate, suggesting spike rate adaptation during contact. Six of the 15 units showed this spike rate adaptation for at least one condition. In addition, two units showed initial spiking at the start of stimulation and then spiking on release. To some degree, these two different types of adaptation may resemble the “slowly” and “rapidly” adapting responses observed in trigeminal ganglion neurons (Lichtenstein, Carvell et al. 1990). However, these adaptation characteristics were not observed in all stimulation conditions, and 7/15 neurons did not show any adaptation effect. Because all neurons in the present study responded to multiple whiskers they are likely to receive a complex combination of RA and SA afferents from different whiskers. It was therefore not possible to precisely classify adaptation characteristics, and these effects were not analyzed further.

Instead, we focus on change in spike rate related to speed and direction. Figure 6.2B shows these effects for the neural data shown in Figure 6.2A. The plots shows the mean spike rate with error bars indicating the standard deviation over the 29 trials. In one direction, the rate appears to increase with speed, while in the other the rate decreases. The slowest speed shows a significant difference in spike rate between the two directions.

6.4.2. Spike rate is closely related to stimulus direction and to stimulus speed

Unsurprisingly, we found that for most neurons, response duration was increased for slower speed stimuli, but was unaffected by direction of stimulation. More surprising, however, is that neurons tended to slightly increase spike rate for slower speed stimuli. Figure 6.3A generalizes these effects over all neurons, comparing average spike rate and response duration for the slowest speed with the two higher speeds. Each point represents the average response of one unit. Responses to stimulation at both 90°/*s* as well as 180°/*s* were found to have significantly higher spike rates than responses to stimulation at 360°/*s*. ($p = 0.026$ and $p = 0.0003$, respectively, paired t-test). Thus on average, this group of neurons responded to slower stimuli with longer responses and slightly higher spike rates.

Strong effects were observed when we compared the response to the directionality of the stimulus. Figure 6.3B compares the average spike rate and response duration for the caudal-rostral (x-axis) and rostral-caudal (y-axis) directions for the 90°/*s*, 180°/*s* and 360°/*s*. Each point represents the average response of a single unit. The spike rate is significantly different (paired t-test, $p = 0.04$) between the two directions.

The tuning of the firing-rate of individual cells to speed and direction was further explored using an ANOVA test. The statistical comparisons of data for each cell were evaluated using ANOVA at the 95% confidence level ($a = 0.05$). The 3-factor ANOVA looked at main effects on firing rate and allowed for the evaluation of cells that were tuned to the contact phases, speed, and direction. The contact phases included pre-contact, contact, and post-contact. Contact was defined using the thresholds described previously (shown in Figure 6.2A, vertical lines).

Analyzing the spike rates, 80% of the units had higher rates for stimulation in the caudal to rostral direction than in the rostral to caudal direction. Comparing the spike rates at 90°/*s* to 360°/*s*, 67% of units showed higher rates for the slower stimulus speed. We found that all of the cells (100%) showed a

significant ($p < 0.05$) change in firing rate during contact, indicating that they were involved in the sensory response. The majority of cells (73%) were tuned for direction and 83% of cells were tuned for speed. Over half of the population (66%) was tuned for both speed and direction, and all cells were tuned for at least one of these variables. As a population the average firing rates were slightly higher for caudal-rostral stimulation and tended to decrease as movement speed increased, although the activity of individual cells exhibited a variety of relationships with the stimulus types.

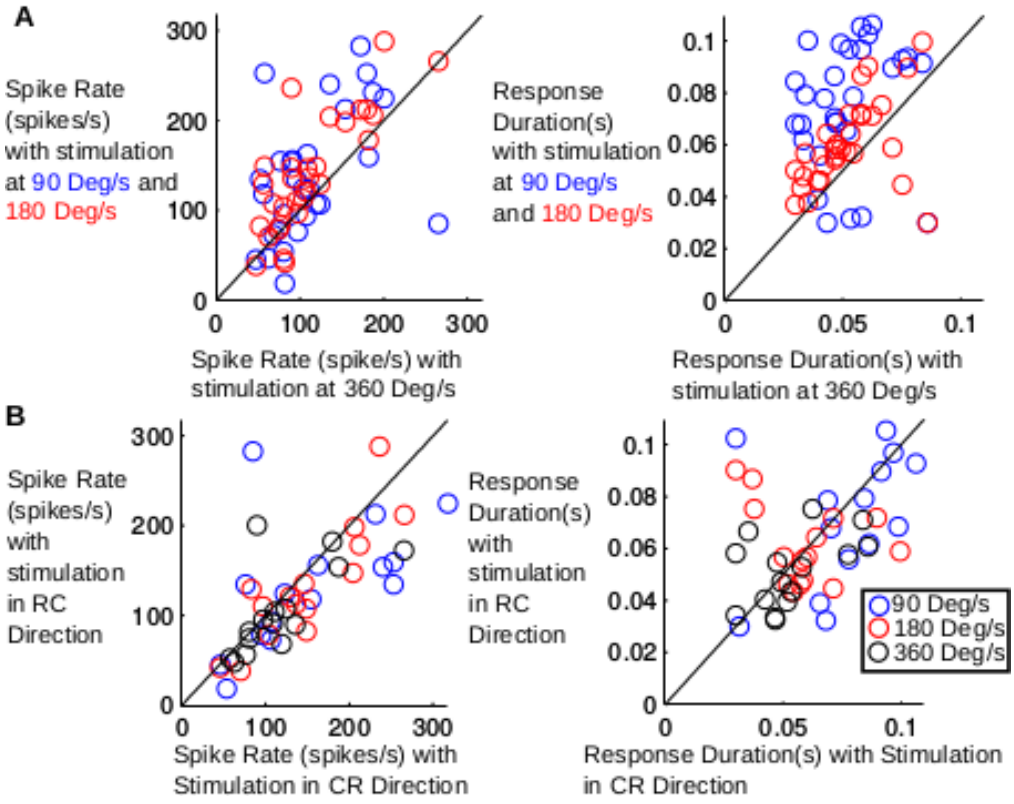

Figure 6.3: Comparison of the average spike rate and duration in response to stimuli (A) Comparison of the average spike rate and duration of the response during stimulation at 360°/s vs stimulation at 90°/s and 180°/s. There is a clear trend in increased response durations at 90°/s and 180°/s, with the 90°/s stimulation lasting the longest. There is a significant increase in spike rate in the 90°/s and 180°/s conditions when compared to the 360°/s condition. **(B)** Comparison of spike rate and duration of the response during stimulation in the caudal-rostral direction vs stimulation in the rostral-caudal direction. There is a statistically significant increase in spike rate in the caudal-rostral direction, but there is no significant change in the response duration.

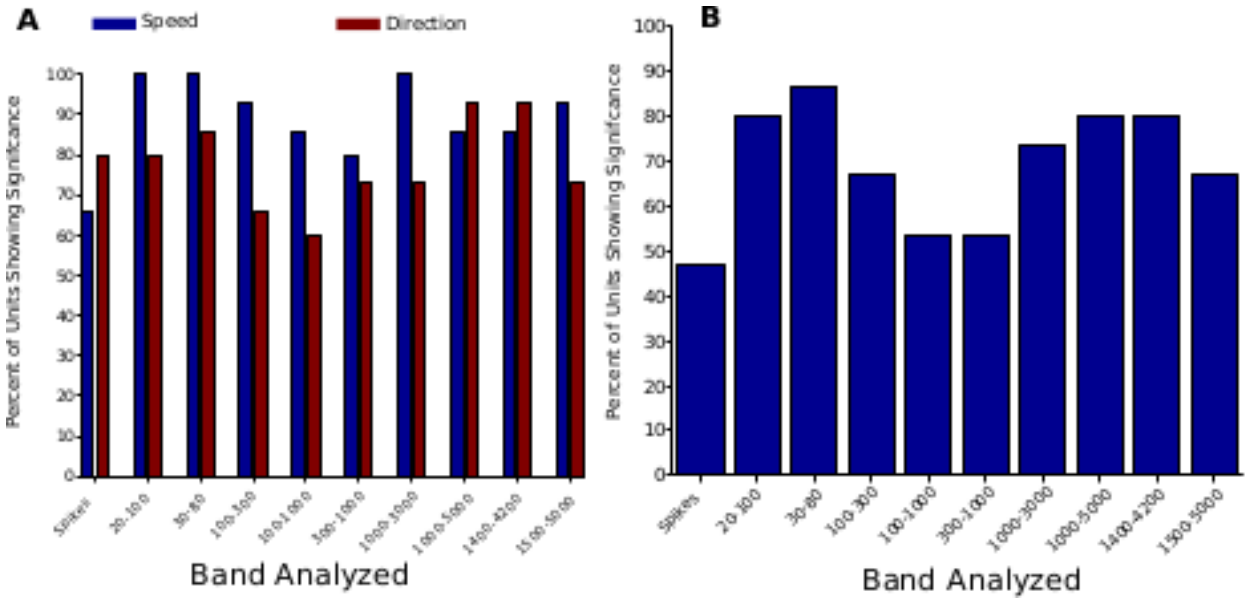

Figure 6.4: Percentage of recording sites with a significant tuning to speed, direction, or both as determined by an ANOVA analysis of signal power in different frequency bands. Average power in each band was computed from the output from a bank of bandpass filters and significance levels were set at $p < 0.05$. **(A)** Percentage of recording sites with a significant tuning to speed or direction. Several bands driven by multi-unit activity (1,000–3,000 Hz, 1,000–5,000 Hz) are sensitive to both speed and direction. **(B)** Percentage of recording sites with significant tuning to both speed and direction. In several bands driven by multi-unit activity (1,000–3,000 Hz, 1,000–5,000 Hz) more than 80% of recording sites are sensitive to both speed and direction. In contrast, 66% of single unit spike rates were sensitive to both conditions.

6.4.3. Multi-unit activity is more strongly tuned for speed and direction than single unit spike rates

As described above, the analysis of single unit spike rates showed a significant variation with speed and direction in 66% of units. Although this suggests that spike rate is modulated by the experimental variables, not all neurons show a significant response to both conditions. It is possible that some neurons are sensitive to direction of the stimulus and others more sensitive to the speed.

To improve understanding of how these variables are encoded by the population of neurons in the trigeminal nuclei, we examined the variation in multi-unit activity across multiple frequency bands of the multi-unit response. The recorded broad-band neural signals were filtered into different narrow bands

using a filterbank of bandpass filters with different bandwidths and the signal envelope in each band was computed. Using the average signal envelope amplitude in each phase of the trial, the ANOVA procedure above was run on the average power for each band (with $p < 0.05$ as the criterion for significance).

The results of this analysis are shown in Figure 6.4. Figure 6.4A shows the percentage of units recorded which show significant differences as a function of speed or direction. This percentage is shown for the single unit spike rate and also for different frequency bands of the LFP (some overlapping). A majority of units in all conditions were sensitive to speed or direction. Sensitivity to speed was higher in five LFP bands than in the single unit spike rate. In many units, the spike rate was significantly different as a function of direction. The LFPs bands which had the lowest percentage of units sensitive to direction were between 100 and 3000Hz.

Interestingly, over 80% of units are sensitive to both speed and direction when measured over bands containing large amounts of multi-unit activity (1000–3000 Hz, 1500–4200 Hz). Broadly, all frequency bands have a higher percentage of units which are sensitive to the conditions than the single unit spike rates. Interpreting the broad-band local field potential as a correlate of population activity, this suggests a robust population representation of speed and direction in the trigeminal nuclei.

In summary, the change in the power of the envelope of the multi-unit activity is, in general, significantly different for different stimulus conditions (speed and direction). We therefore next investigated the possibility of decoding experimental condition from the local field potentials and spike trains recorded experimentally.

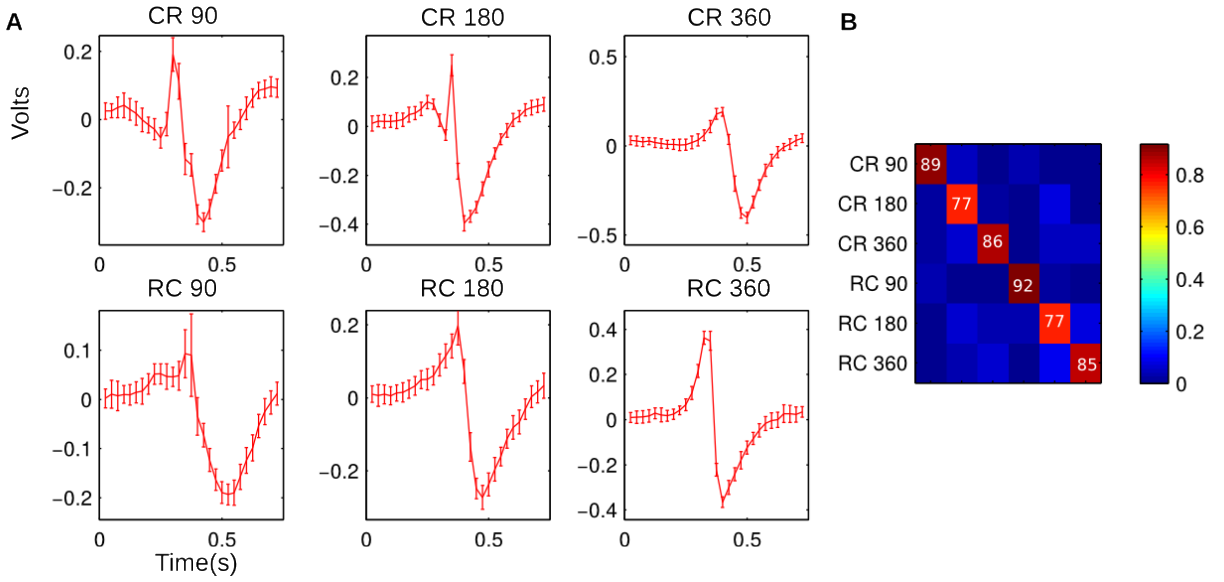

Figure 6.5: This figure shows the result of a template-matching classification method using the broad-band local field potentials. Using a cross-validation approach for each neuron, the training data (consisting of the raw microelectrode recording filtered between 1 and 10000 Hz) was used to estimate a template for each experimental condition. The test data were then compared to each template and the log likelihood calculated. To make classification asynchronous, the template was tested at different lags and the lowest error selected for that condition. The experimental condition with the lowest difference was used to classify the test data. Panel A shows the template waveforms for an example recording site. The templates are very distinct, with the standard deviation showing a relatively low trial-to-trial variability. Panel B shows the average confusion matrix for the template classification. The numbers in Panel B are the per- condition probability of correct classification.

6.4.4. Local field potentials enable more accurate classification of speed and direction than single unit spike trains

To further test the encoding of speed and direction in these brainstem neurons, we considered the problem of classifying, or decoding, the experimental condition from the local field potentials and spike trains recorded experimentally. This analysis represents a lower bound on the performance of an optimal estimator of speed and direction based on the field potentials or spike trains of individual neurons.

Importantly, this analysis does not imply that these methods are used by the nervous system. Rather, the approach simply analyzes how distinct the neural responses are in the experimental conditions. This

analysis was performed on the broadband local field potentials using the maximum likelihood classifiers defined in Materials and Methods using a leave-one-out cross validation approach. Figure 6.5A shows the mean local field potentials and standard deviation estimated over the 29 trials at a single recording site. These templates are used for the maximum likelihood classification. As can be seen, there is a distinct template waveform for each condition. Figure 6.5B shows the confusion matrix averaged over all recording sites. The average probability of correctly identifying the experimental condition was 84%. The distinct template waveforms for the LFPs result in high classification rates. Assuming this activity reflects the overall population activity, this suggests a robust population encoding.

The maximum likelihood classification with leave-one-out cross-validation was also applied to the single unit spike trains to determine the experimental condition. The normalized PSTH was interpreted as the probability of firing a spike in a particular time bin of the response. This approach represents a lower bound on the performance of an optimal detector that takes into account the statistics of the stimulus conditions and the statistical relationship between spike times. Figure 6.6A shows an example PSTH for each experimental condition from a single unit. Fig 6.6B shows the confusion matrix for classification, averaged over all units. The average probability of correctly identifying the experimental condition was 64% (well above the 16.67% chance level for six classes). Classification rates seem to be highest for the lowest speeds, which may be related to a larger total number of spikes in each trial.

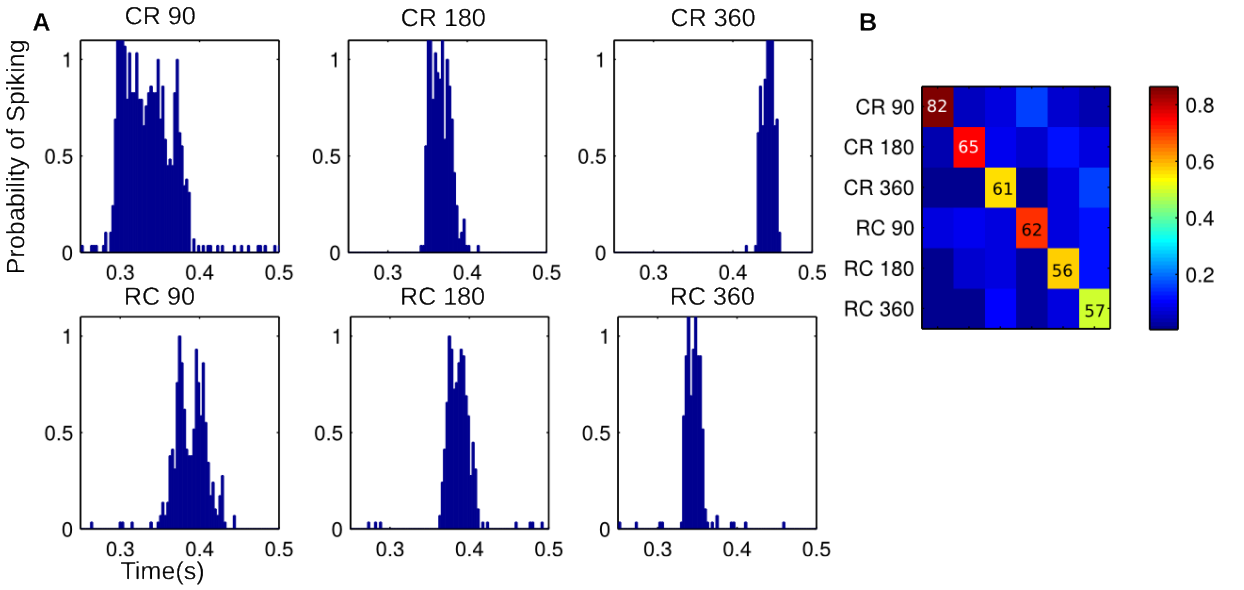

Figure 6.6: This figure shows the results of a classification scheme using the spike train from a single unit. Using a cross-validation approach, the training data for each unit was used to calculate the PSTH. This was normalized to get the probability of firing a spike in each bin. For the test spike train, the probability of observing the spike train given each condition was calculated, assuming independent probabilities of spiking in each time bin. This was repeated for different lags and the highest probability selected for that condition. The condition with the highest probability was used to classify the test spike train (a maximum likelihood approach). Panel A shows the normalized PSTHs for an example unit. Panel B shows the average confusion matrix over all units. The average probability of correct classification is lower than when using the LFPs. Although not necessarily indicative of how the neural system decodes these neural responses, these results, along with Figure 6.5, suggest that the population response is more robust than the response of a single unit.

Interestingly, the classification using the LFP is more reliable, likely due to conditions which are more easily discriminated. Comparing the probability of correct classification over the 15 recording sites, the probability of successful classification using the LFP was found to be significantly higher than the probability of correct classification using the spike trains (Wilcoxon rank-sum test, $p = 0.0021 < 0.05$). Assuming that the LFP is the reflection of the aggregate activity of the population of neurons in this region of the brainstem, it suggests that the population response is very robust. On the other hand, the lower classification rate for an individual spike train suggests that spike trains have higher trial-to-trial variability.

6.5. Discussion

6.5.1. Cell types in the trigeminal nuclei

Together, spinal trigeminal nuclei oralis and interpolaris are important stations in processing information arriving from the trigeminal ganglion through to the cerebellum, superior colliculus, thalamus and ultimately sensory cortex (Jacquin, Barcia et al. 1989, Jacquin, Golden et al. 1989, Jacquin, Chiaia et al. 1990, Furuta, Nakamura et al. 2006, Bokor, Acsady et al. 2008). Previous studies of sensory information processing within the trigeminal nuclei have focused on receptive field size (Jacquin, Golden et al. 1989, Timofeeva, Lavellee et al. 2004, Furuta, Urbain et al. 2010) and the physiology of angular tuning in projection and local circuit neurons (Furuta, Nakamura et al. 2006, Nakamura, Narumi et al. 2009, Hemelt, Kwegyir-Afful et al. 2010).

Although much remains to be understood about processing in the trigeminal nuclei, it is well established that single whisker receptive fields are associated with local circuit neurons (Jacquin, Golden et al. 1989, Bennett-Clarke, Chiaia et al. 1992, Veinante, Jacquin et al. 2000, Furuta, Timofeeva et al. 2008), while multi-whisker receptive fields are associated with neurons that project to more central structures (Bennett-Clarke, Chiaia et al. 1992, Veinante, Jacquin et al. 2000, Erzurumlu, Chen et al. 2006). As yet, however, there is little understanding of the role of multi-whisker receptive fields, which are a defining feature of these projection neurons. The experiments of the present work were therefore designed to investigate the responses of neurons in the trigeminal brainstem to tactile stimulation of the entire whisker array.

6.5.2. Angular tuning vs. direction tuning

Responses of primary sensory neurons in the trigeminal ganglion are known to exhibit strong angular tuning (Zucker and Welker 1969, Lichtenstein, Carvell et al. 1990, Shoykhet, Shetty et al. 2003, Jones, Lee et al. 2004, Szwed, Bagdasarian et al. 2006), and this tuning is also found within the trigeminal nuclei (Sosnik, Haidarliu et al. 2001, Furuta, Nakamura et al. 2006). Specifically, the receptive fields of neurons

in rostral interpolaris exhibit angular tuning for upward deflections, while neurons in the caudal regions do not exhibit such tuning bias (Furuta, Nakamura et al. 2006) .

Intriguingly, one recent study tested the consistency of angular tuning across primary and secondary somatosensory cortical areas, as well as ventroposterior medial thalamus and superior colliculus (Hemelt, Kwegyir-Afful et al. 2010). Results showed that in all regions a small number of neurons display consistent angular tuning for at least some vibrissae (Hemelt, Kwegyir-Afful et al. 2010). An unresolved question, then, is how angular tuning is transformed into directional tuning, in which a neuron exhibits selectivity for stimulus motion in a particular direction across multiple whiskers.

Multi-whisker receptive fields in interpolaris can be explained by the spatial extent of the dendritic trees of projection neurons (Veinante, Jacquin et al. 2000). Although little is known about how trigeminal neurons interconnect to create functional neural circuits, it is likely that directional tuning can be achieved through lateral inhibition. While there is no clear evidence for lateral inhibition in SpVi, PrV circuits show lateral inhibition of the principal whisker by adjacent whiskers (Lo, Guido et al. 1999, Minnery and Simons 2003). Similar circuitry may also operate within regions of oralis and interpolaris. This type of computation may be particularly important given that SpVi projection neurons with large multi-whisker receptive fields excite higher-order midbrain and diencephalic cells thought to mediate head orientation towards an externally generated vibrissa deflection (Jacquin, Barcia et al. 1989).

A second possible mechanism for directional tuning lies in the mechanical response of the vibrissae to rapid directional deflections. The intrinsic curvature of the vibrissae (Knutsen, Biess et al. 2008, Ritt, Andermann et al. 2008, Quist and Hartmann 2012, Quist, Seghete et al. 2014) ensures that both bending and vibrations will be much larger when stimulation is delivered from caudal to rostral instead of from rostral to caudal. Although angular tuning at the level of a single whisker offers high spatial resolution,

integration of sensory information across multiple whiskers provides more robust information about contact as well as the ability to localize

towards a moving object (Hemelt and Keller 2007, Hemelt and Keller 2008, Bezdudnaya and Castro-Alamancos 2011, Favaro, Gouvea et al. 2011, Bezdudnaya and Castro-Alamancos 2014).

6.5.3. Population codes for speed and direction

The results presented here suggest that as a population, the spike rate of trigeminal brainstem neurons encodes information about both stimulus direction and speed. In general, more cells were tuned for speed, but many cells were tuned to direction as well, and more than half the population was tuned to both variables. The results of decoding the stimulus condition with the single unit responses and the LFPs have interesting implications for population encoding in these structures. Single unit classification was well above chance, but worse than decoding using the LFPs. The LFPs have low trial-to-trial variability and a classification rate of around 90%. These results indicate that the population provides a more reliable estimate of these variables than individual units, and that while trial-to-trial variability in spikes is fairly high, redundancy helps encode physical parameters reliably.

Summarizing, these brainstem regions appear to contain a robust population-level representation of speed and direction of a real object moving through the whisker field. As in cortical regions (O'Doherty, Lebedev et al. 2012, Orsborn, Dangi et al. 2012, Fifer, Hotson et al. 2014, Hall, Nazarpour et al. 2014, Kao, Stavisky et al. 2014, Wang, Zhang et al. 2014, Christie, Tat et al. 2015), local field potentials and multi-unit activity may be sufficient for stimulation and decoding within trigeminal sensory nuclei. Further studies of single unit decoding in the trigeminal nuclei are still warranted, however, given that individual spike trains are likely to be encoding additional features of the stimulus, such as relative angles or surface texture information.

6.5.4. Potential behavioral significance

Previous work in the head-fixed animal has demonstrated that responses in SpVi are minimal during non-contact whisking (Yu, Derdikman et al. 2006, Moore, Mercer Lindsay et al. 2015). In view of the present finding that trigeminal brainstem neurons respond to directed motion over multiple whiskers, we predict that these neurons will respond most strongly to coherent motion of a tactile stimulus across the array. This type of stimulation could be generated by grooming behavior (sweeps of the forepaws across the face), by moving prey, or by a conspecific (Anjum, Turni et al. 2006, Bobrov, Wolfe et al. 2014). Thus we suggest that these brain regions are likely to be involved in detecting, tracking, and orienting to an external moving stimulus.

Detecting and orienting behaviors generally must be executed quickly. SpVi could mediate these movements via fast reflex loops through the facial motor nucleus (Kleinfeld, Berg et al. 1999), simultaneously modulating attention and alertness through its projections to the laterodorsal tegmental nucleus and pedunculopontine tegmental nucleus (Bosman, Houweling et al. 2011). SpVi also projects to the superior colliculus and has extensive reciprocal projections to the cervical spine (Matsushita, Ikeda et al. 1982, Phelan and Falls 1991), consistent with a role in whisker-based control of head orientation and position. With the assumption that following along a wall or floor could often generate directionally-coherent motion across the array (The, Wallace et al. 2013, Arkley, Grant et al. 2014), we suggest that SpVi may specifically contribute to keeping the head in a particular posture relative to these surfaces.

The placement of SpVi within the larger context of the trigemino-thalamocortical system suggests that it could also play an important role in allowing the rat to determine if an object is moving within the array, even while the whiskers themselves are actively moving. The reasoning here is as follows: in addition to its extensive involvement in brainstem reflex loops, SpVi is the start of the paralemniscal pathway, which projects through the posteromedial nucleus of the thalamus (PoM) to primary somatosensory cortex

(Bosman, Houweling et al. 2011). PoM is constitutively inhibited by zona incerta (ZI), but ZI is itself inhibited by primary motor cortex (M1). Thus information transmission from SpVi to cortex is gated by activity in M1 (Diamond and Ahissar 2007). This circuitry suggests that whisking commands sent from M1 could inhibit ZI, potentially releasing PoM from inhibition and allowing activity from SpVi to reach primary somatosensory cortex.

Once information from SpVi is allowed through PoM, it is sent to layers 5a and 1 of primary somatosensory cortex. This information is likely processed by layer 5 (L5) pyramidal neurons, which have dendrites in both layer 1 (L1) and L5. Intriguingly, concurrent input to the L1 and L5 dendrites of these neurons has been implicated in sensory feature association (Larkum 2013). The proposed mechanism is that the apical tufts of L5 pyramidal neurons harbor an initiation zone for calcium-mediated plateau potentials triggered by concurrent input to the L5 and L1 compartments. These calcium spikes can cause whole-cell depolarization, potentially allowing these cells to become more responsive to subsequent inputs to either compartment. This mechanism would allow paralemniscal inputs to upregulate L5 cells and thereby modulate the output of the cortical column. In this manner, the paralemniscal pathway may modulate the output of cortex with information specifically about externally-generated touch during active touch. This mechanism would allow the perception of a mismatch between the expected input (generated by active touch alone), compared with the actual input that combines both active touch and exogenous movement.

In the context of established trigeminal circuit organization, the present finding that SpVi encodes both direction and speed of an external stimulus predicts the following: during passive touch, when a rat is not whisking and encounters movement across the whisker array, information from SpVi is not allowed through the paralemniscal pathway (through PoM) to cortex. Passive tactile information is sent through the lemniscal pathway, from PrV to VPM to primary somatosensory cortex. At the same time SpVi sends

passive touch information through short-latency circuits to spinal/hindbrain/midbrain centers, allowing orienting behaviors.

In contrast, when a rat is actively whisking and encounters movement within the whisker array, the information is processed not only though the lemniscal and short-latency reflex systems, but is also processed in parallel by the paralemniscal pathway through PoM to cortex, where it may upregulate the output of L5 pyramidal cells, allowing the rat to disambiguate the sensation of touch due to internally vs. externally generated movement. SpVi may therefore allow the rat to more clearly perceive the sensory stimuli generated by moving external objects, even during active touch.

Chapter 7: Three-dimensional facial features and vibrissal morphology of the mouse: a comparison to with the rat and seal

A version of this chapter is in preparation for submission to Current Biology as: Bresee CS*, Belli HM*, Hartmann MJZ (2018) "Three-dimensional facial features and vibrissal morphology of the mouse: a comparison to with the rat and seal"

*authors contributed equally

7.1. Abstract

The mouse is a ubiquitous model system in both translational and basic neuroscience. Therefore, quantitatively modeling the anatomy of mouse whiskers and other cranial sensory structures has potentially great value to experimentalists. Additionally, using anatomical characterization techniques already established in other species allows cross-species comparisons that can illuminate trends that may hold true for whisker-based active touch in general. We generated equations describing the orientation, length, and curvature of each whisker using the three-dimensional locations of the whisker basepoints as fundamental parameters. We then compared these models to equivalent models in the rat and seal. For the mouse, whisker length decreases exponentially caudal-to-rostral, and an upper bound constrains curvature. The azimuthal resting angle of the whiskers varies rostro-caudally, and the resting elevation varies dorso-ventrally. The rat and mouse are, unsurprisingly, more similar to each other than they are to the seal. The mouse appears to be almost a scaled-down rat, in terms of the angular distance between facial features. However, the two species vary in terms of the proportional Euclidian distance between facial features, with rats having proportionately more oblong faces. This difference raises the possibility that because mice and rats occupy similar niches, the angular distances between sensory structures might be selected for, allowing a particular cross-modal spatial integration that may be advantageous, while other aspects of face shape may vary for other reasons (feeding, sexual selection, etc.). Finally, Elevation angle varies only dorso-ventrally for all three species, which is a striking commonality across such distantly related clades. This

may be because this is the plane of whisking for the rodents, and roughly the plane of forward movement through the water for the seal. This consistency in elevation may facilitate comparisons across columns while moving whiskers through space.

7.2. Introduction

Whiskers are a prominent facial feature of nearly all mammals, ranging from seals and sea lions to rodents. Previous studies have quantified the whiskers and whisker arrays of the rat, as well as the harbor seal (Graff, Belli et al. (in preparation), Brecht, Preilowski et al. 1997, Towal, Quist et al. 2011, Ginter, DeWitt et al. 2012, Belli, Bresee et al. 2018). These species use their whiskers for very different purposes. Both rats and mice are small terrestrial burrowing crepuscular omnivores. Mice lean slightly more towards insectivory than rats, though both species occupy a niche that relies on quick reproduction and quantity rather than quality of offspring to maintain their populations, mice emphasize this strategy slightly more than rats, and rats are an occasional predator of mice (Yoshimura and Ueki 1981, Berry and Bronson 1992, Shiels, Flores et al. 2012, Feng and Himsworth 2013). In contrast, seals are large semi-aquatic diurnal predators with much slower reproduction rates and longer generation times (Burns 2009).

Given this similarity in niche between mice and rats, and their differences with seals, one might expect vast differences in sensory capabilities. To a certain extent this is true, though surprising similarities also exist. Rats and mice move their whiskers back and forth at frequencies between 5-25 Hz (Berg and Kleinfeld 2003) and can use their whiskers to determine the size, location, and texture of objects (Carvell and Simons 1990, Carvell and Simons 1995) (Grant, Mitchinson et al. 2009) (Krupa, Matell et al. 2001) (Mehta S. B., Whitmer D. et al. 2007, Pammer, O'Connor et al. 2013) (Vincent 1912, Vincent 1913). Although seals don’t actively whisk, it has been shown that they too can discriminate objects through direct whisker contact, similarly to the rat and mouse. Seals also use their whiskers underwater during predation, to sense water flow and/or turbulence during wake tracking (Dehnhardt and Kaminski 1995).

Similarly, rats can use their whiskers to track airflow in order to facilitate finding an escape from an arena (Yu, Graff et al. 2016).

Due perhaps to the differences in niches between the two rodents and the seal one may expect the arrangement and morphology of vibrissal arrays of the rat and harbor seal to be different, and those of the rat and mouse to be similar. However, the similarities in sensory capability across all three species might predict that there are similarities in morphology. In the present work, we provide the first detailed quantification of the whisker array morphology of the mouse using normalized parameters established in Belli 2018. We then compare the quantification of the mouse vibrissal array in the present work to the whisker arrays of the rat and seal presented in Belli and Bresee 2018 and Graff et al. in prep. We discuss implications for evolution (e.g. is a rat a scaled-up mouse or the mouse a scaled-down rat?), as well as theories regarding the neuroethology of whisker orientation to species-specific behavior, especially with regard to active sensing.

7.3. Methods

The Animal Care and Use Committee of Northwestern University approved of all procedures in advance.

7.3.1. Data collection

A total of 467 macrovibrissae whiskers from eight mice were collected for the present work. All animals were male C57BL/6J mice between the ages of 6 and 8 weeks.

7.3.1.1. Surgery and anesthesia

Animals were anesthetized with a mixture of ketamine/xylazine/acepromazine injected intraperitoneally (100 mg/kg ketamine hydrochloride, 10 mg/kg xylazine hydrochloride, and 3 mg/kg acepromazine maleate in a saline vehicle). The toe pinch withdraw reflex was assessed every fifteen minutes and booster doses of

anesthetic were administered as needed to maintain a deep plane of anesthesia. The animal was supported on a heating pad and secured in a stereotaxic apparatus with bite block and ear bars. Next, to ensure that no vibrissae touched any surface, we performed a surgery to allow head fixation without the bite block and ear bars. An incision was made along the scalp midline, and three skull screws were inserted to form a triangle, with one screw in each temporal bone, and one screw in the frontal bone. A bridge of dental acrylic (methyl methacrylate) was then built between the arm of the stereotaxic unit and the skull screws. Care was taken to leave the skull landmarks lambda and bregma exposed (Paxinos and Watson, 1985). The ear bars and bite block were removed after the acrylic cured, ensuring that no object touched any part of the animal's face or vibrissae.

7.3.1.2. Microscribe™ data acquisition

The Microscribe consists of a passively movable five degree-of-freedom mechanical arm with a probe of known length on the tip. A user manipulates the arm to place the probe tip at a particular position. The device reports (x, y, z) coordinates of this spatial location relative to a previously defined origin, (0,0,0). The default tip for the Microscribe is a steel cone measuring 24.5mm in length x 5.0mm in diameter, with a slope of 0.5. Manufacturer listed precision for this tip is 0.13mm and mean accuracy is 0.23mm. This tip was too thick to maneuver easily between whiskers, so we created a custom tip consisting of a pin vice (Starrett; 75.0mm in length x 5.0mm in diameter) and a probe. The pin vice was machined to thread into the Microscribe™ and held the probe, which was a 0.5mm by 25mm tungsten concentric bipolar electrode (FHC). 15mm of the electrode extended from the pin vice. We followed manufacturer's instructions to re-calibrate the custom tip before collecting data from each animal.

The experimenter held the Microscribe™ and sequentially placed it at a series of points on each of the anatomical structures of interest. The 3D coordinates (x, y, z) at the position of the Microscribe™ tip were recorded by pressing a trigger button. We digitized multiple facial features for each of the eight mice,

including the skull features lambda and bregma, points corresponding to the corners and contours of the nostrils, eyes, mouth, rostrum, incisors, and pinnae, the basepoint of each whisker, and 4 – 6 points along each whisker.

7.3.1.3. Error assessment

We defined an origin for the Microscribe™ by making a small divot in a piece of laboratory labeling tape on the operating table near the animal. At the start of each experiment we calibrated the Microscribe™ by sampling this origin from five different orientations. The mean resolution over all scans and experiments was 0.5mm. This error estimate includes any slight eccentricities of the tip, any deviation due to hand tremor of the user, and the intrinsic precision limitations of the device. Note also that the 0.5mm error does not compound along the length of the whisker because each point along the whisker is an independent observation for that whisker.

7.3.1.4. 2D whisker scanning

After data collection with the Microscribe™ was finished, animals were euthanized with an overdose of the ketamine-xylazine-acepromazine combination and subsequent decapitation. Whiskers from seven of the eight mice (mice 1-7) were cut at their base, using forceps and micro scissors, and stored for one or two days in folded rectangles of aluminum foil. The whiskers were then scanned on a flatbed scanner (Epson Perfection 4180 Photo) at a resolution of 2,400 dpi (10.6μm per pixel), along with a ruler for calibration (1mm resolution). Whiskers from the eighth mouse were accidentally lost.

7.3.2. Definition and quantification of whisker morphological parameters

Whisker array morphology was quantified using a total of eight parameters. The arc length (S) and the intrinsic curvature coefficient (A) describe 2D whisker geometry. The 3D coordinates of the whisker

basepoints are denoted as r_{bp}, θ_{bp}, and φ_{bp}, and the orientation at which the whiskers emerge from the pad are described by the three angles θ_w, φ_w, ζ_w.

7.3.2.1. Quantifying whisker arc length and the intrinsic curvature coefficient

The 2D images of whiskers from seven mice (mice 1-7) were imported into Matlab™ to measure their arc length (*S*) and curvature coefficient (*A*). To measure 2D arc length (*S*), from scanned whisker images, an experimenter manually clicked on the base and tip of the whisker. Image processing code located the next darkest pixel closest to the base, and continued this process to the whisker tip. Whisker arc length was then calculated by summing the lengths of the segments between points. Measurement error was estimated as two pixels on each end of the whisker, or ~ 10.6μm per pixel x 2 pixels per endpoint x 2 endpoints = ~42.4μm.

Previous studies in rats have shown that the 2D shape of a whisker can be approximated by the parabola $y = Ax^2$ (Knutsen et al. 2008; Towal et al. 2011). The coefficient *A* is called the "intrinsic curvature coefficient," or simply "curvature coefficient." As will be shown in Results (Figure 7.3), we found that a quadratic fit was also a good approximation for whisker curvature in mice.

We determined the value for *A* following the steps described in a previous study (Belli et al., 2018). The whisker was first oriented concave up, with its basepoint at the origin (0,0) and initial portion of the whisker aligned with the x-axis such that the majority of the whisker lay in the first quadrant. Because previous studies have indicated that only the proximal ~65% of the whisker remains planar, the arc length of the whisker was truncated to 65%.

To determine what fraction of this truncated whisker to align with the x-axis we performed an optimization routine that minimized the difference between the smoothed traced whisker and the curve fit $y = Ax^2$. The

optimization iteratively aligned between 1% and 30% of the whisker's proximal arc length with the x-axis. At each alignment, the curve y = y = Ax^2 was fit to the smoothed, truncated whisker. We calculated the mean squared error (MSE) between the curve fit and the actual whisker trace at each of the alignments. On average across all whiskers, the MSE was found to be smallest when a point 8% from the base along the truncated whisker was used to align the whisker with the x-axis. Therefore, the *A* coefficient for each whisker was determined from a curve fit in which the whisker's proximal 8% was aligned with the x-axis.

7.3.2.2. Choice of coordinate system

Establishing the reference frame in which to define the whisker pad parameters (r_{bp}, θ_{bp}, φ_{bp}, θ_w, φ_w, ζ_w) required us to first choose an origin and horizontal plane in which to orient the mouse's head.

As in our most recent description of the morphology of the rat whisker array and facial structures (Belli et al., 2018), the origin was chosen to be the mean position of all whisker basepoint locations on both left and right sides of the array. This choice placed the origin near the center of the muzzle, inside the animal's head (Figure 7.1A). Note that this procedure required "matched" basepoints between right and left sides, so if a particular whisker identity was present on only one side it was omitted from the calculation of the origin.

Again, following the approach used in previous studies (Towal et al., 2011, Belli et al., in revision), we defined the "average whisker row plane" as the horizontal (x-y) plane. A plane was fit to the basepoints of each of the five whisker rows using least squares, and the mean of these five planes defined the average whisker row plane (Figure 7.1B).

With the x-y plane established as the average row plane, the x-axis was defined as the line connecting the centroids of the left and right arrays with the left side of the animal negative. The y-axis was defined to be

orthogonal to the x-axis, with the positive y-axis pointing rostrally. Lastly, the axis perpendicular to the x-y plane is the z-axis. (Figure 7.1C)

7.3.2.3. Quantifying 3D coordinates of the whisker basepoints

Having chosen an origin and horizontal plane, the 3D coordinates of all recorded points on the animal's head, including the whisker basepoints, could be determined.

Previous studies have defined the position and orientation of the whiskers using a standard spherical coordinate system (Towal, Quist et al. 2011). This standard coordinate system is mathematically amenable to running simulations (Hobbs, Towal et al. 2015, Hobbs, Towal et al. 2016, Hobbs, Towal et al. 2016, Yang and Hartmann 2016, Zhuang, Kubilius et al. 2017), but has the disadvantage that corresponding right and left whiskers have completely different coordinates. In other words, a conventional head-centered spherical coordinate system neglects the bilateral symmetry of the head. We therefore chose to use a more intuitive coordinate system that mirrors the left array across the midline. All equations and figures in the present work are defined in terms of right-sided whisker arrays. These "array-centered" axis conventions apply equally well to both sides of the head, with the caveat that the coordinates on the left side of the animal no longer follow the right-hand rule.

The three basepoint coordinates (r_{bp}, θ_{bp}, φ_{bp}) are illustrated in Figure 7.1D. The radius (r_{bp}) is defined as the straight-line distance between the basepoint and the origin, and is closely related to the size of the mouse's mystacial pads. The coordinate θ_{bp} describes the rostro-caudal location of the whisker basepoint along the positive x-axis. If the whisker is rostral [caudal] to the x-z coronal plane, it has a positive [negative] value of θ_{bp}. The dorsoventral location of the basepoints with respect to the x-y horizontal plane is described by the coordinate φ_{bp}. If the basepoint location is dorsal [ventral] to this horizontal plane it has a positive [negative] value of φ_{bp}.

7.3.2.4. Quantifying the 3D angles at which the whiskers emerge from the face

The "angles of emergence" describe the orientation of the whiskers as they emerge from the mystacial pad at their basepoint locations. In the present work, the angles are defined as Euler angles applicable to the right array.

The angles θ_w and φ_w both describe the orientation of the approximately linear potion of the whisker, near its base; neither of these angles depends on the intrinsic curvature of the whisker. As shown in Figure 7.1E, the angle θ_w is the angle of emergence in the horizontal plane, and ranges between 0° (whisker points caudally) and 180° (whisker points rostrally). Values of θ_w greater than 180° indicate that the whisker points across the rostro-caudal midline of the animal. The angle φ_w describes the elevation of the whisker (Figure 7.1F). Values range between ±90°, with 90° indicating that the whisker points dorsally and -90° ventrally.

Because each whisker has an intrinsic curvature, a third angle, ζ_w, is required to describe the roll about the whiskers' own axis, as illustrated in Figure 7.1G. If the whisker is oriented concave forward, it has an angle of ζ_w = 90°, while concave backwards is ζ_w = -90°, and concave dorsal and ventral are 180° and 0°, respectively (Figure 7.1G).

As indicated earlier, the angles of emergence are defined only for whiskers of the right array. All left side whisker arrays were mirrored across the y-z plane, and figures and equations in the present work are presented in terms of right-sided whisker arrays.

To find the angles of emergence, we performed an optimization using the built-in Matlab™ function "fminsearch." The optimization parameters were θ_w, φ_w, ζ_w, as well as S and A. Starting with the whisker point cloud in standard position and orientation, we sorted the individual points within the cloud by

distance from the basepoint. The x, y, z coordinates of all points were smoothed with a moving average filter (window size of five points), and the whisker was then resampled into 500μm segments and its base translated to the origin. The routine next varied θ_w, φ_w, ζ_w, S, and A to fit an idealized whisker model to the point cloud. The model whisker began with its base at the origin, and its proximal portion aligned along the negative y-axis. The model was initially oriented concave down. To match the idealized model with the whisker point cloud, we performed an Euler rotation sequence in the order y-axis (roll, ζ_w), x-axis (pitch, φ_w), z-axis (yaw, θ_w). These rotations were extrinsic about the global y-x-z axes. The parameters S and A were also varied to best match the idealized model to the point cloud. The optimization minimized the mean sum squared distance between the whisker point cloud and the points in the idealized whisker model.

Figure 7.1: Whisker basepoint coordinates and angles of emergence. Panels A-D describe whisker basepoint coordinates, while subplots E-G describe whisker emergence angles. **(A)** The green dot shows the origin, i.e., the average of all left and right whisker basepoint locations. The origin is not on the snout surface, but rather in the bilateral center of the array. **(B)** The average whisker row plane (the mean of the five planes fit individually to each of the five whisker rows A-E) defines the horizontal plane. **(C)** Axis conventions in the context of the head. The positive x-axis points through the centroid of the right array, the positive y-axis points rostrally, and the positive-z axis points dorsally. **(D)** Whisker basepoints are described in spherical coordinates as radius (r_{bp}), azimuth angle (θ_{bp}), and elevation angle (φ_{bp}). The angle θ_{bp} lies in the x-y plane, and θ_{bp} = 0° lies along the intersection of the x-y and x-z planes. θ_{bp} = -90° lies caudal to the coronal plane and θ_{bp} = +90° lies rostral. Similarly, the angle φ_{bp} lies within the y-z plane and φ_{bp} = 0° lies along the intersection of the x-z and x-y planes. φ_{bp} = -90° lies ventral to the horizontal plane and φ_{bp} = +90° lies dorsal. **(E)** A top-down view of the mouse's face, illustrates the coordinate system for θ_w. The dashed line represents the vector aligned with the proximal region of the whisker that is approximately linear. The angle θ_w describes the rostral/caudal angle at which the whisker emerges from the mouse's cheek. Values range from 0° to 360°, with θ_w = 0° lying along the negative y-axis. The value of θ_w is independent of the whisker's intrinsic curvature. **(F)** A front-on view of the mouse's face, illustrates the coordinate system for φ_w. The angle φ_w describes the dorsal-ventral angle at which the proximal portion of the whisker emerges from the mouse's cheek. Values range from -90° to 90°, where φ_w = 0° lies along the positive x-axis. The value of φ_w is independent of the whisker's intrinsic curvature of the whisker. **(G)** The angle ζ_w defines the orientation of the whisker about its own axis. Solid and dashed lines represent extreme positions of the whisker in the front and top views. Although ζ_w is formally calculated as a rotation about the y-axis (which points rostral-caudal), this panel illustrates ζ_w for the case that θ_w = 90° and φ_w = 0° in order to show the whisker in a more natural position. ζ_w = 0° points concave down, ζ_w = 180° concave up, ζ_w = 90° concave forward, and ζ_w = -90° concave back.

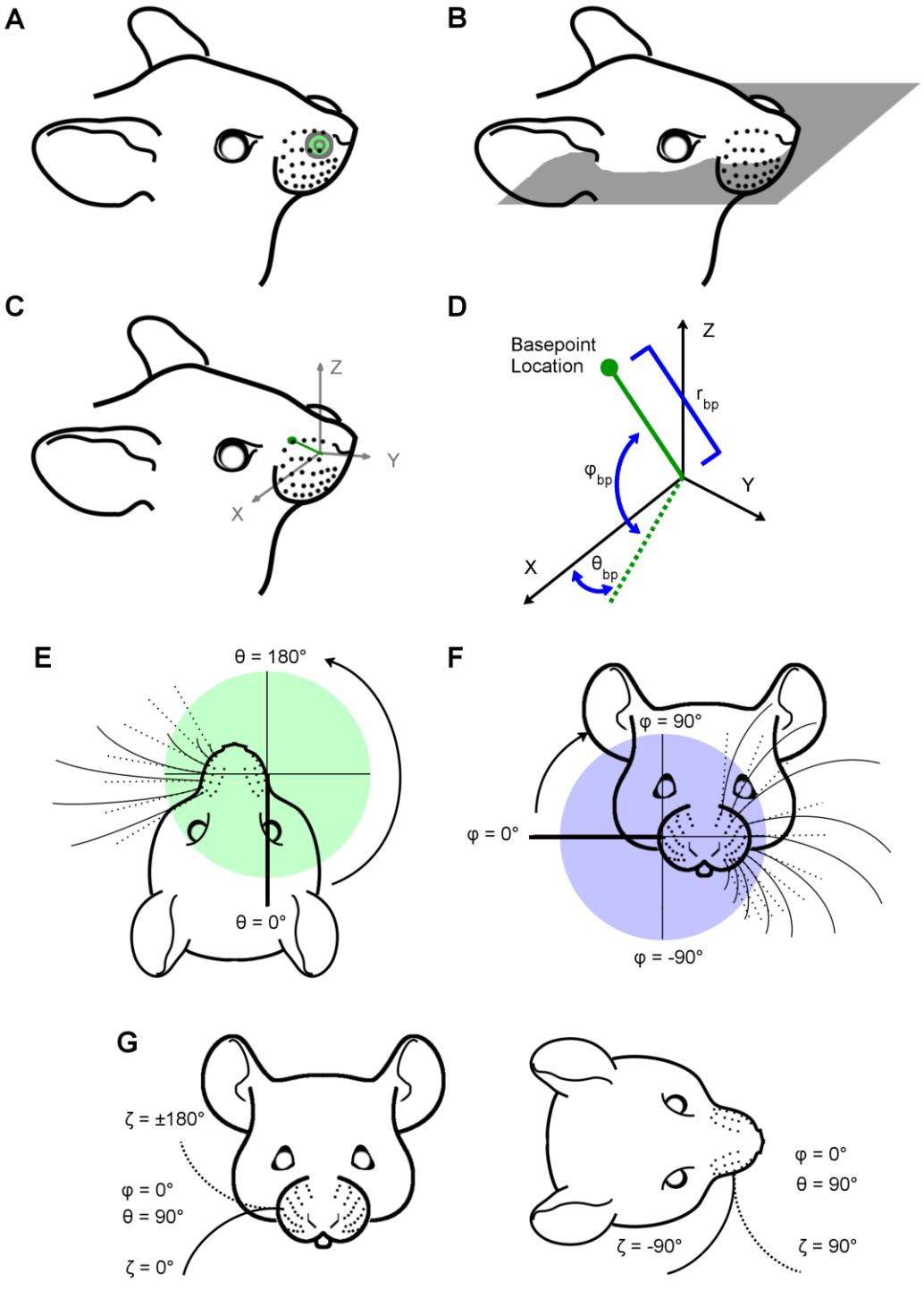
A
B
C
Z
Y
X
D
Basepoint
Location
Z
r_{bp}
φ_{bp}
Y
X
θ_{bp}
E
θ = 180°
θ = 0°
F
φ = 90°
φ = 0°
φ = -90°
G
ζ = ±180°
φ = 0°
θ = 90°
ζ = 0°
φ = 0°
θ = 90°
ζ = -90°
ζ = 90°

7.4. Statistical Analysis of morphological parameters

7.4.1. Intrinsic curvature and arc length and as functions of θ_{bp} and φ_{bp}

A total of 357 unique 2D scanned images of whiskers were obtained from seven of the eight mice. Values of whisker arc length were obtained from all 357 scans and values of the intrinsic curvature coefficient were obtained for 324 of the scans. To identify outliers, the mean and standard deviation were calculated for whiskers grouped by their row and column identity. We eliminated whiskers greater than two standard deviations above or below the mean. Out of the dataset of 357 scans, 14 outliers (3.92%) for arc length (S) were removed yielding a total of 343 whiskers. Out of the dataset of 324 scans for curvature coefficient, 12 outliers (3.70%)were eliminated yielding a total of 312 whiskers for analysis.

We constructed models for S and A as functions of θ_{bp} and φ_{bp}. To avoid overfitting, models were not fit directly to the entire dataset for each parameter. Instead, the best fit model was found for each mouse individually. We used the following methods to select the best fit models:

First, we divided each dataset for S and A with outliers removed into seven subgroups by mouse identity. For each of the seven mice, histograms of S and A were found to not be quite normally distributed. We therefore analyzed the data both with and without applying log-transformations to the S and A coefficients to improve normality.

Second, linear regression models were then constructed for each mouse using both the original non-transformed and the log-transformed data. We tested whether S and A were univariately associated with θ_{bp} and/or φ_{bp}, for both original and log transformed data. Specifically, we tested the null hypothesis that the regression coefficients for θ_{bp} and/or φ_{bp} were equal to zero. If the p-value for the independent variable coefficients was less than or equal to 0.05, we rejected the null hypothesis and a second order model (square of θ_{bp} and/or square of φ_{bp}) was fit. The hypothesis that the regression coefficients for these higher

order terms were equal to zero was then tested. For each quadratic order coefficient in the model, if the p-value was greater than 0.05, the model remained first order. We did not find any models for whiskers from an individual mouse to have independent variable predictors greater than second-order.

Third, if both basepoint parameters (θ_{bp} and φ_{bp}) were univariately associated to either first or second order with either the original data or log-transformed *A* or *S*, both parameters were included in a multivariable linear regression model for each individual mouse. The method of "forward selection" was again used to introduce the terms as first linear predictors. We tested the hypothesis that the regression coefficients for θ_{bp} or φ_{bp} were equal to zero. If the p-value for the independent variable coefficients was less than or equal to 0.05, a second order model (square of θ_{bp} and/or square of φ_{bp}) was fit and we again tested the hypothesis that the regression coefficients for these higher order terms were equal to zero. We also considered the Akaike Information Criterion (AIC) as an additional metric to avoid overfitting. The higher order model was selected only if the AIC for that model was more than two points lower than the lower order model, and the independent variable coefficients were significant.

We then compared the best fit simple or multivariable linear regression models across all seven mice, for the original data and log-transformed *A* or *S*. An overall model, based on data from all mice together, was fit only after considering the results of the models fit to each individual mouse. A parameter (i.e., θ_{bp}, φ_{bp}, or their squares) was included in the overall model only if it had first appeared as a significant predictor in at least six of the seven individual mouse models. Each of these parameters was then retained or discarded in the overall model using the same forward selection methods described for the individual models. To avoid overfitting, the order of the combined model was not allowed to exceed the highest order of six out of seven of the individual mouse models.

7.4.2. Angles of emergence (θ_w, φ_w, and ζ_w) and basepoint radius (r_{bp}) as functions of θ_{bp} and φ_{bp}

A total of 461 3D basepoint coordinates (r_{bp} θ_{bp} φ_{bp}) and 3D angles of emergence (θ_w, φ_w, ζ_w), were obtained from the eight mice. To identify outliers for each parameter, the mean and standard deviation were calculated for whiskers grouped by their row and column identity. As before, the value of a given parameter for a particular whisker was eliminated if it was greater than two standard deviations above or below the mean.

Out of the dataset of 461 whiskers, 21 outliers (4.56%) were removed for r_{bp}, 14 outliers (3.04%) were removed for θ_{bp}, 19 outliers (4.12%) were removed for φ_{bp}, 19 outliers (4.12%) were removed for θ_w, 16 outliers (3.47%) were removed for φ_w, and 13 outliers (2.82%) were removed for ζ_w. Thus, after outlier removal, 440 values remained for r_{bp}, 447 values remained for θ_{bp}, 442 values remained for and φ_{bp} and θ_w, 445 values remained for φ_w, and 448 values remained for ζ_w.

We next constructed models for r_{bp} θ_w, φ_w, and ζ_w as functions of θ_{bp} and φ_{bp}. To avoid overfitting, the best fit model for the parameters r_{bp}, θ_w, φ_w, and ζ_w, was found for each of the eight mice individually. We first determined that that the parameters r_{bp}, θ_w, φ_w, and ζ_w were all normally distributed for each of the eight mice. Therefore, a log-transformation was not necessary and linear regression models were then constructed for each mouse as follows.

First, for each mouse, we tested whether r_{bp}, θ_w, φ_w, and ζ_w were univariately associated with θ_{bp} and/or φ_{bp} using the forward selection procedure described previously. We did not find any models for whiskers from an individual mouse to have statistically significant independent variable predictors greater than second-order.

Second, if both basepoint parameters (θ_{bp} and φ_{bp}) were univariately associated to either first or second order with r_{bp}, θ_w, φ_w, and ζ_w, then both parameters were included in a multivariable linear regression model for each individual mouse. Again, linear predictors were added to the models using the method of "forward selection." We tested the hypothesis that the regression coefficients for θ_{bp} and/or φ_{bp} were equal to zero. If the p-value for the independent variable coefficients was less than or equal to 0.05, a second order model (square of θ_{bp} and/or square of φ_{bp}) was fit and we retested the hypothesis that the regression coefficients for these higher order terms was equal to zero. We also considered the Akaike Information Criterion (AIC) to avoid overfitting. The higher order model was selected only if both the independent variable coefficients were significant and the AIC for the higher order model was more than two points lower than the lower order model.

Finally, for each parameter (r_{bp}, θ_w, φ_w, and ζ_w), the best fit univariate or multivariable function of θ_{bp} and/or φ_{bp} was compared across all eight mice. An overall model, based on data from all mice together, was fit only after taking into account the results of the models fit to each individual mouse. This overall model was fit similarly to the individual models, except that a parameter was included in the final combined model only if it had first appeared as a significant predictor in at least six of the eight individual mouse models. If a parameter met this criterion it was initially included in the model, and retained or discarded using the same forward selection methods described for the individual models. For ζ_w in particular we also fit individual models by each row, using the same general method of forward selection while avoiding over-fitting.

7.5. Mouse skull and facial feature quantification

7.5.1. Positioning skull and facial features in standard orientation

The (x, y, z) coordinates of the skull and facial features collected using the Microscribe™ were imported into Matlab™. These coordinates were then rotated and translated to match the axis conventions shown in Figure 7.1.

7.5.2. Defining the bregma-lambda plane

Bregma is located at the intersection of the sagittal and coronal sutures, while lambda is demarcated by the intersection of the sagittal and lambdoid skull sutures. In the mouse, the lambdoid suture exhibits a characteristic rostral deviation from the coronal plane as it intersects the sagittal suture, forming a rostral-pointing triangle with an open caudal side. We recorded the 3D coordinates of bregma and the 3D coordinates of the visually-estimated centroid of the lambdoid triangle.

We then calculated the 3D distance between the points for bregma and lambda. The angular offset between the bregma-lambda line and the average row plane was found by dividing the height difference between bregma and lambda by the 3D distance between bregma and lambda (hypotenuse). The inverse sine of this ratio yields the angle between the bregma-lambda line and the average row plane.

7.5.3. Digitization of lateral semicircular canal orientation

The data used for the lateral canal coordinates came from serial CT scans of Mus musculus skull, specimen TMM M-3196, available through the digital morphology database DigiMorph.org (ref). The specimen was originally scanned along the coronal axis, for a total of 480 slices. Each 1024 x 1024 pixel slice is 0.02961mm thick, with 0.02961mm interslice spacing and a field of reconstruction of 28mm. These images result in a resolution of 0.02734mm in x and y (within each coronal plane slice) and an interslice resolution of 0.02961mm in z.

We used Reconstruct™ to record the 3D coordinates of the bony labyrinth and other skull features in serial coronal CT images. Structures traced included the entire left and right bony labyrinths, the left and right external auditory meatuses, the lambdoid, sagittal, and coronal sutures, and the lateral corners of the left and right upper incisors. Data were imported into Matlab™ and we manually identified the (x, y, z) coordinates of the following skull features: (1) bregma and lambda; (2) the locations at which each of the two lateral canals terminated in a crista; (3) the lateral-most point of each of the two lateral canals; (4) five distinct points around the circumference of each auditory meatus; (5) the lateral corners of the incisors.

Points from the CT scan data were brought into the same reference frame as the Microscribe™ data by aligning a subset of corresponding points between the two datasets. These points included bregma, lambda, and the corners of the incisors. We found the translations and rotations that brought these points into register, and then applied these same translations and rotations to the points for all other features.

We found the angle between the semicircular canal plane and the average whisker row plane. To do this, the Matlab™ function affine_fit (Sun 2016) was fit to the left and right lateral semicircular canals. This Matlab function finds the plane of best fit to a set of points based on the least squares of the normal distance of the set of points to the plane. The angle between the horizontal canal plane and the average row plane was then calculated as the arccosine of the dot product of the normal vectors of the two planes.

7.6. Results

The first three sections of Results describe the morphology of the mouse, and the last three sections compare the morphology of the mouse with two other species, the rat and the harbor seal. As described in Methods, all models were obtained using linear regression, avoiding overfitting by selecting the model that had the least dispersion about the identity line for observed values plotted against predicted values.

7.6.1. Relationship between basepoint coordinates and row and column identity in the mouse

We began by quantifying the basepoint coordinates (θ_{bp}, φ_{bp}, r_{bp}) for each whisker, identified by its row and column position. These data are reported in the Appendix, as Table A.2. As expected, θ_{bp} was closely linearly related to column identity (Col) and φ_{bp} was linearly related to row identity (*Row*):

$$\theta_{bp} = 11.688\ Col - 41.244,\ \text{Adj. } R^2 = 0.844 \qquad \text{(eq. 7.1)}$$

$$\varphi_{bp} = -16.785\ Row + 56.294,\ \text{Adj. } R^2 = 0.920 \qquad \text{(eq. 7.2)}$$

In Equations 7.1 and 7.2, *Col* varies from 1 to 7, *Row* varies from 1 to 5, and θ_{bp} and φ_{bp} have units of degrees. Note that the whiskers in Column 1 are traditionally termed the "Greek arc." Numbering the columns starting with 1 is untraditional, but follows the nomenclature introduced in Belli et al., 2018. This numbering choice accommodates comparisons with species that do not have an easily identifiable Greek arc.

Equation 7.1 indicates that θ_{bp} increases with column number, from caudal to rostral across the mystacial pad, while Equation 7.2 indicates that φ_{bp} decreases with row number, from dorsal to ventral. These relationships are easily seen when θ_{bp} and φ_{bp} are plotted as functions of column and row identity (Figure 7.2A), and the quality of the equation fits are presented in Figure 7.2B. Figure 7.2C visualizes the strong relationship between θ_{bp} and column, and between φ_{bp} and row, across all whiskers of the array.

A third coordinate, r_{bp}, is needed to fully describe basepoints in spherical coordinates. We first found r_{bp} as a function of row and column position:

$$r_{bp} = -0.2127Col + 0.37195Row + 3.9652,\ \text{Adj. } R^2 = 0.612 \qquad \text{(eq. 7.3)}$$

r_{bp} is more variable than θ_{bp} or φ_{bp}, reflected by the lower R^2. This variability is partially due to head size differences across individual mice.

Because one goal of this model is to describe the array independently of rows and columns, we next looked at the relationship between r_{bp} and the basepoint parameters θ_{bp} and φ_{bp}. As plotted in Figure 7.2D, r_{bp} was found to be linearly related to both variables:

$$r_{bp} = -0.015159\ \theta_{bp} - 0.016497\ \varphi_{bp} + 4.4388,\ \text{Adj. } R^2 = 0.551 \qquad \text{(eq. 7.3b)}$$

where θ_{bp} and φ_{bp} are in degrees and r_{bp} is in millimeters.

This new equation is qualitatively similar and quantitatively close to the equation predicting r_{bp} by row and column, as would be expected from the tight relationships between θ_{bp} and column, and φ_{bp} and row. Similarly to r_{bp} as a function of row and column, the variability is higher for r_{bp} than for θ_{bp} or φ_{bp}, as shown by the lower R^2 and the dispersion about the identity line in Figure 7.2E. Figure 7.2F illustrates the variation of r_{bp} across the array, and reveals the narrowing of the rat's snout rostrally and dorsally. Values for r_{bp} are lower in more rostral and dorsal regions of the array, indicating that left and right whisker basepoints are closer to the origin, and hence to each other, in these regions.

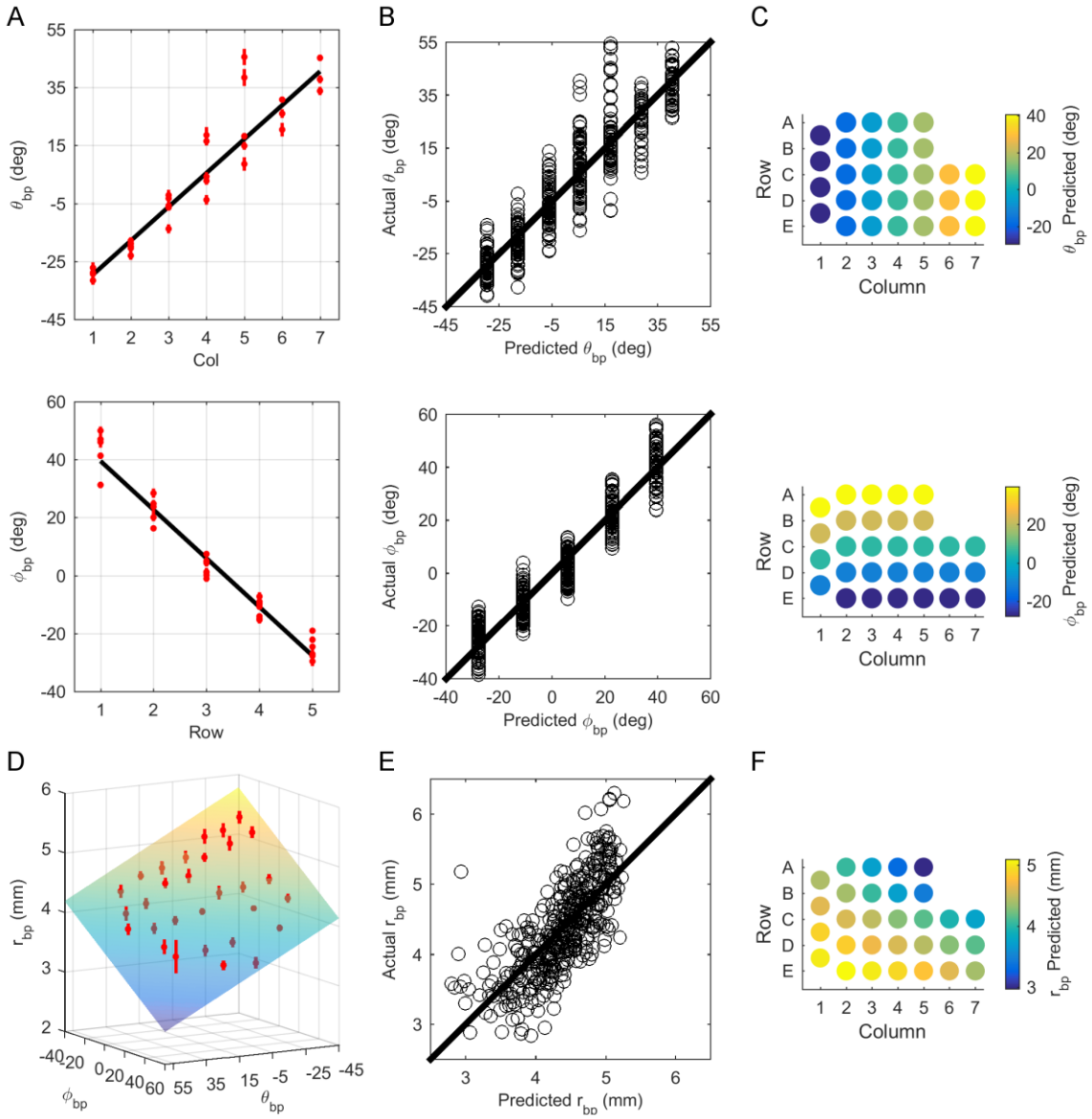

Figure 7.2: Relationships between basepoint coordinates and row and column position in the array. **(A)** The basepoint coordinate θ_{bp} increases linearly with column identity (Col), while the basepoint coordinate φ_{bp} decreases linearly as a function of *Row*. Red dots show mean values of each parameter when grouped by whisker row column identity, with the red bars representing standard error of the mean (SEM). Equations 7.1 and 7.2 are shown as black lines. **(B)** The quality of the fits for Equations 7.1 and 7.2 are shown in plots of actual vs. predicted values for θ_{bp} and φ_{bp}. **(C)** Equations 7.1 and 7.2 are used to visualize the variation of θ_{bp} and φ_{bp} across the mouse whisker array. **(D)** The basepoint coordinate r_{bp} is inversely correlated with both θ_{bp} and φ_{bp}. Equation 7.3b is shown as a plane. Red dots represent mean values of r_{bp} when grouped by whisker identity, and red bars show SEM. **(E)** A plot of actual vs. predicted values for r_{bp} reveals a higher variability fit (Adj R^2 = 0.551) than for θ_{bp} or φ_{bp}. **(F)** Equation 7.3b is used to estimate value for r_{bp} across the array. Consistent with visual intuitions for the shape of a mouse's snout, larger values of r_{bp} are found in caudal-ventral regions of the array, and smaller values in the rostral-dorsal regions.

7.6.2. Two-dimensional shape: arc length and curvature coefficient

The most basic description of two-dimensional (2D) whisker geometry includes the arc length (*S*) and the intrinsic curvature coefficient (*A*). We quantified these two parameters as functions of the basepoint coordinates θ_{bp} and φ_{bp}.

Arc length was best described as an exponential function of θ_{bp}:

$$S = e^{-0.018444\,\theta_{bp} + 2.4595}, Adj.R^2 = 0.671 \qquad \text{(eq. 7.4a)}$$

To provide a more intuitive sense for how whisker length will vary across the array, Equation 7.4a can be rewritten:

$$S = \frac{11.6990}{e^{0.018444\theta_{bp}}}, Adj.R^2 = 0.671 \qquad \text{(eq. 7.4b)}$$

In both equation 7.4a and 7.4b θ_{bp} is in degrees and *S* is in mm.

The negative coefficient in front of θ_{bp} in Equation 7.4a indicates that *S* decays exponentially from caudal to rostral, and this relationship is plotted in Figure 7.3A. This subplot also confirms the intuition provided by Equation 7.4b: whisker arc length is approximately ~11.7mm near the center of the array, where $\theta_{bp} = 0$, and changes exponentially from there. Experimental values for arc length vary between ~2 and ~30mm over the entire pad. The quality of the fit for Equations 7.4ab is shown in the plot of actual vs. predicted values for *S* (Figure 7.3B), while Figure 7.3C provides visual intuition for variations in *S* across the array. As expected, caudal whiskers have the largest arc lengths.

As described in Methods, whisker curvature was quantified using the 2D parameterization $y = Ax^2$. The curvature coefficient, A, was best described as a linear function of θ_{bp}:

$$A = 0.00036882\ \theta_{bp} + 0.016726,\ \text{Adj. } R^2 = 0.233 \qquad \text{(eq. 7.5)}$$

where θ_{bp} is in degrees and A is in 1/mm. Notice that both Equations 7.4ab and 7.5 depend only on θ_{bp}, indicating that 2D whisker geometry on the mouse is relatively invariant to variations in the ventral-dorsal direction (θ_{bp}).

The positive coefficient in front of θ_{bp} in Equation 7.5 indicates that A increases from caudal to rostral across the mouse whisker array, and this relationship is plotted in Figure 7.3D. However, due to the high variability in A for the rostral whiskers, the coefficient of determination is low ($R^2 = 0.233$).

Based on analogy with the rat (Belli et al., 2018), we investigated the relationship between curvature coefficient and arc length. Figure 7.3E illustrates this relationship, and highlights that our measurements for curvature are particularly variable for short whiskers. However, Figure 7.3E also reveals the presence of a strong upper bound on the relationship between A and S. The equation for this upper bound was found by performing a sliding window analysis, in which the maximum value for A was computed for arc lengths between 2 and 6mm, then 3 and 7mm, and so on up to the window S = 26 – 30mm. The best equation was fit to those 14 maximal points and found to be:

$$A = 0.2942\ e^{-0.2618S} + 0.01234, Adj.R^2 = 0.9938 \qquad \text{(eq. 7.6)}$$

In Equation 7.6, S has units of mm and A has units of 1/mm.

Equation 7.6 is visualized for whiskers across the array in Figure 7.3F and clearly shows that the upper bound on whisker curvature is higher in the rostral portions of the pad: shorter whiskers tend to be more curved than longer whiskers.

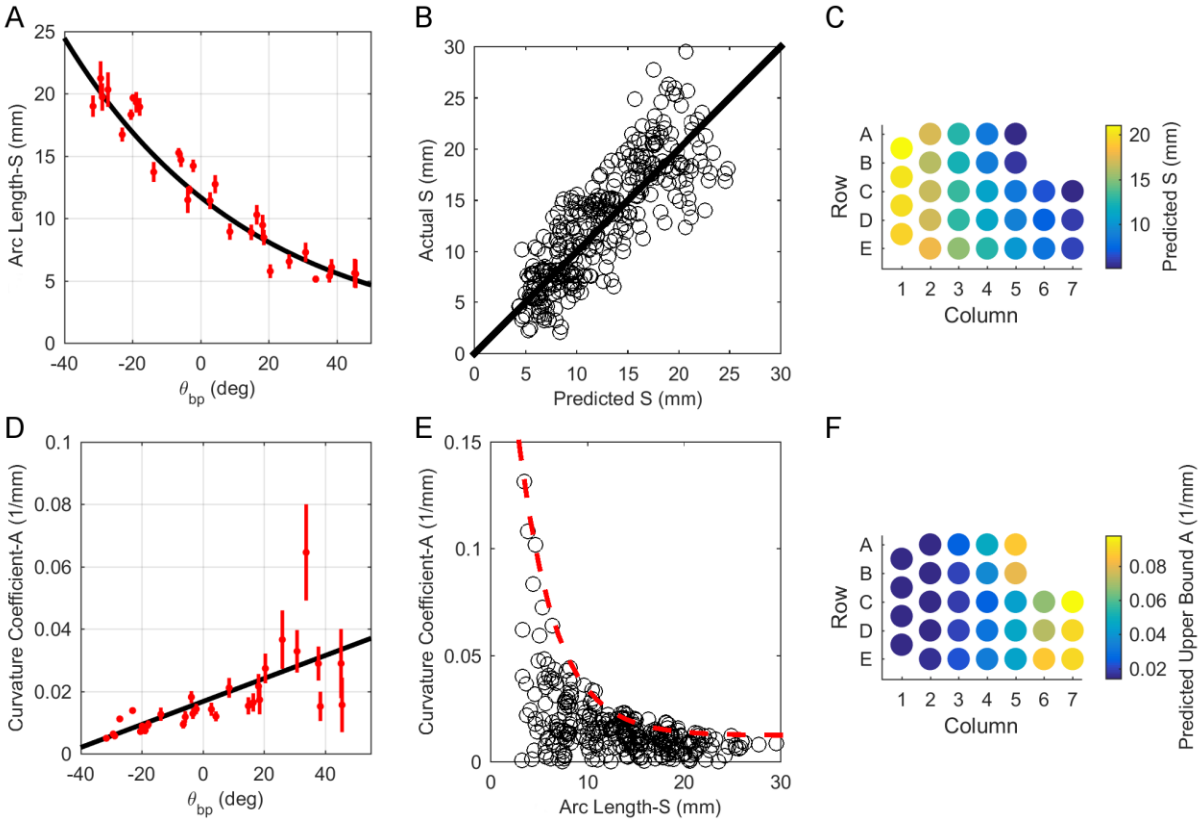

Figure 7.3: Relationship between 2D whisker geometry and basepoint coordinates. (A) Whisker arc length (*S*) can be described as a decaying exponential function of θ_{bp} from caudal to rostral across the array. The black line represents Equation 7.4ab. Means ± SEM when grouped by whisker identity are shown in red. **(B)** A plot of actual vs. predicted values shows the quality of the fit based on Equation 7.5. **(C)** Plotting Equation 7.4ab shows, unsurprisingly, that arc length decreases from rostral to caudal across the array. **(D)** The curvature coefficient, *A*, can be de described as a linearly increasing function of θ_{bp} from caudal to rostral across the array, but the quality of the fit is low because rostral whiskers have highly variable curvature. The black line represents Equation 7.5. Means ± SEM when grouped by whisker identity are shown in red. **(E)** When *A* is plotted as a function of *S*, the shorter whiskers are clearly seen to have more variable curvature than longer whiskers. This relationship is bounded by the curve given by Equation 7.6 (red dashed line). **(F)** When grouped by whisker identity, the upper bound on curvature (Equation 7.6) is highest for the rostral whiskers.

7.6.3. Angles of emergence of the whiskers as a function of basepoint coordinates

The 3D angles of emergence (θ_w, φ_w, ζ_w) were quantified as functions of the basepoint coordinates θ_{bp} and φ_{bp}.

The azimuthal angle of emergence, θ_w, was best described as a linear function of θ_{bp}:

$$\theta_w = 1.0356\ \theta_{bp} + 82.548,\ \text{Adj. } R^2 = 0.544 \qquad \text{(eq. 7.7a)}$$

Although Equation 7.7a represents the best relationship we could find while avoiding overfitting, the adjusted R^2 is quite low (0.544). Moreover, the plot of actual vs. predicted values (Figure 7.4B) reveals moderately high dispersion about the identity line, highlighting significant limitations on the predictive value of Equation 7.7a.

However, when the A row was eliminated the fit improved dramatically, as indicated by a tighter actual vs predicted relationship (data not shown), and higher R^2. The equation for θ_w, omitting the A-row is qualitatively and quantitatively similar to the equation including the whole array:

$$\theta_w = 0.922\ \theta_{bp} + 85.1,\ \text{Adj. } R^2 = 0.739 \qquad \text{(eq. 7.7b)}$$

Figure 7.4C shows the prediction using Equation 7.7b plotted across the entire array. The colormap of θ_w values across the array confirms the visual intuition that more caudal whiskers emerge at an angle that points more caudally than the rostral whiskers.

The elevation angle, φ_w, was found to vary linearly only with φ_{bp}:

$$\varphi_w = 1.0002\ \varphi_{bp} + 10.241,\ \text{Adj. } R^2 = 0.76 \qquad \text{(eq. 7.8)}$$

In Equation 7.7a/b and 7.8 all variables have units of degrees.

The positive coefficients in Equation 7.7a/b and 7.8 indicate that θ_w increases from caudal to rostral across the array while φ_w increases from ventral to dorsal (from the E to the A row). These relationships are plotted in Figure 7.4A.

This relationship is shown in Figure 7.4D. The prediction given by Equation 7.8 reflects that we chose the best fitting model, as shown by the relative uniformity and low dispersion of actual vs. predicted values for φ_w about the identity line. Figure 7.4F shows the prediction for φ_w using Equation 7.8 when plotted by row and column identity and confirms the intuition that whiskers in more dorsal rows emerge at more elevated angles than whiskers in more ventral rows.

The angle ζ_w, describing the twist of the whisker about its own axis, was not found to be well-predicted by any predictor variables, as indicated by the high dispersion and asymmetry about the identity line in Figure 7.4E. Of the predictors tested ζ was best described as a linear function of φ_{bp}:

$$\zeta_w = 0.70632\ \varphi_{bp} + 36.097,\ \text{Adj. } R^2 = 0.134 \qquad \text{(eq. 7.9a)}$$

Figure 7.4G shows values for ζ_w grouped by whisker identity and plotted as a function of φ_{bp} (means ± standard errors) shown in red, with Equation 7.9a shown in black. Furthermore, this relationship only holds for whiskers with arc length (S) greater than or equal to 8mm. Whiskers shorter than this were excluded from this analysis due to size constraints forcing shorter whiskers to be traced by the MicroScribe using a small number of points, leaving very few points on the whisker that curve away from the more linear basal portion -- points which particularly influence the calculation of ζ_w.

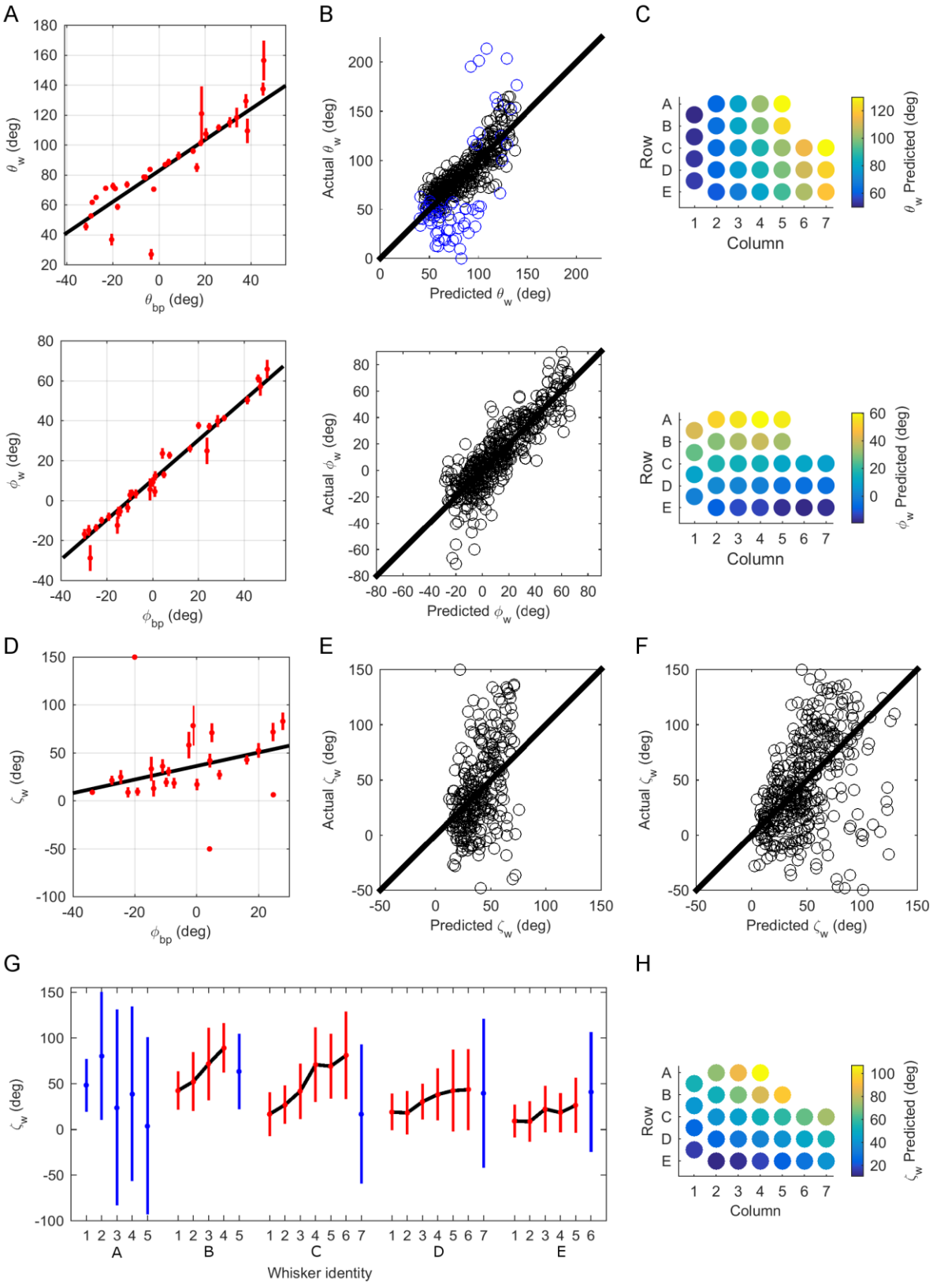
A
B
C
D
E
F
G
H
θ_w (deg)
θ_{bp} (deg)
Actual θ_w (deg)
Predicted θ_w (deg)
ϕ_w (deg)
ϕ_{bp} (deg)
Actual ϕ_w (deg)
Predicted ϕ_w (deg)
ζ_w (deg)
Actual ζ_w (deg)
Predicted ζ_w (deg)
Row
Column
Whisker identity

Figure 7.4: Relationship between whisker angles of emergence and basepoint coordinates. (A) The azimuthal emergence angle θ_w can be described as a linear function of θ_{bp} and the elevation emergence angle φ_w can be described as a linear function of φ_{bp}. Mean values ± SEM are shown in red, and the lines of best fit (Equations 7.7a and 8) are plotted in black. **(B)** Relative uniformity and low dispersion of actual vs. predicted values about the identity lines, compared to similar plots for competing models (data not shown), indicate the best-fitting model. The top plot shows the fit using Equation 7.7. A-row whiskers are highlighted in blue, showing that these whiskers in particular are the least well-fit with this model. **(C)** Variation in response variable, θ_w and φ_{bp}, by whisker identity across the array, using Equation 7.7b (top) and 8(bottom). **(D)** The angle that represents the twist of the whisker about its own axis, ζ_w, is not well-predicted by θ_{bp} or φ_{bp}, or a combination, but φ_{bp} is the most predictive of the variables tested. Mean ± SE is shown in red, and the line of best fit (Equation 7.9a) is plotted in black. While the fit is poor, Equation 7.9a may serve as a first-order prediction for ζ_w in lieu of a more predictive model. **(E)** Evidence of the poor fit of Equation 7.9 is demonstrated by the actual vs. predicted values for ζ_w having wide and nonhomogeneous variance about the identity line. **(F)** The fit improves when the A-row and the rostral-most column in each row are omitted. **(G)** When ζ_w is plotted against whisker identity, arranged by row and column, an increasing trend by column, within rows B-E, can be observed. Red and blue points and black lines represent means, and red and blue lines show standard deviations. Blue lines indicate data that was omitted from the second model. **(H)** Predicted values of z across the array using Equation 7.9b.

Visual inspection of the data indicated that some subsets of whiskers were particularly contributing to this lack of fit. Figure 7.4G highlights that the A-row and the most rostral column within each row are more variable than other whiskers. We therefore omitted these whiskers and re-fit to the remaining 319 data points. The relationship between actual and predicted values is still more diffuse than would be ideal, but the fit improves and the predictive ability of the model improves dramatically, as indicated by the higher R^2. The resulting equation is remarkably similar to that for the rat (Belli, Bresee et al. 2018):

$$\zeta_w = 0.67197\theta_{bp} + 0.9874\varphi_{bp} + 44.465,.\ R^2 = 0.342 \qquad \text{(eq. 7.9b)}$$

where all variables are in degrees.

While the current analysis could not find a well-fit and strongly predictive model for ζ_w that included all the whiskers, it is still possible that ζ_w does not vary randomly. We believe it is likely that ζ_w does have some order, in part because this parameter is ordered in a highly related species (Belli, Bresee et al. 2018), and a moderately predictive model can be found using a subset of the data. Also, visual observation of

mice gives the impression of a generally ordered whisker array, with more rostral whiskers not only pointing forward, as predicted by Equation 7.7, but also curving forward, and more ventral and caudal whiskers curving downward and backward. In agreement with these qualitative observations, when ζ_w is plotted against whisker row and column, as shown in Figure 7.4I, some structure becomes visually appreciable. There is an increasing trend by column, and this trend is significant for rows B-E, based on simple linear regressions fit to individual rows, excluding whiskers from the most rostral column in each row, and with θ_{bp} as the predictor variable (φ_{bp} was not found to be a significant predictor variable in this analysis). These models are in general moderately to minimally predictive (*Row* A, NS; *Row* B p = 9.66e-05, R^2=0.22; *Row* C, p = 5.45e-08, R^2= 0.28; *Row* D, p = 0.00313, R^2 = 0.0829; *Row* E, p = 0.00753, R^2 = 0.0848) but again hint that, while mouse ζ_w is highly variable and difficult to measure in the mouse, this parameter does not vary completely randomly across the array.

Although there may exist a better statistical relationship describing ζ_w that we simply have not captured, due in part to mouse whiskers being extremely small, we also believe the poor fit is due to the choice of the average whisker row plane as horizontal. It is possible that choosing an alternative head pitch would provide a stronger relationship for ζ_w as a function of θ_{bp} and/or φ_{bp}, an idea elaborated on further in Discussion.

7.6.4. Comparisons of basepoint parameters across species

Using the relationships quantified in previous sections of Results, we compared the equations for basepoint coordinates for the mouse vibrissal array with the same equations for the rat (Belli et al., 2018). This direct comparison is straightforward for the mouse and rat, because these two species have a very similar number of rows and columns of macrovibrissae. Figure 7.5A compares θ_{bp} as a function of *Col* for the mouse and rat. For the more caudal columns, θ_{bp} is just slightly larger for the mouse, whereas for the more rostral

columns, θ_{bp} is just slightly larger for the rat, with the average difference being only 1.8458°. This indicates that θ_{bp} occupies a slightly larger range of angles in the rat than in the mouse.

Table 7.1 Comparison of equations across all three species.

Parameter	Species	Equation
Azimuthal basepoint	Mouse:	$\theta_{bp} = 11.688\ Col - 41.244$, *Adj*. $R^2 = 0.844$
	Rat:	$\theta_{bp} = 13.364\ Col - 48.635$, *Adj*. $R^2 = 0.873$
Elevation basepoint	Mouse:	$\varphi_{bp} = -16.785\ Row + 56.294$, *Adj*. $R^2 = 0.920$
	Rat:	$\varphi_{bp} = -26.301\ Row + 1.4867\ Row^2 + 68.005$, *Adj*. $R^2 = 0.954$
Radial basepoint	Mouse:	$r_{bp} = -0.015159\ \theta_{bp} - 0.016497\ \varphi_{bp} + 4.4388$, *Adj*. $R^2 = 0.551$
	Rat:	$r_{bp} = 0.000511\ \theta_{bp}^2 - 0.0295\ \theta_{bp} - 0.0162\ \varphi_{bp} + 6.50$, *Adj*. $R^2 = 0.65$
	Seal:	$r_{bp} = 0.4905\ \theta_{bp} + 36.489$, *Adj*. $R^2 = 0.834$
Arc length	Mouse:	$S = \exp(-0.018444\ \theta_{bp} + 2.4595)$, *Adj*. $R^2 = 0.671$
	Rat:	$S = \exp(0.02460\ \theta_{bp} + 3.12)$, *Adj*. $R^2 = 0.85$
	Seal:	$S = \exp(-0.0321\ \theta_{bp} - 0.0114\ \varphi_{bp} + 3.764)$, *Adj*. $R^2 = 0.735$
Upper bound on intrinsic curvature	Mouse:	$y = Ax^2$, $A = 0.2942\ exp(-0.2618\ S) + 0.01234$, *Adj*. $R^2 = 0.9938$
	Rat:	$y = Ax^2$, $A = 0.0746\ exp(0.0506\ S) + 0.00479$, *Adj*. $R^2 = 0.95$
	Seal:	$y = Ax^3$, $A = exp(-0.030799\ S) - 7.2348$, *Adj*. $R^2 = 0.837$
Azimuthal angle of emergence	Mouse:	$\theta_w = 1.0356\ \theta_{bp} + 82.548$, *Adj*. $R^2 = 0.544$ (version A) $\theta_w = 0.922\ \theta_{bp} + 85.1$, *Adj*. $R^2 = 0.739$ (version B)
	Rat:	$\theta_w = 0.598\ \theta_{bp} - 0.314\ \varphi_{bp} + 67.4$, *Adj*. $R^2 = 0.64$
	Seal:	$\theta_w = 1.770\ \theta_{bp} - 1.100\ \varphi_{bp} + 138.42$
Elevation angle of emergence	Mouse:	$\varphi_w = 1.0002\ \varphi_{bp} + 10.241$, *Adj*. $R^2 = 0.76$
	Rat:	$\varphi_w = 1.04\ \varphi_{bp} + 6.68$, *Adj*. $R^2 = 0.85$
	Seal:	$\varphi_w = 1.570\ \varphi_{bp} - 20.928$
Twist angle of emergence	Mouse:	$\zeta_w = 0.70632\ \varphi_{bp} + 36.097$, *Adj*. $R^2 = 0.134$ (version A) $\zeta_w = 0.67197\ \theta_{bp} + 0.9874\ \varphi_{bp} + 44.465$, $R^2 = 0.342$ (version B)
	Rat:	$\zeta_w = 0.876\ \theta_{bp} + 0.845\ \varphi_{bp} + 37.9$, *Adj*. $R^2 = 0.42$
	Seal:	$\zeta_w = 1.866\ \theta_{bp} - 1.540\ \varphi_{bp} - 24.447$

Figure 7.5: Comparison of basepoint coordinates across species. (A) θ_{bp}, as predicted by whisker column, spans a slightly larger range across all seven columns on the rat than on the mouse, but is essentially identical. **(B)** Similarly, φ_{bp}, as predicted by whisker row, covers a similar range for the rat and mouse across all five rows. **(C)** Top: Rat whisker arrays are larger than mouse whisker arrays, as shown by the height of the surfaces plotting radial distance of the whisker basepoints from the origin as continuous

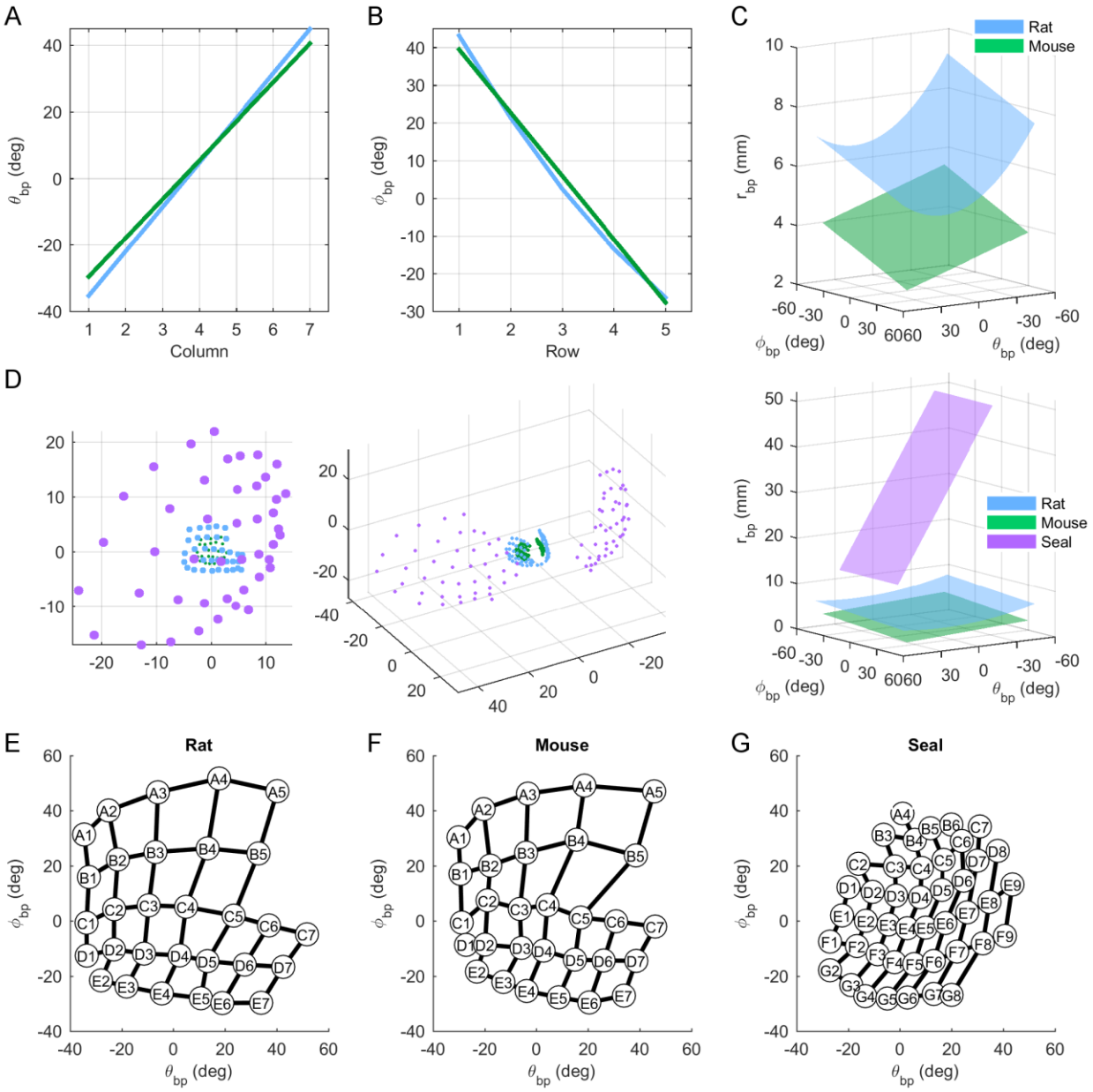

values within the space spanned by the observed values of θ_{bp} and θ_{bp}. Bottom: similar plot showing that the seal array is much larger and shaped differently than the rat and mouse array. The caudal most whisker basepoints on the seal are located ~6-12x further out radially from the origin on the seal than on the rat and mouse. **(D)** When predicted basepoint position (θ_{bp}, θ_{bp}, r_{bp}) is converted to cartesian coordinates (x, y, z) and plotted in 3D, differences in scaling and layout become visually appreciable. The rat and mouse arrays are very similar, aside from an increase in scale of the rat, and the seal is much larger and has a more diffuse whisker array compared to both the rat and mouse. **(E)** Mean whisker basepoint locations for θ_{bp} and φ_{bp}, for each whisker identity (row, column) in the mouse (left), rat (center), and seal (right). Note that this implicitly normalizes for r_{bp}. All axes are equal. The spatial layout of mouse and rat whiskers are similar, but the seal whisker basepoints are much closer together in angular distance. In all figures data for the mouse is green, the rat is blue, and the seal is purple.

Figure 7.5B compares φ_{bp} as a function of *Row* position for the mouse and the rat. For the most ventral column (Col=1), φ_{bp} is just slightly larger for the rat, whereas for the most dorsal column (Col=5), φ_{bp} is slightly smaller for the mouse. This indicates that φ_{bp} occupies an almost identical range of values in the rat as in the mouse. Similarly to θ_{bp}, the mean difference between φ_{bp} in the rat and the mouse by whisker identity was only 1.0373°, with φ_{bp} being very slightly more elevated in the mouse than in the rat.

The radial basepoint (r_{bp}) provides a quantification of the distance from each individual whisker basepoint to the center of the vibrissal arrays of each animal (the mean of all matched left and right whisker basepoints). Thus, r_{bp} can be taken as a quantification of mystacial pad size. As can be seen in Figure 7.5C (top), r_{bp} is larger in the rat compared to the mouse. We found that the values for rat r_{bp} were on average 56.13% larger than the mouse, with a range of 36.06% for the D5 whisker (the most similar) and 77.83% for the A1 whisker (the least similar). These values suggest that the mystacial pad of the rat is roughly 1.5 times larger than that of the mouse. This difference in size contrasts with the remarkable similarity between the two species for average basepoint azimuthal angle (θ_{bp}) and basepoint elevation angle (φ_{bp}) by whisker identity.

The seal has many more rows and columns than the rat and mouse, but can be compared to them using basepoint coordinates θ_{bp} and φ_{bp}. Figure 7.5C (bottom) again shows shows r_{bp} for the rat and mouse, but now with the addition of the seal, highlighting the large difference in scale between the pinniped and rodents. Figure 7.3C shows that the rostral-most basepoints are located 2-3x further out radially for the seal than for the mouse and rat respectively, and the caudal most whisker basepoints on the seal mystacial pad are located 6-10x further radially.

To further give a sense of the difference in scale between species, Figure 7.5D shows the basepoints of each, in standard orientation and position (a 3D cartesian coordinate system with the mean of the whisker

basepoints at the origin and the x-y plane parallel to the average whisker row plane). Note that, in terms of mm distance between basepoints, the seal array is much less dense than the rat and mouse arrays.

Finally, we normalized for the size of the mystacial pad by considering only the angular spacing of whisker basepoints across species. Figure 7.5E shows the locations of the whisker basepoints by row and column identity when plotted as a function of φ_{bp} and θ_{bp} for the rat, mouse, and seal. Again, the mouse and rat whisker arrays show striking similarities. The same number of whiskers occupy roughly equal areas in φ_{bp} and θ_{bp} coordinates. This consistency in angular distance, coupled with the difference in size indicated by the difference in r_{bp}, suggests that the rat array is roughly a scaled-up version of a mouse array, or that the mouse is a scaled-down version of the rat array.

Comparing the rat and mouse to the seal in angular distances highlights that, though the seal has approximately 50% more whisker basepoints, these basepoints occupy an area in φ_{bp} and θ_{bp} coordinates that is slightly smaller than the area of the whisker basepoints occupied by the rat and mouse. While in terms of distance in mm the seal whiskers basepoints are spaced further apart than the rat or mouse whisker basepoints, the seal whisker basepoints are actually closer together than rat or mouse in terms of angular distance.

7.6.5. Relationship between arc length and curvature across species

We compared the relationships that describe two-dimensional whisker geometry in the mouse to those same relationships found for the rat and harbor seal. Figure 7.6A shows S as a function of θ_{bp} in the mouse vs. S as a function of θ_{bp} in the rat. Means ± standard errors (SE) for data grouped by whisker identity (points and vertical lines), along with the best fit curves, are shown. Although the most caudal whiskers on the rat are more than twice the length of the most caudal whiskers on the mouse, the most rostral whiskers

are roughly equal lengths. Thus, S is much more variable across the rat array than the mouse array, and is reflected by the steeper decay in the exponential function.

Figure 7.6B plots the relationships for the rat and mouse from Figure 7.6A as planes constant in φ_{bp}, against *S*, and as a function of θ_{bp} and φ_{bp} in the seal. Although there are some deviations in the dorsal-ventral plane for the seal, *S* varies much more in the rostral-caudal plane. The most caudal and ventral whiskers on the seal can be up to three times longer than similarly located whiskers on the rat and as much as six times longer than similarly located whiskers on the mouse.

Figure 7.6C shows curvature coefficient (A) as a function of θ_{bp} in the mouse, along with *A* as a function of θ_{bp} in the rat. Again, mean ± SE when grouped by whisker identity and the best fit curves are shown in blue for the rat and green for the mouse. In both the rat and mouse, *A* as a function of θ_{bp} is highly variable, and does not significantly differ between species. In considering cross-species comparisons of whisker curvature, it is important to note that seal whiskers tend to be less curved than mouse and rat whiskers, and also can be parameterized by the cubic function y = *A*x3, in contrast to the quadratic relationship of rat or mouse whiskers.

We therefore cannot directly compare the curvature coefficient of seal whiskers with that of mouse and rat whiskers. Given that predicting mean curvature coefficient is challenging in both the mouse and rat due to high variability by whisker identity, especially for the rostral whiskers, Figure 7.6D plots curvature coefficient (A) vs. *S* in both the mouse and rat. The approximated upper bound to each of these datasets is indicated. For approximately 10mm <*S* < 30mm, the upper bound on the rat is greater than that on the mouse.

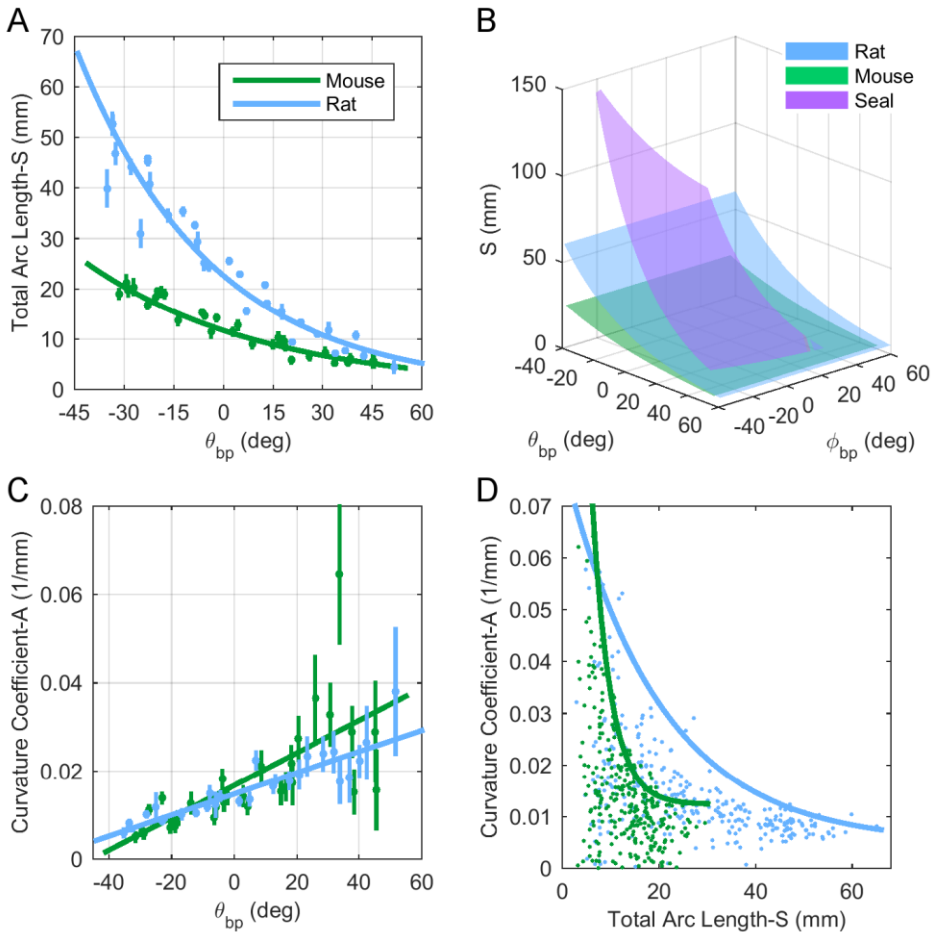

Figure 7.6: Relationship between 2D whisker geometry and basepoint coordinates across species. (A) Whisker arc length (*S*) can be described as a decaying exponential function of θ_{bp} from caudal to rostral across the array in the both the rat (blue) and mouse (green). The curves represent equations of best fit and dots show means ± standard error (SE) when grouped by whisker ID. *S* decays more rapidly as a function of θ_{bp} in the rat than in the mouse. **(B)** The relationships from (A) can be drawn as 3D surfaces to compare against the relationship for *S* as a function of basepoint coordinates in the seal. As expected, seal whiskers are much longer than rat whiskers, which are longer than mouse whiskers across the array. **(C)** Curvature coefficient (A) can be de described as a linearly increasing function of θ_{bp} from caudal to rostral across the array in both the rat (blue) and mouse (green). The fit lines represent the best fit equations, and means ± SE when grouped by whisker identity are shown as dots and vertical bars. We do not observe any specific differences between these two relationships. **(D)** When *A* is plotted against *S*, the upper bound on this relationship is much larger in the rat than in the mouse for whiskers where 10mm < *S* < 30mm.

7.6.6. Angles of emergence of the whiskers as a function of basepoint coordinates across species

We next compared the 3D angles of emergence (θ_w, φ_w, ζ_w) across the mouse, rat, and seal.

As shown in Figure 7.7A, mouse whiskers tend to emerge from the cheek with an azimuthal angle that points more rostrally than in the rat. θ_w is higher for the rostral whiskers in the mouse than for the rat. In fact, the mean value for θ_w in columns 6 and 7 of the mouse is 119.7862°, whereas it is only 96.9370° in the rat. In contrast, θ_w is more similar between the mouse and the rat for the most caudal whiskers (mean θ_w for columns 1 and 2 of the mouse is 59.2643° vs. 51.0411° for the rat). θ_w is higher for seal whiskers than in both mouse and rat whiskers at every location on the array, indicating that seal whiskers are universally oriented further forward, especially among the rostral and ventral whiskers.

Comparing elevation angle (φ_w) across the mouse, rat, and seal, shows that mouse whiskers lie at almost uniformly higher elevation angles than rat whiskers, as indicated by the almost parallel lines offset by about 4° (Figure 7.7B). Seal whiskers, on the other hand, lie at lower elevation angles than both mouse and rat whiskers at all values of φ_w.

Although the prediction for ζ_w in the mouse is poor, we still chose to compare it to the equations for the rat and seal (Figure 7.7C), as it allowed for a first-pass comparison among all three species at a single common head pitch (e.g. the average whisker row plane). This comparison shows the greatest differences in ζ_w across species in the dorsal whiskers.

In general, ζ_w was found to be much more variable for the rat and mouse than for the seal. This is likely attributable to two factors: 1) Individual seal whiskers have lower curvature (parameterized by a cubic polynomial f(x) = *A*x3, vs. the quadratic polynomial used to characterize mouse and rat whiskers, f(x) = *A*x2). 2) Seal whiskers are much longer in total arc length than mouse and rat whiskers, allowing for

proportionately higher resolution of measurements per whisker. Thus, the seal data, which were acquired using laser scans, have far more points than the data collected for the rat and mouse using the MicroScribe (which was especially limiting for shorter, more rostral whiskers).

Using the equations for the mouse found in the present work, Figure 7.7D plots the full 3D model of the average mouse vibrissal array. Using the set of equations that parameterize the average rat vibrissal array (Belli et al., 2018) and the average seal whisker array (Graff et al., in prep) we compared the model of the mouse in the present work to that of the rat and seal. Figure 7.7E shows that the rat vibrissal array is nearly a scaled-up version of the mouse array. However, Figure 7.7F shows that the seal whisker array points much more ventrally and rostrally than the mouse vibrissal array.

7.6.7. Relationship of facial markers to basepoint parameters (θ_{bp} and φ_{bp}) across species

We quantified the location of facial and skull features on the mouse array relative to the whisker basepoints. Figure 7.8A shows points recorded from the facial features of one individual mouse and one rat. Figure 7.8B also shows facial feature location, but now in 2D angular location of right-hand side facial and skull features relative to the origin, with the mouse on the left and the rat on the right, from (Belli, Bresee et al. 2018). These data allow the comparison of the relative locations of features without the difference in scaling dominating, and highlight a striking similarity between the two species, for the skull and facial feature locations relative to the whisker basepoints. Figure 7.8C compliments these data with the straight-line distances between facial features of the mouse, highlighting the clustering of rostral structures versus caudal structures.

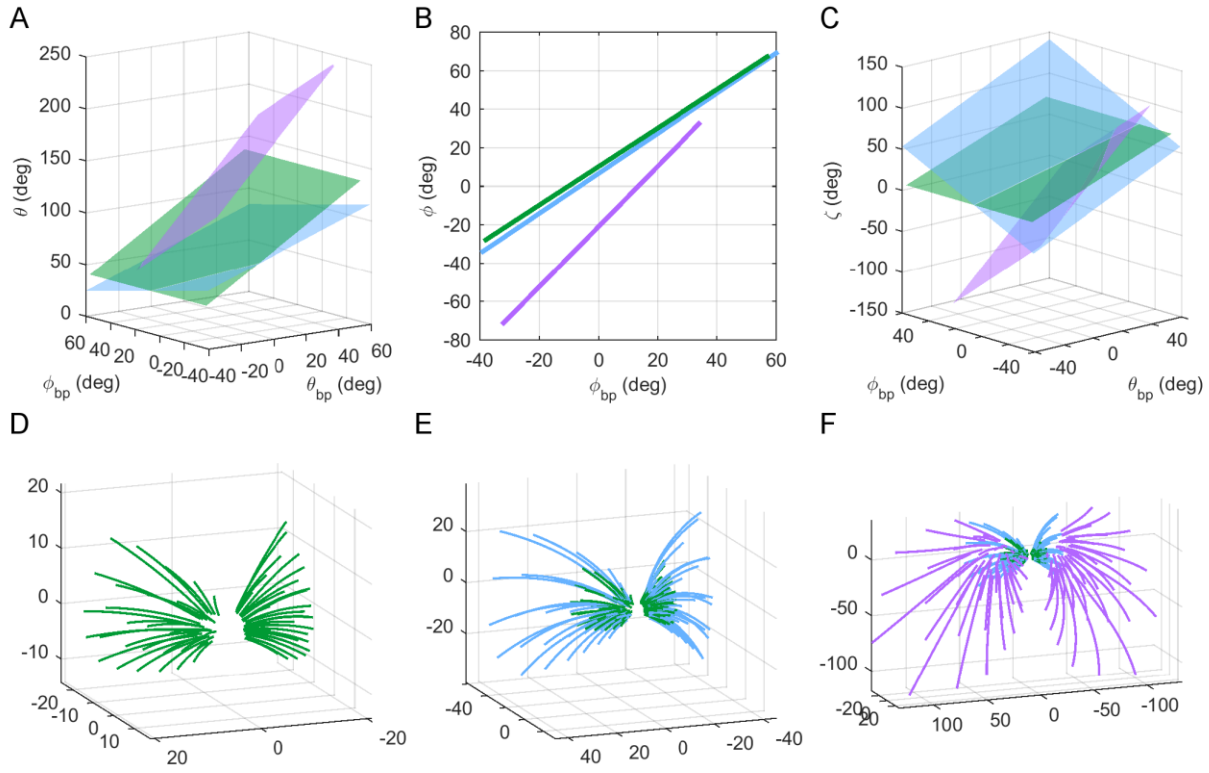

Figure 7.7: Relationship between basepoint coordinates and angles of emergence across species. (A) Whiskers in mice (green) are oriented slightly more forward than in rats (blue), especially for the rostral whiskers. Seal whiskers (purple) are oriented much further forward than both mouse and rat whiskers. **(B)** Mouse whiskers are almost uniformly slightly more elevated than rat whiskers by about 4° across the array, but seal whiskers hang lower than mouse whiskers and ventral rat whiskers. **(C)** ζ_w is highly variable across species using first-order approximations. **(D)** Full 3D model of the average mouse vibrissal array. **(E)** The orientation of the mouse whiskers is very similar to that in the rat. **(F)** Seal whiskers hang much lower and point forward more than mouse whiskers.

Although the angular locations of facial and skull features are similar between mouse and rat, the angular offset of certain features may differ, which is important for quantifying head pitch. For example, (Belli, Bresee et al. 2018) cited the offset of the bregma-lambda plane from the average whisker row plane to be about 8°. However, in the mouse, this offset was found to be on average about 22.1°, with a range of 17.0° to 27.6° across all eight mice and with a median of 21.3°.

7.7. Discussion

Previous studies have quantified the whisker arrays of species using a standardized set of axis conventions and alignment of the head with the average whisker row plane (Belli, Bresee et al. 2018). This choice of head orientation allowed for a direct numerical comparison of the whisker basepoint positions and angle of emergence across a variety of species. The present work builds on this methodological approach by quantifying the vibrissal array of the mouse, and comparing these results to previous models of the rat and seal.

7.7.1. Locations of whisker basepoints

7.7.1.1. Whiskers of mice, rats, and seals are arranged in grid-like arrays

We found a strong relationship between θ_{bp} and column, and between φ_{bp} and row in the mouse (Equations 7.1 and 7.2, and Figure 7.2) and across rats and mice (Figure 7.5 A and B, Table 7.1), reflecting a grid-like arrangement of whiskers. In the mouse, θ_{bp} was found to linearly increase with column and φ_{bp} was found to linearly decrease with row. We found the same trends in the rat, except that φ_{bp} quadratically decreased with row. Although we did not directly compare the equations for θ_{bp} and φ_{bp} in the rat and mouse to the same equations for the seal due to a different number of whisker rows and columns, the qualitative relationship between the independent and dependent parameters remains the same, e.g. θ_{bp} in the seal linearly increases with column and φ_{bp} quadratically decreases with row.

Figure 7.8: Comparison between the facial features of the mouse and rat. (A) Points on two individual animals' faces describing eyes, ears, nose, and mouth, shown with the whisker models in blue for rats and in green for mice. Vertical grid lines represent 10mm, while and horizontal grid lines represent 20mm. **(B)** Angular distance between various facial and skull features on the mouse (left) and rat (right). **(C)** Average absolute distance between named facial and skull features and whisker basepoint parameters on the mouse (distance in millimeters from zero, green, to 20, blue).

A

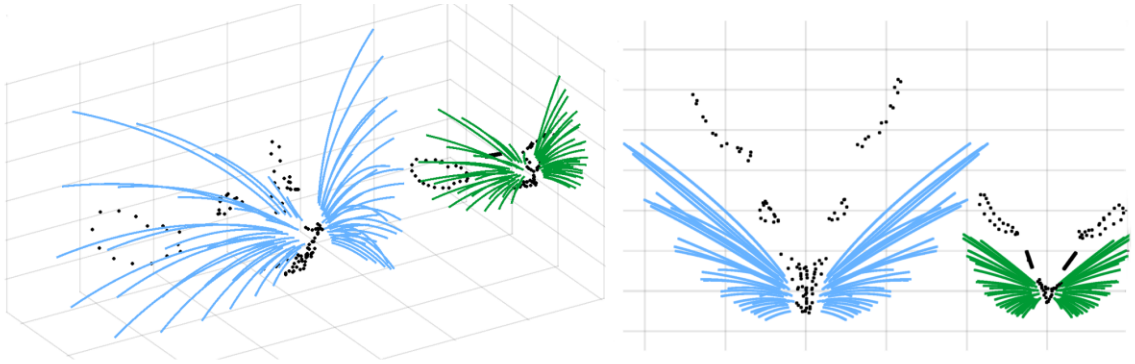

B

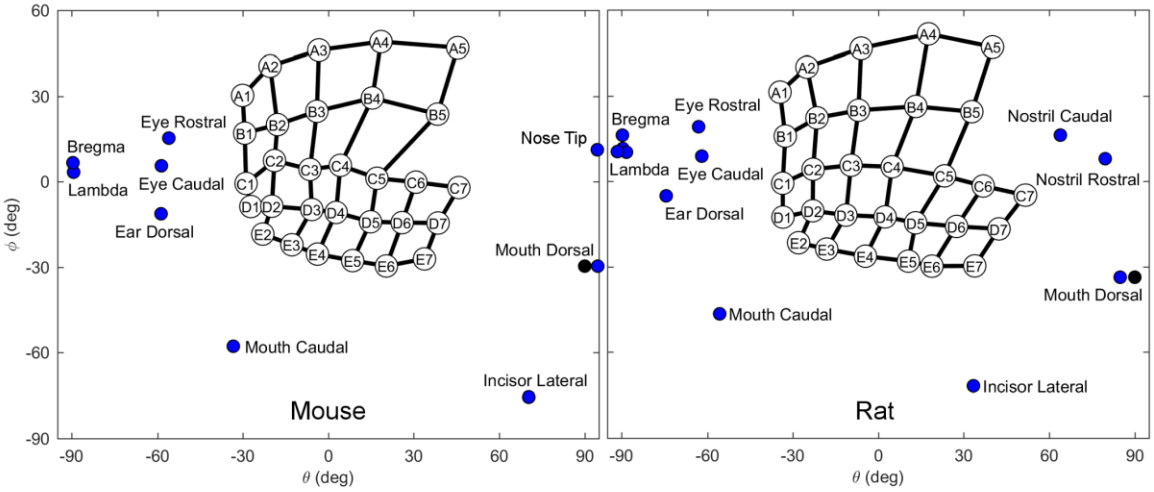

C

	Origin	Mouth Do.	Rt. A3 B.P.	Lt. A3 B.P.	Rt. C3 B.P.	Lt. C3 B.P.	Nose Tip	Rt. Incisors La.	Lt. Incisors La.	Rt. Mouth Cd.	Lt. Mouth Cd.	Lt. Eye Rs.	Rt. Eye Rs.	Lt. Eye Cd.	Rt. Eye Cd.	Bregma	Rt. Ear Do.	Rt. Ear Canal	Lambda	Lt. Ear Canal	Lt. Ear Do.
Origin	0	2.4	2.9	2.9	3.4	3.5	3.5	3.9	4	6	6.5	7.8	8.1	11	12	15	17	17	17	17	17
Mouth Do.	2.4	0	4.6	4.3	4.5	4.1	2.6	2.9	2.8	6.3	6.4	9.7	10	13	14	18	18	18	19	19	19
Rt. A3 B.P.	2.9	4.6	0	3.7	2.4	5.5	4.2	6.3	6.6	7.6	9.3	8.7	7.2	13	11	16	17	18	17	19	19
Lt. A3 B.P.	2.9	4.3	3.7	0	5.5	2.5	3.8	6.4	6.2	8.8	7.8	7.1	9.1	11	13	16	19	19	18	18	17
Rt. C3 B.P.	3.4	4.5	2.4	5.5	0	6.8	5	5.3	5.8	6	9.1	9.9	7.1	13	10	16	16	17	18	19	19
Lt. C3 B.P.	3.5	4.1	5.5	2.5	6.8	0	4.7	5.5	5.1	8.3	5.8	6.6	10	9.9	13	16	19	18	17	17	16
Nose Tip	3.5	2.6	4.2	3.8	5	4.7	0	5.5	5.4	8.6	8.7	11	11	14	15	19	20	20	21	21	20
Rt. Incisors La.	3.9	2.9	6.3	6.4	5.3	5.5	5.5	0	0.8	3.9	4.7	9.8	10	12	13	17	17	16	18	17	17
Lt. Incisors La.	4	2.8	6.6	6.2	5.8	5.1	5.4	0.8	0	4.5	4.3	9.7	11	12	13	17	17	16	18	17	17
Rt. Mouth Cd.	6	6.3	7.6	8.8	6	8.3	8.6	3.9	4.5	0	6	10	8.4	12	10	15	13	13	16	15	16
Lt. Mouth Cd.	6.5	6.4	9.3	7.8	9.1	5.8	8.7	4.7	4.3	6	0	7.9	11	9.2	13	15	17	15	16	13	13
Lt. Eye Rs.	7.8	9.7	8.7	7.1	9.9	6.6	11	9.8	9.7	10	7.9	0	7.8	4	10	9.7	15	15	11	12	11
Rt. Eye Rs.	8.1	10	7.2	9.1	7.1	10	11	10	11	8.4	11	7.8	0	10	3.8	9.6	10	12	11	15	16
Lt. Eye Cd.	11	13	13	11	13	9.9	14	12	12	12	9.2	4	10	0	11	8.1	15	14	9.4	9	7.2
Rt. Eye Cd.	12	14	11	13	10	13	15	13	13	10	13	10	3.8	11	0	7.8	6.7	9.2	9.1	14	16
Bregma	15	18	16	16	16	16	19	17	17	15	15	9.7	9.6	8.1	7.8	0	9.6	9.7	1.9	9.8	10
Rt. Ear Do.	17	18	17	19	16	19	20	17	17	13	17	15	10	15	6.7	9.6	0	4.7	9.5	14	17
Rt. Ear Canal	17	18	18	19	17	18	20	16	16	13	15	15	12	14	9.2	9.7	4.7	0	9.3	9.9	14
Lambda	17	19	17	18	18	17	21	18	18	16	16	11	11	9.4	9.1	1.9	9.5	9.3	0	9.5	10
Lt. Ear Canal	17	19	19	18	19	17	21	17	17	15	13	12	15	9	14	9.8	14	9.9	9.5	0	4.5
Lt. Ear Do.	17	19	19	17	19	16	20	17	17	16	13	11	16	7.2	16	10	17	14	10	4.5	0

mm between structures: 0 2.5 5 7.5 10 12.5 15 17.5 20 22.5

7.7.1.2. Whisker pad shape differs between species

The expressions for r_{bp} varied across all three species. In the seal, r_{bp} linearly decreased with θ_{bp} (Table 7.1), while in the mouse, r_{bp} was found to linearly decrease with both θ_{bp} and φ_{bp} (Equation 7.3, Figure 7.2, Table 7.1). The equation for r_{bp} in the rat, however decreased linearly with θ_{bp}, but varied quadratically with φ_{bp} (Table 7.1), suggesting significant curvature in the dorsoventral direction. These results in particular were interesting as in theory whisker pads are not linear; however, they did not meet the criteria to suggest a statistically higher order fit, aside for in the dorsoventral dimension in the rat. In all three animals, the most ventral and/or caudal whiskers are located the furthest from the mean position of all whisker basepoints.

7.7.1.3. Rat and mouse arrays are similar and seal arrays are proportionately denser

When holding r_{bp} constant, by analyzing whisker basepoint location in φ_{bp} and θ_{bp} space, we found that the mouse and rat whisker basepoints occupy remarkably similar positions (Figure 7.1 E-G). This similarity likely reflects a relatively recent evolutionary divergence (10 MYA, as estimated by (Steppan, Adkins et al. 2004) and similar ecological niches between the two species. Seals whisker pads are much larger than rat or mouse, and the whiskers are spaced farther apart. However, when comparing the seal to the rat and mouse in φ_{bp} and θ_{bp} space we found the seal whisker basepoint locations to be much closer together, and to occupy an overall smaller area, compared to the rodents. This does not mean that the seal has greater spatial resolution, as the seal whiskers are spaced farther apart in absolute terms than rat or mouse whiskers.

Seals may have proportionately denser arrays simply because they have larger faces, and so can fit more follicles proportionately closer together on their larger mystacial pads. If whisker pads are not normalized for scale, it is obvious that mouse arrays are by far the densest, with an entire mouse array able to comfortably fit between two caudal seal whiskers (Figure 7.5D). Also, based on the schematic shown in

Figure 7.1 in (Dehnhardt, Mauck et al. 1998), harbor seal follicles are much longer than they are wide, with the schematic of the follicle stating a length of 1-2 cm, and showing an approximate 1:5 aspect ratio. Therefore, an approximate width of a seal follicle will be 200um. In comparison, the rat follicle cross section shown in Figure 7.1A, in ((Fundin, Rice et al. 1994) shows a length of 650 um, but also a width of about 200um, for an aspect ratio of about 1:3. It is possible that whisker follicles tend to be on about the same scale as these two follicles are, whether because that scale is optimal for whisker follicles or because of a shared inherited developmental program for growing a whisker follicle. If seal follicles are only about twice as wide and up to four times as long as rat follicles, while the seal mystacial pad is much larger in area, then the seal could have many more whiskers and a proportionately denser array than rats and still have enough space between follicles to allow for a range of movement comparable to or exceeding that of rats.

7.7.2. Whisker shape

7.7.2.1 Rostral whiskers are shorter than caudal, and in the seal dorsal whiskers are shorter than ventral.

The 2D whisker geometry varied most across species. Although the longest seal whiskers are six times longer than mouse whiskers and three times longer than rat whiskers, all species have in common that arc length (S) exponentially decays with θ_{bp}, i.e. rostral whiskers are much shorter than caudal whiskers (Equation 7.4, Figure 7.3, 7.6, Table 7.1). In both rat and mouse whiskers, S is only significantly dependent on θ_{bp}, but in the seal, there is a dependency on both θ_{bp} and φ_{bp}, indicating exponential decay of S in both the caudal to rostral and ventral to dorsal directions. However, this dependency in the seal was based on a sample size of only 44 whiskers, implying that additional analysis may be required to achieve adequate statistical power and confirm this result.

7.7.2.2 Rat and mouse whiskers exhibit quadratic curvature, while seal whiskers exhibit cubic.

Whisker curvature also varied widely across species. While rat and mouse whiskers are best parameterized by the quadratic function $y = Ax^2$ (Equation 7.5, 7.6, Figure 7.6, Table 7.1), seal whiskers follow the cubic parameterization $y = Ax3$, where x represents points along the length of the whisker (Table 7.1). We refer to *A* as the quadratic curvature coefficient in the rat and mouse, and as the cubic curvature coefficient in the seal. The equations for predicting quadratic curvature coefficient as a function of θ_{bp} in the rat and mouse were highly variable (Adj. $R^2 = 0.339$ and 0.233 respectively). The rostral whiskers accounted for the highest amount of variability, leading us to instead place an upper bound on quadratic curvature coefficient in these two species as a function of *S*. In the seal, the equation for predicting the cubic curvature coefficient as a function of θ_{bp} and *S* yielded much higher adjusted R^2 values (0.667 and 0.837, respectively). However, this estimate was only based on 44 whiskers, and variability among the rostral whiskers could still be present with more whiskers.

7.7.3. Whisker position at rest

7.7.3.1. Whisker rostrocaudal orientation at rest varies among the three species.

The present work quantified the angles of emergence as functions of θ_{bp} and φ_{bp}. Although θ_w was reported in the rat and seal to be linear functions of both θ_{bp} and φ_{bp}, θ_w was found to only significantly linearly increase with θ_{bp} in the mouse (Figure 7.7, Table 7.1). Mice have a slightly larger range of θ_w than rats, with the rostral and dorsal whiskers slightly more angled forward than rat whiskers (higher θ_w), and ventral and caudal whiskers angled slightly more backward (lower θ_w). The greater range of azimuthal angle for mouse whiskers could reflect a greater need to monitor a large range of space around the head of the smaller and perhaps more commonly predated species. We also found θ_w to be higher in general in seals than in both mice and rats, indicating that seal whiskers are oriented more forward at rest. Having whiskers oriented near the front of the seal's mouth could be particularly advantageous for wake detection or during prey capture.

7.7.3.2 Whisker elevation at rest varies by dorsoventral position in the array, for all three species.

We found φ_w to be a linearly increasing function of φ_{bp} across all three species (Figure 7.7, Table 7.1). We also found mouse whiskers to be more elevated than rat whiskers by approximately 4° degrees across the entire array. Higher elevation angles in mice could reflect an increased need to sense objects located above them (such as downdrafts from predatory birds), or surrounding their heads, as opposed to in front of the mouth. Smaller body mass may increase time spent in non-horizontal environments, and therefore the need to sense laterally and dorsally during burrowing or climbing in the complex 3D structures of shrubs, grasses, or tunnels. Alternatively, greater elevation could reflect a difference in degree of predatory behavior between mice and rats, with more predatory species favoring whiskers surrounding the mouth to aid in bite targeting or prey capture. Interestingly, the much more predatory seal shows even less elevation than rats. Again, this would place seals' whiskers at and below the mouth, which could be advantageous for tracking wakes and hunting.

Interestingly, in all three species φ_w is only related to φ_{bp}, and does not vary with θ_{bp}, indicating that elevation is constant within a row. In other words, for all three species, the resting elevation of all whiskers does not differ within the plane of actuation (the average row plane). This similarity across rats, mice, and seals is especially striking when one contrasts the relatively recent divergence of mice and rats (~10 mya (Steppan, Adkins et al. 2004)) with the more ancient last common ancestor of all three (~90 MYA (Meredith, Janecka et al. 2011)). For a qualitative sense for the state of the mammalian clade in this era, consider that the last common ancestor of seals, mice, and rats likely lived even before the split between laurasiatheria (the clade comprising carnivora, along with chiroptera, artiodactyla, perissodactyla, and others) and euarchontiglires (the clade comprising rodentia along with lagomorpha, primatomorpha, and others). Given the less derived state of this stem boreoeutherian, it is tempting to speculate that the similarity in pattern of whisker elevation is meaningful for whiskers in general.

The mobility of whiskers theoretically poses a complex computational problem, rendering the inference of the global location of stimuli applied to distal segments of the whisker ambiguous, unless the animal can somehow monitor the spatial location of the whisker. As demonstrated in this work, it is possible to characterize the position of a whisker using three angles, two describing the angle of emergence of the basal portion. The fact that whiskers start from an equivalent resting position all across a row may relieve the brain from the need to calculate one of these angles when monitoring whisker position. Moreover, in the rat the change in elevation and torsion with whisking are both highly stereotyped and predictable based on protraction angle (Knutsen, Biess et al. 2008). This predictability means that, in rats, the anatomy and physiology of the whisker pad effectively holds all angles but protraction (θ) constant for a given θ, leaving the brain the much less daunting task of only calculating this one angle as opposed to three. It is tempting to speculate that mice and seals may also show similar predictability in φ and ζ for a given θ. However, even if mice and seals do not show this type of predictability, the fact that they also show φ held constant within a row at rest means that the brain does not have to re-calculate φ for each whisker when identifying the location of stimuli moving through a resting row.

7.7.3.3. For all species, the twist of the whisker about its own axis varies rostro-caudally and dorso-ventrally

While the prediction for ζ_w as a linear function of both θ_{bp} and φ_{bp} across all 171 whiskers in the seal was strong (Adj. R^2 = 0.784), it was less strong in the rat (Adj. R^2 = 0.417), and only weak and borderline significant as a function of φ_{bp} in the mouse (Adj. R^2 = 0.134), unless particular groups of whiskers were eliminated (Adj. R^2 = 0.342) (Equation 7.9, Figure 7.4, 7.7, Table 7.1). While quantifying and finding a significant trend for ζ_w is inherently more challenging for smaller whiskers with fewer data points, due to the definition of the parameter as the whisker's twist about its own axis, we also believe that a significant trend for ζ_w simply may be more prevalent at an alternative head pitch besides the average whisker row plane used in the present work. Head pitch may be important not only in finding significant relationships

between whisker basepoint angles and emergence angles, but also in identifying ethologically relevant head orientations for active sensing. Perhaps certain aspects of whisker arrays have evolved to serve particular functions that are most behaviorally relevant at a given head pitch relative to gravity, such as wind sensing, or sensing the texture of the ground, or vertical tree bark.

7.7.4. Other facial features

Finally, the present work quantifies the location of facial and skull features relative to whisker basepoints in θ_{bp} and φ_{bp} space, and measures the distance between these features and select whisker basepoints on the mouse (Figure 7.8). A comparison is also drawn to the rat, showing the similarity in θ_{bp} and φ_{bp} locations of these features, as well as the percent increase or decrease in the distances between such features relative to the rat.

7.7.5. Rats are scaled-up mice

We found that the rat and mouse are extremely similar, not only in terms of whisker array morphology, but in terms of overall facial feature positions, with the main difference being overall size (Figures 7.5, 7.8). This finding agrees with the finding of Cai et al. (Cai, Cho et al. 2007), that the molar-to-mandible ratio scales linearly between mice and rats. However, the question of whether mice are scaled-down rats, or rats are scaled-up mice remains an open one. Kimura et al. (Kimura, Jacobs et al. 2013) investigate scaling in the mouse/rat lineage by investigating the size of fossil molars from a probable common ancestor of mice and rats (Antemus chinjiensis), as well as later extinct murines. Their data indicate that Antemus molars are on the same scale as modern mouse molars, not modern rat molars. Based on the larger size of modern rats compared to their probable common ancestor with mice, one might therefore speculate that, evolutionarily speaking, rats are in fact scaled-up mice.

In all, rats and mice are extremely similar, while seals are unsurprisingly very different in many respects. However, there still exist striking similarities among all three species, which are surprising given the vast difference in niche and the many millions of years of evolution since their last common ancestor lived. These commonalities could reflect retained traits from a distant common ancestor, which were perhaps retained because they are advantageous for whisker-based tactile sensing in general, whether by a carnivorous marine mammal, or by omnivorous terrestrial rodents. At the same time, the differences among these species could reflect important sensory adaptations to their respective niches.

Chapter 8: Discussion

8.1. Summary

Touch sensors move in relation to each other, as the skin deforms or the animal moves its whiskers. Therefore, in touch in general, and especially in the vibrissal system, the brain cannot rely solely on sensor position to encode stimulus location in the external world. Rather, the shape and movement of an animal's body fundamentally affects the spatial information available to the system. Thus, considering embodiment and motion is imperative to understanding somatosensation.

To address the role of embodiment in sensorimotor integration it is essential to observe anatomy in detail, along with motor and sensory physiology. It is first important to use an appropriate model organism, which highlights the system of interest, and makes the study of that system more accessible. Ultimately, expanding from one model system to others allows the testing of generalizability of principles found in the initial system. This thesis contributes to the general understanding of the role of embodiment in sensorimotor integration by first adding to the body of evidence that the rat whisker system is an "expert" system for the sense of touch, by showing that rat whiskers are sensitive enough to allow the animal to sense the direction of air currents. We then catalogue rat whisker system morphology in detail, apply this knowledge to kinematic predictions of whisker protraction, observe sensory processing with multiple whiskers, and finally beginn to generalize these analyses to species other than the rat.

We begin by showing that rats can not only use their whiskers in the context of direct tactile contact, but can also use them to sense and follow the direction of air currents. We trained five rats in a five-alternative forced choice task in which an escape hole was cued by a fan blowing towards the start box. After vibrissal removal rats performance on wind-following dropped – resulting in more incorrect choices and larger deviations from a straight-line path – in contrast to the unchanged performance of control rats running

towards a visual cue. In a follow-up experiment we showed that rats that could not detect lower windspeeds had larger performance decrements after whisker trimming.

We next characterize the geometry of individual whiskers. We observed whisker geometry by using a combination of meta-analysis and direct observation of whisker through simple transmitted light microscopy. We found four main results: 1) The ratio of base diameter to whisker arc length varies by position in the array, and is dominated by the whisker's row position. 2) The portion of the whisker length that contains the medulla increases linearly with whisker length, so that, relative to short whiskers, long whiskers have a longer fraction of their length that contains medulla. 3) Similarly, the medulla's base diameter varies linearly with whisker base diameter, but more proportionately to base diameter, such that the ratio of medulla diameter to total diameter at the base increases only slightly for longer whiskers. 4) Whiskers at a particular rostro-caudal position in the array have roughly a constant "taper," defined as slope from base to tip, with a variable ratio of base to tip diameter, consistent with a whisker tip that is worn down to varying and unpredictable degrees with use. In short, a large whisker is not simply a scaled-up small whisker. This fact has important implications both for scientists studying the natural sensing system of the rat, and for engineers attempting to make biomimetic whisker sensors, namely, that even if whiskers across the array are faced with equivalent perturbations they will bend and vibrate differently. These different resulting perturbations may furnish the animal with a diverse bank of sensors with which to sample the external world.

Next, we show that not only is each whisker unique in slope and internal structure, but also that the length, curvature, and three-dimensional orientation of each whisker vary across the array. We used a digitizing probe to collect three-dimensional coordinates of multiple points along the whiskers and other cranial sensory structures of rats. We then made a statistical model of the array, using the three-dimensional locations of the whisker basepoints as fundamental parameters to generate equations describing the length,

curvature, and orientation of each whisker. Using coordinates like this allows the future comparison of the rat with other whiskered species that may have a different arrangement of whiskers. The model shows that whisker length increases exponentially from rostral to caudal, that whiskers cannot curve more than 50% of their length, and that whiskers "fan out" approximately equally in dorsal-ventral and rostral-caudal directions. This work sets the stage for future evolutionary and neuroethological comparisons with the sensory accessory structures of other species, and again provides valuable data for engineers seeking to design bio-inspired whisker sensory arrays.

We then show that the embodiment of the rat is also key to generalizable motor control, as the geometry of the follicles and muscles in the rat whisker pad facilitates equivalent motor control across even the smallest and largest whiskers in the array. Previous chapters have shown that rats have substantial variations in whisker morphology and orientation across the array. By simulating the kinematics of whisker protraction, based on observed pad anatomy, we now show that the follicle array is structured in such a way as to coordinate the movement of these multiple diverse sensors. Results indicate that if any intrinsic muscle across the pad is shortened by a given percent, the associated whisker will rotate the same number of degrees, regardless of whisker identity. In essence, the anatomy of the system allows the lower motor neurons to generalize a rate code across the entire array.

This thesis then offers an explanation for how the brain might make sense of inputs from these multiple diverse sensors to enable tactile perception. We show that neurons in the trigeminal brainstem (SpVi and possibly SpVo) encode the speed and direction of multi-whisker stimulation moving through a stationary array. To do this, we recorded both single-unit spikes and local field potentials from fifteen multi-whisker responsive sites in the brainstem trigeminal complex, while systematically varying the speed and direction of whole-array whisker stimulation. We found that spike rate varied depending on both speed and direction, generally encoding caudal to rostral and slower stimulation with higher spike rates. We found that local field potential responses were more predictive of stimulus characteristics than spike trains,

indicating that stimulus speed and direction may be encoded more at the level of the population than single neuron. SpVi has a particularly interesting placement in the whisker system, as its target, PoM thalamus, is inhibited by zona incerta, which itself is inhibited by whisker motor cortex. Whisking commands sent from M1 could inhibit Zi, releasing PoM from inhibition, and only then passing information from SpVi to whisker somatosensory cortex. Moreover, PoM neurons target L5 and L1, and it has been shown that concurrent input to the apical tufts and basal dendrites of L5 pyramidal neurons triggers calcium-mediated plateau potentials (Larkum 2013). Therefore, information about the speed and direction of stimuli moving through the array could upregulate L5 cells and modulate the response of the cortical column to more fine-grained tactile information coming through parallel pathways.

We conclude by taking the first steps toward generalizing these sorts of investigations of embodiment to other species. We construct a model of the cranial sensory structures of a closely related species, the mouse, and compare this species' anatomy to that of the rat and to the much more distantly related seal. We used a technique similar to that mentioned in Chapter 2, collecting three-dimensional coordinates of points along whiskers and other cranial sensory structures, and generating equations describing the orientation, length, and curvature of each whisker.

The results for the mouse are strikingly similar to that of the rat, with the main difference being a much smaller scale. The two species are very similar in terms of angular distance between structures, and vary slightly in terms of the proportional Euclidian distance between facial features, with mice having ears proportionately farther apart. This difference raises the possibility that the angular distances between sensory structures might be selected for due to the similar niches of mice and rats, allowing a particular cross-modal spatial integration that may be advantageous, while other aspects of face shape may vary for other reasons (feeding, sexual selection, etc.).

We also compare our models of the rat and mouse to qualitatively similar models of the seal, documented in a different publication. Elevation angle varies only dorso-ventrally for all three species, which is surprising for such distantly related clades. This may be because this dimension is perpendicular to the plane of whisking for the rodents, and is perpendicular to the plane of whisker actuation and forward movement through the water for the seal. This consistency in elevation may facilitate multi-whisker processing by holding one angle constant across a row, relieving the brain from having to calculate this angle.

8.2. Main findings and implications

This thesis begins by presenting the first scientific publication documenting rats use of whisker-based information to sense airflow. In the past it has been speculated, and even asserted, that mammals use whiskers to sense the direction of air currents. However, the work presented here is the first scientific investigation of this faculty, and the first actual evidence that animals can use whiskers to sense the wind.

The majority of this thesis then investigates embodiment in the rat whisker system in detail, first byestablishing that a whisker at a given position in a rat's whisker pad is unique, in terms of slope from base to tip, internal structure, length, curvature, and 3D spatial orientation at rest. This information is essential to an overall understanding of the importance of embodiment, not just for the rat, but, to the extent that the rat is used as a model system, for sensory neuroscience in general. Some previous studies have assumed homogeneity of whiskers in various respects (for example (Boubenec, Shulz et al. 2012, Quist, Seghete et al. 2014)) and these assumptions can impact modeling and therefore predictions of the sensory information available to the rat.

Importantly, other work (Yu paper) shows that whisker shape and orientation determine the mechanical response of the whisker to airflow. The direction of airflow determines the bending direction of the

whisker, while airflow speed and whisker length and diameter at the base contribute to bending magnitude. Crucially, the orientation of the whisker also contributes to bending magnitude. Therefore, the anemotaxis behavior reported here could be facilitated by the systematic variation of rat whisker morphology also described in this thesis. The three parameters that most contribute to differences in whisker mechanical response to airflow – whisker lenth, diameter, and orientation – vary in smooth gradients across the pad. Therefore, these differences could allow the rat to determine airflow direction and speed from the response of a polulation of trigeminal ganglion neurons with receptive fields distributed across the pad.

The detailed observations of rat whisker morphology presented here also show that many other parameters vary systematically across the array, and usually in smooth gradients. The detailed descriptions of these differences across the array provide a rich dataset to inform future experiments. For example, one could investigate whether some of this systematic variation might have evolved to facilitate active sensing. The present work describes the variation across the array, but these measurements can also be used to define parameters in simulations.

It is theoretically possible to use these future simulations to predict the forces and moments at the base of whiskers in a simulated array, as that array interacts with stimuli. By simulating different array morphologies, it will be possible to test whether systematic differences described here might be evolved to differentiate various stimuli. In short, using the present data to create models, perturb them in controlled ways, and simulate forces, it will be possible to compare the sensory data that differently embodied rats would have, regardless of whether we can yet model the neural representation of the incoming stimuli.

This thesis also demonstrates one specific mechanism by which embodiment can simplify neural control of movement. We simulate protraction using the observed internal anatomy of the whisker pad, and show that the consistency in the resulting movement predicts that all whiskers will move equivalently for a given rate

of activation of their lower motor neurons. This finding is only a prediction, but it invites further experiments directly observing lower motor neuron activity, for example, through electrophysiological recordings or stimulation in the facial nucleus, while recording video of resulting whisker movement. Regardless of whether this prediction holds true in the actual system, however, the present finding could be taken as a proof of concept that embodiment can, in principle, simplify neural control of movement.

This thesis starts to "close the loop" between the coordinated use of these multiple diverse sensors, and the resulting sensation, by observing the electrophysiological sensory results of multi-whisker stimulation. We show that multi-whisker responsive secondary sensory neurons, specifically in the spinal trigeminal nucleus interpolaris, encode the speed and direction of stimuli moving through the array, and may pass this information to whisker somatosensory cortex specifically during whisking. This multi-whisker integration is impressive at such low levels as secondary sensory neurons.

It is tempting to speculate that some of the systematic variation documented in Chapters 1 and 2 may contribute to rats' ability to accomplish this early integration. The intrinsic curvature of vibrissae results in differences in bending and vibration depending on the angle at which the whisker interacts with an object, with a strike to the concave side resulting in a larger response than the convex side. The fact that the orientation of the whisker's intrinsic curvature (ζ) changes across the array, with both row and column, means that a stimulus moving through the array in a given direction will result in a unique pattern of bending and vibration across all whiskers. This difference in mechanical response opens the possibility that stimulus movement could be represented with a population code across multiple ganglion neurons. For example, a population of primary sensory neurons that constitute the receptive field of a secondary sensory neuron in SpVi may have the greatest response to stimuli moving along the path through the array that encounters the most whiskers in a concave orientation. The least response should be to stimuli moving through the array in the direction that encounters the most whiskers with a convex orientation towards the

stimulus, and intermediate directions should have intermediate activity. If every whisker is contacted by the stimulus, the path eliciting greatest activity would likely be ventral-to-dorsal, given the pattern of orientations shown in Chapter 2. However, if only the longest whiskers are considered, then caudo-to-rostral stimulation may be close to the most effective stimulus, while rostro-to-caudal stimuli should be least effective (Chapter 3, Figure 3.7). The experiment reported here did in fact find greater activity in response to caudal-to-rostral stimulation. This hypothesized role for embodiment in sensory processing could be investigated further, simply by varying the direction of stimulus through the array while keeping track of the orientation of the whiskers encountered. Similarly, one could alter the curvature of whiskers, by using chemical relaxing agents and/or heat, and again record electrophysiological activity in SpVi while passing a stimulus through the array in various directions.

In the last part of this thesis we expand the intricate observations of whisker array morphology to new species, highlighting species-specific differences, but also some striking similarities. In particular, we hypothesize that constant elevation within a row might be an important aspect of whisker organization. It is possible that this constant elevation within a row simplifies monitoring of whisker angle, by essentially holding the elevation angle constant while the whiskers move through space in roughly the rostro-caudal plane, either by whisking or by the animal moving forward. This could be part of what allows multi-whisker integration at early stages.

Taken in its entirety, this work vastly increases the precision with which we can model the embodiment of the rat whisker system, shows how this embodiment could facilitate motor control, and begins to add multi-whisker sensory processing to the overall conceptual model of rat embodied active sensation.

8.3. Future work

To be able to make further inferences about active touch in general, we are beginning experiments that quantify the whisker array and other sensory cranial structure morphology across a broad range of species. We hypothesize that (1) the axis of actuation of whiskers is an important organizing principle for the whisker basepoint layout, that (2) niche/habit is an important factor affecting whisker length, curvature, and the degree to which the whisker array is "grid-like", that (3) both independent variables will affect whisker orientation, and that (4) evolutionary relatedness will have an effect on all dependent variables, but may not be as important a factor as niche. We will survey a broad range of species, choosing contrasts that allow us to perform "natural experiments" to control for these variables. Very preliminary data from the rabbit array suggests that, in some ways, rabbit arrays are arranged very differently than the rat and mouse, and are even more different from the rat than the rat is from the cat and seal, despite the fact that rabbits are more closely related to mice and rats than to the carnivores.

The above analysis of mammalian sensorimotor embodiment is highly "whisker-centric". This particular perspective is very much intentional in the current work, but future work does not necessarily need to be limited to this frame of reference. Further studies using these three-dimensional models of cranial sensory structures will also vary head pitch and origin.

The current model of intrinsic muscle contraction leading to protraction is limited to non-collision whisking. However, future models will seek to reconstruct the inner follicle wall and the whisker shaft, and model the whisker bending within the follicle in response to an external collision. This will allow the modeling of forces and moments not only at the base of the whisker, but also within the three-dimensional follicle, and potentially predict the activity of primary sensory neurons.

REFERENCES

Adineh, V. R., B. Liu, R. Rajan, W. Yan and J. Fu (2015). "Multidimensional characterisation of biomechanical structures by combining Atomic Force Microscopy and Focused Ion Beam: A study of the rat whisker." Acta Biomaterialia **21**: 132-141.

Ahissar, E. and A. Arieli (2001). "Figuring space by time." Neuron **32**: 185–201.

Ahissar, E. and P. M. Knutsen (2008). "Object localization with whiskers." Biol Cybern **98**(6): 449-458.

Ahissar, E., R. Sosnik and S. Haidarliu (2000). "Transformation from temporal to rate coding in a somatosensory thalamocortical pathway." Nature **406**(6793): 302-306.

Ahl, A. S. (1986). "The Role of Vibrissae in Behavior: a Status Review." Veterinary Research Communications **10**: 245-268.

Anjum, F., H. Turni, P. G. Mulder, J. van der Burg and M. Brecht (2006). "Tactile guidance of prey capture in Etruscan shrews." Proc Natl Acad Sci U S A **103**(44): 16544-16549.

Anthwal, N., L. Joshi and A. S. Tucker (2013). "Evolution of the mammalian middle ear and jaw: adaptations and novel structures." J Anat **222**(1): 147-160.

Arkley, K., R. A. Grant, B. Mitchinson and T. J. Prescott (2014). "Strategy Change in Vibrissal Active Sensing during Rat Locomotion." Current Biology **24**(13): 1507-1512.

Bach-y-Rita, P. (2003). "Seeing With the Brain." INTERNATIONAL JOURNAL OF HUMAN–COMPUTER INTERACTION **15**(2): 285–295.

Baker, T. C. and L. P. Kuenen (1982). "Pheromone source location by flying moths: a supplementary non-anemotactic mechanism." Science **216**(4544): 424-427.

Baverstock, H., N. S. Jeffery and S. N. Cobb (2013). "The morphology of the mouse masticatory musculature." J Anat **223**(1): 46-60.

Belli, H. M., C. S. Bresee, M. M. Graff and M. J. Z. Hartmann (2018). "Quantifying the three-dimensional facial morphology of the laboratory rat with a focus on the vibrissae." PLoS One **13**(4): e0194981.

Belli, H. M., A. E. Yang, C. S. Bresee and M. J. Hartmann (2017). "Variations in vibrissal geometry across the rat mystacial pad: base diameter, medulla, and taper." J Neurophysiol **117**(4): 1807-1820.

Bennett-Clarke, C. A., N. L. Chiaia, M. F. Jacquin and R. W. Rhoades (1992). "Parvalbumin and calbindin immunocytochemistry reveal functionally distinct cell groups and vibrissa-related patterns in the trigeminal brainstem complex of the adult rat." Journal of Comparative Neurology **320**(3): 323–338.

Berchtold, M. W., H. Brinkmeier and M. Muntener (200). "Calcium Ion in Skeletal Muscle: Its Crucial Role for Muscle Function, Plasticity, and Disease." Physiological Reviews **80**(3): 1215-1265.

Berg, R. W. and D. Kleinfeld (2003). "Rhythmic whisking by rat: retraction as well as protraction of the vibrissae is under active muscular control." J Neurophysiol **89**(1): 104-117.

Berry, R. J. and F. Bronson, H. (1992). "LIFE HISTORY AND BIOECONOMY OF THE HOUSE MOUSE." Biol Rev **67**: 519-550.

Bezdudnaya, T. and M. A. Castro-Alamancos (2011). "Superior colliculus cells sensitive to active touch and texture during whisking." J Neurophysiol **106**(1): 332-346.

Bezdudnaya, T. and M. A. Castro-Alamancos (2014). "Neuromodulation of whisking related neural activity in superior colliculus." J Neurosci **34**(22): 7683-7695.

Bhattacharyya, U. and U. Singh Bhalla (2015). "Robust and Rapid Air-Borne Odor Tracking without Casting(1,2,3)." eNeuro **2**(6).

Birdwell, J. A., J. H. Solomon, M. Thajchayapong, M. A. Taylor, M. Cheely, R. B. Towal, J. Conradt and M. J. Hartmann (2007). "Biomechanical models for radial distance determination by the rat vibrissal system." J Neurophysiol **98**(4): 2439-2455.

Birdwell, J. A., J. H. Solomon, M. Thajchayapong, M. A. Taylor, M. Cheely, R. B. Towal, J. Conradt and M. J. Z. Hartmann (2007). "Biomechanical models for radial distance determination by the rat vibrissal system." Journal of Neurophysiology **98**(4): 2439-2455.

Bobrov, E., J. Wolfe, R. P. Rao and M. Brecht (2014). "The representation of social facial touch in rat barrel cortex." Curr Biol **24**(1): 109-115.

Bokor, H., L. Acsady and M. Deschenes (2008). "Vibrissal responses of thalamic cells that project to the septal columns of the barrel cortex and to the second somatosensory area." J Neurosci **28**(20): 5169-5177.
Bosman, L. W., A. R. Houweling, C. B. Owens, N. Tanke, O. T. Shevchouk, N. Rahmati, W. H. Teunissen, C. Ju, W. Gong, S. K. Koekkoek and C. I. De Zeeuw (2011). "Anatomical pathways involved in generating and sensing rhythmic whisker movements." Front Integr Neurosci **5**(53): 53.
Boubenec, Y., D. Shulz and G. Debregeas (2012). "Whisker encoding of mechanical events during active tactile exploration." Frontiers in Behavioral Neuroscience **6**(74): e00074.
Boubenec, Y., D. E. Shulz and G. Debregeas (2012). "Whisker encoding of mechanical events during active tactile exploration." Frontiers in Behavioral Neuroscience **6**.
Brecht, M., B. Preilowski and M. Merzenich (1997). "Functional architecture of the mystacial vibrissae." Behavioural Brain Research **84**: 81-97.
Brecht, M., B. Preilowski and M. M. Merzenich (1997). "Functional architecture of the mystacial vibrissae." Behavioural Brain Research **84**(1-2): 81-97.
Budick, S. A., M. B. Reiser and M. H. Dickinson (2007). "The role of visual and mechanosensory cues in structuring forward flight in Drosophila melanogaster." Journal of Experimental Biology **210**(23): 4092-4103.
Bureau, I., F. von Saint Paul and K. Svoboda (2006). "Interdigitated paralemniscal and lemniscal pathways in the mouse barrel cortex." PLoS Biol **4**(12): e382.
Burns, J. (2009). Harbor Seal and Spotted Seal: Phoca vitulina and P. largha. Encyclopedia of Marine Mammals (Second Edition). W. F. Perrin, B. Würsig and J. G. M. Thewissen**:** 533-542.
Burton, R. F. (2006). "A new look at the scaling of size in mammalian eyes." Journal of Zoology **0**(0): 060423083931007-???
Bush, N. E., C. L. Schroeder, J. A. Hobbs, A. E. T. Yang, L. A. Huet, S. A. Solla and M. J. Z. Hartmann (2016). "Decoupling kinematics and mechanics reveals coding properties of trigeminal ganglion neurons in the rat vibrissal system." eLife.
Byers, M. R. and W. K. Dong (1989). "Comparison of Trigeminal Receptor Location and Structure in the Periodontal Ligament of Different Types of Teeth From the Rat, Cat, and Monkey." THE JOURNAL OF COMPARATIVE NEUROLOGY **279**: 117-127.
Cai, J., S. W. Cho, J. Y. Kim, M. J. Lee, Y. G. Cha and H. S. Jung (2007). "Patterning the size and number of tooth and its cusps." Dev Biol **304**(2): 499-507.
Campagner, D., M. H. Evans, M. R. Bale, A. Erskine and R. S. Petersen (2016). "Prediction of primary somatosensory neuron activity during active tactile exploration." Elife **5**.
Cang, J., R. C. Renteria, M. Kaneko, X. Liu, D. R. Copenhagen and M. P. Stryker (2005). "Development of precise maps in visual cortex requires patterned spontaneous activity in the retina." Neuron **48**(5): 797-809.
Carl, K., W. Hild, J. Mampel, C. Schilling, R. Uhlig and H. Witte (2012). "Characterization of Statical Properties of Rat's Whisker System." IEEE Sensors Journal **12**(2): 340-349.
Carvell, G. E. and D. J. Simons (1990). "Biometric analyses of vibrissal tactile discrimination in the rat." Journal of Neuroscience **10**(8): 2638-2648.
Carvell, G. E. and D. J. Simons (1995). "Task-related and subject-related differences in sensorimotor behavior during active touch " Somatosensory and Motor Research **12**(1): 1-9.
Casas, J. and O. Dangles (2010). "Physical ecology of fluid flow sensing in arthropods." Annu Rev Entomol **55**: 505-520.
Catania, K. C. (2013). "Stereo and serial sniffing guide navigation to an odour source in a mammal." Nature Communications **4**.
Chapin, J. K. and C. S. Lin (1984). "Mapping the body representation in the si cortex of anesthetized and awake rats." Journal of Comparative Neurology **229**(2): 199-213.
Chernova, O. F. (2003). "Architectonic and diagnostic significance of hair cortex and medulla." Biology Bulletin **30**(1): 53-62.
Chernova, O. F. (2006). "Evolutionary aspects of hair polymorphism." Biology Bulletin **33**(1): 43-52.
Chernova, O. F. and V. F. Kulikov (2011). "Structural differences between the shafts of mammalian vibrissae and hairs and their causes." Dokl Biol Sci **438**: 182-185.

Christie, B. P., D. M. Tat, Z. T. Irwin, V. Gilja, P. Nuyujukian, J. D. Foster, S. I. Ryu, K. V. Shenoy, D. E. Thompson and C. A. Chestek (2015). "Comparison of spike sorting and thresholding of voltage waveforms for intracortical brain-machine interface performance." J Neural Eng **12**(1): 016009.

Clauset, A., C. R. Shalizi and M. E. J. Newman (2009). "Power-Law Distributions in Empirical Data." Siam Review **51**(4): 661-703.

Cox, P. G. and N. Jeffery (2008). "Geometry of the semicircular canals and extraocular muscles in rodents, lagomorphs, felids and modern humans." J Anat **213**(5): 583-596.

Cunningham, S. J., M. R. Alley and I. Castro (2011). "Facial bristle feather histology and morphology in New Zealand birds: implications for function." J Morphol **272**(1): 118-128.

Dayan, P. and L. F. Abbott (2001). "Theoretical Neuroscience." vol. 806. **Cambridge, MA:** (MIT Press;).

Dehnhardt, G. and A. Kaminski (1995). "Sensitivity of the Mystacial Vibrissae of Harbor Seals (Phoca-Vitulina) for Size Differences of Actively Touched Objects." Journal of Experimental Biology **198**(11): 2317-2323.

Dehnhardt, G., B. Mauck and H. Bleckmann (1998). "Seal whiskers detect water movements." Nature **394**(6690): 235-236.

Dehnhardt, G., B. Mauck, W. Hanke and H. Bleckmann (2001). "Hydrodynamic trail-following in harbor seals (Phoca vitulina)." Science **293**(5527): 102-104.

Dehnhardt, G., B. Mauck and H. Hyvarinen (1998). "AMBIENT TEMPERATURE DOES NOT AFFECT THE TACTILE SENSITIVITY OF MYSTACIAL VIBRISSAE IN HARBOUR SEALS." Journal of Experimental Biology **201**: 3023–3029.

Deschenes, M., J. Takatoh, A. Kurnikova, J. D. Moore, M. Demers, M. Elbaz, T. Furuta, F. Wang and D. Kleinfeld (2016). "Inhibition, Not Excitation, Drives Rhythmic Whisking." Neuron **90**(2): 374-387.

Diamond, M. E. and E. Ahissar (2007). "When outgoing and incoming signals meet: new insights from the zona incerta." Neuron **56**(4): 578-579.

Diamond, M. E. and E. Arabzadeh (2013). "Whisker sensory system - from receptor to decision." Prog Neurobiol **103**: 28-40.

Diamond, M. E., M. von Heimendahl, P. M. Knutsen, D. Kleinfeld and E. Ahissar (2008). "'Where' and 'what' in the whisker sensorimotor system." Nat Rev Neurosci **9**(8): 601-612.

Dorfl, J. (1982). "The musculature of the mystacial vibrissae of the white-mouse " Journal of Anatomy **135**(AUG): 147-154.

Ebara, S., K. Kumamoto, T. Matsuura, J. E. Mazurkiewicz and F. L. Rice (2002). "Similarities and differences in the innervation of mystacial vibrissal follicle-sinus complexes in the rat and cat: a confocal microscopic study." J Comp Neurol **449**(2): 103-119.

Eckstein, M. P. (2011). "Visual search: a retrospective." J Vis **11**(5).

Erzurumlu, R. S., C. A. Bates and H. P. Killackey (1980). "Differential organization of thalamic projection cells in the brain stem trigeminal complex of the rat." Brain Research **198**: 427-433.

Erzurumlu, R. S., Z. F. Chen and M. F. Jacquin (2006). "Molecular determinants of the face map development in the trigeminal brainstem." Anat Rec A Discov Mol Cell Evol Biol **288**(2): 121-134.

Erzurumlu, R. S. and H. P. Killackey (1980). "Diencephalic projections of the subnucleus interpolaris of the brainstem trigeminal complex in the rat." Neuroscience **5**: 1891-1901.

Erzurumlu, R. S., Y. Murakami and F. M. Rijli (2010). "Mapping the face in the somatosensory brainstem." Nat Rev Neurosci **11**(4): 252-263.

Favaro, P. D., T. S. Gouvea, S. R. de Oliveira, N. Vautrelle, P. Redgrave and E. Comoli (2011). "The influence of vibrissal somatosensory processing in rat superior colliculus on prey capture." Neuroscience **176**: 318-327.

Fee, M. S., P. P. Mitra and D. Kleinfeld (1997). "Central versus peripheral determinants of patterned spike activity in rat vibrissa cortex during whisking." Journal of Neurophysiology **78**(2): 1144-1149.

Feng, A. Y. T. and C. G. Himsworth (2013). "The secret life of the city rat: a review of the ecology of urban Norway and black rats (Rattus norvegicus and Rattus rattus)." Urban Ecosystems **17**(1): 149-162.

Fifer, M. S., G. Hotson, B. A. Wester, D. P. McMullen, Y. Wang, M. S. Johannes, K. D. Katyal, J. B. Helder, M. P. Para, R. J. Vogelstein, W. S. Anderson, N. V. Thakor and N. E. Crone (2014). "Simultaneous neural control of simple reaching and grasping with the modular prosthetic limb using intracranial EEG." IEEE Trans Neural Syst Rehabil Eng **22**(3): 695-705.

Fundin, B. T., F. L. Rice, K. Pfaller and J. Arvidsson (1994). "The innervation of the mystacial pad in the adult rat studied by anterograde transport of HRP conjugates." Experimental Brain Research **99**: 233-246.
Furuta, T., K. Nakamura and M. Deschenes (2006). "Angular tuning bias of vibrissa-responsive cells in the paralemniscal pathway." Journal of Neuroscience **26**(41): 10548-10557.
Furuta, T., E. Timofeeva, K. Nakamura, K. Okamoto-Furuta, M. Togo, T. Kaneko and M. Deschenes (2008). "Inhibitory gating of vibrissal inputs in the brainstem." J Neurosci **28**(8): 1789-1797.
Furuta, T., N. Urbain, T. Kaneko and M. Deschenes (2010). "Corticofugal control of vibrissa-sensitive neurons in the interpolaris nucleus of the trigeminal complex." J Neurosci **30**(5): 1832-1838.
Gaspard, J. C., 3rd, G. B. Bauer, D. A. Mann, K. Boerner, L. Denum, C. Frances and R. L. Reep (2017). "Detection of hydrodynamic stimuli by the postcranial body of Florida manatees (Trichechus manatus latirostris)." J Comp Physiol A Neuroethol Sens Neural Behav Physiol **203**(2): 111-120.
Gibson, J. M. and W. I. Welker (1983). "Quantitative Studies of Stimulus Coding in First-Order Vibrissa Afferents of Rats. 1. Receptive Field Properties and Threshold Distributions." Somatosensory Research **1**(1): 51-67.
Ginter, C. C., T. J. DeWitt, F. E. Fish and C. D. Marshall (2012). "Fused traditional and geometric morphometrics demonstrate pinniped whisker diversity." PLoS One **7**(4): e34481.
Graff, M. M., H. M. Belli, S. Wiezkotten, Y. Kruger, G. Dehnhardt and M. J. Z. Hartmann ((in preparation)). "Three-dimensional morphology of the vibrissal array of the harbor seal (Phoca vitulina).".
Grant, R. A., M. G. Delaunay and S. Haidarliu (2017). "Mystacial Whisker Layout and Musculature in the Guinea Pig (Cavia porcellus): A Social, Diurnal Mammal." Anat Rec (Hoboken) **300**(3): 527-536.
Grant, R. A., S. Haidarliu, N. J. Kennerley and T. J. Prescott (2013). "The evolution of active vibrissal sensing in mammals: evidence from vibrissal musculature and function in the marsupial opossum Monodelphis domestica." J Exp Biol **216**(Pt 18): 3483-3494.
Grant, R. A., B. Mitchinson, C. W. Fox and T. J. Prescott (2009). "Active touch sensing in the rat: anticipatory and regulatory control of whisker movements during surface exploration." Journal of Neurophysiology **101**(2): 862-874.
Green, D. G., M. K. Powers and M. S. Banks (1980). "Depth of focus, eye size, and visual acuity." Vision Res **20**: 827-825.
Grinevich, V., M. Brecht and P. Osten (2005). "Monosynaptic pathway from rat vibrissa motor cortex to facial motor neurons revealed by lentivirus-based axonal tracing." J Neurosci **25**(36): 8250-8258.
Groh, J. M. (2001). "Converting neural signals from place codes to rate codes." Biological Cybernetics **85**: 159-165.
Gunduz, I., M. Jaarola, C. Tez, C. Yeniyurt, P. D. Polly and J. B. Searle (2007). "Multigenic and morphometric differentiation of ground squirrels (Spermophilus, Scuiridae, Rodentia) in Turkey, with a description of a new species." Molecular Phylogenetics and Evolution **43**(3): 916-935.
Haidarliu, S. and E. Ahissar (2001). "Size gradients of barreloids in the rat thalamus." Journal of Comparative Neurology **429**(3): 372-387.
Haidarliu, S., D. Kleinfeld and E. Ahissar (2013). "Mediation of muscular control of rhinarial motility in rats by the nasal cartilaginous skeleton." Anat Rec (Hoboken) **296**(12): 1821-1832.
Haidarliu, S., E. Simony, D. Golomb and E. Ahissar (2010). "Muscle architecture in the mystacial pad of the rat." Anat Rec (Hoboken) **293**(7): 1192-1206.
Hall, T. M., K. Nazarpour and A. Jackson (2014). "Real-time estimation and biofeedback of single-neuron firing rates using local field potentials." Nat Commun **5**: 5462.
Hartline, H. K. (1937). "The response of single optic nerve fibers of the vertibrate eye to illumination of the retna." American Journal of Physiology **121**: 400–415.
Hartmann, M. J. (2009). "Active touch, exploratory movements, and sensory prediction." Integrated Comparative Biology **49**(6): 681-690.
Hartmann, M. J., N. J. Johnson, R. B. Towal and C. Assad (2003). "Mechanical characteristics of rat vibrissae: Resonant frequencies and damping in isolated whiskers and in the awake behaving animal." Journal of Neuroscience **23**(16): 6510-6519.
Hartmann, M. J. Z. (2015). "Vibrissal Mechanical Properties." Scholarpedia.
Harvey, A., R. Bermejo and H. P. Zeigler (2009). "Discriminative whisking in the head-fixed rat: optoelectronic monitoring during tactile detection and discrimination tasks." Somatosensory & Motor Research **18**(3): 211-222.
Hausman, L. A. (1930). "Recent studies of hair structure relationships." Scientific Monthly **30**: 258-278.

Hayashi, H. (1980). "Distributions of vibrissae afferent fiber collaterals in the trigeminal nuclei as revealed by intra-axonal injection of horseradish peroxidase." Brain Research **183**: 442-446.
Hemelt, M. E. and A. Keller (2007). "Superior sensation: superior colliculus participation in rat vibrissa system." BMC Neurosci **8**: 12.
Hemelt, M. E. and A. Keller (2008). "Superior colliculus control of vibrissa movements." J Neurophysiol **100**(3): 1245-1254.
Hemelt, M. E., E. E. Kwegyir-Afful, R. M. Bruno, D. J. Simons and A. Keller (2010). "Consistency of angular tuning in the rat vibrissa system." J Neurophysiol **104**(6): 3105-3112.
Hemmen, v. (2002). "The Map in Your Head: How Does the Brain Represent the Outside World?" CHEMPHYSCHEM **3**: 291 - 298.
Hill, D. N., R. Bermejo, H. P. Zeigler and D. Kleinfeld (2008). "Biomechanics of the vibrissa motor plant in rat: rhythmic whisking consists of triphasic neuromuscular activity." J Neurosci **28**(13): 3438-3455.
Hillenius, W. J. (1994). "Turbinates in Therapsids: Evidence for Late Permian Origins of Mammalian Endothermy." Evolution **48**(2): 207-229.
Hires, S. A., L. Pammer, K. Svoboda and D. Golomb (2013). "Tapered whiskers are required for active tactile sensation." Elife **2**: e01350.
Hires, S. A., L. Pammer, K. Svoboda and D. Golomb (2013). "Tapered whiskers are required for active tactile sensation." Elife **2**.
Hires, S. A., A. Schuyler, J. Sy, V. Huang, I. Wyche, X. Wang and D. Golomb (2016). "Beyond cones: an improved model of whisker bending based on measured mechanics and tapering." J Neurophysiol **116**(2): 812-824.
Hires, S. A. S., Adam; Sy, Jonathan; Huang, Vincent; Wyche, Isis; Wang, Xiyue; Golomb, David (2016). "Beyond Cones: An improved model of whisker bending based on measured mechanics and tapering." Journal of Neurophysiology: 1522-1598.
Hobbs, J. A., R. B. Towal and M. J. Hartmann (2015). "Probability distributions of whisker-surface contact: quantifying elements of the rat vibrissotactile natural scene." J Exp Biol **218**(Pt 16): 2551-2562.
Hobbs, J. A., R. B. Towal and M. J. Hartmann (2016). "Evidence for functional groupings of vibrissae across the rodent mystacial pad." PLoS Comput Biol **12**(1): e1004109.
Hobbs, J. A., R. B. Towal and M. J. Z. Hartmann (2016). "Evidence for Functional Groupings of Vibrissae across the Rodent Mystacial Pad." Plos Computational Biology **12**(1).
Hobbs, J. A., R. B. Towal and M. J. Z. Hartmann (2016). "Spatiotemporal Patterns of Contact Across the Rat Vibrissal Array During Exploratory Behavior." Frontiers in Behavioral Neuroscience **9**.
Huet, L. and M. Hartmann (2016). "Simulations of a Vibrissa Slipping along a Straight Edge and an Analysis of Frictional Effects during Whisking." IEEE Transactions on Haptics **PP**(99): 1-1.
Huet, L. A. and M. J. Hartmann (2014). "The search space of the rat during whisking behavior." J Exp Biol **217**(Pt 18): 3365-3376.
Huet, L. A. and M. J. Z. Hartmann (2014). "The search space of the rat during whisking behavior." Journal of Experimental Biology **217**(18): 3365-3376.
Huet, L. A., C. L. Schroeder and M. J. Hartmann (2015). "Tactile signals transmitted by the vibrissa during active whisking behavior." J Neurophysiol **113**(10): 3511-3518.
Hullar, T. E. (2006). "Semicircular canal geometry, afferent sensitivity, and animal behavior." Anat Rec A Discov Mol Cell Evol Biol **288**(4): 466-472.
Ibrahim, L. and E. A. Wright (1975). "Growth of rats and mice vibrissae under normal and some abnormal conditions." Journal of Embryology and Experimental Morphology **33**(JUL): 831-844.
Jacquin, M. F., J. j. Arends, W. E. Renehan, P. M. Waite and P. J. Shortland (2014). "Whisker-related circuitry in the trigeminal nucleus principalis: Topographic precision." Somatosensory and Motor Research **32**(1): 8-20.
Jacquin, M. F., M. Barcia and R. W. Rhoades (1989). "Structure-Function Relationships in Rat Brainstem Subnucleus Interpolaris: IV. Projection Neurons." THE JOURNAL OF COMPARATIVE NEUROLOGY **282**: 45-62.
Jacquin, M. F., N. L. Chiaia, J. H. Haring and R. W. Rhoades (1990). "Intersubnuclear connections within the rat trigeminal brainstem complex." Somatosensory & Motor Research **7**(4): 399–420.
Jacquin, M. F., J. P. Golden and R. W. Rhoades (1989). "Structure-Function Relationships in Rat Brainstem Subnucleus Interpolaris: III. Local Circuit Neurons." THE JOURNAL OF COMPARATIVE NEUROLOGY **282**: 24-44.

jacquin, M. F., W. E. Renehan, R. W. Rhoades and W. M. Panneton (1993). "Morphology and Topography of Identified Primary Merents in Trigeminal Subnuclei Principalis and Oralis." J Neurophysiol **70**(5): 1911-1936.
Jacquin, M. F., R. W. Rhoades and B. G. Klein (1995). "Structure-Function Relationships in Rat Brainstem Subnucleus Interpolaris. XI. Effects of Chronic Whisker Trimming From Birth." THE JOURNAL OF COMPARATIVE NEUROLOGY **356**: 200-224.
Jacquin, M. F., D. Woerner, A. M. Szczepanik, V. Riecker, R. D. Mooney and R. W. Rhoades (1986). "Structure-function relationships in the rat brainstem subnucleus interpolaris. I. Vibrissa primary afferents." THE JOURNAL OF COMPARATIVE NEUROLOGY **243**.
Jacquin, M. F., D. S. Zahm, T. A. Henderson, J. P. Golden, E. M. Johnson, W. E. Renehan and B. G. Klein (1993). "Structure-function relationships in the rat brainstem subnucleus interpolaris. X. mechanisms underlying enlarged spared whisker projections after infraorbital nerve injury at birth." The Journal of Neuroscience **13**(7): 2946-2964.
Jadhav, S. P. and D. E. Feldman (2010). "Texture coding in the whisker system." Current Opinion in Neurobiology **20**(3): 313-318.
Jin, T. E., V. Witzemann and M. Brecht (2004). "Fiber types of the intrinsic whisker muscle and whisking behavior." J Neurosci **24**(13): 3386-3393.
Jones, L. M., D. A. Depireux, D. J. Simons and A. Keller (2004). "Robust temporal coding in the trigeminal system." Science **304**(5679): 1986-1989.
Jones, L. M., S. Lee, J. C. Trageser, D. J. Simons and A. Keller (2004). "Precise temporal responses in whisker trigeminal neurons." J Neurophysiol **92**(1): 665-668.
Kan, Q. H., R. Rajan, J. Fu, G. Z. Kang and W. Y. Yan (2013). "Elastic modulus of rat whiskers-A key biomaterial in the rat whisker sensory system." Materials Research Bulletin **48**(12): 5026-5032.
Kao, J. C., S. D. Stavisky, D. Sussillo, P. Nuyujukian and K. V. Shenoy (2014). "Information Systems Opportunities in Brain–Machine Interface Decoders." Proceedings of the IEEE **102**(5): 666-682.
Kerr, F. W. L. and W. R. Lysak (1964). "Somatotopic Organization of Trigeminal-Ganglion Neurones." Arch Neurol. **11**(6): 593-602.
Khammes-El Homsi, N. and S. Aulagnier (2010). "Unexpected morphometric differentiation of the Algerian mouse, Mus spretus (Rodentia: Muridae) from Kabylie of Djurdjura (Algeria)." Mammalia **74**(2): 199-207.
Khan, A. G., M. Sarangi and U. S. Bhalla (2012). "Rats track odour trails accurately using a multi-layered strategy with near-optimal sampling." Nature Communications **3**.
Khatri, V., R. Bermejo, J. C. Brumberg, A. Keller and H. P. Zeigler (2009). "Whisking in air: encoding of kinematics by trigeminal ganglion neurons in awake rats." J Neurophysiol **101**(4): 1836-1846.
Kiltie, R. A. (2000). "Scaling of visual acuity with body size in mammals and birds Blackwell Science, Ltd." Functional Ecology **14**: 226–234.
Kimura, Y., L. L. Jacobs and L. J. Flynn (2013). "Lineage-specific responses of tooth shape in murine rodents (murinae, rodentia) to late Miocene dietary change in the Siwaliks of Pakistan." PLoS One **8**(10): e76070.
Kleinfeld, D., E. Ahissar and M. E. Diamond (2006). "Active sensation: insights from the rodent vibrissa sensorimotor system." Current Opinion in Neurobiology **16**(4): 435-444.
Kleinfeld, D., R. W. Berg and S. M. O'Connor (1999). "Anatomical loops and their electrical dynamics in relation to whisking by rat." Somatosensory & Motor Research **16**(2): 69.
Kleinfeld, D. and M. Deschenes (2011). "Neuronal Basis for Object Location in the Vibrissa Scanning Sensorimotor System." Neuron **72**(3): 455-468.
Kleinfeld, D., M. Deschenes, F. Wang and J. D. Moore (2014). "More than a rhythm of life: breathing as a binder of orofacial sensation." Nature Neuroscience **17**(5): 647-651.
Knutsen, P. M., A. Biess and E. Ahissar (2008). "Vibrissal kinematics in 3D: Tight coupling of azimuth, elevation, and torsion across different whisking modes." Neuron **59**(1): 35-42.
Knutsen, P. M., M. Pietr and E. Ahissar (2006). "Haptic object localization in the vibrissal system: behavior and performance." J Neurosci **26**(33): 8451-8464.
Koehl, M. A. R. (2006). "The fluid mechanics of arthropod sniffing in turbulent odor plumes." Chemical Senses **31**(2): 93-105.

Koenigswald, W. v., U. Anders, S. Engels, J. A. Schultz and I. Ruf (2010). "Tooth Morphology in Fossil and Extant Lagomorpha (Mammalia) Reflects Different Mastication Patterns." Journal of Mammalian Evolution **17**(4): 275-299.

Koka, K., H. G. Jones, J. L. Thornton, J. E. Lupo and D. J. Tollin (2011). "Sound pressure transformations by the head and pinnae of the adult Chinchilla (Chinchilla lanigera)." Hear Res **272**(1-2): 135-147.

Koralek, K., K. F. Jensen and H. P. Killackey (1988). "Evidence for two complementary patterns of thalamic input to the rat somatosensory cortex." Brain Research **463**: 346-351.

Krupa, D. J., M. S. Matell, A. J. Brisben, L. M. Oliveira and M. A. L. Nicolelis (2001). "Behavioral properties of the trigeminal somatosensory system in rats performing whisker-dependent tactile discriminations." Journal of Neuroscience **21**(15): 5752-5763.

Kwegyir-Afful, E. E., S. Marella and D. J. Simons (2008). "Response properties of mouse trigeminal ganglion neurons." Somatosensory & Motor Research **25**(4): 209–221.

Larkum, M. (2013). "A cellular mechanism for cortical associations: an organizing principle for the cerebral cortex." Trends Neurosci **36**(3): 141-151.

Latzke, P. M. and R. Hesse (1988). Textile Fasern: Rasterelektronenmikroskopie der Chemie- und Naturfassern. Frankfurt/Main, Deutscher Fachverlag.

Lefort, S., C. Tomm, J. C. Floyd Sarria and C. C. H. Petersen (2009). "The Excitatory Neuronal Network of the C2 Barrel Column in Mouse Primary Somatosensory Cortex." Neuron **61**(2): 301-316.

Leiser, S. C. and K. A. Moxon (2006). "Relationship between physiological response type (RA and SA) and vibrissal receptive field of neurons within the rat trigeminal ganglion." J Neurophysiol **95**(5): 3129-3145.

Leiser, S. C. and K. A. Moxon (2007). "Responses of trigeminal ganglion neurons during natural whisking behaviors in the awake rat." Neuron **53**(1): 117-133.

Lichtenstein, S., G. E. Carvell and D. J. Simons (1990). "Responses of rat trigeminal ganglion neurons to movements of vibrissae in different directions." Somatosensory & motor research **7**(1): 47–65.

Lindstedt, S. (2014). "Krogh 1929 or 'the Krogh principle'." J Exp Biol **217**(Pt 10): 1640-1641.

Lo, F., W. Guido and R. S. Erzurumlu (1999). "Electrophysiological Properties and Synaptic Responses of Cells in the Trigeminal Principal Sensory Nucleus of Postnatal Rats." Journal of Neurophysiology **82**(5): 2765-2775.

Lottem, E. and R. Azouz (2011). "A unifying framework underlying mechanotransduction in the somatosensory system." J Neurosci **31**(23): 8520-8532.

Lucianna, F. A., A. L. Albarracin, S. M. Vrech, F. D. Farfan and C. J. Felice (2016). "The mathematical whisker: A review of numerical models of the rat's vibrissa biomechanics." Journal of Biomechanics **49**(10): 2007-2014.

Ma, P. M. (1991). "The Barrelettes-Architectonic Vibrissal Representations in the Brainstem Trigeminal Complex of the Mouse. I. Normal Structural Organization." The Journal of Comparative Neurology **309**: 161-199.

Mameli, O., S. Stanzani, A. Russo, R. Romeo, R. Pellitteri, M. Spatuzza, M. A. Caria and P. L. De Riu (2008). "Hypoglossal nuclei participation in rat mystacial pad control." Pflugers Arch **456**(6): 1189-1198.

Marshall, K. L., M. Chadha, L. A. deSouza, S. J. Sterbing-D'Angelo, C. F. Moss and E. A. Lumpkin (2015). "Somatosensory substrates of flight control in bats." Cell Rep **11**(6): 851-858.

Martin, Y. B., P. Negredo, J. A. Villacorta-Atienza and C. Avendano (2014). "Trigeminal intersubnuclear neurons: morphometry and input-dependent structural plasticity in adult rats." J Comp Neurol **522**(7): 1597-1617.

Matesz, C. (1981). "Peripheral and central distribution of fibres of the mesencephalic trigeminal root in the rat " Neuroscience Letters **27**: 13-17.

Matsushita, M., M. Ikeda and N. Okado (1982). "The cells of origin of the trigeminothalamic, trigeminospinal and trigeminocerebellar projections in the cat." Neuroscience **7**(6): 1439-1454.

Matthews, D. W., M. Deschenes, T. Furuta, J. D. Moore, F. Wang, H. J. Karten and D. Kleinfeld (2015). "Feedback in the brainstem: an excitatory disynaptic pathway for control of whisking." J Comp Neurol **523**(6): 921-942.

McGlone, F. and D. Reilly (2010). "The cutaneous sensory system." Neurosci Biobehav Rev **34**(2): 148-159.

McGovern, K. A., C. D. Marshall and R. W. Davis (2015). "Are vibrissae viable sensory structures for prey capture in northern elephant seals, Mirounga angustirostris?" Anat Rec (Hoboken) **298**(4): 750-760.

Mehta S. B., Whitmer D., Figueroa R, Williams B. A. and D. Kleinfeld (2007). "Active Spatial Perception in the Vibrissa Scanning Sensorimotor System." PLoSBIOLOGY **5**(2): e15. doi:10.1371/journal.pbio.0050015.

Meister, M. C., D. (2013). "Rats maintain a binocular field centered on the horizon." F1000Research **2**: 4.

Meredith, R. W., J. E. Janecka, J. Gatesy, O. A. Ryder, C. A. Fisher, E. C. Teeling, A. Goodbla, E. Eizirik, T. L. L. Simão, T. Stadler, D. L. Rabosky, R. L. Honeycutt, J. J. Flynn, C. M. Ingram, C. Steiner, T. L. Williams, T. J. Robinson, A. Burk-Herrick, M. Westerman, N. A. Ayoub, M. S. Springer and W. J. Murphy (2011). "Impacts of the Cretaceous Terrestrial Revolution and KPg Extinction on Mammal Diversification." Science **334**(28): 521-524.

Meyer, H. S., D. Schwarz, V. C. Wimmer, A. C. Schmitt, J. N. Kerr, B. Sakmann and M. Helmstaedter (2011). "Inhibitory interneurons in a cortical column form hot zones of inhibition in layers 2 and 5A." Proc Natl Acad Sci U S A **108**(40): 16807-16812.

Meyer, H. S., V. C. Wimmer, M. Oberlaender, C. P. de Kock, B. Sakmann and M. Helmstaedter (2010). "Number and laminar distribution of neurons in a thalamocortical projection column of rat vibrissal cortex." Cereb Cortex **20**(10): 2277-2286.

Minnery, B. S. and D. J. Simons (2003). "Response Properties of Whisker-Associated Trigeminothalamic Neurons in Rat Nucleus Principalis." J Neurophysiol **89**: 40–56.

Mitchinson, B., R. A. Grant, K. Arkley, V. Rankov, I. Perkon and T. J. Prescott (2011). "Active vibrissal sensing in rodents and marsupials." Philos Trans R Soc Lond B Biol Sci **366**(1581): 3037-3048.

Mitchinson, B. and T. J. Prescott (2013). "Whisker movements reveal spatial attention: a unified computational model of active sensing control in the rat." PLoS Comput Biol **9**(9): e1003236.

Moore, J. D., M. Deschenes, T. Furuta, D. Huber, M. C. Smear, M. Demers and D. Kleinfeld (2013). "Hierarchy of orofacial rhythms revealed through whisking and breathing." Nature **497**(7448): 205-210.

Moore, J. D., N. Mercer Lindsay, M. Deschenes and D. Kleinfeld (2015). "Vibrissa self-motion and touch are reliably encoded along the same somatosensory pathway from brainstem through thalamus." PLoS Biol **13**(9): e1002253.

Mosconi, T., T. A. Woolsey and M. F. Jacquin (2010). "Passive vs. active touch-induced activity in the developing whisker pathway." Eur J Neurosci **32**(8): 1354-1363.

Muchlinski, M. N. (2010). "A comparative analysis of vibrissa count and infraorbital foramen area in primates and other mammals." J Hum Evol **58**(6): 447-473.

Muchlinski, M. N., E. L. Durham, T. D. Smith and A. M. Burrows (2013). "Comparative histomorphology of intrinsic vibrissa musculature among primates: implications for the evolution of sensory ecology and "face touch"." Am J Phys Anthropol **150**(2): 301-312.

Murlis, J., J. S. Elkinton and R. T. Carde (1992). "ODOR PLUMES AND HOW INSECTS USE THEM." Annual Review of Entomology **37**: 505-532.

Nakamura, S., T. Narumi, K. Tsutsui and T. Iijima (2009). "Difference in the functional significance between the lemniscal and paralemniscal pathways in the perception of direction of single-whisker stimulation examined by muscimol microinjection." Neurosci Res **64**(3): 323-329.

Ndiaye, A., G. Pinganaud, F. VanderWerf, C. Buisseret-Delmas and P. Buisseret (2000). "connections between the trigeminal mesencephalic nucleus and superior colliculus in the rat." Neuroscience Letters **294**(1): 17-20.

Neimark, M. A., M. L. Andermann, J. J. Hopfield and C. I. Moore (2003). "Vibrissa resonance as a transduction mechanism for tactile encoding." Journal of Neuroscience **23**(16): 6499-6509.

Nicolelis, M. (1996). "Beyond maps: A dynamic view of the somatosensory system." Brazilian Journal of Medical and Biological Research **29**(4): 401–412.

Nord, S. G. (1968). "Receptor Field Characteristics of Single Cells in the Spinal Trigeminal Complex." Experimental Neurology **21**: 236-243.

O'Doherty, J. E., M. A. Lebedev, Z. Li and M. A. Nicolelis (2012). "Virtual active touch using randomly patterned intracortical microstimulation." IEEE Trans Neural Syst Rehabil Eng **20**(1): 85-93.

O'Higgins, P., S. N. Cobb, L. C. Fitton, F. Groning, R. Phillips, J. Liu and M. J. Fagan (2011). "Combining geometric morphometrics and functional simulation: an emerging toolkit for virtual functional analyses." J Anat **218**(1): 3-15.

O'Higgins, P., L. C. Fitton, R. Phillips, J. Shi, J. Liu, F. Gröning, S. N. Cobb and M. J. Fagan (2012). "Virtual Functional Morphology: Novel Approaches to the Study of Craniofacial Form and Function." Evolutionary Biology **39**(4): 521-535.

Orsborn, A. L., S. Dangi, H. G. Moorman and J. M. Carmena (2012). "Closed-loop decoder adaptation on intermediate time-scales facilitates rapid BMI performance improvements independent of decoder initialization conditions." IEEE Trans Neural Syst Rehabil Eng **20**(4): 468-477.

Pammer, L., D. H. O'Connor, S. A. Hires, N. G. Clack, D. Huber, E. W. Myers and K. Svoboda (2013). "The Mechanical Variables Underlying Object Localization along the Axis of the Whisker." Journal of Neuroscience **33**(16): 6726-6741.

Pammer, L., D. H. O'Connor, S. A. Hires, N. G. Clack, D. Huber, E. W. Myers and K. Svoboda (2013). "The mechanical variables underlying object localization along the axis of the whisker." J Neurosci **33**(16): 6726-6741.

Paternoster, R., R. Brame, P. Mazerolle and A. Piquero (1998). "Using the correct statistical test for the equality of regression coefficients." Criminology **36**(4): 859-866.

Paul, F. A. M. (1972). "When? Why? and How?: Some Speculations on the Evolution of the Vertebrate Integument." American Zoologist **12**(1): 159-171.

Paxinos, G., C. Watson, M. Pennisi and A. Topple (1985). "Bregma, lambda and the interaural midpoint in stereotaxic surgery with rats of different sex, strain and weight." Journal of Neuroscience Methods **13**: 139-143.

Penfield, W. B., Edwin (1937). "Somatic Motor And Sensory Representation In The Cerebral Cortex Of Man As Studied By Electrical Stimulation." Brain **60**(4): 389–443.

Peschansk, M. (1984). "TRIGEMINAL AFFERENTS TO THE DIENCEPHALON IN THE RAT." Neuroscience **12**(2): 465-487.

Petersen, C. C. (2007). "The functional organization of the barrel cortex." Neuron **56**(2): 339-355.

Petreanu, L., T. Mao, S. M. Sternson and K. Svoboda (2009). "The subcellular organization of neocortical excitatory connections." Nature **457**(7233): 1142-1145.

Pfaff, C., T. Martin and I. Ruf (2015). "Bony labyrinth morphometry indicates locomotor adaptations in the squirrel-related clade (Rodentia, Mammalia)." Proc Biol Sci **282**(1809): 20150744.

Phelan, K. D. and W. M. Falls (1991). "THE SPINOTRIGEMINAL PATHWAY AND ITS SPATIAL RELATIONSHIP TO THE ORIGIN OF TRIGEMINOSPINAL PROJECTIONS IN THE RAT." Neuroscience **40**(2): 477-496.

Pierret, T., P. Lavellee and M. Deschenes (2000). "Parallel Streams for the Relay of Vibrissal Information through Thalamic Barreloids." The Journal of Neuroscience **20**(19): 7455–7462.

Pocock, R. I. (1914). "On the facial vibrissae of mammalia." Proceedings of the Zoological Society of London 889-912.

Populin, L. C. and T. C. T. Yin (1998). "Pinna Movements of the Cat during Sound Localization." J Neurosci **18**(11): 4233–4243.

Quist, B. W. and M. J. Hartmann (2012). "Mechanical signals at the base of a rat vibrissa: the effect of intrinsic vibrissa curvature and implications for tactile exploration." J Neurophysiol **107**(9): 2298-2312.

Quist, B. W., V. Seghete, L. A. Huet, T. D. Murphey and M. J. Hartmann (2014). "Modeling forces and moments at the base of a rat vibrissa during noncontact whisking and whisking against an object." J Neurosci **34**(30): 9828-9844.

Quist, B. W., V. Seghete, L. A. Huet, T. D. Murphey and M. J. Z. Hartmann (2014). "Modeling Forces and Moments at the Base of a Rat Vibrissa during Noncontact Whisking and Whisking against an Object." Journal of Neuroscience **34**(30): 9828-9844.

Rajan, R., J. P. Clement and U. S. Bhalla (2006). "Rats smell in stereo." Science **311**(5761): 666-670.

Ranade, S., B. Hangya and A. Kepecs (2013). "Multiple Modes of Phase Locking between Sniffing and Whisking during Active Exploration." Journal of Neuroscience **33**(19): 8250-8256.

Richardson, F., H. A. Peterson, W. V. Bingham and W. T. Shepherd (1909). "A study of Sensory control in the rat." Psychological Monographs **12**: 1-124.

Ritt, J. T., M. L. Andermann and C. I. Moore (2008). "Embodied information processing: Vibrissa mechanics and texture features shape micromotions in actively sensing rats." Neuron **57**(4): 599-613.

Robinson, R. (1981). "Rex mutant in the Norway rat." Journal of Heredity **72**(2): 131-132.

Rowe, T. B., T. E. Macrini and Z. X. Luo (2011). "Fossil evidence on origin of the mammalian brain." Science **332**(6032): 955-957.

Ruf, I., S. Frahnert and W. Maier (2009). "The chorda tympani and its significance for rodent phylogeny." Mammalian Biology - Zeitschrift für Säugetierkunde **74**(2): 100-113.

Rust, M. K. and W. J. Bell (1976). "Chemo-anemotaxis: a behavioral response to sex pheromone in nonflying insects." Proc Natl Acad Sci U S A **73**(7): 2524-2526.

Sane, S. P., A. Dieudonne, M. A. Willis and T. L. Daniel (2007). "Antennal mechanosensors mediate flight control in moths." Science **315**(5813): 863-866.
Sarko, D. K., F. L. Rice and R. L. Reep (2011). Mammalian tactile hair: divergence from a limited distribution. New Perspectives on Neurobehavioral Evolution. J. I. Johnson, H. P. Zeigler and P. R. Hof. Oxford, Blackwell Science Publ. **1225:** 90-100.
Schlanbusch, P., T. S. Jensen, D. Demontis, V. Loeschcke and C. Pertoldi (2011). "A craniometric investigation of the field vole Microtius agrestis in Denmark - population substructure." Hystrix-Italian Journal of Mammalogy **22**(2): 227-255.
Seneviratne, S. S. and I. L. Jones (2008). "Mechanosensory function for facial ornamentation in the whiskered auklet, a crevice-dwelling seabird." Behavioral Ecology **19**(4): 784-790.
Shiels, A. B., C. A. Flores, A. Khamsing, P. D. Krushelnycky, S. M. Mosher and D. R. Drake (2012). "Dietary niche differentiation among three species of invasive rodents (Rattus rattus, R. exulans, Mus musculus)." Biological Invasions **15**(5): 1037-1048.
Shortland P. J., Demaro J. A., Shang F., Waite P. M. E. and J. M. F. (1996). "Peripheral and Central Predictorsof Whisker Afferent Morphology in the Rat Brainstem." THE JOURNAL OF COMPARATIVE NEUROLOGY **375**(481-501).
Shoykhet, M., D. Doherty and D. J. Simons (2000). "Coding of deflection velocity and amplitude by whisker primary afferent neurons: implications for higher level processing." Somatosensory & Motor Research **17**(2): 171–180.
Shoykhet, M., P. Shetty, B. S. Minnery and D. J. Simons (2003). "Protracted Development of Responses to Whisker Deflection in Rat Trigeminal Ganglion Neurons." J Neurophysiol **90**: 1432–1437.
Simons, D. J. (1978). "Response properties of vibrissae units in rat si somatosensory neocortex " Journal of Neurophysiology **41**(3): 798-820.
Simpson, J. I. and W. Graf (1981). "EYE-MUSCLE GEOMETRY AND COMPENSATORY EYE MOVEMENTS IN LATERAL-EYED AND FRONTAL-EYED ANIMALS." Ann N Y Acad Sci **374**: 20-30.
Smear, M., R. Shusterman, R. O'Connor, T. Bozza and D. Rinberg (2011). "Perception of sniff phase in mouse olfaction." Nature **479**(7373): 397-U149.
Smola, A. and S. Vishwanathan (2008). "Introduction to Machine Learning." Cambridge University, UK: 32-34.
Solomon, J. H. and M. J. Z. Hartmann (2008). "Artificial Whiskers Suitable for Array Implementation: Accounting for Lateral Slip and Surface Friction." Ieee Transactions on Robotics **24**(5): 1157-1167.
Solomon, J. H. and M. J. Z. Hartmann (2010). "Extracting object contours with the sweep of a robotic whisker using torque information." International Journal of Robotics Research **29**: 1233-1245.
Solomon, J. H. and M. J. Z. Hartmann (2011). "Radial distance determination in the rat vibrissal system and the effects of Weber's law." Philosophical Transactions of the Royal Society B-Biological Sciences **366**(1581): 3049-3057.
Sosnik, R., S. Haidarliu and E. Ahissar (2001). "Temporal Frequency of Whisker Movement. I. Representations in Brain Stem and Thalamus." J Neurophysiol **86**(1): 339–353.
Sreenivasan, V., K. Karmakar, F. M. Rijli and C. C. Petersen (2015). "Parallel pathways from motor and somatosensory cortex for controlling whisker movements in mice." Eur J Neurosci **41**(3): 354-367.
Steppan, S., R. Adkins and J. Anderson (2004). "Phylogeny and divergence-date estimates of rapid radiations in muroid rodents based on multiple nuclear genes." Syst Biol **53**(4): 533-553.
Sun, F. (2016). "Affine A Surface." Matlab File Exchange Retrieved June 30, 2017, from https://www.mathworks.com/matlabcentral/fileexchange/60502-affine-fit-x-.
Szwed, M., K. Bagdasarian, B. Blumenfeld, O. Barak, D. Derdikman and E. Ahissar (2006). "Responses of trigeminal ganglion neurons to the radial distance of contact during active vibrissal touch." J Neurophysiol **95**(2): 791-802.
Takatoh, J., A. Nelson, X. Zhou, M. M. Bolton, M. D. Ehlers, B. R. Arenkiel, R. Mooney and F. Wang (2013). "New modules are added to vibrissal premotor circuitry with the emergence of exploratory whisking." Neuron **77**(2): 346-360.
The, L., M. L. Wallace, C. H. Chen, E. Chorev and M. Brecht (2013). "Structure, function, and cortical representation of the rat submandibular whisker trident." J Neurosci **33**(11): 4815-4824.
The, L., M. L. Wallace, C. H. Chen, E. Chorev and M. Brecht (2013). "Structure, Function, and Cortical Representation of the Rat Submandibular Whisker Trident." Journal of Neuroscience **33**(11): 4815-4824.

Thurlow, W. R. and P. S. Runge (1967). "Effect of Induced Head Movements on Localization of Direction of Sounds." The Journal of the Acoustical Society of America **42**(2): 480-488.
Timofeeva, E., P. Lavellee, D. Arsenault and M. Deschenes (2004). "Synthesis of Multiwhisker-Receptive Fields in Subcortical Stations of the Vibrissa System." J Neurophysiol **91**: 1510–1515.
Timofeeva, E., C. Merette, C. Emond, P. Lavallee and M. Deschenes (2003). "A Map of Angular Tuning Preference in Thalamic Barreloids." The Journal of Neuroscience **23**(33): 10717–10723.
Towal, R. B. and M. J. Hartmann (2008). "Variability in velocity profiles during free-air whisking behavior of unrestrained rats." J Neurophysiol **100**(2): 740-752.
Towal, R. B., B. W. Quist, V. Gopal, J. H. Solomon and M. J. Z. Hartmann (2011). "The Morphology of the Rat Vibrissal Array: A Model for Quantifying Spatiotemporal Patterns of Whisker-Object Contact." Plos Computational Biology **7**(4).
Urbain, N. and M. Deschenes (2007). "Motor cortex gates vibrissal responses in a thalamocortical projection pathway." Neuron **56**(4): 714-725.
van Breugel, F. and M. H. Dickinson (2014). "Plume-tracking behavior of flying Drosophila emerges from a set of distinct sensory-motor reflexes." Curr Biol **24**(3): 274-286.
van der Loos, H. and T. A. Woolsey (1973). "Somatosensory Cortex: Structural Alterations following Early Injury to Sense Organs." Science **179**(4071): 395-398.
Van Horn, R. N. (1970). "Vibrissae Structure in the Rhesus Monkey." Folia Primatol **13**: 241–285.
Varga, Z. s., H. Jia, B. Sakmann and A. Konnerth (2011). "Dendritic coding of multiple sensory inputs in single cortical neurons in vivo." Proceedings of the National Academy of Sciences of the United States of America **108**(37): 15420.
Veinante, P. and M. Deschenes (1999). "Single- and Multi-Whisker Channels in the Ascending Projections from the Principal Trigeminal Nucleus in the Rat." The Journal of Neuroscience **19**(12): 5085–5095.
Veinante, P., M. F. Jacquin and M. Deschenes (2000). "Thalamic Projections From the Whisker-Sensitive Regions of the Spinal Trigeminal Complex in the Rat." THE JOURNAL OF COMPARATIVE NEUROLOGY **420**: 233–243.
Vickers, N. J. (2000). "Mechanisms of animal navigation in odor plumes." Biol Bull **198**(2): 203-212.
Vincent, S. B. (1912). "The Function of the Vibrissae In the Behavior of the White Rat." Animal Behavior Monographs **1**(5): 84.
Vincent, S. B. (1913). "The tactile hair of the white rat." Journal of Comparative Neurology **23**(1): 1-35.
Voges, D., K. Carl, G. J. Klauer, R. Uhlig, C. Schilling, C. Behn and H. Witte (2012). "Structural Characterization of the Whisker System of the Rat." IEEE Sensors Journal **12**(2): 332-339.
Wallace, D. J., D. S. Greenberg, J. Sawinski, S. Rulla, G. Notaro and J. N. D. Kerr (2013). "Rats maintain an overhead binocular field at the expense of constant fusion." Nature **498**(7452): 65-69.
Wallach A., K. Bagdasarian and E. Ahissar (2016). "On-going computation of whisking phase by mechanoreceptors." Nature Neuroscience **19**(3): 487–493.
Wang, D., Q. Zhang, Y. Li, Y. Wang, J. Zhu, S. Zhang and X. Zheng (2014). "Corrigendum: Long-term decoding stability of local field potentials from silicon arrays in primate motor cortex during a 2D center out task (2014 J. Neural Eng. 11 036009)." Journal of Neural Engineering **11**(4): 049501.
Weijnen, J. A. W. M. (1998). "Licking Behavior in the Rat: Measurement and Situational Control of Licking Frequency." Neuroscience and Biobehavioral Reviews **22**(6): 751–760.
Welker, C. (1971). "Microelectrode delineation of fine grain somatotopic organization of SmI cerebral neocortex in albino rat." Brain Research **26**(2): 259-275.
Welker, W. (1964). "Analysis of sniffing of the albino rat." Behaviour: 223-244.
Williams, C. M. and E. M. Kramer (2010). "The Advantages of a Tapered Whisker." Plos One **5**(1).
Williams, M. N., D. S. Zahrn and M. F. Jacquin (1994). "Differential Foci and Synaptic Organization of the Principal and Spinal Trigeminal Projections to the Thalamus in the Rat." European Journal of Neuroscience **6**: 429-453.
Wolfe, J., D. N. Hill, S. Pahlavan, P. J. Drew, D. Kleinfeld and D. E. Feldman (2008). "Texture coding in the rat whisker system: Slip-stick versus differential resonance." Plos Biology **6**(8): 1661-1677.
Wolfe, J., C. Mende and M. Brecht (2011). "Social Facial Touch in Rats." Behavioral Neuroscience **125**(6): 900-910.
Woolston, D. C., J. R. La Londe and J. M. Gibson (1983). "Corticofugal influences in the rat on responses of neurons in the trigeminal nucleus interpolaris to mechanical stimulation." Neuroscience Letters **36**: 43-48.

Xiang, C., J. j. Arends and M. F. Jacquin (2014). "Whisker-related circuitry in the trigeminal nucleus principalis: Ultrastructure." Somatosensory & Motor Research **31**(3): 141–151.
Yan, W., Q. Kan, K. Kergrene, G. Kang, X.-Q. Feng and R. Rajan (2013). "A truncated conical beam model for analysis of the vibration of rat whiskers." Journal of Biomechanics **46**(12): 1987-1995.
Yang, A., H. Belli, B. CS and M. Hartmann (2016). "Some effects of vibrissal geometry on the mechanical properties of vibrissae." Journal of Neurophysiology: in review.
Yang, A. and M. Hartmann (2016). "Whisking kinematics enables object localization in head-centered coordinates based on tactile information from a single vibrissa." Frontiers in Behavioral Neuroscience: in review.
Yang, A. E., H. M. Belli, B. C. S. and M. J. Z. Hartmann (2016). "Some effects of vibrissal geometry on the mechanical properties of vibrissae." Journal of Neurophysiology: in review.
Yang, A. E. T. and M. J. Z. Hartmann (2016). "Whisking Kinematics Enables Object Localization in Head-Centered Coordinates Based on Tactile Information from a Single Vibrissa." Frontiers in Behavioral Neuroscience **10**: e00145.
Yoshimura, H. and S. A. Ueki (1981). "Mouse-killing and hyperemotionality in rats induced by three different kinds of experimental manipulations: A comparative study." Physiological Psychology **9**(3): 269-275.
Yu, C., D. Derdikman, S. Haidarliu and E. Ahissar (2006). "Parallel thalamic pathways for whisking and touch signals in the rat." PLoS Biol **4**(5): e124.
Yu, Y., M. Graff and M. J. Z. Hartmann (2016). "Mechanical responses of rat vibrissae to airflow." Journal of Experimental Biology **219**: 937-948.
Yu Y., G. M., Hartmann MJZ (2016). "Mechanical responses of rat vibrissae to airflow." Journal of Experimental Biology **In Press**.
Yu, Y. S. W., M. M. Graff, C. S. Bresee, Y. B. Man and M. J. Z. Hartmann (2016). "Whiskers aid anemotaxis in rats." Science Advances **2**(8): e1600716
Zhuang, C., J. Kubilius, M. Hartmann and D. Yamins (2017). Toward Goal-Driven Neural Network Models for the Rodent Whisker-Trigeminal System. Neural Information Processing Systems (NIPS) 30.
Zimmerfaust, R. K., C. M. Finelli, N. D. Pentcheff and D. S. Wethey (1995). "Odor Plumes and Animal Navigation in Turbulent Water-Flow - a Field-Study." Biological Bulletin **188**(2): 111-116.
Zucker, E. and W. I. Welker (1969). "Coding of somatic sensory input by vibrissae neurons in the rat's trigeminal ganglion." Brain Research **12**(1): 138-156.

APPENDIX

A.1 Supplementary materials for Chapter 2

Stage	
0	Gentle rats
	⬇ 3 days of gentling
1a	Fan 3 only, checkpoint off, correction on
	⬇ Rat performs ~30 loops within 20 minutes
1b	Fan 3 only, checkpoint on, correction on
	⬇ Rat performs ~30 loops within 20 minutes
2a	Fans 2 and 4 only, checkpoints off, correction on
	⬇ Rat performance > 60% correct
2b	Fans 2 and 4 only, checkpoints on, correction on
	⬇ Rat performance > 60% correct
3a	Fans 1, 3, and 5 only, checkpoints off, correction on
	⬇ Rat performance > 40% correct
3b	Fans 1, 3, and 5 only, checkpoints on, correction on
	⬇ Rat performance > 40% correct
4a	All five fans, checkpoints on, correction on
	⬇ Rat performance > 40% correct
4b	All five fans, checkpoints on, correction off
	⬇ Performance reaches a plateau
5a	**Experiment:** All five fans, checkpoints on, correction off, with vibrissae
	⬇ Rat performance > 40% correct for more than 10 sequential days
5b	**Experiment:** All five fans, checkpoints on, correction off, without vibrissae

Figure A.1.S1. Rats learned to perform the task through a series of behavioral shaping stages. Rats were trained in four stages of increasing difficulty. In stages 1 to 4 the number of fans was gradually increased from a single fan to five fans. Fans were added symmetrically about fan 3. Each stage was composed of two sub-stages to adjust the difficulty of the task. The criteria for stage advancement were

adjusted to reflect the difficulty of the training stage. Stage 5a marks the beginning of the experiment and was determined retroactively to begin when the rat performed greater than 40% for 10 consecutive days with an average performance above 55%. In stage 5b vibrissae were cut off and the experiment was performed for an additional 10 days.

Reward Criteria	
1	Rat is in the holding box. One fan is activated.
2	The door opens, releasing the rat into the arena.
3	The rat moves towards the hole located directly in front of the running fan.
4	The rat is required to cross the correct checkpoint trigger.
5	The rat is required to cross a circular trigger around the correct hole.
6	The rat goes down the hole and follows a tunnel to find a fresh water reward.
7	The rat runs up a ramp to return to the holding box, where it receives a second sugar water reward.
8	The rat begins the next trial.

Figure A.1.S2. Reward delivery was contingent on performance. (1) The rat started in the holding box and one of the five fans was activated. (2) After a ten second delay, the motorized door lifted automatically. (3) The rat left the holding box and ran towards the airflow source. (4) To prevent the rat from making a choice close to the fan, it was required to cross the checkpoint trigger before (5) reaching the hole corresponding to the activated fan. Note that when the rat reached any of the hole triggers, the fan was turned off and the holding box door was shut. In cases when the rat failed (chose either the first or second trigger incorrectly, or both), all rewards were withheld, but the rat was allowed to navigate through the tunnels as normal. (6) Upon the successful completion of steps 1 - 5 a solenoid valve opened beneath the table, making an audible click and releasing a fresh water reward. The rat travelled down the hole and through a tunnel system to the reward. (7) The rat then traversed a ramp back to the holding box

to complete the trial and receive a second sugar water reward. The second reward was contingent upon the rat having received the first reward. (8) The rat started another trial. This process was repeated for a minimum of 45 trials per day per rat. For control rats, fans were replaced with LEDs.

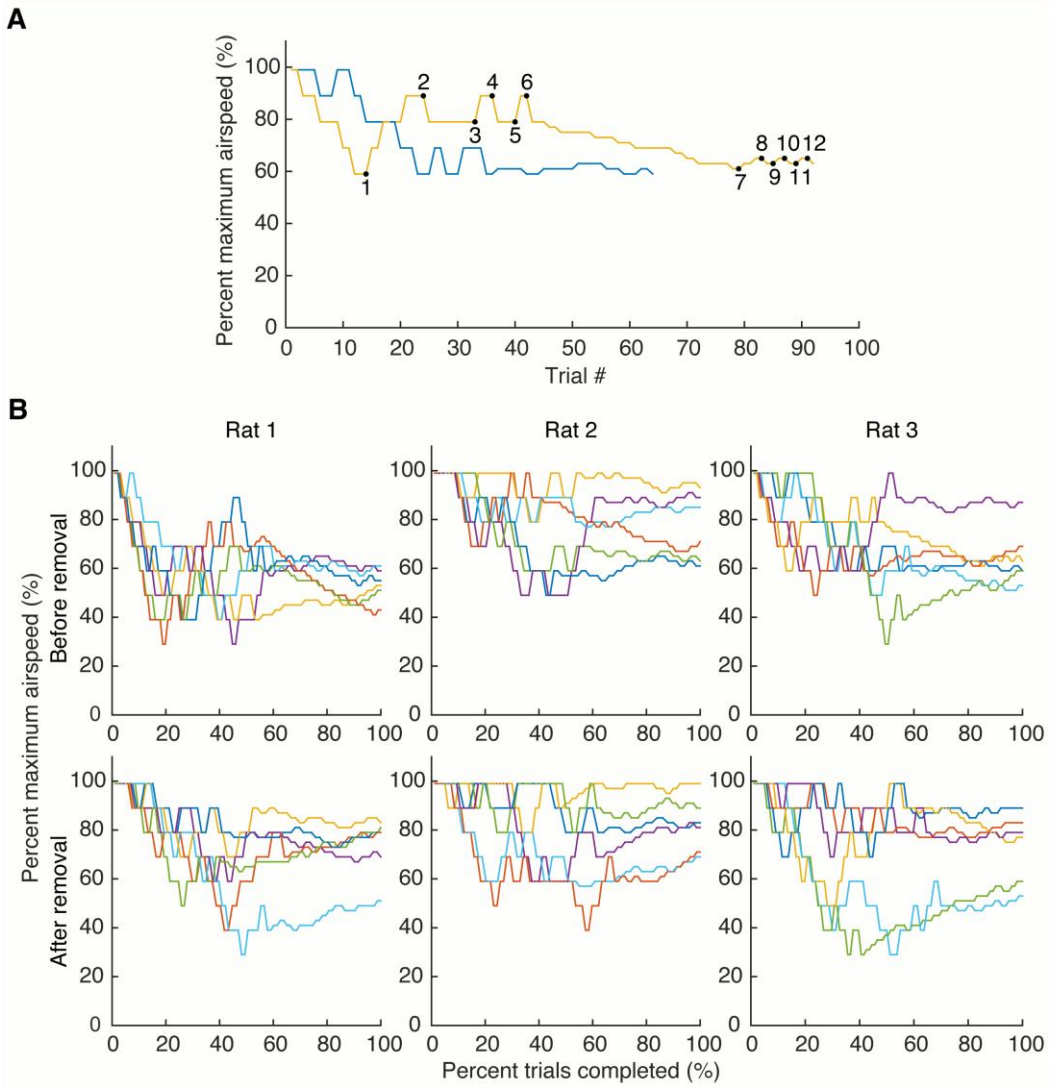

Figure A.1.S3. Fan speed was adjusted to determine rat localization thresholds. (A) Two days of typical performance of Rat 3 on the 2-up/2-down threshold experiment. Reversals for one day are labeled (black dots). Percent of maximum fan speed is shown as a function of trial number. (**B**) Performances of Rats 1, 2, and 3 six days before and six days after vibrissal removal are shown. Percent of maximum fan speed is shown as a function of percent trial completed. Days used are listed in table S3. Sequential days are color coded: blue; red; yellow; purple; green; cyan.

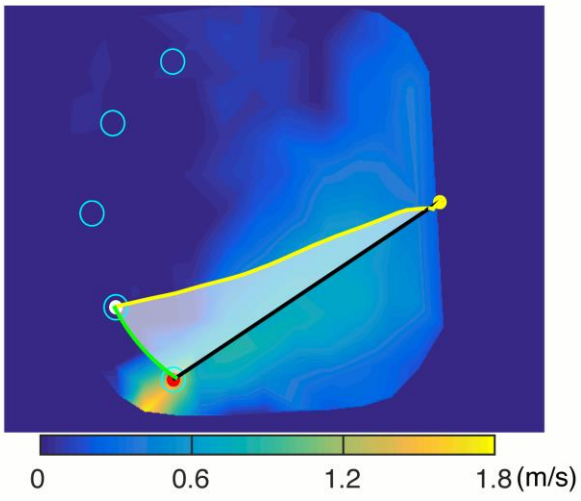

Figure A.1.S4. Path length deviation was quantified based on the rat's trajectory. The deviation was computed as the area enclosed by the straight-line path from the door to the activated fan (black line connecting the yellow dot to the red dot), the actual trajectory taken by the rat to the incorrect fan (yellow curve connecting yellow dot to white dot), and the arena boundary (green curve), divided by the length of the straight-line path.

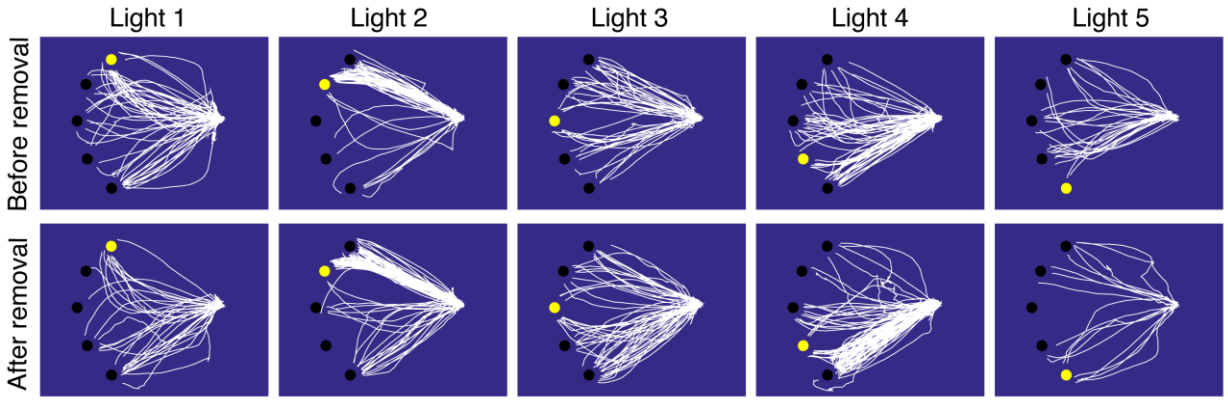

Figure A.1.S5. Vibrissal removal does not affect the rats' ability to find a light source. Trajectories of all incorrect trials for all three rats trained to localize a light source on the ten days before (top row) and after vibrissal removal (bottom row). Trajectories show equal deviation from the ideal straight-line path before and after vibrissal removal.

Table A.1.S1. Descriptive statistics for locomotion. No significant changes by group were observed in locomotor speed, number of pauses, or duration of pauses as the rats traversed the arena before and after whisker removal. A 0.075 m/s lower bound was imposed to exclude pauses from the locomotor speed analysis. Similarly, the minimum measurable duration of 50 ms (determined by the camera frame rate) imposed a *de facto* lower bound for the pause duration analysis.

	Group	Min.	Lower quartile	Median	Upper quartile	Max.	Skewness	Kurtosis
Locomotor speed (m/s)								
Before removal	**Airflow**	0.075	0.3450	0.8583	1.5405	5.3155	1.0428	3.6063
	Light	0.075	0.2510	0.7450	1.4405	5.2457	1.1565	3.8733
After removal	**Airflow**	0.075	0.3593	0.8347	1.4753	4.5891	1.052	3.6672
	Light	0.075	0.2454	0.6957	1.3971	4.8058	1.2167	4.0061
Number of pauses								
Before removal	**Airflow**	1	9	20	34	48	0.3868	1.8570
	Light	7	18	23.5	44	52	0.2166	1.6614
After removal	**Airflow**	3	8	12.5	36	48	0.5863	1.6860
	Light	16	21	32	46	57	0.3588	1.8714
Duration of pauses (s)								
Before removal	**Airflow**	0.05	0.25	0.55	1.10	18.1	5.1178	47.8660
	Light	0.05	0.4	0.75	1.5	29.7	6.5809	72.5227
After removal	**Airflow**	0.05	0.3	0.55	1.1	19.95	6.5353	64.3533
	Light	0.05	0.3	0.65	1.55	32.55	5.9915	61.8888

Table A.1.S2. Median values of the performance and deviation data. The Wilcoxon rank-sum test checks for differences in the median values. The trends in seen in the median values are similar to those expressed by the mean values shown in Figs. 2 and 3.

Median performance values (%)		
	Before vibrissal removal	**After vibrissal removal**
Rat 1	61.17	60.98
Rat 2	67.44	46.50
Rat 3	62.50	55.60
Rat 4	56.32	46.02
Rat 5	57.67	43.18
Rat 6	82.68	79.33
Rat 7	72.08	69.60
Rat 8	82.89	84.87
Median deviation values (cm)		
	Before vibrissal removal	**After vibrissal removal**
Rat 1	111.31	119.37
Rat 2	106.31	133.73
Rat 3	101.17	126.54
Rat 4	106.09	126.01
Rat 5	133.91	147.76
Rat 6	145.41	170.81
Rat 7	116.09	125.71
Rat 8	139.04	100.84

Table A.1.S3. Completion criteria for the localization threshold experiment vary by rat. For rat 2, only the shaded days were used in the analysis.

Rat 1				
	Before vibrissal removal		**After vibrissal removal**	
Day	**Number of reversals at 10% + number of reversals at 2%**	**Total number of trials**	**Number of reversals at 10% + number of reversals at 2%**	**Total number of trials**
1	**6+7**	**93**	**6+6**	**66**
2	**6+3**	**106**	**6+6**	**67**
3	**6+5**	**64**	**6+6**	**63**
4	**6+6**	**87**	**6+6**	**72**
5	**6+6**	**87**	**6+5**	**93**
6	**6+6**	**76**	**6+5**	**83**
Rat 2				
	Before vibrissal removal		**After vibrissal removal**	
Day	**Number of reversals at 10% + number of reversals at 2%**	**Total number of trials**	**Number of reversals at 10% + number of reversals at 2%**	**Total number of trials**
1	**6+3**	**61**	**6+6**	**50**
2	**6+7**	**68**	**6+5**	**82**
3	**6+5**	**88**	**2+0**	**25**
4	**5+0**	**47**	**6+5**	**80**
5	**6+6**	**63**	**6+4**	**75**
6	**6+0**	**57**	**6+7**	**78**
7	**6+7**	**69**	**3+0**	**35**
8	**6+6**	**61**	**2+0**	**41**
9	**6+1**	**64**	**6+6**	**69**
10	**6+6**	**54**	**6+1**	**91**
Rat 3				
	Before vibrissal removal		**After vibrissal removal**	
Day	**Number of reversals at 10% + number of reversals at 2%**	**Total number of trials**	**Number of reversals at 10% + number of reversals at 2%**	**Total number of trials**
1	**6+6**	**64**	**6+6**	**87**
2	**6+6**	**82**	**6+6**	**63**
3	**6+6**	**92**	**6+6**	**96**
4	**6+6**	**67**	**6+6**	**82**
5	**6+6**	**93**	**6+6**	**101**
6	**6+6**	**81**	**6+6**	**80**

A.2. Supplementary materials for Chapter 3

Table A.2.S1. Equations describing rat whisker array parameters in terms of row and column:

$$r_{bp} = -1.31\ Col + 0.127\ Col^2 + 9.46,\ \text{Adj. } R^2 = 0.51 \quad \text{(Eq. A.1.1)}$$

$$S = e^{-0.344\ Col + 4.36},\ \text{Adj. } R^2 = 0.86 \quad \text{(Eq. A.1.2)}$$

$$A = 0.00317\ Col + 0.00333,\ \text{Adj. } R^2 = 0.30 \quad \text{(Eq. A.1.3)}$$

$$\theta_w = 2.73\ Row + 8.21\ Col + 28.0,\ \text{Adj. } R^2 = 0.54 \quad \text{(Eq. A.1.4)}$$

$$\varphi_w = -17.8\ Row + 65.6,\ \text{Adj. } R^2 = 0.78 \quad \text{(Eq. A.1.5)}$$

$$\zeta_w = 16.3\ Col - 18.5\ Row + 40.5,\ \text{Adj. } R^2 = 0.50 \quad \text{(Eq. A.1.6)}$$

Table A.2.S2 Relationships between rat row and column position and basepoint coordinates:

Whisker ID	rbp (mm)	θbp (degrees)	φbp (degrees)
A1	7.73	-35.2	31.4
A2	6.73	-25.0	39.5
A3	6.06	-5.98	45.8
A4	5.95	17.6	50.9
A5	5.91	40.2	47.1
B1	7.80	-32.6	15.9
B2	6.84	-22.2	21.9
B3	6.03	-7.83	25.0
B4	5.46	12.4	26.3
B5	5.45	31.9	23.7
C1	8.46	-33.6	-0.677
C2	7.38	-22.9	3.95
C3	6.42	-8.63	5.66
C4	5.76	4.92	5.39
C5	5.56	23.3	1.60
C6	5.82	36.9	-1.63
C7	6.45	51.6	-5.50
D1	8.84	-33.5	-12.6
D2	7.77	-23.0	-9.79
D3	7.04	-12.2	-11.9
D4	6.36	1.63	-12.0
D5	6.12	13.2	-14.1
D6	6.31	28.5	-15.8
D7	6.30	42.5	-16.7
E2	8.42	-28.0	-21.6
E3	8.05	-16.8	-23.8
E4	7.33	-4.48	-26.3
E5	6.96	6.91	-28.0
E6	6.77	20.7	-29.2
E7	6.74	33.9	-29.7

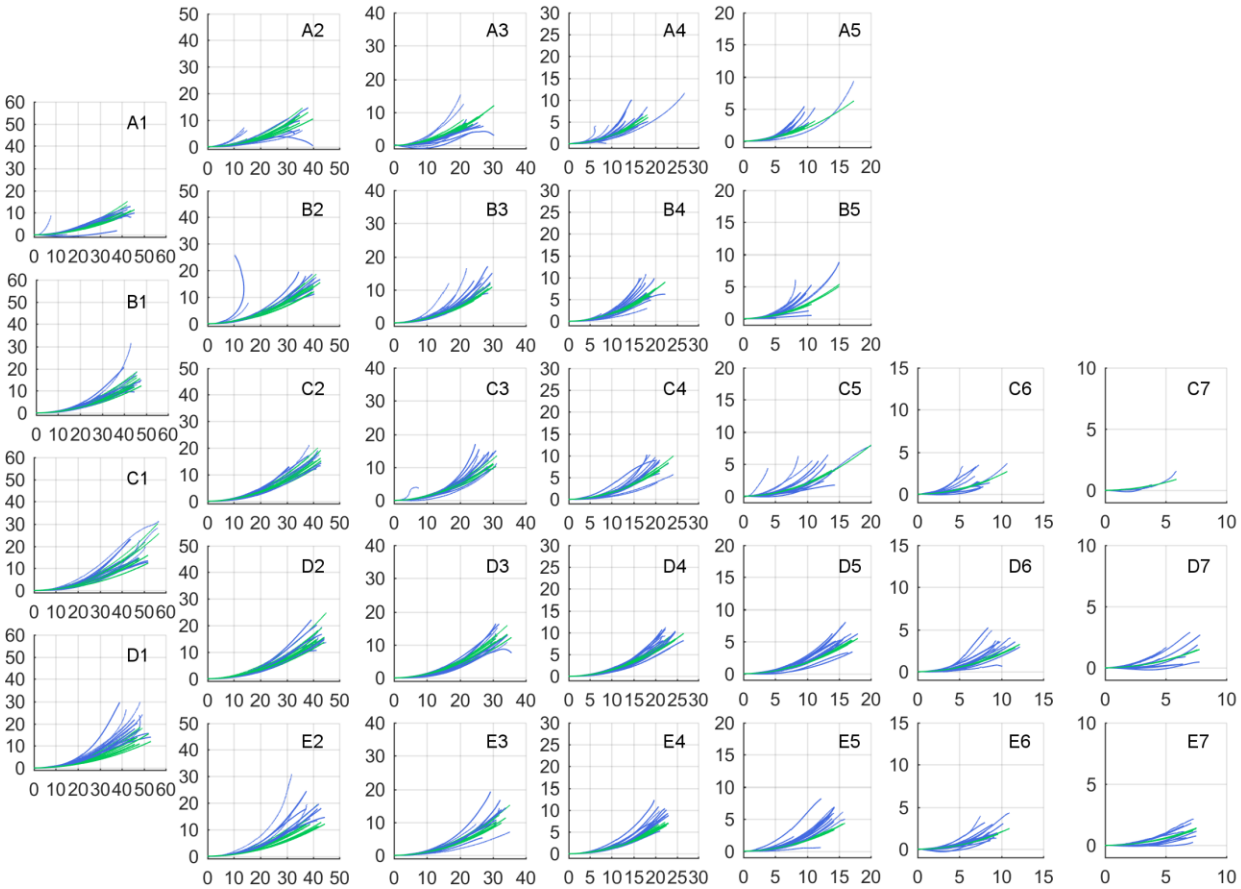

Figure A.2.S1 Equation 4.5 captures approximate whisker shape, but intrinsic curvature is highly variable, even for whiskers with the same row and colum identity. In all subplots both axes have units of mm. Axes are square and equal so that the whisker aspect ratio is depicted accurately. Each subplot traces for a different whisker identity (row and column. Blue traces illustrate the scanned whiskers, smoothed and oriented to align with the x-axis as described in Ch. 4.3 *Methods*. Green traces represent the fit for each whisker based on Eq. 4.5 from the main text. To create each equation-based whisker, x values were obtained from each experimentally-measured whisker and the equation $y = Ax^2$ was then plotted. There are exactly as many green traces (equation-based whiskers) in each subplot as there are blue traces (experimentally-measured whiskers). However, there appear to be fewer green traces because they overlap each other a great deal. The overlap occurs because θbp is very similar for all whisker with a given row and column identity. This figure illustrates that Eu. 4.5 captures the approximate shape of the whiskers, but cannot capture the high variability in whisker curvature, especially for the more rostral whiskers. Intrinsic whisker curvature is bounded by a strict upper threshold (Figure 4.6E), but exhibits high variability below that threshold.

A.3: Supplementary materials for Chapter 7

Table A.3.S1: Equations describing mouse whisker array parameters in terms of row and column:

$r_{bp} = 0.372\ \text{Row} - 0.215\ \text{Col} + 3.97$, Adj. $R^2 = 0.62$ (Eq. A.2.2)

$S = e^{-0.244\ Col + 3.33}$, Adj. $R^2 = 0.73$ (Eq. A.2.3)

$A = 0.00539\ \text{Col} - 0.00249$, Adj. $R^2 = 0.32$ (Eq. A.2.4)

$\theta_w = 12.8\ \text{Col} + 37.0$, Adj. $R^2 = 0.52$ (Eq. A.2.5)

$\varphi_w = -17.5\ \text{Row} + 68.7$, Adj. $R^2 = 0.76$ (Eq. A.2.6)

$\zeta_w = -12.2\ \text{Row} + 77.2$, Adj. $R^2 = 0.15$ (Eq. A.2.7)